CUBIC ARCHITECTURES ON THE NANOSCALE: THE SENSING AND CATALYTIC PROPERTIES OF SILVER AND GOLD DIMERS AND PLATINUM-SILVER ALLOYS

A Dissertation
Presented to
The Academic Faculty

by

Justin Andrew Bordley

In Partial Fulfillment
of the Requirements for the Degree
Doctor of Philosophy in the
School of Chemistry and Biochemistry

Georgia Institute of Technology
May 2016

CUBIC ARCHITECTURES ON THE NANOSCALE: THE SENSING AND CATALYTIC PROPERTIES OF SILVER AND GOLD DIMERS AND PLATINUM-SILVER ALLOYS

Approved by:

Dr. Mostafa A. El-Sayed, Advisor
School of Chemistry and Biochemistry
Georgia Institute of Technology

Dr. Christopher W. Jones
School of Chemical and Biomolecular Engineering
Georgia Institute of Technology

Dr. Z. John Zhang
School of Chemistry and Biochemistry
Georgia Institute of Technology

Dr. Joseph P. Sadighi
School of Chemistry and Biochemistry
Georgia Institute of Technology

Dr. Paul H. Wine
School of Chemistry and Biochemistry
Georgia Institute of Technology

Date Approved: March 25, 2016

ACKNOWLEDGEMENTS

The entirety of this thesis would not be possible without the significant contributions I have received from co-workers, friends, and family. Specifically I would like to acknowledge Dr. Mostafa El-Sayed. I cannot thank you enough for the knowledge that I have gained as your student. I have valued your input, support, and guidance throughout my work as a graduate student. Along with Dr. El-Sayed, I would like to acknowledge my committee members: Dr. Christopher Jones, Dr. Z. John Zhang, Dr. Joesph Sadighi, and Dr. Paul Wine. I have greatly appreciated your input and feedback on my graduate work. I would like to give a special acknowledgement to Dr. Christopher Jones. I would not have completed this program without your advice and feeback.

My thesis research was greatly enhanced through the many collaborative efforts put forth by fellow graduate students, post-docs, and research scientists. I would like to thank my group members, both past and present, for your support and encouragement. Specifically I would like to acknowledge Dr. Nasrin Hooshmand, Dr. Mahmoud Mahmoud, Brian Snyder, Dr. Megan Mackey, Dr. Lauren Austin, Dr. Rachel Near, Mena Aioub, Daniel O’Neil, Dr. Xiongwu Kang, Dr. Paul Szyzmanski, and Dr. Steven Hira. Also, I would like to thank all of the friends that I have made along the way. Your friendship cannot be replaced and I am eternally grateful.

Lastly, I would like to acknowledge my family. The strength, intelligence, and resilience that I have today would not be possible without your love and support. Thank you for never doubting me and always challenging me to accomplish my dreams. Most importantly I want to thank my wife, Dr. Chelsea Wyss Bordley. Thank you for putting up with me. Your encouragement over the past five years has driven me to achieve things that I never thought possible. I like you and I love you.

TABLE OF CONTENTS

LIST OF TABLES

LIST OF FIGURES

LIST OF SYMBOLS AND ABBREVIATIONS

nm	nanometer
PEMFC	Polymer Electrolyte Membrane Fuel Cell
LSPR	Localized Surface Plasmon Resonance
SERS	Surface Enhanced Raman Spectroscopy
A	pre-exponential factor
τ	decay constant
λ	wavelength
λ_0	peak wavelength of individual nanoparticle
s	separation distance
D	diameter of a sphere
γ	shape factor
a	major axis length
b	minor axis length
A_a	depolarization factor
CO	carbon monoxide
Ni	Nickel
Pt	Platinum
DFT	Density Functional Theory
Au	Gold
Ag	Silver
DDA	Discrete Dipole Approximation

k	magnetic field
E	electric field
a.u.	arbitrary units
L	edge length of a cube
LAP_1	longitudinal antenna plasmon
TCP_2	transverse cavity plasmon
D	length of individual nanoparticle along interparticle axis
d	separation distance between interacting dipoles
SF	sensitivity factor
V	volume of a theoretical system
r_{eff}	effective spherical radius of a theoretical system
π	pi
RIU	refractive index units
Al	Alumminum
Ga	Galium
Sb	Tin
n	refractive index
SPRS	Surface Plasmon Resonance Spectroscopy
Q_{ext}	extinction efficiency
C_{ext}	extinction cross section
D	length along diagonal of a cube
R	distance between interacting charge distributions
W	electrostatic interaction energy

Σ	summation
P	individual or atomic charge density
Φ	electromagnetic field
μ	dipole moment
Q	quadrupole moment
UV	Ultra Violet
α	dipole polarizability
$\mathbf{E_0}$	incident electric field vector
ε_m	dielectric permittivity of the surrounding medium
ε	dielectric permittivity of the metal
ε_0	vacuum perimitivity
ε_R	real dielectric permittivity
ε_I	imaginary dielectric permittivity
IR	Infra Red
κ	orientation factor
A	ampere
Å	angstrom
eV	electronvolt
a	lattice parameter
i	measured current
i_k	kinetic current
i_d	diffusion limited current
υ	kinematic viscocity

C_0	concentration of oxygen
D_0	diffusion coefficient of oxygen
F	Faradays constant
j	current density
j_k	kinetic current density
j_d	diffusion limited current density
lcd	low current density
hcd	high current density

SUMMARY

This thesis explores both the optical and catalytic properties of cubic shaped nanoparticles. The investigation begins with the sensing capabilities of cubic metal dimers. Of all the plasmonic solid nanoparticles, single Ag or Au nanocubes exhibit the strongest electromagnetic fields. When two nanoparticles are in close proximity to each other the formation of hot spots between plasmonic nanoparticles is known to greatly enhance these electromagnetic fields even further. The sensitivity of these electromagnetic fields as well as the sensitivity of the plasmonic extinction properties is important to the development of plasmonic sensing. However, an investigation of the electromagnetic fields and the corresponding sensing capabilities of cubic shaped dimers are currently lacking.

In Chapters 2-5 the optical properties of cubic dimers made of either silver or gold are examined as a function of separation distance, surrounding environment, and dimer orientation. A detailed DDA simulation of Au–Au and Ag-Ag dimers oriented in a face-to-face configuration is conducted in Chapter 2. In this Chapter a distance dependent competition between two locations for hot spot formation is observed. The effect of this competition on the sensing capabilities of these dimers is further explored in Chapters 3 and 4. This competition originates from the generation of two different plasmonic modes. Each mode is defined by a unique electromagnetic field distribution between the adjacent nanocubes.

In Chapter 4 the maximum value of the electromagnetic field intensity is investigated for each mode. Notably the magnitude of the electromagnetic field is not

directly proportional to its extinction intensity. Furthermore, the sensitivity of a plasmonic mode does not depend on its extinction intensity. The sensitivity is rather a function of the magnitude of the electromagnetic field intensity distribution. Also, the presence of a high refractive index substrate drastically affects the optical properties and subsequent sentivity of the dimer. In Chapter 5 the sensing properties of a cubic dimer is investigated as a function of orientation. As the separation distance of the nanocube dimer is decreased the orientation of the dimer drastically affects its coupling behavior. The expected dipole-dipole exponential coupling behavior of the dimer is found to fail at a separation distance of 14 nm for the edge-to-edge arrangement. The failure of the dipole-dipole coupling mechanism results from an increased contribution from the higher order multipoles (eg. quadrupole-dipole). This behavior begins at a separation distance of 6 nm for the face-to-face dimer. As a result, the relative ratio of the multipole to the dipole moment generated by the edge-to-edge dimer must be larger than the ratio for the face-to-face orientation.

In the last section of this thesis the catalytic properties of cubic nanoparticles composed of a platinum-silver alloy are investigated. The catalytic activity and selectivity towards a given reaction is intimately related to the physical and electronic structure of the catalyst. These cubic platinum-silver alloys are utilized as catalysts for the oxygen reduction reaction (ORR). A maximum enhancement in the specific activity (3.5 times greater than pure platinum) towards the ORR is observed for the cubic platinum-silver alloy with the lowest platinum content. This activity is investigated as a function of the physical structure of a cubic shaped catalyst as well as the electronic modifications induced by the formation of a platinum-silver alloy.

CHAPTER 1

CUBIC METAL NANOPARTICLES

1.1. Introduction

Metal nanoparticles are unique materials which exhibit both optical and electronic properties that are vastly different than what is observed in their bulk state. One of the earliest examples of this phenomenon can be found in the glass walls of the 1,600-year-old Roman Lycurgus cup[1]. The green and red color seen in Figure 1.1 is due to the inclusion of both gold and silver nanoparticles into the construction of this cup. However, gold and silver are widely known to be either yellow or grey in color. How was it possible to fabricate a piece of glass that is either red or green in color through the addition of materials which are either yellow or grey? The answer to this question is that the color of gold and silver nanoparticles is different than the color of their bulk counterparts. When the size of these metals is reduced to the nanometer regime, a new material is produced whose color indicates the generation of new and unique optical and electronic properties.

Figure 1.1. A Roman glass chalice depicting a scene involving King Lycurgus of Thrace can appear either jade green (left) or blood red (right) when illuminated with light from either the front (left) or the back (right)[1].

These new properties of metal nanomaterials are not restricted to the development of a new color. Decreasing the size of any metal below 100 nm can introduce new and advantageous electronic, optical, and physical properties[2, 3]. Since the construction of the Lycurgus cup, the utilization of various metal nanomaterials has proven to be an effective approach towards the development of new, sensitive, and cost effective products and catalysts within chemical industry. Current products and devices range from gold functionalized lateral flow immunoassays[4] (home pregnancy tests), to silver coated anti-microbial band aids[4], to even the now commonly utilized catalytic converter[3]. The development of new devices has largely been fueled by improvements in both the synthesis and characterization of metal nanoparticles within the last 30 years. For example, this new synthetic control has led to the generation of new optical[5-9], biomedical[10-19], and catalytic[20-26] applications which utilize metal nanoparticles.

Two important applications within this developing field are plasmonic nanoparticle sensors and polymer electrolyte membrane fuel cells (PEMFCs). However, the current implementation of plasmonic metal nanoparticles as sensing platforms for targeted molecular detection is limited by the current sensitivity[27]; and PEMFCs are limited by an expensive catalyst loading and subsequent cost[24]. Recent advancements that address these limitations have expanded beyond confining the size of a metal nanoparticle and now have begun to explore the effects of controlling its composition and shape. Of the various shapes that are now synthetically accessible, the nanocube is a nanoparticle shape which exhibits strong and unique optical and catalytic properties. However, the sensing capabilities of cubic plasmonic nanoparticles as well as the activity of cubic shaped metal catalysts have yet to be fully understood.

1.2. Cubic Metal Nanoparticles as Plasmonic Sensors

1.2.1 Optical Properties of Metal Nanoparticles

The optical properties of metal nanoparticles have been utilized within the world well before the origin of these properties was understood. The Romans unknowingly formed gold and silver nanoparticles within the glass of the Lycurgus cup, however, it was not until 1856 when Michael Faraday was the first to suggest the formation of small gold nanoparticles as the source of strong coloring found within the cup[27]. After Faraday's report of the strong red color produced by gold nanoparticles a German scientist named Gustav Mie was first to theoretically explain this phenomenon with a full solution to Maxwell's equations for a spherical nanoparticle of arbitrary size[28]. While this phenomenon now known as a localized surface plasmon resonance (LSPR) is not restricted to individual particles[29], consideration of systems beyond metal nanoparticles is out of the scope of this thesis. The following sections will focus on the origin of the

LSPR and the effect of nanoparticle shape on the resultant optical properties, electromagnetic field generation, and sensing capabilities.

1.2.1.1. Spherical Metal Nanoparticles

As the size of an individual particle becomes much smaller than the wavelength of light with which it is interacting, it can be assumed that the phase of the electric field felt by the particle is uniform. The interaction of a metal nanoparticle with an incident photon of light can then be reduced to an electrostatic interaction between the electrons of the material and the uniform electric field. This is known as the quasistatic approximation. When the frequency of the oscillating electric field is resonant with the oscillating response of the electrons within the material a LSPR is generated. A full mathematical description of the conditions which support a LSPR can be found in Appendix B; however, here this phenomenon can be generalized for a spherical metal nanoparticle. As seen in Figure 1.2 an incident electromagnetic field with the appropriate resonant wavelength induces a uniform oscillatory response of the free conduction band electrons within the metal[30-32].

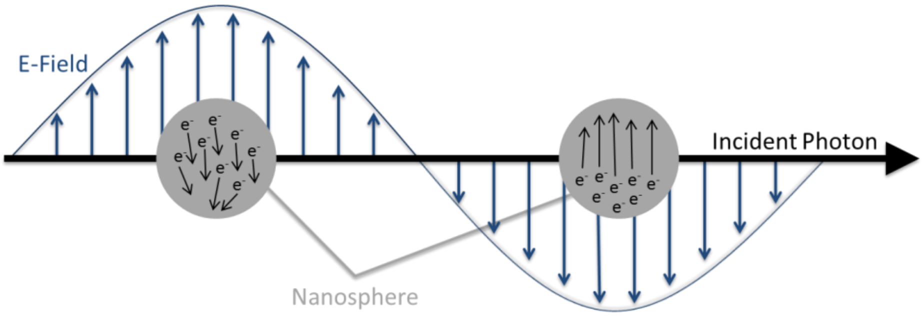

Figure 1.2. A generalized schematic for the plasmonic response of the “free” conduction band electrons to an incident resonant electromagnetic field. The direction of the oscillating electric field component of the incident electromagnetic field (blue arrows) induces a uniform polarization (black arrows) of the conduction band electrons which begin to oscillate. This response is known as a localized surface plasmon resonance (LSPR).

This resonant oscillation of the free conduction band electrons results in a strong extinction (absorption and scattering) of the incident field by the metal nanoparticle. Two metals that exhibit strong optical properties which originate near the visible region of the electromagnetic spectrum are silver and gold[33, 34]. Both the peak location of the gold and silver LSPR and the strength of their optical properties are highly desirable for new optical sensing devices. Their sensing capabilities are further enhanced by the generation of a strong electromagnetic field near the surface of these nanoparticles as the conduction band electrons couple with a resonant electromagnetic field. This property has been exploited most prominently for enhancing the detection limits of Raman spectroscopy and has led to the development the technique now known as surface enhanced Raman spectroscopy (SERS)[35, 36].

Since Mie’s first solution to Maxwell’s equations for a single spherical nanoparticle, the plasmonic systems examined have expanded to more complex architectures and compositions. The complexity of these solutions precludes exact solutions to Maxwell’s equations given current theoretical capabilities. However, various approximations and theoretical methods have been developed in the last 100 years which now provide a framework for studying new complex plasmonic systems[27]. It is now well understood that both the resonant wavelength which generates a LSPR and the electromagnetic field that is generated is strongly dependent on the size, shape, composition, and proximity of an individual nanoparticle to another material (either a second plasmonic nanoparticle or even a non-plasmonic substrate)[37, 38]. The focus of the following sections will be on the effect of the proximity of a neighboring nanoparticle as well as the shape of the individual nanoparticle on the sensing capabilities of silver and gold plasmonic systems and therefore only these external factors will be elaborated on further.

1.2.1.2. Sensitivity to a Neighboring Metal Nanoparticle

Recent advancements in the sensing capabilities of plasmonic nanoparticles in close proximity to each other have led to a new direction for plasmonic sensing. As two plasmonic nanoparticles are brought in close proximity to each other, a coupling between the resonant electronic oscillations of each nanoparticle results in a drastic increase in the electromagnetic field[33, 39] generated between the two nanoparticles and a characteristic red-shift in the LSPR[40-42] (Figure 1.3). As the separation distance is decreased the electromagnetic field that is generated near the surface of the particles increases on the order of 3500-4500 times greater than their single nanoparticle counterparts[33]. This enhanced electromagnetic field has provided improved detection and sensing capabilities over single plasmonic nanoparticles[43]. Also, the sensitivity of the LSPR to the separation distance of a nanoparticle has been utilized as a versatile targeted molecular sensing and distance determination technique[15-17, 43].

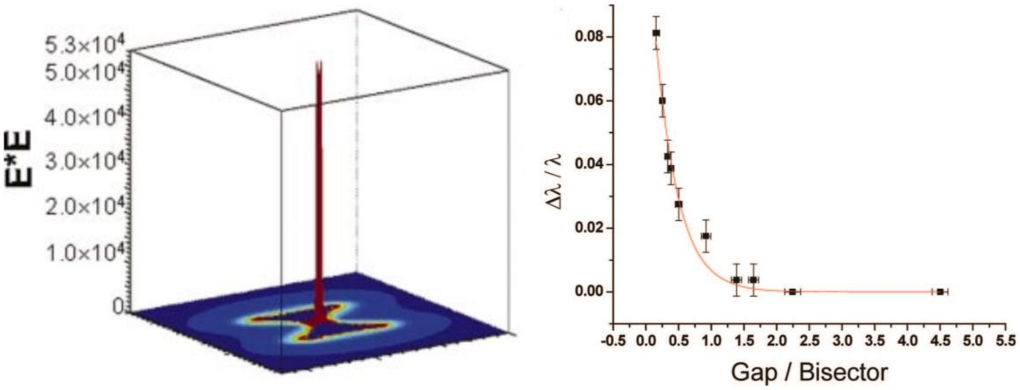

Figure 1.3. The calculated electromagnetic field enhancement between two prism shaped nanoparticled oriented tip-to-tip exhibit an increase in the electromagnetic field by four orders of magnitude (left)[33]. The fractional red shift in the LSPR peak position is plotted as a function of the gap distance between two prism shaped nanoparticles oriented tip-to-tip (right)[44].

An understanding of this coupling behavior was first approximated by the plasmon ruler equation[45]. A full description of the theoretical development of the plasmon ruler can be found in Appendix B; however this relationship can be summarized by utilizing the quasistatic approximation for a two particle system. Upon excitation of a system containing two particles with a resonant photon a uniform dipole would be formed by each nanoparticle. As a result, coupling between two nanoparticles can be estimated by an interaction between two individual dipoles across a set separation distance. This interaction has been shown to be very nearly approximated by a first order exponential decay behavior, $y = Ae^{-(x/\tau)}$. When expressed as a function of the fractional shift in the LSPR position ($\Delta\lambda/\lambda_0$) with respect to the separation distance normalized to the size of an individual nanoparticle (s/D) the plasmon ruler equation takes the form[45]:

$$\frac{\Delta\lambda}{\lambda_0} = Ae^{\left(\frac{-\frac{s}{D}}{\tau}\right)} \tag{4}$$

Where the pre-exponential factor, A, and decay constant, τ, can be used to qualitatively characterize both the coupling strength and decay length of a two particle system respectively. Since the derivation of the plasmon ruler equation, the coupling between gold and silver nanoparticle dimers has been explored further and it has been found that both the pre-exponential factor and the decay constant can vary depending on either the metal type or shape[46]. The decay constant that is observed for both silver and gold pairs is strongly dependent on the shape of the nanoparticles and exhibits larger decay constants for shapes with sharp corners or edges (ie. prisms and cubes)[46].

1.2.1.3. The Effect of Nanoparticle Shape

One of the first notable examples of the dependence of a LSPR on the shape of a gold or silver nanoparticle was an investigation of the optical properties of a gold nanorod[34]. The extinction spectrum of a rod shaped nanoparticle exhibits two regions of the electromagnetic spectrum which support a resonant plasmonic oscillation (Figure 1.4). These two plasmonic modes are considered the longitudinal and transverse plasmons[34]. Due to the shape of a nanorod, there are two primary axes (either the particle length/major axis or diameter/minor axis) along which polarization of the conduction band electrons can occur. Differences in length scale of these axes result in two resonances with different energies.

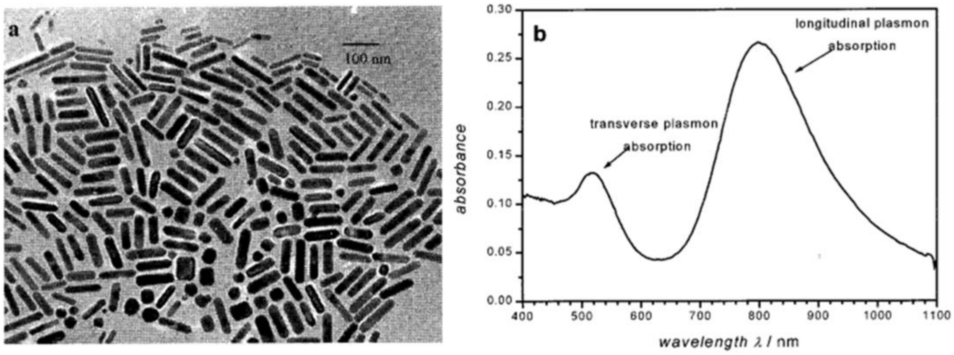

Figure 1.4. A transmission electron microscopy (TEM) image (a) and corresponding extinction spectrum (b) of rod shape gold nanoparticles[34].

The generation of the electromagnetic field near the surface of a nanoparticle is also sensitive to its shape. In 1982 Liao and Wokaun described the shape dependence of the electromagnetic field, known as the lightning rod effect[47], as a product of two simple factors[48]. The first describes the dipolar fields of the particle and the second is purely a geometric factor. It is this second factor, the geometric factor, which introduces a shape dependence to the generation of an electromagnetic field near the surface of the nanoparticle. Equation 3 describes this dependence and shows that the magnitude of the shape factor, γ, depends on the dimensions of the two axes a (long axis) and b (short axis)[48]:

$$\gamma = 1.5\left(\frac{a}{b}\right)^2 (1 - A_a) \qquad 3$$

where A_a is the depolarization factor which primarily determines the magnitude of the shift in the LSPR energy due to the shape of the nanoparticle. As the difference between the dimensions of the two primary axes increases (a<<b) and the shape of the nanoparticle becomes more needle-like, the shape factor also increases. This results in the generation of an intense electromagnetic field near the surface of the nanoparticle. A notable example of this effect can be seen in the electromagnetic field generated by a

cubic shaped nanoparticle[49]. The sharp corners and edges of a cubic shape have been found to induce a concentration of the electromagnetic field that is similar to the lightning rod effect. When the focusing of the electromagnetic field near the corners and edges of cubic shaped nanoparticles is coupled to the enhancements observed for two nanoparticles in close proximity to each other, a cubic dimer is a highly desirable sensing platform[35, 36, 50, 51].

1.3. Cubic Metal Nanoparticles as Catalysts

1.3.1 Catalytic Properties of Metal Nanoparticles

Reducing the size of an individual particle into this nanometer regime will also begin to introduce drastic increases in the surface area to volume ratio as well as changes in the chemisorption properties of the particle surface[52, 53]. Both of these aspects are important characteristics which control the activity and selectivity of catalyst materials. Since the rate of catalyzed reactions is directly related to the number of available active sites present on the catalyst[54], maximizing the surface area of a catalyst is a viable and effective approach towards maximizing reaction rates. Tuning the adsorption energy of reacting species on the surface of a catalyst is also a vital component to maximizing the activity and selectivity of a catalyst. The heat of adsorption of reactants on the surface of a catalyst is strongly dependent on the physical and electronic structure of the active sites present on the catalyst. Consequently, the synthetic control over the surface structure present on a nanoparticle catalyst is highly desirable for the development of new active and selective catalyst materials. The following sections will discuss current developments regarding the effects of catalyst size, composition and shape on the catalytic activity of metal nanoparticles.

1.3.1.1. The Effect of Catalyst Size

The colloidal synthesis of metallic nanoparticles with a controlled size, composition and shape has drastically increased in the last 30 years. As a result, the ability to exploit and begin to understand the effects of these characteristics on the catalytic activity of a metal nanoparticle catalyst has grown. The size of a metal catalyst is the most commonly exploited advantage of nanoparticle catalysts. Reducing the size of the catalyst will increase the number of active sites available on a given catalyst and will maximize the activity per unit mass of catalyst required for a specific process or device[54]. In this respect, reducing the dimensions of a catalyst to a nanometer size allows for a maximum utilization of the available atoms within a sample for catalysis and reduction in cost.

In 2010 Linic and co-workers found that the mass activity of a set of silver nanocubes, nanowires, and nanospheres towards ethylene epoxidation consistently increased as the size of the catalyst decreased regardless of the catalyst shape[55]. However, it is interesting to note that when the size of nanoparticle catalysts were decreased below 10 nm this trend is not consistently upheld[53]. This effect was also observed when the size of platinum nanoparticles utilized for the oxygen reduction reaction was reduced below 2 nm. As seen in Figure 1.5, both the specific activity and mass activity of the catalyst were lost when particles were reduced to this size. This was attributed an increased strength of oxygen adsorption which subsequently inhibited the desorption of the reduced product[56].

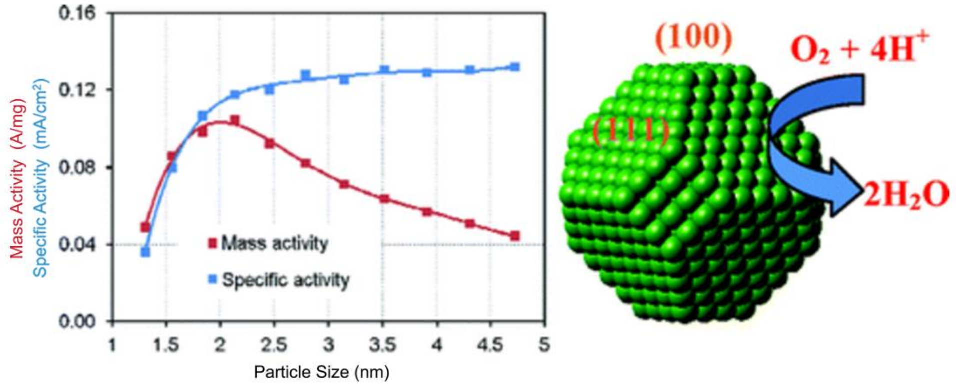

Figure 1.5. The specific and mass activities of spherical platinum nanoparticles towards the oxygen reduction reaction as a function of particle size (left). To the right a generalized picture of this reaction on the surface of spherical nanoparticles is depicted[56].

The performance of Ni nanoparticle catalysts utilized for the Fischer-Tropsch synthesis of hydrocarbons from synthesis gas was also found to be size dependent[3]. However, increasing the number of active sites was not the only advantage to decreasing the size of the catalyst used in this study. Here the heat of adsorption of CO was found to be dependent on the size of the Ni nanoparticle catalyst. The subsequent production of hydrocarbons could then be maximized by tuning the heat of adsorption of CO on the surface of these Ni catalysts. The differences between the size dependent properties of silver, platinum, and nickel nanoparticle catalysts for these various reactions introduces a high degree of complexity towards the development of new catalyst materials. However, it is clear that tuning the size of a metal nanoparticle catalyst is vital component to maximize catalytic activity for a given reaction.

1.3.1.2. The Effect of Catalyst Composition

Recent synthetic developments in alloy formation on the nanoscale have initiated an exploration into the effect of alloy composition on the activity of nanoparticle catalysts. In 2011 this effect was explored through investigation of the activity of Pt based alloy catalysts towards the oxidation of CO. This study showed the catalytic activity of the alloy catalyst correlated well with partially vacant Pt 5d orbitals which could be influenced by the alloy composition[57]. Similarly, the catalytic activity of gold nanoparticles towards the oxidation of glucose was found to be dependent on the alloy composition of the catalyst. The electronic structure of the gold surface atoms was modified from solid gold particles through the synthetic placement of gold atoms atop a palladium nanostructure. As seen in Figure 1.6, DFT studies suggested this arrangement of isolated gold atoms on the surface of the palladium nanostructure induced a slight electron transfer to the gold atoms. These electron rich gold atoms exhibited an increased electron transfer to molecular oxygen, resulting in an enhanced activity of the composite catalyst towards the subsequent oxidation of glucose[58].

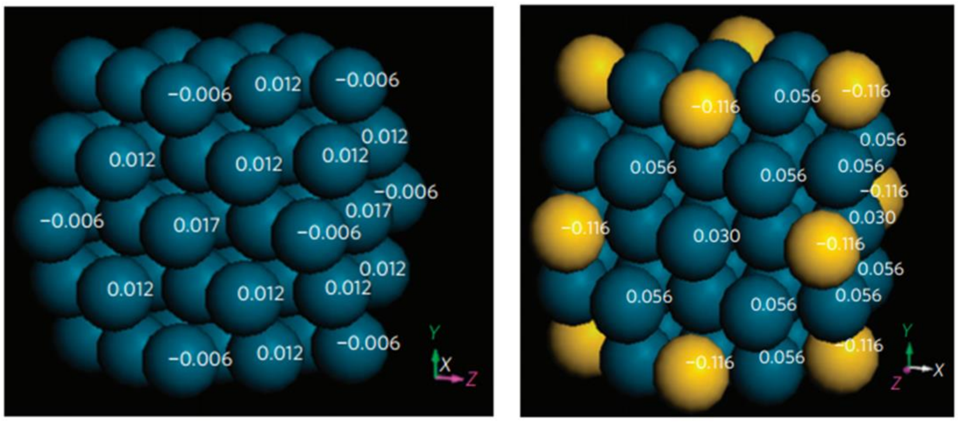

Figure 1.6. DFT calculations of Pd (left) and Au/Pd (right) nanocubes containing 55 atoms. Au atoms are displayed in yellow and Pd in blue, some values have been omitted for clarity[58].

Substantial attention has recently been devoted to the investigation of platinum based alloy nanocatalysts as cathode materials for PEMFCs. One aspect of PEMFCs that is currently inhibiting its commercialization is the sluggish kinetics of the oxygen reduction reaction on the platinum based cathode[24]. In 2004 Norskov and co-workers[59] theoretically investigated the activity of various metal catalysts towards the oxygen reduction reaction. As seen in Figure 1.7, the activity of these materials was strongly correlated to the oxygen and OH binding energies on the surface of each catalyst. It was suggested that the activity of platinum towards this reaction could be further enhanced through alloy formation. Upon alloying with a second metal the oxygen and OH binding energy on the catalyst surface could be tuned to maximize the catalyst activity[60].

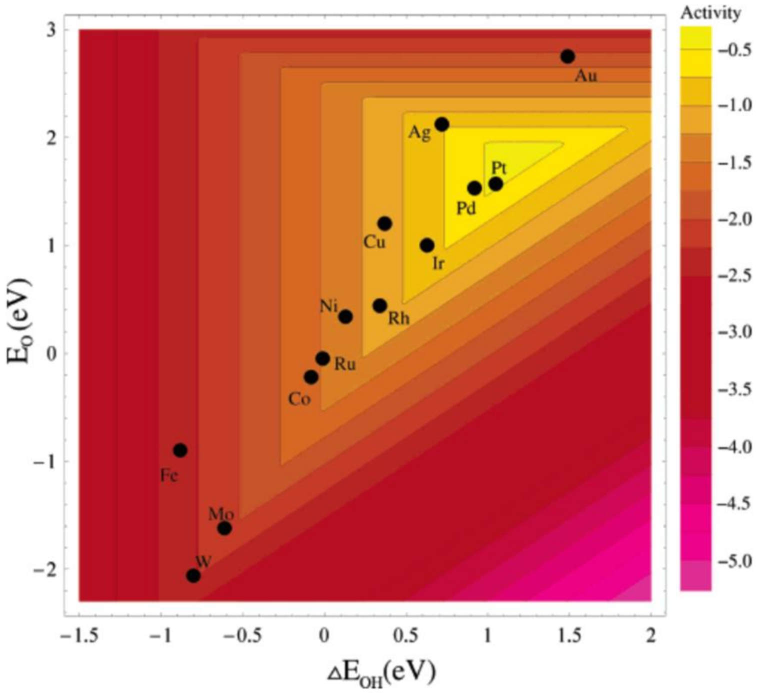

Figure 1.7. The theoretical adsorption energy of O and OH species on the surface of various metals is plotted as a function of the corresponding theoretical catalytic activity towards the oxygen reduction reaction. The catalytic activity increases from purple to yellow[59].

1.3.1.3. The Effect of Catalyst Shape

The shape of an individual nanoparticle has also been found to affect its catalytic activity. In 2004 El-Sayed and co-workers found that the activity of platinum nanoparticles towards the reduction of hexacyannoferrate was strongly dependent on the shape of the nanoparticle[61]. Cubic, tetrahedral, and roughly spherical platinum particles with sizes ranging from 5 to 7 nm were tested. A direct correlation between the catalytic activity and the composition of surface sites present for each shape was elucidated. The tetrahedral shaped catalyst exhibited the highest activity and was also estimated to contain the highest fraction of surface atoms in either edge or corners sites. These sites are characteristically under-coordinated compared to other sites present on the catalyst surface and are proposed to be more active towards this reaction.

The shape dependent catalytic properties of nanoparticles have been further explored since 2004. It is now known that the composition of surface sites present on the catalyst surface is not the only important aspect of shape which can contribute to activity. An aspect now under consideration is the lattice plane exposure of a catalytic nanomaterial. The identity of the exposed lattice plane on the surface of a nanoparticle can be precisely tuned through controlling the shape of the catalyst particle and has been found to influence both the selectivity and activity of the catalyst. A recent study on the platinum catalyzed hydrogenation of benzene exhibited a preferential production of cyclohexene on a (100) faceted platinum surface whereas a combination of both cyclohexane and cylcohexene was produced over a (111) surface. This selectivity dependence has also been attributed to preferential cis olefin production during alkene cis-trans isomerization reactions over (111) platinum surfaces[62]. As seen in Figure 1.8, the tetrahedral shaped catalysts favor the production of cis olefin production, whereas, spherical nanoparticles favor the production of the trans olefin.

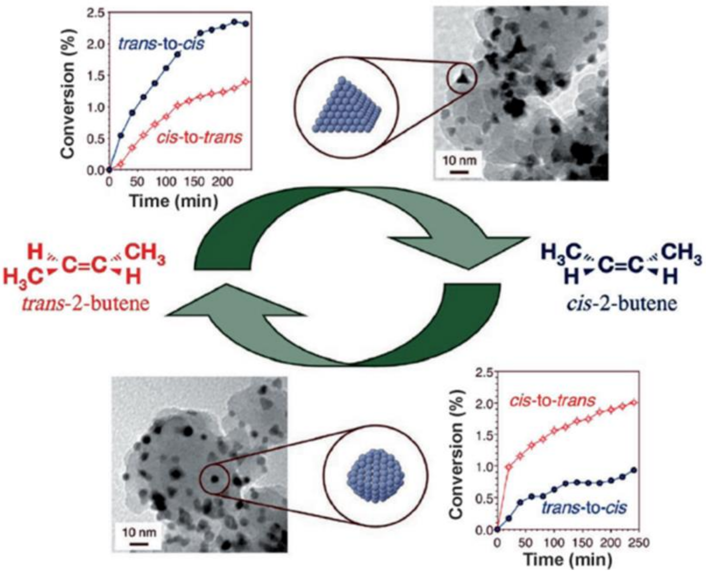

Figure 1.8. The catalytic selectivity of platinum nanoparticle catalysts as a function of catalyst shape. Tetrahedral nanoparticles (top) exhibit a selectivity for conversion to the cis isomer, whereas spherical nanoparticles (bottom) exhibit a selectivity for the trans isomer[62].

Beyond influencing the selectivity of a nanoparticle catalyst, the lattice plane exposure has also been shown to be a vital component in tuning the adsorption energy of reacting material on the surface of a catalyst. In 2007 an intriguing study of the catalytic activity of platinum alloy surfaces found a strong dependence of the catalytic activity towards the oxygen reduction reaction on the identity of the lattice plane on the surface of the catalyst. Three Pt_3Ni surfaces with either a (111), (100), or (110) morphology were investigated and the activity was found to increase in the order (100) < (110) < (111)[63]. It was suggested that the high activity observed for the (111) surface was due to a low surface coverage by OH_{ads}. The percent coverage of OH_{ads} on the (110) and (100) surfaces led to an inhibition of O_2 adsorption and thus a decrease in activity compared to the (111) surface. The complexity of enhancing the catalytic activity and selectivity of a nanoparticle catalyst is obvious and strongly reaction dependent. The specific interatomic distances and coordination arrangement which are exhibited by different lattice planes have proven to drastically influence the selectivity and activity of a catalyst material towards a given reaction.

These findings have highlighted the importance of controlling the lattice plane exposure, and thus the shape, of nanoparticle catalyst in order to develop new and improved catalyst materials. In particular, the uniform exposure of a cubic shaped nanoparticle by the (100) lattice plane offers a unique opportunity to investigate the catalytic properties of a (100) surface. If the composition of a platinum alloy could also be controlled without significant differences in the catalyst shape, this catalyst particle would allow for a controlled investigation of the catalytic activity of a (100) morphology with a tunable electronic surface structure (ie. d-band position/vacancy).

1.4. Concluding Remarks

The utilization of nanomaterials for sensing and catalytic applications is developing into a promising platform for industrial and commercial production. However, the development of the next generation of plasmonic nanoparticle sensors and metal nanoparticle catalysts hinges upon an increased understanding of the effect of nanoparticle shape on the plasmonic sensitivity and catalytic activity of these materials. With the recent advancements in the synthetic control of the size, composition and shape of various metal nanoparticle structures, the investigation of a variety of commercially viable nanomaterials is possible. A cubic architecture warrants specific interest due to its sharp corners and edges as well as the exclusive (100) lattice plane termination on its surface.

The aim of this thesis is to explore the effect of a cubic nanoparticle shape on the optical properties of plasmonic sensing systems as well as the effect of this shape on the catalytic properties of metal catalysts. Through a theoretical investigation of cubic shaped gold and silver dimers with small separation distances, a new understanding of the currently elusive development of high electromagnetic fields and sensitive optical properties can be achieved. The utilization of cubic shaped catalysts also offers a desirable platform to investigate the catalytic activity of the platinum (100) surface. When coupled with a precise control over alloy formation the cubic shape allows for a unique opportunity to experimentally investigate the ability to tune the chemisorption properties and resultant catalytic activity of a (100) surface.

1.5. References

(1) Merali, Z. This 1,600-Year-Old Goblet Shows that the Romans Were Nanotechnology Pioneers. *Smithsonian Mag.* [Online] **2013** September http://www.smithsonianmag.com/history/this-1600-year-old-goblet-shows-that-the-romans-were-nanotechnology-pioneers-787224/?no-ist (accessed March 10, 2016).

(2) S. Link and M. A. El-Sayed: Shape and Size Dependence of Radiative, Non-Radiative and Photothermal Properties of Gold Nanocrystals. *Int. Rev. Phys. Chem.* **2000**, *19*, 409-453.

(3) A. T. Bell: The Impact of Nanoscience on Heterogeneous Catalysis. *Science* **2003**, *299*, 1688-1691.

(4) W. Stark, P. Stoessel, W. Wohlleben and A. Hafner: Industrial Applications of Nanoparticles. *Chem. Soc. Rev.* **2015**, *44*, 5793-5805.

(5) S. Lal, S. Link and N. J. Halas: Nano-Optics from Sensing to Waveguiding. *Nat. Photonics* **2007**, *1*, 641-648.

(6) A. N. Shipway, E. Katz and I. Willner: Nanoparticle Arrays on Surfaces for Electronic, Optical, and Sensor Applications. *ChemPhysChem* **2000**, *1*, 18-52.

(7) C. E. H. Berger, T. A. M. Beumer, R. P. H. Kooyman and J. Greve: Surface Plasmon Resonance Multisensing. *Anal. Chem.* **1998**, *70*, 703-706.

(8) S. A. Maier and H. A. Atwater: Plasmonics: Localization and Guiding of Electromagnetic Energy in Metal/Dielectric Structures. *J. Appl. Phys.* **2005**, *98.1*, 011101.

(9) C. Ciracì, R. Hill, J. Mock, Y. Urzhumov, A. Fernández-Domínguez, S. Maier, J. Pendry, A. Chilkoti and D. Smith: Probing the Ultimate Limits of Plasmonic Enhancement. *Science* **2012**, *337*, 1072-1074.

(10) E. Dreaden, M. A. Mackey, X. Huang, B. Kang and M. A. El-Sayed: Beating Cancer in Multiple Ways Using Nanogold. *Chem. Soc. Rev.* **2011**, *40*, 3391-3404.

(11) I. H. El Sayed, X. Huang and M. A. El-Sayed: Surface Plasmon Resonance Scattering and Absorption of Anti-Egfr Antibody Conjugated Gold Nanoparticles in Cancer Diagnostics: Applications in Oral Cancer. *Nano Lett.* **2005**, *5*, 829-834.

(12) K. Sokolov, M. Follen, J. Aaron, I. Pavlova, A. Malpica, R. Lotan and R. Richards-Kortum: Real-Time Vital Optical Imaging of Precancer Using Anti-Epidermal

Growth Factor Receptor Antibodies Conjugated to Gold Nanoparticles. *Cancer Res.* **2003**, *63*, 1999-2004.

(13) A. M. Gobin, M. H. Lee, N. J. Halas, W. D. James, R. A. Drezek and J. L. West: Near-Infrared Resonant Nanoshells for Combined Optical Imaging and Photothermal Cancer Therapy. *Nano Lett.* **2007**, *7*, 1929-1934.

(14) X. Huang, X. Peng, Y. Wang, Y. Wang, D. M. Shin, M. A. El-Sayed and S. Nie: A Reexamination of Active and Passive Tumor Targeting by Using Rod-Shaped Gold Nanocrystals and Covalently Conjugated Peptide Ligands. *ACS Nano* **2010**, *4*, 5887 - 5896.

(15) G. Raschke, S. Kowarik, T. Franzl, C. Sönnichsen, T. A. Klar, J. Feldmann, A. Nichtl and K. Kürzinger: Biomolecular Recognition Based on Single Gold Nanoparticle Light Scattering. *Nano Lett.* **2003**, *3*, 935-938.

(16) T. Endo, K. Kerman, N. Nagatani, Y. Takamura and E. Tamiya: Label-Free Detection of Peptide Nucleic Acid−DNA Hybridization Using Localized Surface Plasmon Resonance Based Optical Biosensor. *Anal. Chem.* **2005**, *77*, 6976-6984.

(17) A. Haes, D. Stuart, S. Nie and R. Van Duyne: Using Solution-Phase Nanoparticles, Surface-Confined Nanoparticle Arrays and Single Nanoparticles as Biological Sensing Platforms. *J. Fluoresc.* **2004**, *14*, 355-367.

(18) C. R. Yonzon, D. A. Stuart, X. Zhang, A. D. McFarland, C. L. Haynes and R. P. Van Duyne: Towards Advanced Chemical and Biological Nanosensors—an Overview. *Talanta* **2005**, *67*, 438-448.

(19) O. V. Salata: Applications of Nanoparticles in Biology and Medicine. *J Nanobiotechnol* **2004**, *2*, 3.

(20) I. Moiseev: Catalysis: 2000 Ad1. *Kinet. Catal.* **2001**, *42*, 1-22.

(21) R. Cortright, R. Davda and J. A. Dumesic: Hydrogen from Catalytic Reforming of Biomass-Derived Hydrocarbons in Liquid Water. *Nature* **2002**, *418*, 964-967.

(22) J. Zheng, D. A. Cullen, R. V. Forest, J. A. Wittkopf, Z. Zhuang, W. Sheng, J. G. Chen and Y. Yan: Platinum–Ruthenium Nanotubes and Platinum–Ruthenium Coated Copper Nanowires as Efficient Catalysts for Electro-Oxidation of Methanol. *ACS Catal.* **2015**, *5*, 1468-1474.

(23) S. E. Voltz, C. R. Morgan, D. Liederman and S. M. Jacob: Kinetic Study of Carbon Monoxide and Propylene Oxidation on Platinum Catalysts. *Ind. Eng. Chem. Prod. Res. Dev.* **1973**, *12*, 294-301.

(24) H. A. Gasteiger, S. S. Kocha, B. Sompalli and F. T. Wagner: Activity Benchmarks and Requirements for Pt, Pt-Alloy, and Non-Pt Oxygen Reduction Catalysts for Pemfcs. *Appl. Catal., B* **2005**, *56*, 9-35.

(25) R. Burch, J. Breen and F. Meunier: A Review of the Selective Reduction of No X with Hydrocarbons under Lean-Burn Conditions with Non-Zeolitic Oxide and Platinum Group Metal Catalysts. *Appl. Catal., B* **2002**, *39*, 283-303.

(26) N. T. Phan, M. Van Der Sluys and C. W. Jones: On the Nature of the Active Species in Palladium Catalyzed Mizoroki–Heck and Suzuki–Miyaura Couplings–Homogeneous or Heterogeneous Catalysis, a Critical Review. *Adv. Synth. Catal.* **2006**, *348*, 609-679.

(27) S. K. Ghosh and T. Pal: Interparticle Coupling Effect on the Surface Plasmon Resonance of Gold Nanoparticles: From Theory to Applications. *Chem. Rev.* **2007**, *107*, 4797-4862.

(28) M. G: Contributions to the Optics of Turbid Media, Especially Colloidal Metal Solutions. *Ann. Phys.* **1908**, *25*, 377.

(29) R. Ritchie: Plasma Losses by Fast Electrons in Thin Films. *Phys. Rev.* **1957**, *106*, 874.

(30) L. M. Liz-Marzán: Tailoring Surface Plasmons through the Morphology and Assembly of Metal Nanoparticles. *Langmuir* **2006**, *22*, 32-41.

(31) K. L. Kelly, E. Coronado, L. L. Zhao and G. C. Schatz: The Optical Properties of Metal Nanoparticles: The Influence of Size, Shape, and Dielectric Environment. *J. Phys. Chem. B* **2003**, *107*, 668-677.

(32) S. Link and M. A. El-Sayed: Optical Properties and Ultrafast Dynamics of Metalic Naocrystals. *Annu. Rev. Phys. Chem.* **2003**, *54*, 331 - 366.

(33) E. Hao and G. C. Schatz: Electromagnetic Fields around Silver Nanoparticles and Dimers. *J. Chem. Phys.* **2004**, *120*, 357-366.

(34) S. Link and M. A. El-Sayed: Spectral Properties and Relaxation Dynamics of Surface Plasmon Electronic Oscillations in Gold and Silver Nanodots and Nanorods. *J. Phys. Chem. B* **1999**, *103*, 8410-8426.

(35) M. A. Mahmoud, C. E. Tabor and M. A. El-Sayed: Surface-Enhanced Raman Scattering Enhancement by Aggregated Silver Nanocube Monolayers Assembled by the Langmuir-Blodgett Technique at Different Surface Pressures. *J. Phys. Chem. C* **2009**, *113*, 5493-5501.

(36) M. A. Mahmoud, B. Snyder and M. A. El-Sayed: Surface Plasmon Fields and Coupling in the Hollow Gold Nanoparticles and Surface-Enhanced Raman Spectroscopy. Theory and Experiment. *J. Phys. Chem. C* **2010**, *114*, 7436-7443.

(37) M. M. Miller and A. A. Lazarides: Sensitivity of Metal Nanoparticle Surface Plasmon Resonance to the Dielectric Environment. *J. Phys. Chem. B* **2005**, *109*, 21556-21565.

(38) P. K. Jain, K. S. Lee, I. H. El-Sayed and M. A. El-Sayed: Calculated Absorption and Scattering Properties of Gold Nanoparticles of Different Size, Shape, and Composition: Applications in Biological Imaging and Biomedicine. *J. Phys. Chem. B* **2006**, *110*, 7238-7248.

(39) N. N. Nikolay, A. A. Petar and O. Minoru: Near-Field Properties of a Gold Nanoparticle Array on Different Substrates Excited by a Femtosecond Laser. *Nanotechnology* **2007**, *18*, 305703.

(40) L. Gunnarsson, T. Rindzevicius, J. Prikulis, B. Kasemo, M. Käll, S. Zou and G. C. Schatz: Confined Plasmons in Nanofabricated Single Silver Particle Pairs: Experimental Observations of Strong Interparticle Interactions. *J. Phys. Chem. B* **2004**, *109*, 1079-1087.

(41) O. L. Muskens, V. Giannini, J. A. Sánchez-Gil and J. Gómez Rivas: Optical Scattering Resonances of Single and Coupled Dimer Plasmonic Nanoantennas. *Opt. Express* **2007**, *15*, 17736-17746.

(42) A. M. Funston, C. Novo, T. J. Davis and P. Mulvaney: Plasmon Coupling of Gold Nanorods at Short Distances and in Different Geometries. *Nano Lett.* **2009**, *9*, 1651-1658.

(43) S. Dodson, M. Haggui, R. Bachelot, J. Plain, S. Li and Q. Xiong: Optimizing Electromagnetic Hotspots in Plasmonic Bowtie Nanoantennae. *J. Phys. Chem. Lett.* **2013**, *4*, 496-501.

(44) C. E. Tabor, R. Murali, M. A. Mahmoud and M. A. El-Sayed: On the Use of Plasmonic Nanoparticle Pairs as a Plasmon Ruler: The Dependence of the near-Field Dipole Plasmon Coupling on Nanoparticle Size and Shape. *J. Phys. Chem. A* **2009**, *113*, 1946-1953.

(45) P. K. Jain, W. Huang and M. A. El-Sayed: On the Universal Scaling Behavior of the Distance Decay of Plasmon Coupling in Metal Nanoparticle Pairs: A Plasmon Ruler Equation. *Nano Lett.* **2007**, *7*, 2080-2088.

(46) C. Tabor, R. Murali, M. Mahmoud and M. A. El-Sayed: On the Use of Plasmonic Nanoparticle Pairs as a Plasmon Ruler: The Dependence of the near-Field Dipole Plasmon Coupling on Nanoparticle Size and Shape†. *J. Phys. Chem. A* **2008**, *113*, 1946-1953.

(47) J. Gersten and A. Nitzan: Electromagnetic Theory of Enhanced Raman Scattering by Molecules Adsorbed on Rough Surfaces. *J. Phys. Chem.* **1980**, *73*, 3023-3037.

(48) P. Liao and A. Wokaun: Lightning Rod Effect in Surface Enhanced Raman Scattering. *J. Phys. Chem.* **1982**, *76*, 751-752.

(49) I. O. Sosa, C. Noguez and R. G. Barrera: Optical Properties of Metal Nanoparticles with Arbitrary Shapes. *J. Phys. Chem. B* **2003**, *107*, 6269-6275.

(50) J. Chen, B. Wiley, J. McLellan, Y. Xiong, Z.-Y. Li and Y. Xia: Optical Properties of Pd-Ag and Pt-Ag Nanoboxes Synthesized Via Galvanic Replacement Reactions. *Nano Lett.* **2005**, *5*, 2058-2062.

(51) Q. Zhang, W. Li, C. Moran, J. Zeng, J. Chen, L.-P. Wen and Y. Xia: Seed-Mediated Synthesis of Ag Nanocubes with Controllable Edge Lengths in the Range of 30− 200 Nm and Comparison of Their Optical Properties. *J. Am. Chem. Soc.* **2010**, *132*, 11372-11378.

(52) R. Schlögl and S. B. Abd Hamid: Nanocatalysis: Mature Science Revisited or Something Really New? *Angew. Chem. Int. Ed.* **2004**, *43*, 1628-1637.

(53) R. Narayanan and M. A. El-Sayed: Some Aspects of Colloidal Nanoparticle Stability, Catalytic Activity, and Recycling Potential. *Top. Catal.* **2008**, *47*, 15-21.

(54) R. K. Sharma, P. Sharma and A. Maitra: Size-Dependent Catalytic Behavior of Platinum Nanoparticles on the Hexacyanoferrate (Iii)/Thiosulfate Redox Reaction. *J. Colloid Interface Sci.* **2003**, *265*, 134-140.

(55) P. Christopher and S. Linic: Shape- and Size-Specific Chemistry of Ag Nanostructures in Catalytic Ethylene Epoxidation. *Chemcatchem* **2010**, *2*, 78-83.
(56) M. Shao, A. Peles and K. Shoemaker: Electrocatalysis on Platinum Nanoparticles: Particle Size Effect on Oxygen Reduction Reaction Activity. *Nano Lett.* **2011**, *11*, 3714-3719.

(57) B. Qiao, A. Wang, X. Yang, L. F. Allard, Z. Jiang, Y. Cui, J. Liu, J. Li and T. Zhang: Single-Atom Catalysis of Co Oxidation Using Pt1/Feox. *Nat. Chem.* **2011**, *3*, 634-641.

(58) H. Zhang, T. Watanabe, M. Okumura, M. Haruta and N. Toshima: Catalytically Highly Active Top Gold Atom on Palladium Nanocluster. *Nat. Mat.* **2012**, *11*, 49-52.

(59) J. K. Nørskov, J. Rossmeisl, A. Logadottir, L. Lindqvist, J. R. Kitchin, T. Bligaard and H. Jonsson: Origin of the Overpotential for Oxygen Reduction at a Fuel-Cell Cathode. *J. Phys. Chem. B* **2004**, *108*, 17886-17892.

(60) J. Wu and H. Yang: Platinum-Based Oxygen Reduction Electrocatalysts. *Acc. Chem. Res.* **2013**, *46*, 1848-1857.

(61) R. Narayanan and M. A. El-Sayed: Shape-Dependent Catalytic Activity of Platinum Nanoparticles in Colloidal Solution. *Nano Lett.* **2004**, *4*, 1343-1348.

(62) K. An and G. A. Somorjai: Size and Shape Control of Metal Nanoparticles for Reaction Selectivity in Catalysis. *ChemCatChem* **2012**, *4*, 1512-1524.

(63) V. R. Stamenkovic, B. Fowler, B. S. Mun, G. Wang, P. N. Ross, C. A. Lucas and N. M. Marković: Improved Oxygen Reduction Activity on Pt3ni (111) Via Increased Surface Site Availability. *Science* **2007**, *315*, 493-497.

CHAPTER 2

THE FORMATION OF HOT SPOTS BETWEEN CUBIC DIMERS[1]

2.1. Motivation

Recently, the properties of plasmonic metal nanoparticles have been the subject of intense research due to the interesting properties of their localized surface plasmon resonance (LSPR). The LSPR is the collective oscillatory motion of electrons resulting from the coherent excitation of the "free" electrons in the conduction band of the metal.[2] Consequently, plasmonic metal nanoparticles exhibit unique absorption, scattering, and surface localized electromagnetic field intensities.[3] For nanoparticles composed of gold and silver, the LSPR is finely tunable and strongly dependent of the shape, size, composition of the nanostructure[3, 4], and the dielectric function of both the metal and the surrounding medium[5, 6]. As a result, both silver and gold nanoparticles have been utilized in many applications including: biological imaging[7, 8], selective photothermal therapy [9, 10], surface enhanced Raman Scattering (SERS)[11] , optical wave guiding , and biochemical sensing[12-17].

It is well known that when two or more nanostructures get in close proximity to each other, the development of both a new set of hybridized plasmonic modes and enhanced[18-27] optical fields (hot spots) occurs. This is primarily due to the spatial proximity of the individual plasmonic nanoparticles. Interaction between the electromagnetic fields generated by each nanoparticle induces the formation of hybridized collective plasmonic modes. At nanoscale separations, the hot spots produced in these composite frameworks exhibit noteworthy enhancements in Raman scattering[28-

[33], fluorescence [34, 35], infrared absorption[36, 37] ; which have been useful for a variety of applications.[5-13]

Studies of aggregates composed of solid plasmonic nanoparticles made of either gold (Au) or silver (Ag) exhibit the strongest scattering, and thus imaging properties. Upon plasmonic excitation, the nanocube shape is known to develop its strongest electromagnetic field (hot spot) around its corners. However, the aggregation of two or more nanocubes is known to preferentially orient the cubes in a face-to-face configuration. This immediately raises a question regarding the mechanism for the spatial development of hot spots in Ag or Au nanocube aggregates which are oriented face-to-face: Will the hybridized collective plasmonic modes create hot spots between neighboring faces or between the neighboring corners?

Herein, the development of hot spots at the junction of two cubic nanostructures having sharp corners was followed. The Discrete Dipole Approximation (DDA) was used to theoretically investigate the location and structure of hot spots formed between 42 nm Au-Au and Ag-Ag plasmonic metal nanocube dimers in water. Theoretical predictions of the polarization vectors, the spatial distribution of the electromagnetic field enhancement, and the scattering and absorption spectra were obtained by DDA. The electromagnetic field and polarization vector plots along with the optical spectra were used to determine the location and structure of the hot spots formed between the monomers in the dimers as a function of the exciting light polarization, wavelength, and the inter-particle separation of the dimer.

2.2. Theoretical Parameters

The discrete dipole approximation (DDA)[38] is a widely used theoretical technique for modeling the optical properties of plasmonic nanoparticles with various sizes and shapes.[39, 40] Herein, the optical properties of Ag-Ag and Au-Au dimers was calculated using DDSCAT 6.1 code offered publicly by Draine and Flatau.[38] The dimers were modeled as a cubic lattice of point dipoles, which were excited by an external field. Subsequently, the response of the point dipole lattice was solved self-consistently using Maxwell's equations. The calculations were carried out for 42 nm nanocube dimers in water. Values reported by Johnson and Christy[41] and Palik for the dielectric constants of Ag and Au in water were used for this study. Furthermore, with modifications to the DDSCAT 6.1 code conducted by Goodman[42] and Schatz [43]it is possible to calculate the electromagnetic field intensity and the polarization vector orientation and magnitude for a specific wavelength of excitation.

All dimers that were studied were approximated by 148,176 dipoles. Using an increased number of dipoles (500,094) to describe the dimer resulted in a plasmonic spectrum that closely resembles that of the previously calculated spectrum using 148,176 dipoles. As a result, 148,176 dipoles were sufficient to accurately describe the dimer system. For all contour color fill plots shown in this study the distribution of the electromagnetic field enhancement ($|E|^2/|E_0|^2$) was plotted for each homo dimer system; and for all polarization vector plots the magnitude and direction of the electronic response of the homo dimer system to polarized incident light is depicted. These contour plots represent a two-dimensional slice of the particle; however, multiple slices can be chosen in order to gain a composite picture of the three-dimensional distribution of the electromagnetic field around the dimer. For all dipole polarization vector plots reported in this study the number of dipoles were reduced for clarity purposes.

2.3. Results and Discussion

2.3.1. Exciting Light Polarization Requirement for Hot Spot Formation

Intuitively, one would expect that in order to obtain a plasmonic field between two plasmonic nanoparticles, the induced dipoles on the adjacent faces or corners of the dimer couple attractively. Thus, the polarization vector density is increased between the two nanoparticles resulting in an enhanced electromagnetic field between the dimer. Subsequently, the formation of hot spots between two nanoparticles would occur, but would only be expected when the exciting light is polarized parallel to the inter-particle axis. If the exciting light is polarized perpendicular to the inter-particle axis, the induced dipoles on each nanocube would be parallel to each other and thus repel one another at the facing interfaces leading to repulsive coupling between the facing facets and corners (see Figure 2.1). As a result, one would expect the absence of hot spot formation between two cubes aggregated face-to-face when the incident light is polarized perpendicular to the inter-particle axis of the dimer.

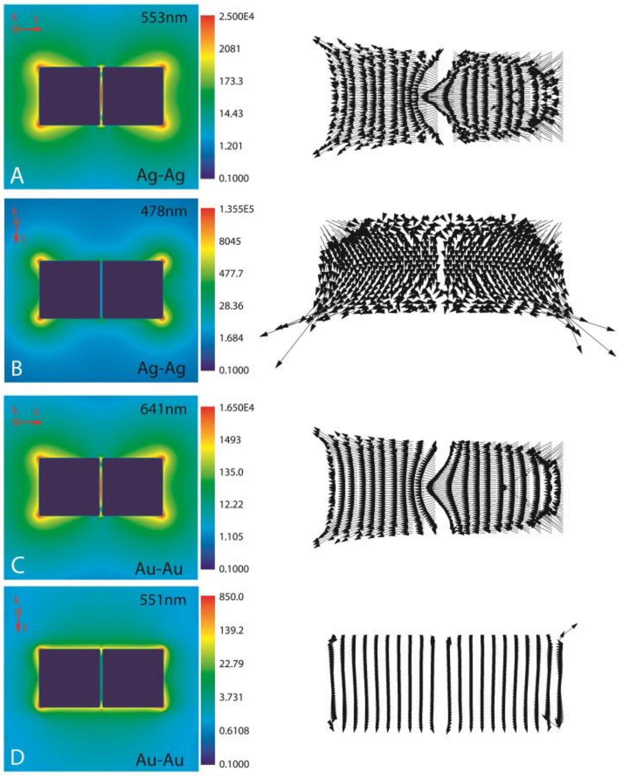

Figure 2.1. The dependence of hot spot formation (left) and polarization vector distribution (right) on the polarization direction of the incident exciting light for the top plane of the homo dimer system. Both hot spot formation and the polarization vector distribution occurs between adjacent faces of Ag-Ag (A) and Au-Au (C) dimers with an inter-particle separation of 2 nm only when the incident exciting light is polarized parallel to the inter-particle axis of the dimer. This is due to the attraction between the dipoles on the facing facets which have opposite polarity. However, when the incident exciting light is polarized perpendicular to the inter-particle axis of the dimer, no hot spots are formed between the dimer due to either head-on dipole-dipole repulsion between dipoles of similar polarity (B) or parallel dipole-dipole repulsion (D) between the dipole polarization vectors on the facing facets.

Figure 2.1 shows the electromagnetic field distribution as well as the dipole polarization vectors for the homo dimers of 42 nm Ag and Au nanocubes separated by 2 nm. The resonant excitation wavelength was chosen to be the wavelength of maximum extinction for the lowest energy plasmonic band in each corresponding extinction spectrum. In Figures 2.1A and 2.1C the excitation light is polarized parallel to the inter-particle axis of the dimer while (2.1B) and (2.1D) it is polarized perpendicular to this axis. From this figure, it is clear that a high field enhancement intensity is observed with parallel excitation (2.1A and 2.1C), but minimal enhancement is observed when the exciting light is polarized perpendicular to the inter particle axis of the dimer (2.1B and 2.1D).

The use of incident excitation polarized light perpendicular to the inter-particle axis does not result in hot spots between either two Ag or Au nanocubes. The high field intensity is observed at the corners located away from the adjacent dimer faces. In this case, there is no attractive electrostatic interaction between the induced dipoles on adjacent faces as they are of similar polarity when perpendicular polarized excitation is used. As shown in Figures 2.1B and 2.1D, the polarization vectors of adjacent faces are oriented parallel to each other resulting in a repulsive type electrostatic interaction between the induced dipoles on each face. Therefore, when incident excitation is perpendicular to the inter-particle axis, it looks as if a nodal plane between the induced dipoles on the adjacent faces of each cube is formed explaining the absence of the hot spots between the two cubes in the dimer. This suggests that for SERS experiments with aggregated nanocubes of silver or gold, the use of un-polarized exciting light, instead of polarized light with an equivalent intensity, should result in better Raman enhancement.

2.3.2. Competition in Forming Hot Spots between Facing Corners or Facing Facets

Along with the effect of incident polarization on the electromagnetic field enhancement between homo dimers, it is important to understand the 3-dimensional distribution of the electromagnetic field enhancement that is produced. As mentioned previously, the contour plot generated from DDA is limited to a two-dimensional representation. However, multiple slices of the dimer can be produced in order to generate a composite picture of the variation in the electric field enhancement along the height of the homo dimer as was carefully carried out for two prisms given a specific threshold enhancement[44]. For the purpose of this letter, we have examined two slices of the dimer, the top and middle plane. Since the bottom plane gives a similar distribution as the top plane (due to the cube symmetry) the results of the two planes analyzed are sufficient to answer the question: Where are the hot spots formed between two nanoparticles?

Figure 2.2 shows the electromagnetic field distribution as well as the dipole polarization vectors for a pair of Ag (shown in 2.2A and 2.2B) and Au dimers (2.2C and 2.2D) with an inter-particle separation of 2 nm. For the Ag and Au, the results for the top plane of the dimer are shown in 2.2A and 2.2C and those for the middle plane, 21 nm below the top surfaces of the dimer, are shown in 2.2B and 2.2D. It is apparent that the intensity of the electromagnetic field between the facing facets of the middle plane of both metals (in 2.2B and 2.2D) is spread along the entire region between the two nanoparticles. This is not also true for the top plane. The top plane of the dimer displays an electromagnetic field that is localized at the corners (in 2.2A and 2.2C). The reason for this could be that the polarized electrons on the top plane are influenced by the focusing effect induced by the sharp vertices of the cubic shape. In the middle plane, the hot spot is mostly between the faces and weakly between the edges, as the middle plane lacks the focusing effect of the corners.

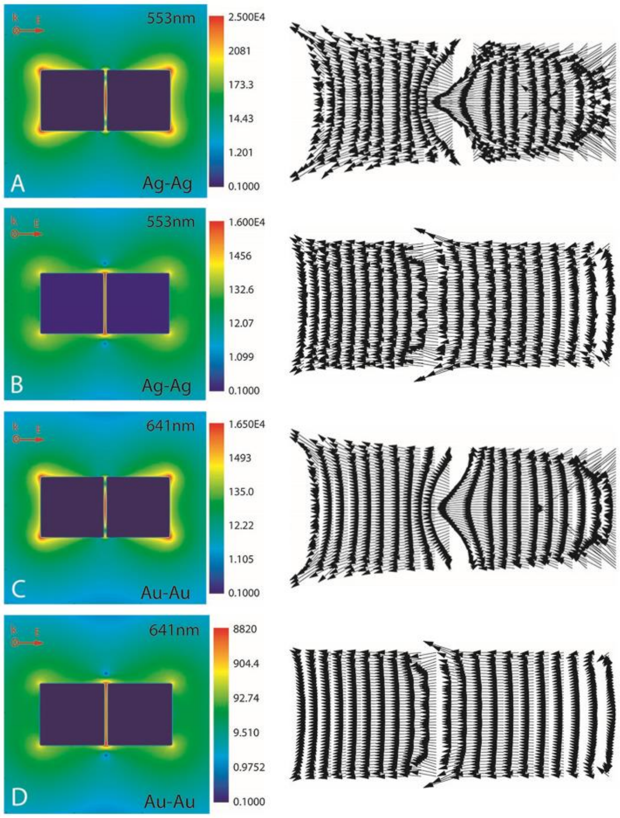

Figure 2.2. A comparison between the shape and mechanism of hot spot formation between a pair of 42 nm silver (A and B) and 42 nm gold (C and D) nanocubes observed on the top plane of each metal pair (A and C) and on the plane 21 nm below the top plane (B and D). The presence of corners in the top plane in A and C attracts (stabilizes) more of the oscillating dipoles at the corners of the structure resulting in a smaller number of dipoles available for the hot spot between the facing facets compared to both B and D, which have no "corner focusing effects."

The dipole polarization vector diagram shown on the right hand side of Figure 2.2 clearly shows the mechanism of the hot spot formation in the cases discussed. For the plane of the dimer that includes the top corners (2.2A and 2.2C), the polarized dipoles in-between the facing facets induce stronger hot spots in the middle of the facets than those formed in the middle plane (in 2.2B and 2.2D). The hot spots in 2.2B and 2.2D are distributed throughout the entire interfacial region, both along the surface and at the edges (corners) of the dimer. It is interesting to point out that the presence of corners in the top plane (in 2.2A and 2.2C) attracts (stabilizes) more of the oscillating dipoles resulting in an electromagnetic field distribution that is localized either at the corners of the structure or directly in the middle of the adjacent faces.

2.3.3. Dependence of the Formation Mechanism of Hot Spots on Inter-Particle Separation

It is well known that the magnitude of the electromagnetic field enhancement, $|E|^2/|E_0|^2$, is a strong function of the dimer separation distance. In this study, a dimer separation lower limit of 2 nm was used in order for classical electrodynamic theory[45] to be valid.[46] Figure 2.3.A and 2.3.D exhibit hot spot generation at the interface of the two adjacent cube faces for a 2 nm inter-particle separation of the dimer. Also, the polarization vectors clearly concentrate between the adjacent faces for both the Au-Au and Ag-Ag nanocubes. The dipoles located at the corners of the adjacent faces of each cube gain more dipole-dipole attractive stability by interacting with the dipoles on the facing facet of the second cube. This increases both the polarization vector density and the electromagnetic field between the centers of the adjacent faces, thus forming the hot spots shown in 2.3A and 2.3D.

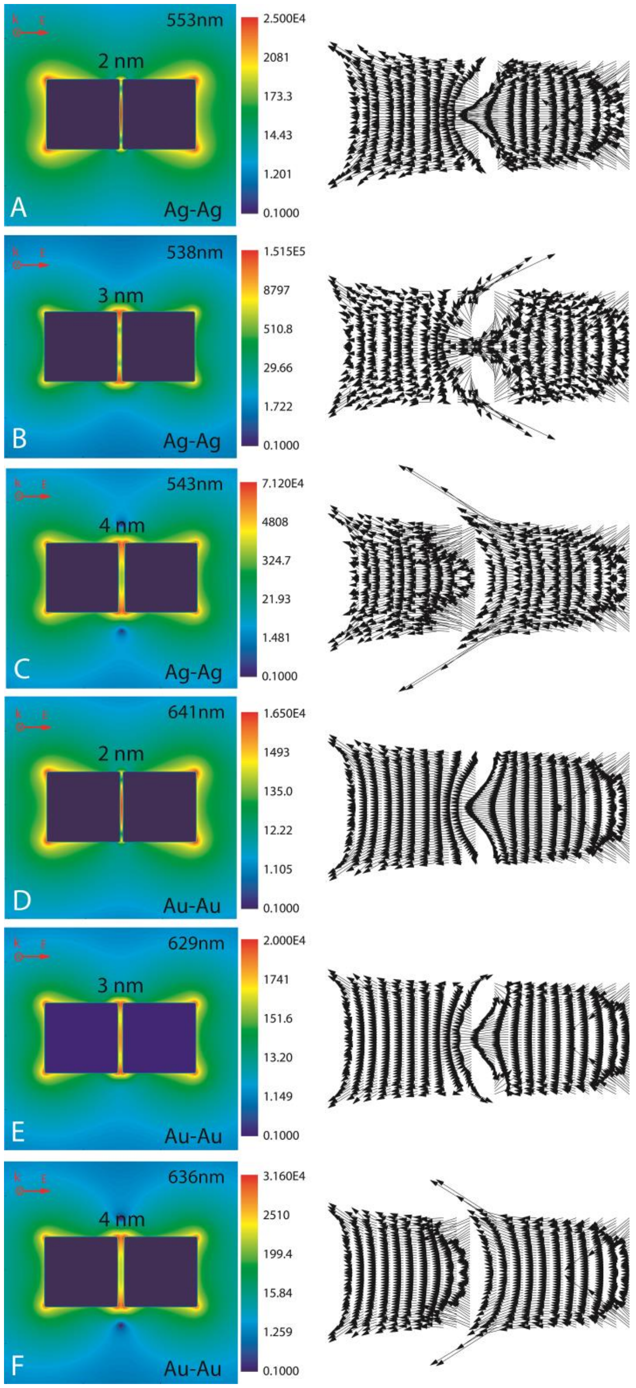

Figure 2.3. The effect of increasing the inter-particle separation from 2 nm to 4 nm on the shape and mechanism of hot spot formation for excitation of the lowest energy plasmonic band of Ag-Ag and Au-Au dimers. For both Ag-Ag and Au-Au dimers, formation of hot spots and the overlap of the polarization vector distribution on the facing facets occur at the center of the facing facets (A and D) for short separation distances (2 nm) and at the corners of the facing facets of the dimer (C and F) for the large inter-particle separation of 4 nm. Formation at both the center and the corners seems to take place at the intermediate separation distance of 3 nm (B and E). All results shown are for the top plane of the homo dimer system.

As the separation distance between the particles in the dimer increases from 2 to 4 nm, the interaction energy between the dipoles on the adjacent faces of each nanocube decreases. Coupling between the centers of adjacent faces becomes incapable of competing with the dipolar interaction between the corners of adjacent faces. As a result, hot spots are formed only at the corners of adjacent faces when the inter-particle separation is 4 nm (2.3C and 2.3F). The largest electromagnetic field enhancement and dipole polarization vector density exhibit a shift towards the corners as the inter-particle separation increases to 4 nm. Consequently, it is evident that the inter-particle separation in the dimer dictates the location of the hot spots between two particles in the plasmonic dimer.

The most interesting behavior, however, is the competition for hot spot formation at an inter-particle separation of 3 nm. As seen in Figure 2.3B and 2.3E, the structure of the hot spots generated between the two nanocubes in the dimer display competitive contributions resulting from both the attractive interaction between the dipoles at the corners and those present on the facing facets of the two particles in the dimer. Most notably, the Ag-Ag dimer clearly exhibits two dominant plasmonic modes; which suggests competitive interaction energies between the dipoles at the corners and those at the center of adjacent faces of the nanocubes of the dimer when the inter-particle separation is at an intermediate distance of 3 nm. At 4 nm separation, the hot spots are formed only from the dipolar coupling between the corner dipoles. Increasing dimer separation to 6nm and 10nm (Figure 2.4) exhibits weaker hot spot formation and no further changes in hot spot location between the dimer.

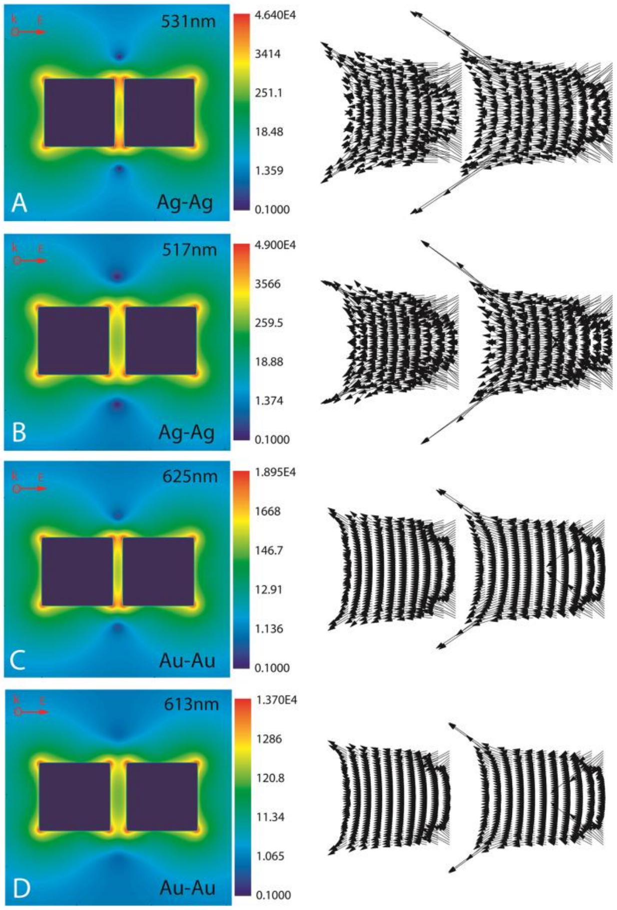

Figure 2.4. The dependence of hot spot formation (left) and polarization vector distribution (right) on the separation distance (6 nm or greater) of the dimer. When the separation distance is increased to 6 nm (A and C) and 10 nm (B and D), the electromagnetic field enhancement between the two nanocubes of the dimer is less than the electromagnetic field observed for a separation distance of 4 nm. Also, the hot spot formation between the two nanocubes continues to concentrate at the corners. Furthermore at a 10 nm separation there is a distinct region of low electromagnetic field intensity that splits the region of high electromagnetic field intensity between the facing corners of the two nanocubes into two distinct regions of high electromagnetic field intensity.

2.3.4. Excitation Wavelength Dependence of Hot Spot Formation

The spectra of plasmonic nanoparticles have different bands of different dipolar or multi-polar origin. Each is characterized by the distribution of the different coherently oscillating electrons that are excited thus by the distribution of the oscillating electrons (giving rise to the dipole polarization vectors) involved in this excitation. At the top of

Figure 2.5 the extinction spectrum of the lowest energy plasmon spectral region for a pair of 42 nm Au nanocubes separated by 2 nm is given. Figure 2.5A-E shows the dependence of the shape of the hot spots and the dipole polarization vector distribution on the wavelength of excitation in the region of the lowest energy LSPR band. As seen in Figure 2.5A and 2.5B, there is a clear dependence of the shape of the hot spot and the corresponding dipole polarization vector distribution on the wavelength of excitation.

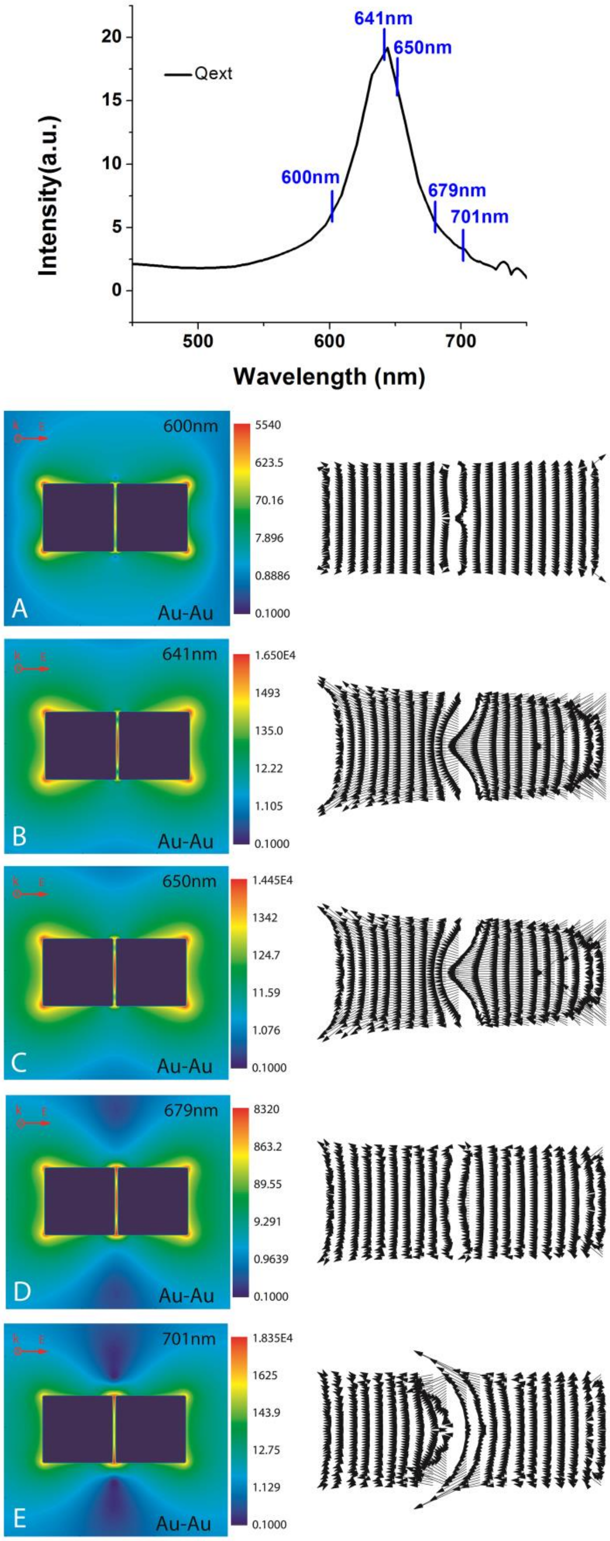

Figure 2.5. The change in the shape of the hot spots and the polarization vector distribution with respect to the change in the wavelength of excitation gives an indication of a mixed surface plasmon extinction spectral band.

For a wavelength of excitation at 600 (2.5A), 641 (2.5B), or 650 nm (2.5C), both the electromagnetic field and the dipole polarization vector distribution which are generated are similar. This leads to the conclusion that the shape of the hot spots between adjacent particles is determined by the dipolar interaction between the polarization vector distributions on the adjacent faces of the particles in the dimer. This is a property of the plasmonic band being excited that is independent of the wavelength of excitation within a single pure plasmonic band. When the wavelength of excitation is 701 nm (2.5E), the hot spots change from being localized at the center of the interface between the two nanocubes to localization at the corners of the adjacent particles. This transition is also mimicked in the distribution of polarization vectors, and corresponds to the appearance of a shoulder in the extinction spectrum at 701 nm. This suggests the appearance of a new plasmonic extinction band. Furthermore, when the wavelength of excitation is 679 nm (2.5D), it is apparent that there is a competition between two different shapes of the hot spot generation. This is clearly due to the overlap between more than one plasmonic extinction bands.

2.4. Concluding Remarks

From the results obtained in this letter, one can make the following conclusions:

(1) For a face-to-face aggregated cubic dimer, the maximum intensity of the hot spots between the facets of two nanoparticles is observed when the exciting light used is polarized parallel to the inter-particle axis of the dimer. No hot spots are formed in the inter-particle gap region if the Ag-Ag or Au-Au dimer is excited with polarization perpendicular to the dimer axis at the resonance wavelength of the lower energy plasmonic band.

(2) At short separation distances e.g. 2 nm, high fields and hot spots are formed between the facing facets of the neighboring particles in the dimer.

(3) At 3 nm, there is a competition between the formation of hot spots between the centers of the facing facets and between the corners of the adjacent facets.

(4) At 4 nm, the high fields are located mostly around the facing corners.

(5) The structure (shape) of the hot spots between the facing facets of two neighboring nanocubes (or any two plasmonic nanoparticles) depends on the distribution, and not the number, of the overlapping dipole polarization vectors on the two facing facets of the dimer.

(6) A pure single plasmonic band gives the same structure of the hot spot and is independent of the wavelength used for excitation. Plasmonic bands that show different hot spot structures at different wavelengths must have mixed plasmonic origin.

For a single “pure” plasmonic band, the dipole polarization vector distribution on the facing facets producing the hot spot, and not the number of the dipoles, is independent of the excitation wavelength of the plasmonic band used for the hot spot formation.

2.5. References

(1) N. Hooshmand, M. A. El-Sayed and J. A. Bordley: Are Hot Spots between Two Plasmonic Nanocubes of Silver or Gold Formed between Adjacent Corners or Facets? A Dda Examination. *J. Phys. Chem. B* **2014**, 5, 2229-2234.

(2) K. A. Willets and R. P. Van Duyne: Localized Surface Plasmon Resonance Spectroscopy and Sensing. *Annu. Rev. Phys. Chem.* **2007**, *58*, 267-297.

(3) S. Link and M. A. El-Sayed: Spectral Properties and Relaxation Dynamics of Surface Plasmon Electronic Oscillations in Gold and Silver Nanodots and Nanorods. *J. Phys. Chem. B* **1999**, *103*, 8410-8426.

(4) M. A. El-Sayed: Some Interesting Properties of Metals Confined in Time and Nanometer Space of Different Shapes. *Acc. Chem. Res.* **2001**, *34*, 257-264.

(5) L. J. Sherry, S.-H. Chang, G. C. Schatz, R. P. Van Duyne, B. J. Wiley and Y. Xia: Localized Surface Plasmon Resonance Spectroscopy of Single Silver Nanocubes. *Nano Lett.* **2005**, *5*, 2034-2038.

(6) G. Xu, Y. Chen, M. Tazawa and P. Jin: Surface Plasmon Resonance of Silver Nanoparticles on Vanadium Dioxide. *J. Phys. Chem. B* **2006**, *110*, 2051-2056.

(7) I. H. El-Sayed, X. Huang and M. A. El-Sayed: Surface Plasmon Resonance Scattering and Absorption of Anti-Egfr Antibody Conjugated Gold Nanoparticles in Cancer Diagnostics: Applications in Oral Cancer. *Nano Lett.* **2005**, *5*, 829-834.

(8) K. Sokolov, M. Follen, J. Aaron, I. Pavlova, A. Malpica, R. Lotan and R. Richards-Kortum: Real-Time Vital Optical Imaging of Precancer Using Anti-Epidermal Growth Factor Receptor Antibodies Conjugated to Gold Nanoparticles. *Cancer Res.* **2003**, *63*, 1999-2004.

(9) A. M. Gobin, M. H. Lee, N. J. Halas, W. D. James, R. A. Drezek and J. L. West: Near-Infrared Resonant Nanoshells for Combined Optical Imaging and Photothermal Cancer Therapy. *Nano Lett.* **2007**, *7*, 1929-1934.

(10) X. Huang, B. Kang, P. C. Chen, I. H. El-Sayed, M. A. El-Sayed, A. K. Oyelere, W. Qian and M. A. Mackey: Comparative Study of Photothermolysis of Cancer Cells with Nuclear-Targeted or Cytoplasm-Targeted Gold Nanospheres: Continuous Wave or Pulsed Lasers. *J. Biomed. Opt.* **2010**, *15*, 058002-058002-7.

(11) Schatz, G. C.; Van Duyne, R. P. Electromagnetic Mechanism of Surface-Enhanced Spectroscopy. *Handbook of Vibrational Spectroscopy*, John Wiley & Sons, Ltd: Hoboken, NJ; 2006.

(12) G. Raschke, S. Kowarik, T. Franzl, C. Sönnichsen, T. A. Klar, J. Feldmann, A. Nichtl and K. Kürzinger: Biomolecular Recognition Based on Single Gold Nanoparticle Light Scattering. *Nano Lett.* **2003**, *3*, 935-938.

(13) T. Endo, K. Kerman, N. Nagatani, Y. Takamura and E. Tamiya: Label-Free Detection of Peptide Nucleic Acid−DNA Hybridization Using Localized Surface Plasmon Resonance Based Optical Biosensor. *Anal. Chem.* **2005**, *77*, 6976-6984.

(14) C. E. H. Berger, T. A. M. Beumer, R. P. H. Kooyman and J. Greve: Surface Plasmon Resonance Multisensing. *Anal. Chem.* **1998**, *70*, 703-706.

(15) A. Haes, D. Stuart, S. Nie and R. Van Duyne: Using Solution-Phase Nanoparticles, Surface-Confined Nanoparticle Arrays and Single Nanoparticles as Biological Sensing Platforms. *J. Fluoresc.* **2004**, *14*, 355-367.

(16) S. A. Maier and H. A. Atwater: Plasmonics: Localization and Guiding of Electromagnetic Energy in Metal/Dielectric Structures. *J. Appl. Phys.* **2005**, *98*, -.

(17) C. R. Yonzon, D. A. Stuart, X. Zhang, A. D. McFarland, C. L. Haynes and R. P. Van Duyne: Towards Advanced Chemical and Biological Nanosensors—an Overview. *Talanta* **2005**, *67*, 438-448.

(18) E. Prodan, C. Radloff, N. J. Halas and P. Nordlander: A Hybridization Model for the Plasmon Response of Complex Nanostructures. *Science* **2003**, *302*, 419-422.

(19) P. K. Jain, S. Eustis and M. A. El-Sayed: Plasmon Coupling in Nanorod Assemblies: Optical Absorption, Discrete Dipole Approximation Simulation, and Exciton-Coupling Model. *J. Phys. Chem. B* **2006**, *110*, 18243-18253.

(20) P. K. Jain, W. Huang and M. A. El-Sayed: On the Universal Scaling Behavior of the Distance Decay of Plasmon Coupling in Metal Nanoparticle Pairs: A Plasmon Ruler Equation. *Nano Lett.* **2007**, *7*, 2080-2088.

(21) P. Olk, J. Renger, M. T. Wenzel and L. M. Eng: Distance Dependent Spectral Tuning of Two Coupled Metal Nanoparticles. *Nano Lett.* **2008**, *8*, 1174-1178.

(22) P. K. Jain and M. A. El-Sayed: Surface Plasmon Coupling and Its Universal Size Scaling in Metal Nanostructures of Complex Geometry: Elongated Particle Pairs and Nanosphere Trimers. *J. Phys. Chem. C* **2008**, *112*, 4954-4960.

(23) A. M. Funston, C. Novo, T. J. Davis and P. Mulvaney: Plasmon Coupling of Gold Nanorods at Short Distances and in Different Geometries. *Nano Lett.* **2009**, *9*, 1651-1658.

(24) J. A. Fan, C. Wu, K. Bao, J. Bao, R. Bardhan, N. J. Halas, V. N. Manoharan, P. Nordlander, G. Shvets and F. Capasso: Self-Assembled Plasmonic Nanoparticle Clusters. *Science* **2010**, *328*, 1135-1138.

(25) M. Hentschel, M. Saliba, R. Vogelgesang, H. Giessen, A. P. Alivisatos and N. Liu: Transition from Isolated to Collective Modes in Plasmonic Oligomers. *Nano Lett.* **2010**, *10*, 2721-2726.

(26) T. J. Davis, D. E. Gomez and K. C. Vernon: Simple Model for the Hybridization of Surface Plasmon Resonances in Metallic Nanoparticles. *Nano Lett.* **2010**, *10*, 2618-2625.

(27) M. Hentschel, D. Dregely, R. Vogelgesang, H. Giessen and N. Liu: Plasmonic Oligomers: The Role of Individual Particles in Collective Behavior. *ACS Nano* **2011**, *5*, 2042-2050.

(28) M. Moskovits: Surface-Enhanced Spectroscopy. *Rev. Mod. Phys.* **1985**, *57*, 783-826.

(29) K. Kneipp, Y. Wang, H. Kneipp, L. T. Perelman, I. Itzkan, R. R. Dasari and M. S. Feld: Single Molecule Detection Using Surface-Enhanced Raman Scattering (Sers). *Phys. Rev. Lett.* **1997**, *78,* 1667-1670.

(30) A. Campion and P. Kambhampati: Surface-Enhanced Raman Scattering. *Chem. Soc. Rev.* **1998**, *27*, 241-250.

(31) H. Xu, J. Aizpurua, M. Käll and P. Apell: Electromagnetic Contributions to Single-Molecule Sensitivity in Surface-Enhanced Raman Scattering. *Phys. Rev. E* **2000**, *62,* 4318-4324.

(32) M. Moskovits: Surface-Enhanced Raman Spectroscopy: A Brief Retrospective. *J. Ram. Spectrosc.* **2005**, *36*, 485-496.

(33) Z. Li, T. Shegai, G. Haran and H. Xu: Multiple-Particle Nanoantennas for Enormous Enhancement and Polarization Control of Light Emission. *ACS Nano* **2009**, *3*, 637-642.

(34) S. Kühn, U. Håkanson, L. Rogobete and V. Sandoghdar: Enhancement of Single-Molecule Fluorescence Using a Gold Nanoparticle as an Optical Nanoantenna. *Phys. Rev. Lett.* **2006**, *97*, 017402.

(35) P. Anger, P. Bharadwaj and L. Novotny: Enhancement and Quenching of Single-Molecule Fluorescence. *Phys. Rev. Lett.* **2006**, *96*, 113002.

(36) F. Neubrech, A. Pucci, T. W. Cornelius, S. Karim, A. García-Etxarri and J. Aizpurua: Resonant Plasmonic and Vibrational Coupling in a Tailored Nanoantenna for Infrared Detection. *Phys. Rev. Lett.* **2008**, *101*, 157403.

(37) M. Osawa: Dynamic Processes in Electrochemical Reactions Studied by Surface-Enhanced Infrared Absorption Spectroscopy (Seiras). *Bull. Chem. Soc. Jpn.* **1997**, *70*, 2861-2880.

(38) B. T. Draine and P. J. Flatau: Discrete-Dipole Approximation for Scattering Calculations. *J. Opt. Soc. Am. A* **1994**, *11*, 1491-1499.

(39) P. K. Jain, K. S. Lee, I. H. El-Sayed and M. A. El-Sayed: Calculated Absorption and Scattering Properties of Gold Nanoparticles of Different Size, Shape, and Composition: Applications in Biological Imaging and Biomedicine. *J. Phys. Chem. B* **2006**, *110*, 7238-7248.

(40) K. L. Kelly, E. Coronado, L. L. Zhao and G. C. Schatz: The Optical Properties of Metal Nanoparticles: The Influence of Size, Shape, and Dielectric Environment. *J. Phys. Chem. B* **2002**, *107*, 668-677.

(41) P. B. Johnson and R. W. Christy: Optical Constants of the Noble Metals. *Phys. Rev. B* **1972**, *6*, 4370-4379.

(42) J. J. Goodman, P. J. Flatau and B. T. Draine: Application of Fast-Fourier-Transform Techniques to the Discrete-Dipole Approximation. *Opt. Lett.* **1991**, *16*, 1198-1200.

(43) K. L. Shuford, M. A. Ratner and G. C. Schatz: Multipolar Excitation in Triangular Nanoprisms. *J. Chem. Phys.* **2005**, *123*, 114713.

(44) E. M. Perassi and E. A. Coronado: The Structure, Energy, Confinement, and Enhancement of Hot Spots between Two Nanoparticles. *J. Phys. Chem. C* **2013**, *117*, 7744-7750.

(45) M. G: Contributions to the Optics of Turbid Media, Especially Colloidal Metal Solutions. *Ann. Phys.* **1908**, *25*, 377.

(46) E. Hao and G. C. Schatz: Electromagnetic Fields around Silver Nanoparticles and Dimers. *J. Chem. Phys.* **2004**, *120*, 357-366.

CHAPTER 3

THE DEVELOPMENT OF NEW PLASMONIC MODES AT SHORT SEPARATION DISTANCES[1]

3.1. Motivation

Gold and silver nanoparticles exhibit unique optical properties which have proven to be useful in a variety of chemical and biological applications. The origin of these unique optical properties derives from two key factors: the polarizability of the free electrons within the metal and the size difference between the nanoparticle and the wavelength of light with which it is interacting[2]. In the 10-100 nm size regime, the free conduction band electrons within the nanometal coherently oscillate in response to an incident electromagnetic field with an appropriate resonant wavelength thus generating a localized surface plasmon resonance (LSPR). This induces strong electromagnetic fields on the surface of the nanoparticle due to the coherent excitation of the conduction band electrons. The coherent excitation consequently decays either[2-6] by giving off strong scattered light or absorption and subsequent conversion to heat. It is these absorption and scattering properties of gold (Au) and silver (Ag) nanoparticles that have led to their utilization in various chemical and biological applications including imaging[7-11], cancer therapeutics[12, 13], solar energy conversion[14], and sensing[6, 15-26].

One of the major advantages to using plasmonic nanoparticles over other strongly absorbing or scattering species derives from their highly sensitive and tunable optical properties. Since the first complete solution for the absorption and scattering properties of a spherical plasmonic nanoparticle in 1908[27], the LSPR has proven to be dependent on the size, shape, composition, and surrounding environment of the particle[3, 28-31]. Thus, the LSPR position can be tuned for a given solar cell or sensing application in order to increase efficiency. The sensitivity of the LSPR position to the nanoparticles surrounding environment has been exploited in nanomedicine as well. More recent studies have shown that the LSPR sensitivity can be further enhanced by the near-field coupling of adjacent plasmonic nanoparticles. When the separation distance between two nanoparticles is decreased below the size of an individual particle, there is both a strong electromagnetic field[5, 32] generated between the two nanoparticles and a characteristic red-shift in the LSPR[33-35]. As a result, this enhanced electromagnetic field has provided improved detection of molecular species by surface enhanced Raman spectroscopy (SERS)[36] over single plasmonic nanoparticles. Also, the sensitivity of the LSPR to the separation distance of a nanoparticle has been utilized as a versatile targeted molecular sensing technique[36-39] on the nanoscale.

While the benefits of using coupled plasmonic nanoparticles have been exploited in many recent studies, an in depth knowledge about the near-field coupling between two nanoparticles has only just begun. The universal scaling behavior of the near-field coupling between two nanoparticles was first observed in 2003[40] and was further corroborated by many theoretical[41, 42] and experimental[43] studies of nanoparticle dimers. It was found that the LSPR peak position of various nanoparticle dimers plotted against the inter-particle separation distance normalized to the size of the particle fit well with a near exponential decay described by the well-known “plasmon ruler equation”[40, 41, 43]. Once this was realized, the coupled field strength and decay length could be extrapolated for various plasmonic nanoparticle pairs. Initial reports have shown that the coupled field strength trends with the expected strength of the electromagnetic fields generated by the corresponding metal[44]. However, the decay length of the coupled field between two nanoparticles was independent of the plasmonic metal type and only varied upon using a different nanoparticle shape. Thus, the shape of the nanoparticle pair can be exploited to obtain strong near-field coupling.

In 2009 Tabor[42] and co-workers reported the theoretical coupled field strengths and decay lengths for gold nanoshperes, nanodisks, nanoprisms, and nanocubes which supports this same shape dependence. It was found that the near-field coupling resulting from gold nanoprisms and nanocubes exhibited decay lengths that were nearly twice the decay lengths observed for gold nanospheres. This can be related to the dependence of the Coulombic restoring force of the oscillating electron cloud within the nanoparticle on its shape[45]. In light of these recent discoveries, nanoparticle shapes that exhibit strong electromagnetic fields show exciting promise as possible chemical and biological nanosensors. However, a large majority of current studies involving the near-field coupling of nanoparticle shapes with high electromagnetic fields have been limited to separation distances larger than 0.1**L** (where **L** is the size of the individual nanoparticle). As a result, an understanding of the near-field coupling behavior of these nanoparticle dimers with separation distances smaller than 0.1**L** has yet to be examined in more detail.

It is important to note, that many mathematical and experimental studies of the coupling between rod shaped[46-49] and spherical nanoparticles[50] in the last five years have shown the importance of both the nonlocal optical response for small nanoparticle separations and even quantum effects at separations approaching the subnanometer regime[51]. For the separation distances studied herein it has been shown that aspects of nonlocality begin to contribute to both the optical and electromagnetic response of a plasmonic dimer, however, these separation distances are still too large to lead to a significant contribution from quantum effects[50]. An interesting study specifically focused on the coupling between cubic nanoparticles was recently published by our group where the electromagnetic field distribution between two 42 nm nanocubes at short separation distances also suggests that both interesting and sensitive near-field plasmonic coupling could be possible[52]. As shown in this study, the plasmonic field distribution on adjacent nanocube faces changes greatly at short separation distances (below 6 nm). In this separation range, the oscillating dipole density distribution changes from being near the corners of the adjacent nanocubes (above 6 nm) to in between the facets at a separation of 2 nm. In the present study, the observed changes in the plasmonic extinction spectra, the failure of the plasmon ruler equation and the corresponding deviation from the exponential decay behavior of the near-field coupling are all examined as function of separation distance. In addition, the plasmonic dipole distribution along the adjacent facets of the dimer has also been carefully examined as a function of the inter-particle separation. The results suggest that the observed failure of the exponential decay predicted by the plasmon ruler equation at inter-particle separations of less than 6 nm coincides with, and thus could be due to, the observed changes in the plasmonic field (dipole) distribution.

3.2. Theoretical Parameters

To model the optical properties and interactions between of the Au-Au or Ag-Ag nanocubes of edge length 42 nm the discrete dipole approximation (DDA) method was used. DDA is a powerful and widely used theoretical technique for modeling the optical properties of plasmonic nanoparticles with various sizes and shapes[3, 4, 53]. The Au-Au and Ag-Ag nanocube dimers investigated herein are represented by a cubic array of point dipoles which are excited by a polarized external electromagnetic field. The corresponding response of the cubic array of point dipoles to the polarized field is solved self consistently using Maxwell's equations and the resulting optical spectra are produced[54]. The advantage of using the DDA method for this study is twofold. It is particularly well suited for modeling the nanocube shape due to the cubic lattice of point dipoles used to describe the system. Also, when using DDA both multipolar and finite size effects are accounted for. This is particularly important due to the size and separation distances of the nanoparticle dimers that were investigated.

The publicly offered DDSCAT 6.1 code developed by Draine and Flatau[55] was used to calculate all optical spectra of the Au-Au and Ag-Ag nanocube dimers. For all calculations the nanocube dimer system was described by 148,176 point dipoles which equates to an acceptable 1 dipole/nm representation. The incident external field was polarized along the inter-particle axis and propagated perpendicular to the inter-particle axis. Also, previously reported values[56] for the dielectric constants for Ag and Au in air were used for each calculation and the refractive index of ethanol was used to modify the corresponding extinction spectrum in order to model a surrounding medium of ethanol for all data collected in this study.

3.3. Results and Discussion

3.3.1. Extinction Spectra

To begin investigating the near-field coupling behavior of 42 nm Au-Au and Ag-Ag nanocube dimers at small separation distances, the extinction spectrum was calculated for each dimer at separation distances ranging from 2-100 nm. As seen in Figure 3.1, a red-shift in the extinction spectrum occurs for both gold and silver dimers as the inter-particle separation distance decreases. This is a common indication of the near-field coupling that occurs between two nanoparticles in close proximity to each other[57, 58].

When the incident electromagnetic field is polarized parallel to the inter-particle axis, which is the case in the present study, an energetically attractive interaction occurs between the oscillating electronic dipoles of each nanoparticle. This induces the observed red-shift of the plasmonic band of the dimer.

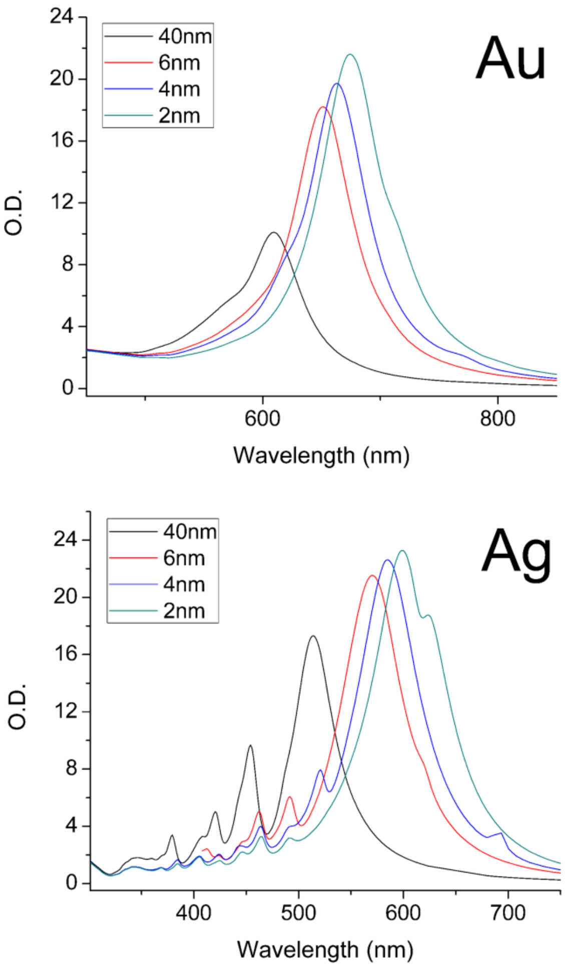

Figure 3.1. The theoretical extinction spectrum for 42 nm Au-Au (top) and Ag-Ag (bottom) dimers at separation distances of 40 nm, 6 nm, 4 nm, and 2 nm (100 nm, 16 nm, 8 nm, and 3 nm were omitted for clarity) was calculated. There is a clear red-shift in the LSPR peak position of multiple plasmonic modes as well as a large increase in the intensity of select plasmonic modes as the separation distance decreases.

It is clear that the coupling between two cubic nanoparticles of either gold or silver is complex. As noted in previous studies[59], for separation distances much smaller than the size of a monomer within the dimer, there is a higher contribution from higher order plasmonic modes to the resulting extinction spectrum. This can be seen by the observed broadening and appearance of a pronounced shoulder within the extinction spectra of the Au-Au dimer as well as the shifting intensity and position of the multiple plasmonic bands within the Ag-Ag dimer. In order to focus our investigation on the plasmonic modes which were most sensitive to the separation distance of each dimer were determined all of the calculated extinction spectra in this study were first deconvoluted into corresponding Lorentzian curves representing the various plasmonic modes of each dimer. As seen in Figure 3.2 and 3.3, the convoluted spectra were simplified into a set of plasmonic bands produced by each dimer at various separation distances.

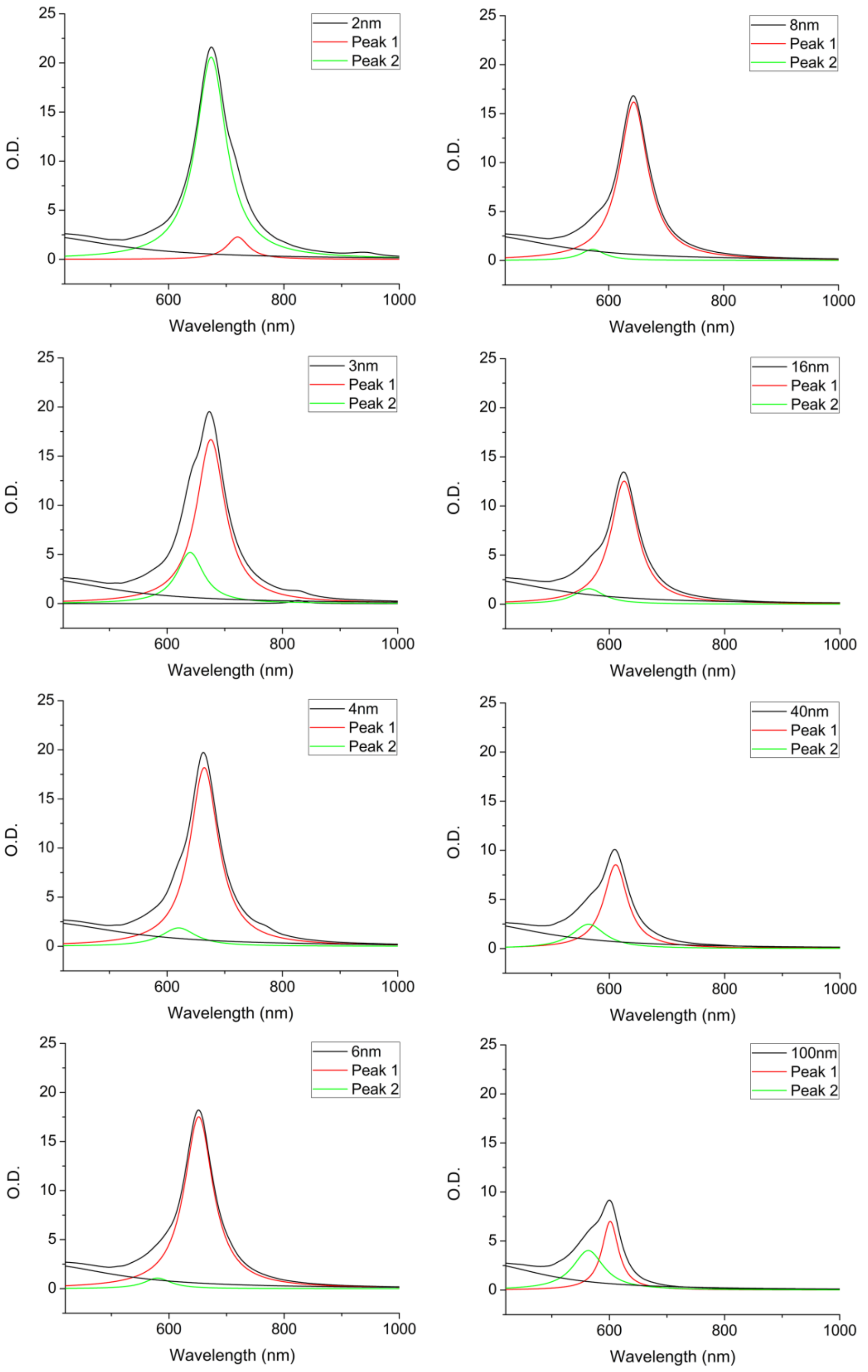

Figure 3.2. The extinction spectrum of a 42nm Au-Au nanocube dimer in ethanol was calculated and deconvoluted into corresponding Lorentzian curves. Multiple peaks were used to defined the entire spectrum; however, for clarity purposes, only those peaks corresponding to peak 1 (red), peak 2 (green) have been identified. Both the peak position and area were optimized using Origin 9.0 and all shown fits correspond to a chi squared value of less than 0.05 and a R^2 value of greater than 0.99.

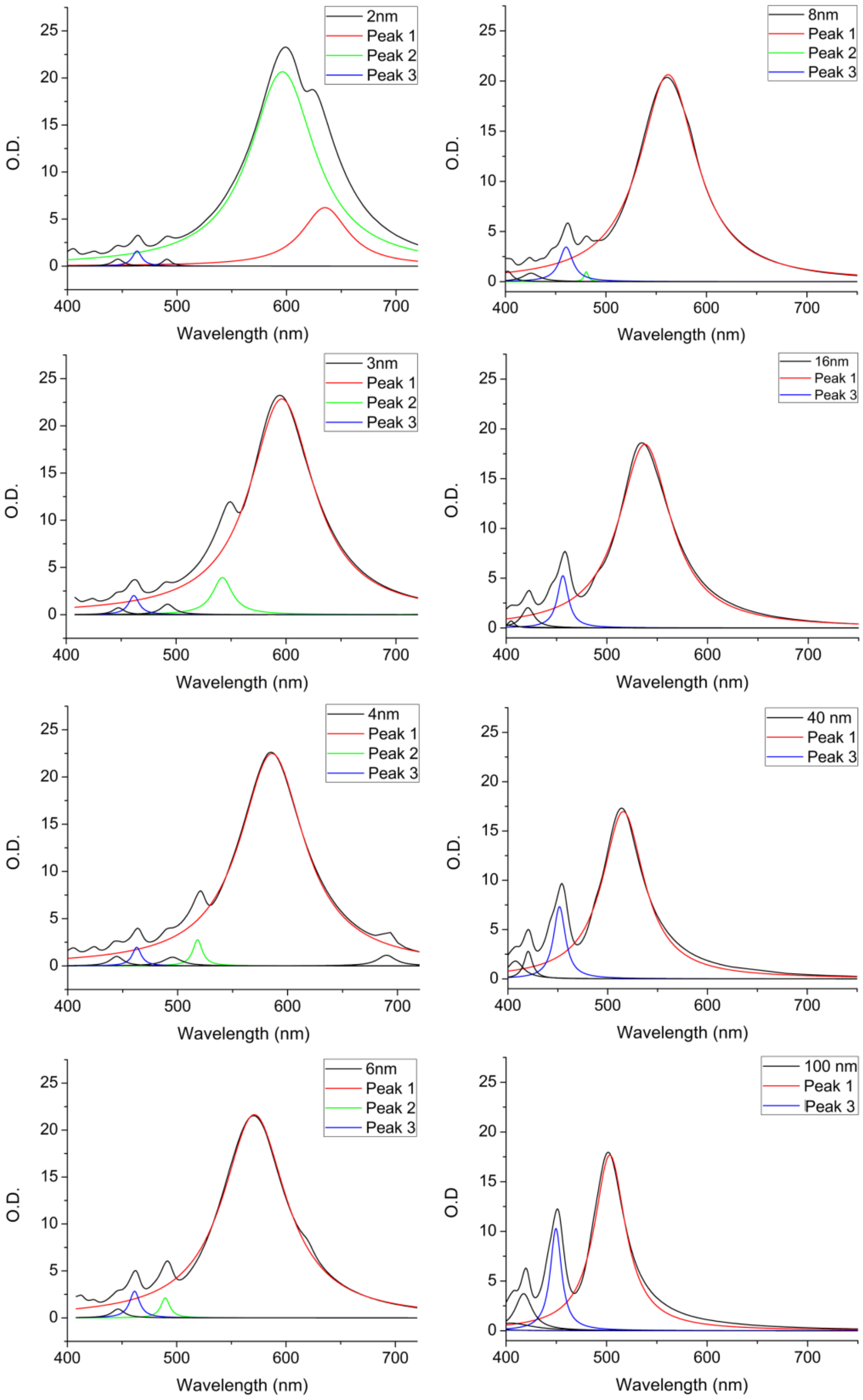

Figure 3.3. The extinction spectrum of a 42nm Ag-Ag nanocube dimer in ethanol was calculated and deconvoluted into corresponding Lorentzian curves. Multiple peaks were used to define the entire spectrum; however, for clarity purposes, only those peaks corresponding to peak 1 (red), peak 2 (green), and peak 3 (blue) have been identified. Both the peak position and area were optimized using Origin 9.0 and all shown fits correspond to a chi squared value of less than 0.05 and a R^2 value of greater than 0.99.

3.3.2. Peak Identification

The resulting set of peaks was then monitored as a function of the separation distance of each dimer. However, this proved difficult due to the constantly shifting peak position and intensity of each band especially at short separation distances. First, in order to ensure a consistent assignment of the individual plasmonic bands within each extinction spectrum, the electromagnetic field was calculated along the height of each dimer at the wavelength corresponding to the maximum intensity of each plasmonic band at separation distances ranging from 6-2 nm. Then the plasmonic bands which were strongly affected by the near-field coupling of the dimer were determined through monitoring the integrated intensity of each peak as a function of separation distance (Figure 3.4).

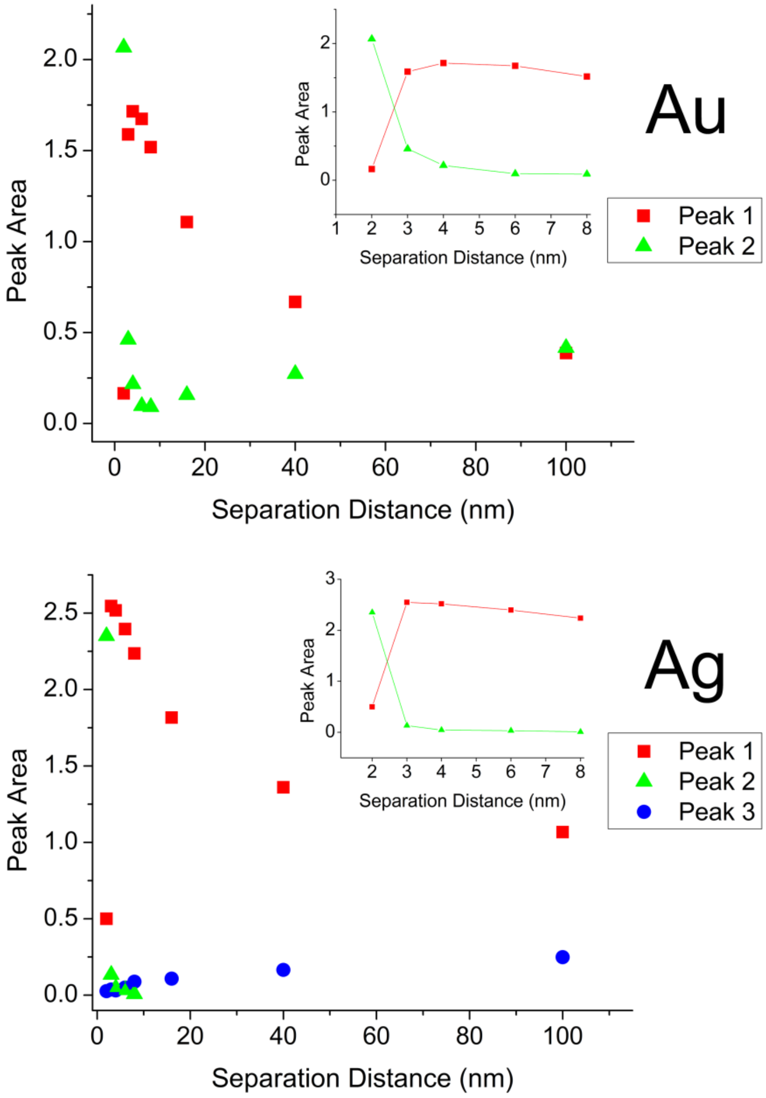

Figure 3.4. The area of prominent plasmonic bands within the extinction spectra was plotted against the separation distance of the dimer. The two plasmonic bands analyzed for the Au-Au dimer (top), peak 1 and 2, show a decrease in peak intensity for peak 1 and an increase in peak intensity of peak 2 (inset) at separation distances below 4 nm. This same trend is observed for the Ag-Ag dimer (bottom) with respect to peak 1 and 2 (peak 3 is not enhanced by the near-field coupling of the dimer; its intensity consistently decreases as the separation distance is decreased).

For the Au-Au dimer, two prominent plasmonic modes exhibited a strong dependence on the separation distance of the dimer. As seen in Figure 3.4, as the separation distance decreases from roughly 100-4 nm there is a progressive increase in the integrated intensity of peak 1 in the Au-Au dimer spectrum. This, however, is not the case at smaller separation distances. When the separation distance approaches 4nm a dampening of peak 1 occurs. As the separation distance continues to decrease the integrated peak intensity of peak 1 begins to drastically decrease. Interestingly, at these small separation distances there is a corresponding increase in the integrated peak intensity of peak 2. It appears that there are two regions of near-field plasmonic coupling that give rise to the enhancement of two distinct plasmonic modes. At separation distances larger than 4nm the major plasmonic resonance resulting from near-field coupling between two Au nanocubes can be represented by peak 1 and at smaller separation distances peak 2 becomes the major plasmonic resonance.

Three major plasmonic modes were monitored as a function of separation distance for the Ag-Ag dimer and a similar trend was observed. As seen in Figure 3.4, there is an increase in the integrated peak intensity of peak 1 as the separation distance decreases. However, at a separation distance of 3 nm the integrated peak intensity begins to drop. At large dimer separations peak 3 appears to be a prominent plasmonic mode; however, upon decreasing the separation distance, the integrated peak intensity of peak 3 consistently decreases. This suggests that this plasmonic mode is not enhanced by the near-field coupling of the dimer and as a result is not included further in this discussion. However, at a separation distance of 8 nm there is an appearance of a new peak, peak 2. This is followed by a drastic increase in its integrated peak intensity as the separation distance is decreased below 4 nm. Again we see that there appears to be two distinct regions of near-field coupling between the nanocube dimer. At separation distances above 4 nm there is an enhancement of the plasmonic mode described by peak 1, and at separation distances below 4 nm there is an enhancement of the plasmonic band described by peak 2.

3.3.3. Electromagnetic Field Distribution

The electromagnetic field distributions corresponding to the two major plasmonic bands within the extinction spectrum at these separation distances, denoted as peak 1 and 2, are shown in Figure 3.5-3.12. The electromagnetic field distributions attributed to peak 1 and peak 2 exhibit characteristic differences and thus support the given plasmonic band assignments. The undeniable overlap between peak 1 and 2 must be noted; however, there is a characteristic localization of the electromagnetic field near the vertices of each dimer for peak 1 and a localization of the electromagnetic field across the adjacent facets of the neighboring particles (especially half way down the height of the dimer) for peak 2.

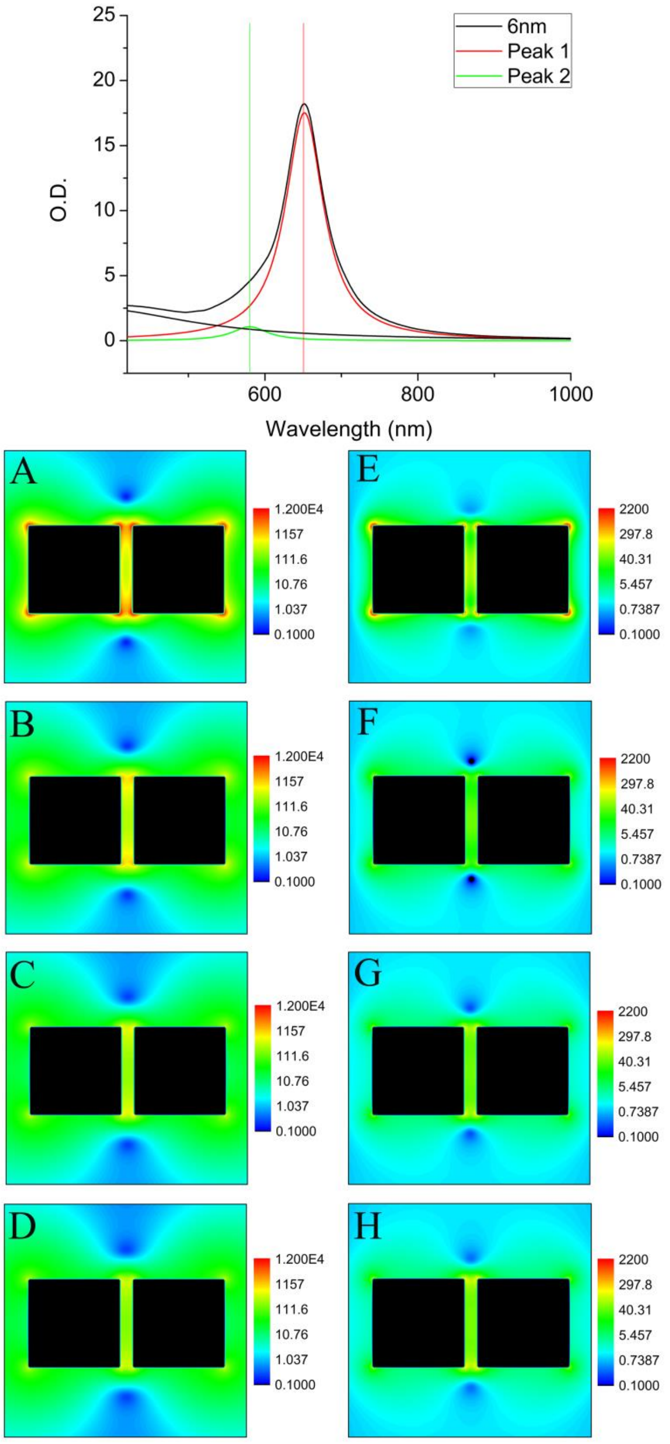

Figure 3.5. The electromagnetic field distribution for peak 1 (left, A-D) and peak 2 (right, E-H) of a 42 nm Au-Au nanocube dimer with an inter-particle separation distance of 6 nm was calculated. The distribution was calculated for 4 different xy slices of the dimer corresponding to the top surface (A and E), 8nm below the top surface (B and F), 15 nm below the top surface (C and G), and the middle of the dimer (D and H). Both peaks display the initial development of the enhanced field distribution between the facets of the adjacent nanocubes.

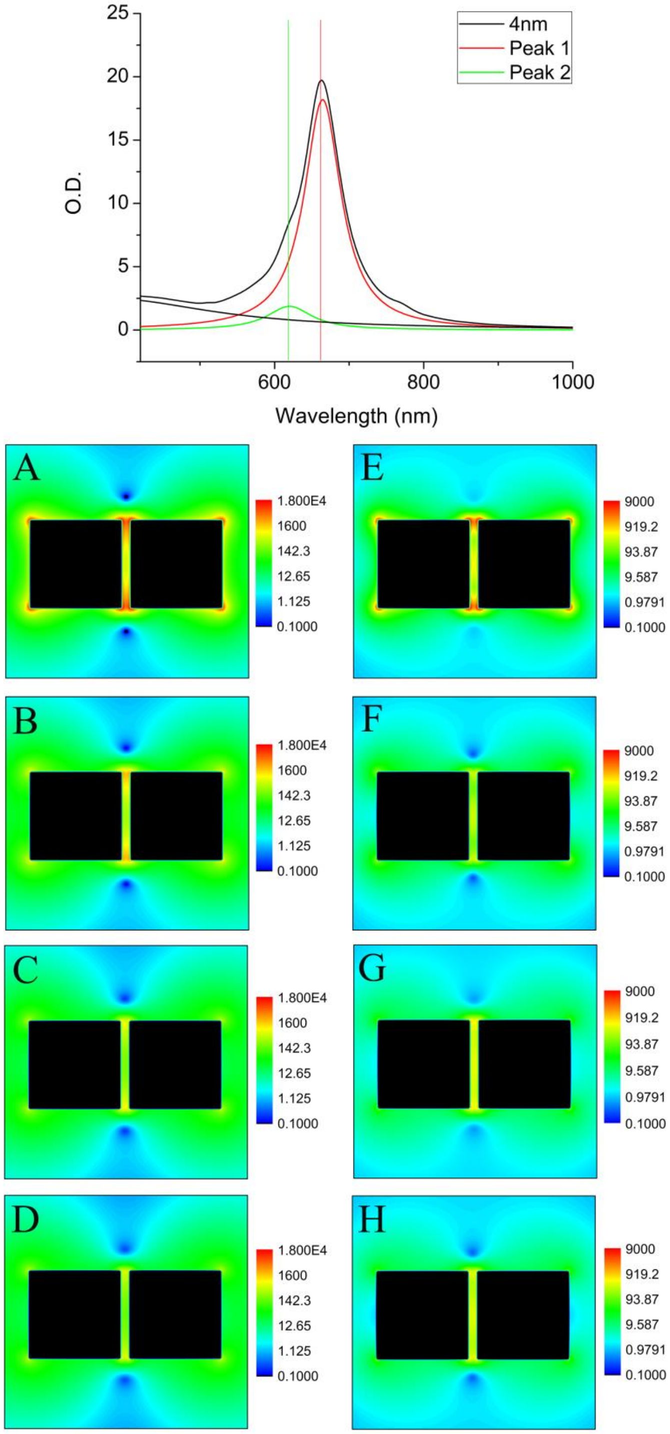

Figure 3.6. The electromagnetic field distribution for peak 1 (left, A-D) and peak 2 (right, E-H) of a 42 nm Au-Au nanocube dimer with an inter-particle separation distance of 4 nm was calculated. The distribution was calculated for 4 different xy slices of the dimer corresponding to the top surface (A and E), 8nm below the top surface (B and F), 15 nm below the top surface (C and G), and the middle of the dimer (D and H). Both peaks display the initial development of the enhanced field distribution between the facets of the adjacent nanocubes.

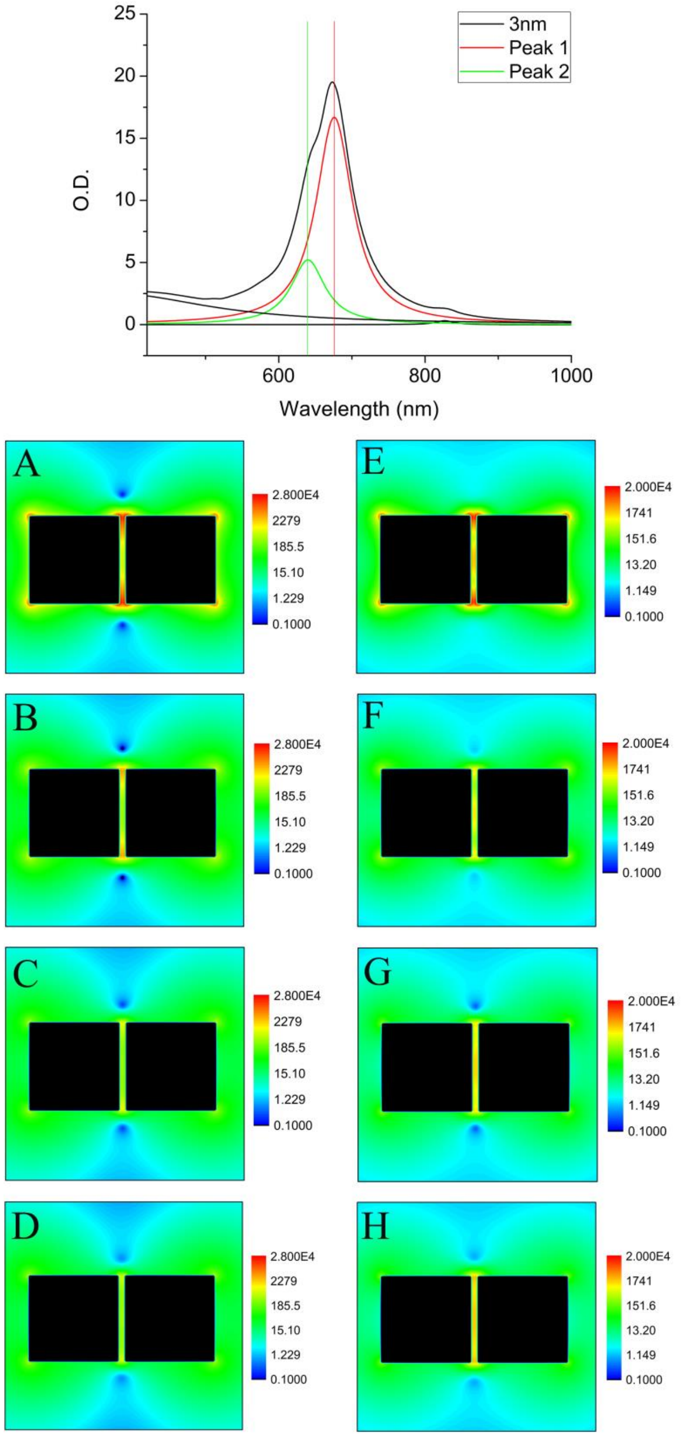

Figure 3.7. The electromagnetic field distribution for peak 1 (left, A-D) and peak 2 (right, E-H) of a 42 nm Au-Au nanocube dimer with an inter-particle separation distance of 3 nm was calculated. The distribution was calculated for 4 different xy slices of the dimer corresponding to the top surface (A and E), 8nm below the top surface (B and F), 15 nm below the top surface (C and G), and the middle of the dimer (D and H). Both peaks display the initial development of the enhanced field distribution between the facets of the adjacent nanocubes.

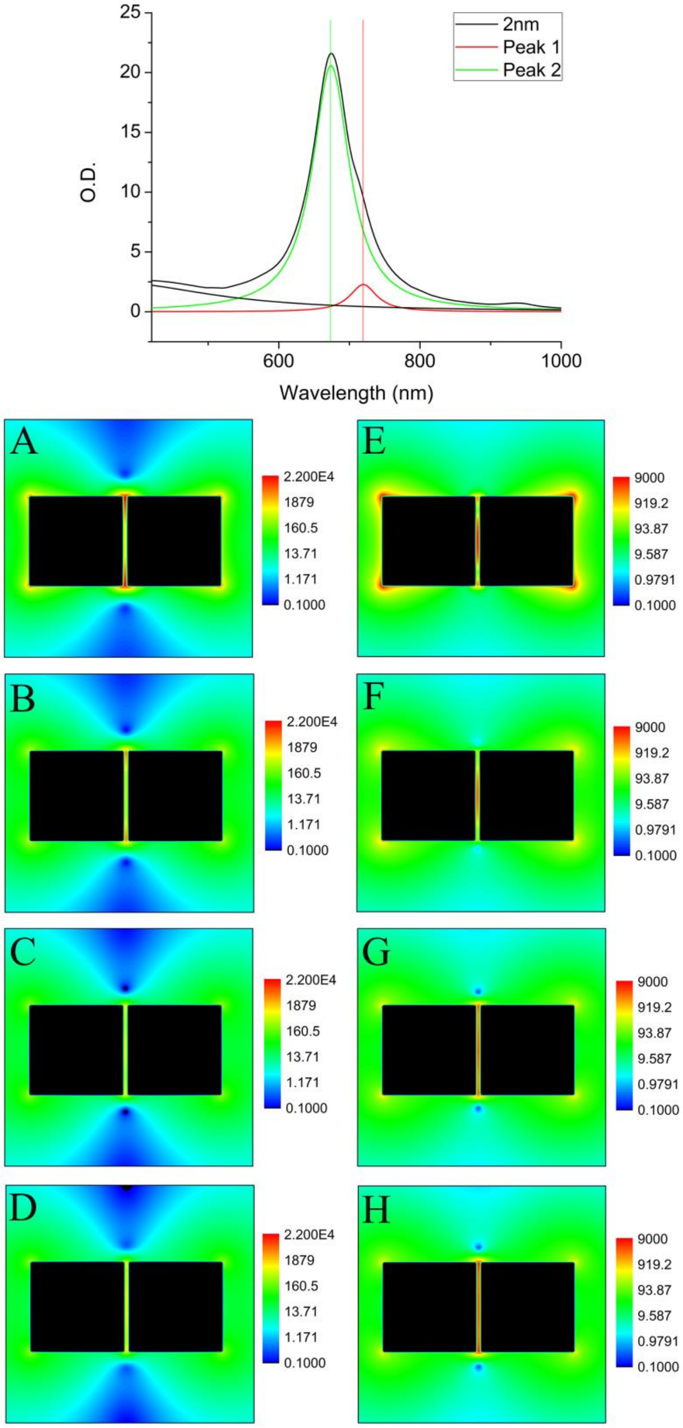

Figure 3.8. The electromagnetic field distribution for peak 1 (left, A-D) and peak 2 (right, E-H) of a 42 nm Au-Au nanocube dimer with an inter-particle separation distance of 2 nm was calculated. The distribution was calculated for 4 different xy slices of the dimer corresponding to the top surface (A and E), 8nm below the top surface (B and F), 15 nm below the top surface (C and G), and the middle of the dimer (D and H). Both peaks display the initial development of the enhanced field distribution between the facets of the adjacent nanocubes.

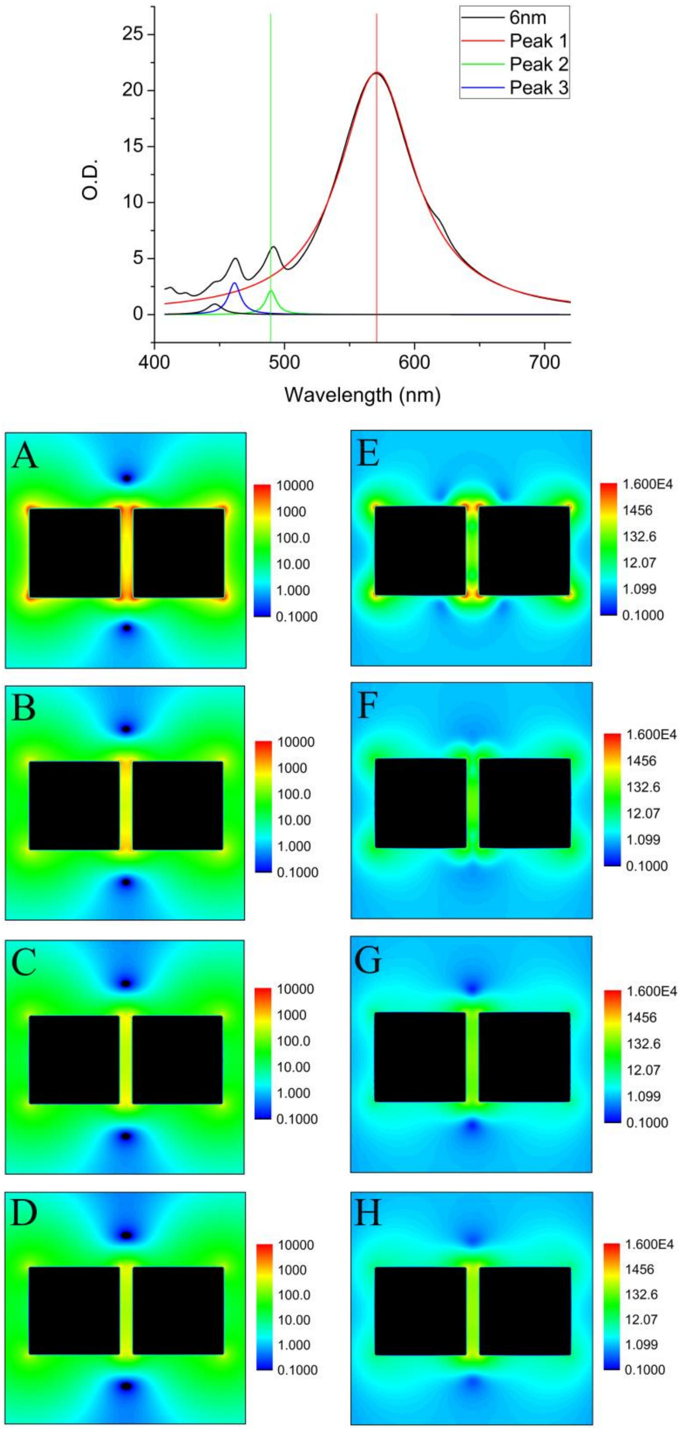

Figure 3.9. The electromagnetic field distribution for peak 1 (left, A-D) and peak 2 (right, E-H) of a 42 nm Ag-Ag nanocube dimer with an inter-particle separation distance of 6 nm was calculated. The distribution was calculated for 4 different xy slices of the dimer corresponding to the top surface (A and E), 8nm below the top surface (B and F), 15 nm below the top surface (C and G), and the middle of the dimer (D and H). Both peaks display the initial development of the enhanced field distribution between the facets of the adjacent nanocubes.

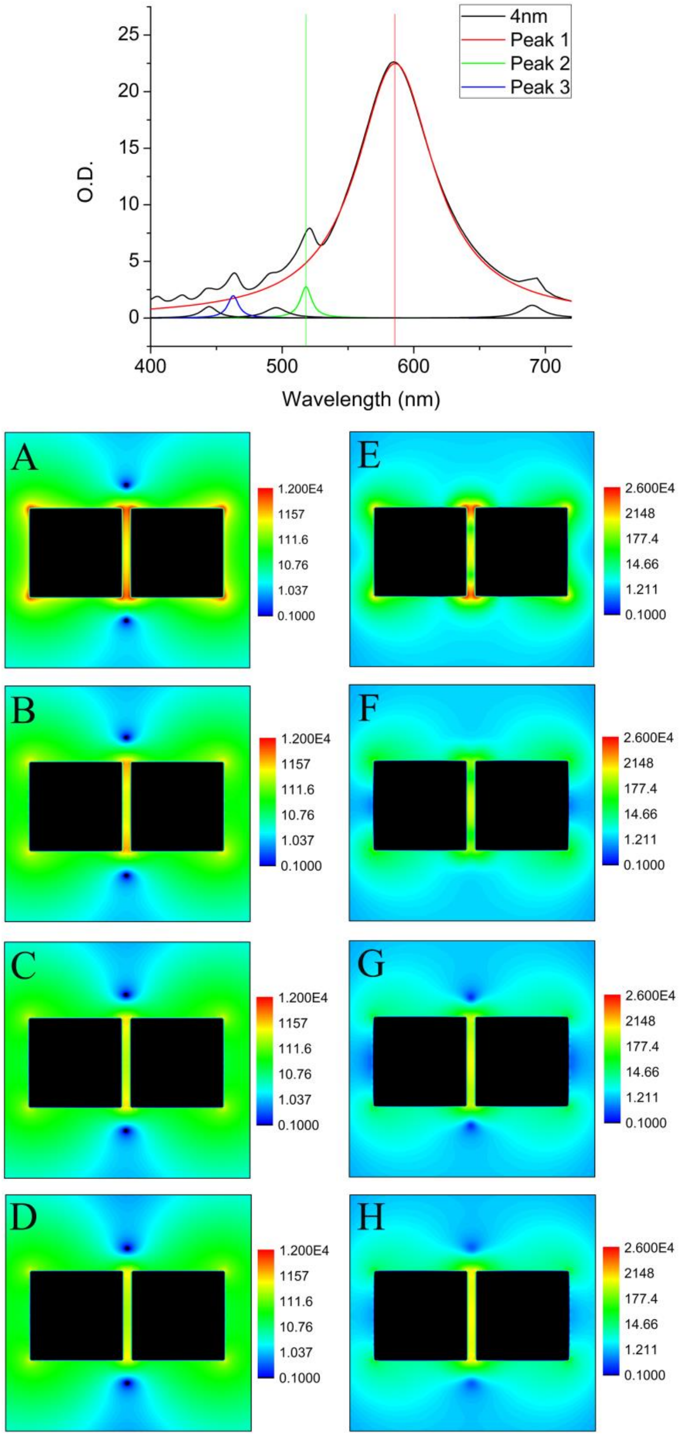

Figure 3.10. The electromagnetic field distribution for peak 1 (left, A-D) and peak 2 (right, E-H) of a 42 nm Ag-Ag nanocube dimer with an inter-particle separation distance of 4 nm was calculated. The distribution was calculated for 4 different xy slices of the dimer corresponding to the top surface (A and E), 8nm below the top surface (B and F), 15 nm below the top surface (C and G), and the middle of the dimer (D and H). Both peaks display the initial development of the enhanced field distribution between the facets of the adjacent nanocubes.

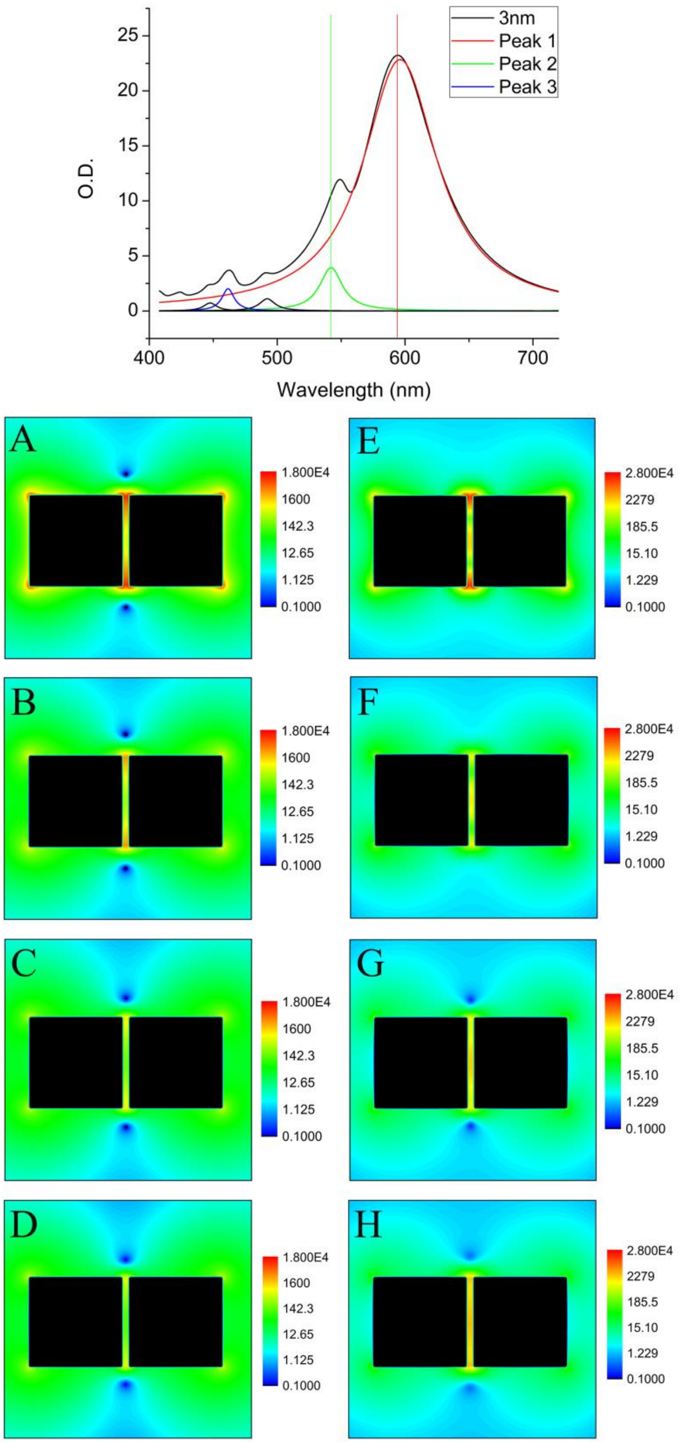

Figure 3.11. The electromagnetic field distribution for peak 1 (left, A-D) and peak 2 (right, E-H) of a 42 nm Ag-Ag nanocube dimer with an inter-particle separation distance of 3 nm was calculated. The distribution was calculated for 4 different xy slices of the dimer corresponding to the top surface (A and E), 8nm below the top surface (B and F), 15 nm below the top surface (C and G), and the middle of the dimer (D and H). Both peaks display the initial development of the enhanced field distribution between the facets of the adjacent nanocubes.

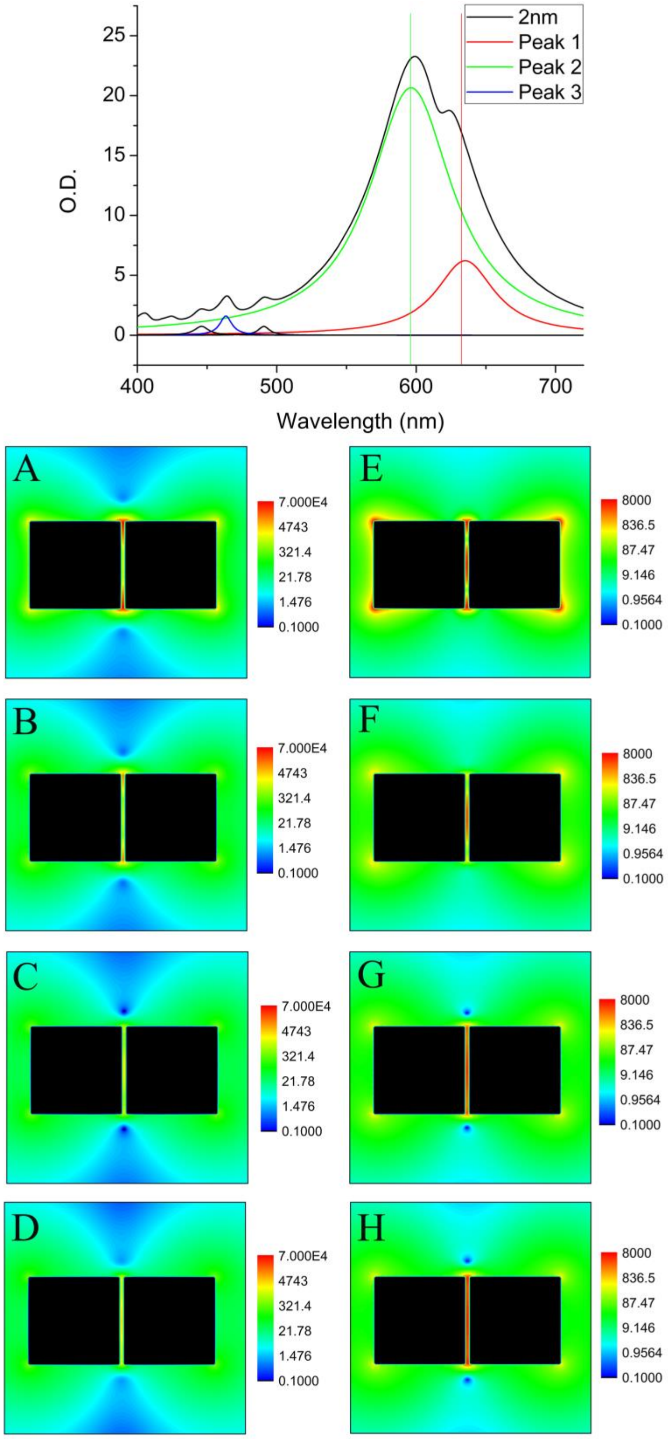

Figure 3.12. The electromagnetic field distribution for peak 1 (left, A-D) and peak 2 (right, E-H) of a 42 nm Ag-Ag nanocube dimer with an inter-particle separation distance of 2 nm was calculated. The distribution was calculated for 4 different xy slices of the dimer corresponding to the top surface (A and E), 8nm below the top surface (B and F), 15 nm below the top surface (C and G), and the middle of the dimer (D and H). Both peaks display the initial development of the enhanced field distribution between the facets of the adjacent nanocubes.

This finding is supported by previous reports of two different plasmonic bands, the longitudinal antenna plasmons (LAP_1) and transverse cavity plasmons (TCP_2), for a pair of flat gap cylindrical antennas at short separation distances[60]. Even though the nanocube dimer exhibits a reduced rotational symmetry compared to the cylindrical antenna dimer, it is interesting to notice the similarities between the polarization of the proposed LAP_1 and TCP_2 modes[60] and the polarization of peak 1 and peak 2 respectively (Figure 3.13-14).

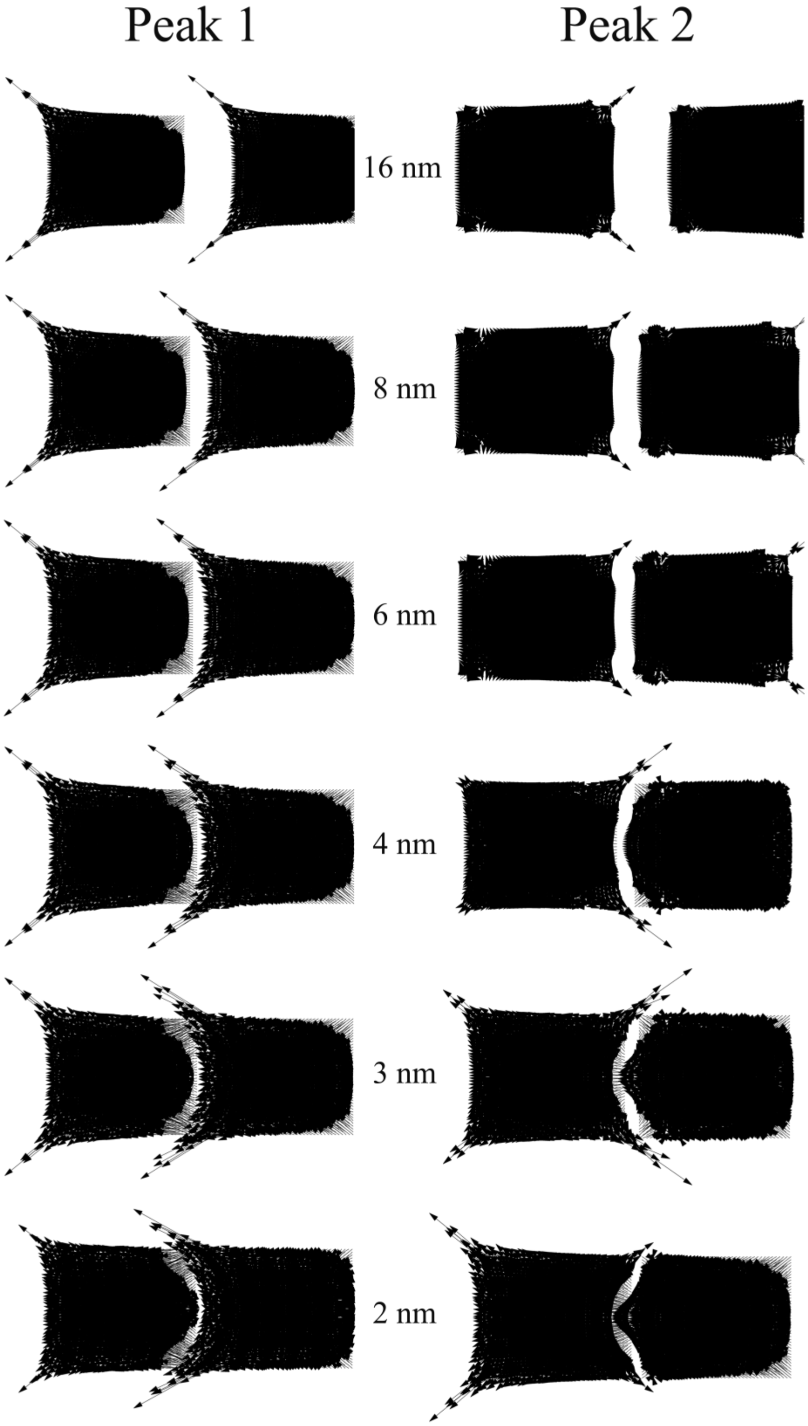

Figure 3.13. The polarization vector field was calculated for peak 1 (left) and peak 2 (right) of a 42 nm Au-Au nanocube dimer at varying separation distances (top xy slice). It is apparent that the identity (ie. polarization distribution) of the peak is consistent at all separation distances. Also, the magnitude of the enhanced polarization vectors present between the faces of adjacent dimers greatly increases at separation distances below 6 nm.

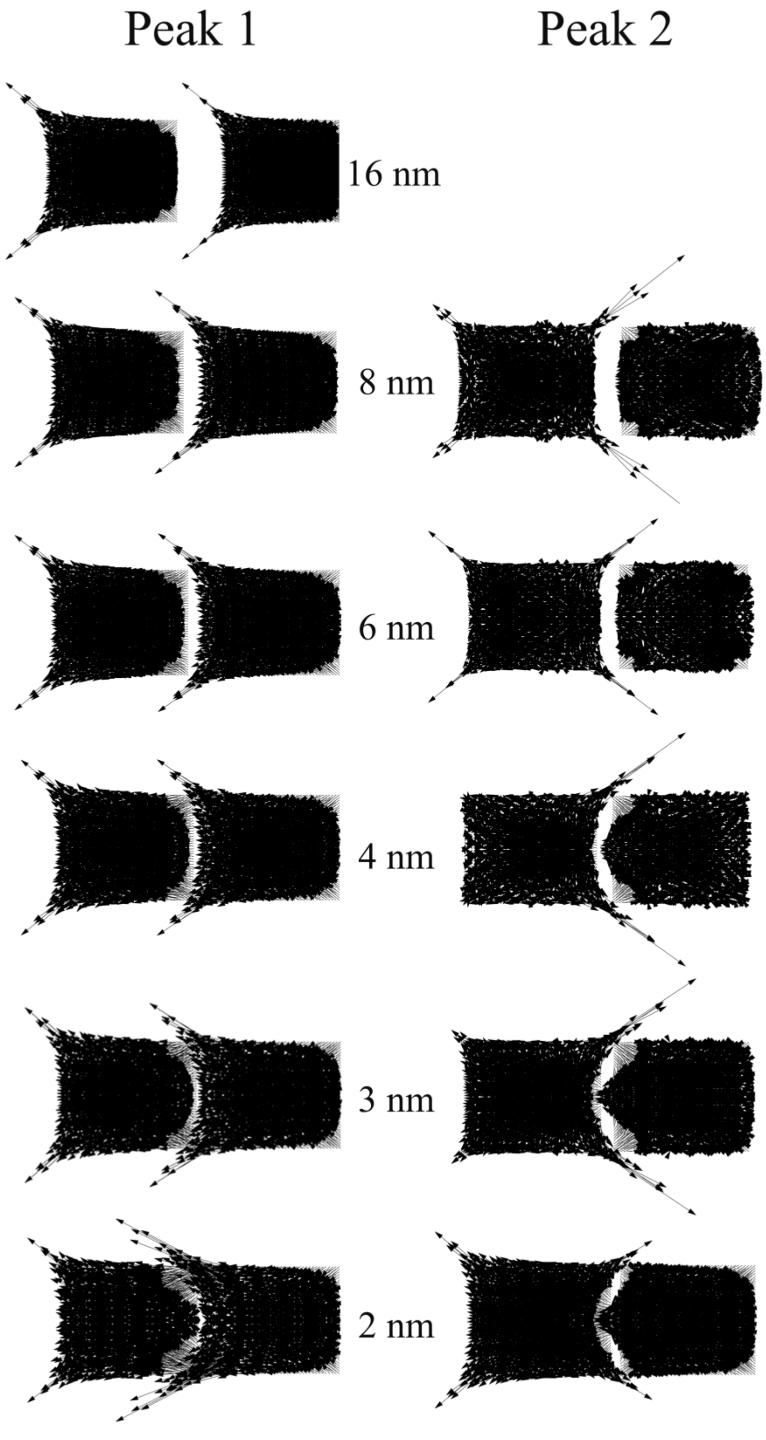

Figure 3.14. The polarization vector field was calculated for peak 1 (left) and peak 2 (right) of a 42 nm Ag-Ag nanocube dimer (top xy slice) at varying separation distances (peak 2 at 16 nm separation is omitted due to its absence in the extinction spectrum). It is apparent that the identity (ie. polarization distribution) of the peak is consistent at all separation distances. Also, the magnitude of the enhanced polarization vectors present between the faces of adjacent dimers greatly increases at separation distances below 6 nm.

3.3.4. Near-Field Coupling Behavior

It has been previously noted[44, 58, 61] that the near-field coupling between two nanoparticles can be described by a simple dipolar model. With this model the polarizability of the two particle/dipole system can be expressed as a function of both the polarizability of the individual nanoparticle and the decay length of the electric field generated by the neighboring particle. Since the polarizability of the nanoparticle is known to be directly proportional to the particle volume ($\mathbf{D}^3$) and the decay length is a function of the inverse cube of the distance[62] ($1/d^3$), the polarizability of the new system will inherently be sensitive to the distance between the interacting dipoles. Thus this sensitivity of the LSPR peak position, or coupling strength, should exhibit an inverse dependence on this distance scaled by the size of the particle $(d/\mathbf{D})^{-3}$. When the LSPR peak position is monitored as a function of the separation distance between the surfaces of two interacting nanoparticles, scaled to the size of the nanoparticles (s/**D**), the expected inverse cubic dependence has been shown to closely follow an exponential decay behavior. Subsequently the near field coupling behavior between two nanoparticles is now commonly described by the plasmon ruler equation[44]:

$$\frac{\Delta\lambda}{\lambda_0} = A * e^{\left(\frac{-\left({}^{s}/_{\boldsymbol{D}}\right)}{\tau}\right)}$$

where the fractional plasmon shift $(\frac{\Delta\lambda}{\lambda_0})$ is a function of the separation distance (scaled to the size of the particle, (s/**D**)) of the dimer, and both A and τ are fit parameters that describe both the coupled field strength and decay length respectively. The dipolar model, however, is not a complete description of plasmonic near-field coupling due to substantial contributions from higher order plasmonic modes, especially at small separation distances.

In order to further understand the near-field coupling behavior of Au-Au and Ag-Ag nanocube dimers at small separation distances, the fractional plasmon shift was plotted against the separation distance scaled to the size of the monomer and fit to the plasmon ruler equation. The fractional plasmon shift was followed for both peak 1 (Figure 3.15) and peak 2 (Figure 3.16) in the extinction spectrum of the Au-Au and Ag-Ag dimer; however, due to the absence of peak 2 in the Ag-Ag dimer extinction spectrum at separation distances greater than 8 nm only peak 1 will be discussed for both dimers. For peak 1 within the Au dimer, the fractional plasmon shift over all separation distances did not fit an expected exponential decay (Figure 3.15). However, it is apparent that peak 1 exhibits the expected exponential coupling behavior at long separation distances. When the data was fit for separation distances greater than 4 nm, characteristic values of $A = 0.12 \pm 0.01$ and $\tau = 0.42 \pm 0.05$ were observed (Figure 3.17) for the Au-Au dimer. These values agree well with previously reported values for the near-field coupling of Au nanocubes[42]. However, as seen in Figure 3.17, it is apparent that as the separation distance is reduced below 6 nm, the near field coupling increases much quicker than expected.

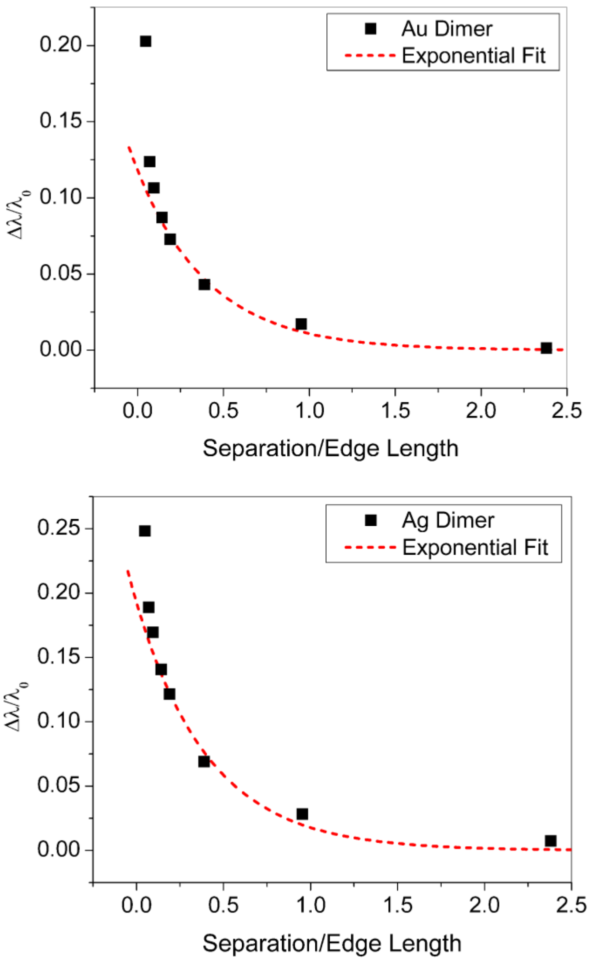

Figure 3.15. The failure of the exponential behavior of the fractional plasmon shift (Δλ/λ) with respect to the inter-particle separation normalized to the particle size, for the 42nm Au-Au (top) and Ag-Ag (bottom) dimer. There is an apparent deviation in the decay behavior of the LSPR peak position of peak 1 that occurs at roughly 6nm for both the Au-Au and Ag-Ag dimer. The exponential fit displayed is based on the calculated behavior of each dimer at a separation distance greater than 6nm and gives coupled field strengths and decay lengths of A = 0.12 and τ = 0.42 and A = 0.19 and τ = 0.42 for Au and Ag dimers respectively.

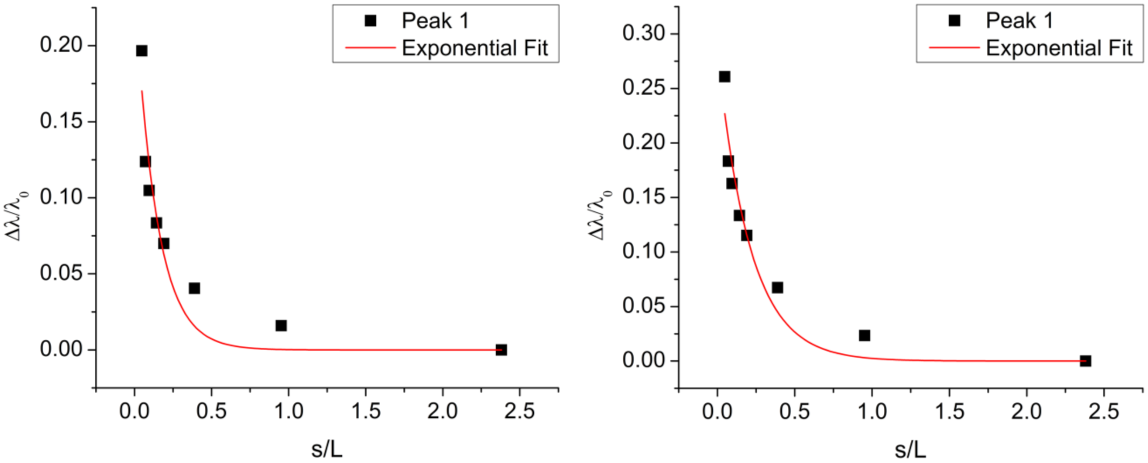

Figure 3.16. The fractional shift in LSPR peak position was plotted against the separation distance, normalized to the size of the individual particle, for peak 1 of the 42nm Au-Au (left) and Ag-Ag (right) dimer over separation distances ranging from 100-2 nm. An exponential fit of the fractional shift in the LSPR over all separation distances did not approximate the data well, giving an R^2 value of 0.89 for Au and 0.95 for Ag. This is in comparison to an R^2 value of 0.99 and 0.98 for the Au and Ag dimer respectively, when only longer separation distance ranging between 100-6 nm were analyzed (Figure 3.15).

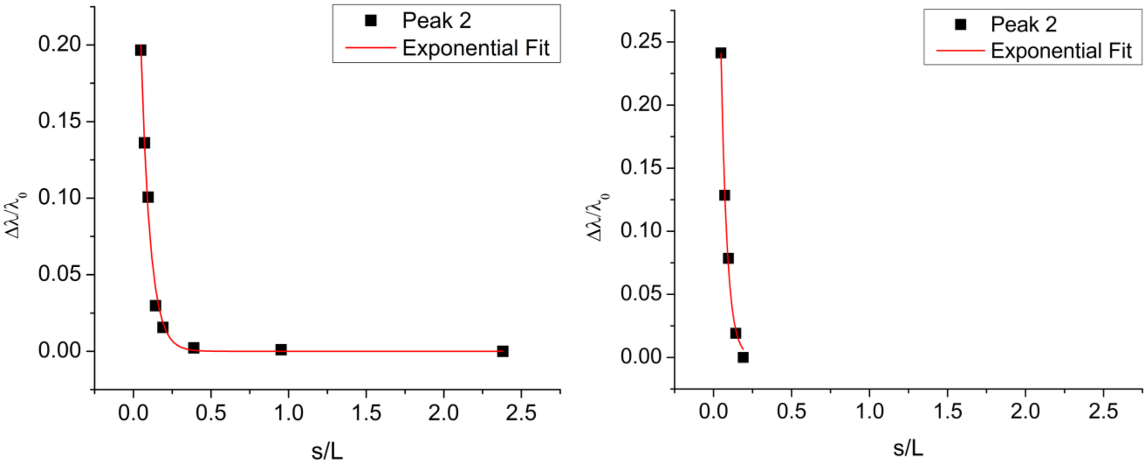

Figure 3.17. The fractional shift in LSPR peak position was plotted against the separation distance, normalized to the size of the individual particle, for peak 2 of the 42nm Au-Au (left) and Ag-Ag (right) dimer. Due to the absence of peak 2 in the Ag-Ag dimer extinction spectrum and the nearly nonexistent coupling of peak 2 in the Au-Au dimer until a separation distance of 8nm, a comparison of the coupling behavior at longer versus shorter separation disatnces was unobtainable.

When the fractional shift in the plasmon position of peak 1 for the Ag dimer was analyzed, the same trend was observed. The coupling behavior over all separation distances could not fit a consistent exponential decay (Figure 3.15). However, when only the separation distances greater than 4 nm were considered (Figure 3.17) the data fit an exponential decay with a coupled field strength and decay length of $A = 0.19 \pm 0.02$ and $\tau = 0.42 \pm 0.06$. This agrees well with an expected increase in the coupled field strength and similar decay length when compared to the Au dimer. Interestingly, this transition in the near field coupling behavior occurs at the same separation distance as the progressive decrease in the area of peak 1 and corresponding increase of the area of peak 2 within both the Au and Ag dimer extinction spectrum. Thus there appears to be a correlation between the observed changes in the extinction spectrum and the near-field coupling behavior of the dimer.

Due to the apparent transition in the near-field coupling behavior occurring at a separation distance below 6 nm, the electromagnetic field distribution was determined for the top surface of both the Au and Ag dimer at separation distances ranging from 16-2 nm. As mentioned previously, Hooshmand and co-workers[45] recently suggested that the distribution of the electromagnetic field enhancement which occurs between nanocube dimers is very sensitive to the separation distance of the dimer. As seen in Figure 4 and Figure 5, that is also the case here. At a separation distance of 16 nm, the density of oscillating dipoles is localized around the corners of the nanocube dimer for both peak 1 (Figure 4) and peak 2 (Figure 5) of the Au dimer. As the separation distance decreases, there is an apparent delocalization of the oscillating dipole density along the interfacial region of the adjacent nanocubes. This delocalization becomes drastic at a separation distance of 2 nm where the oscillating dipoles are almost entirely distributed on the facing facets between the two nanocubes. This affect is even more pronounced when the distribution of the oscillating dipole density is considered for subsequent slices along the height of the dimer (Figure 3.5-3.12).

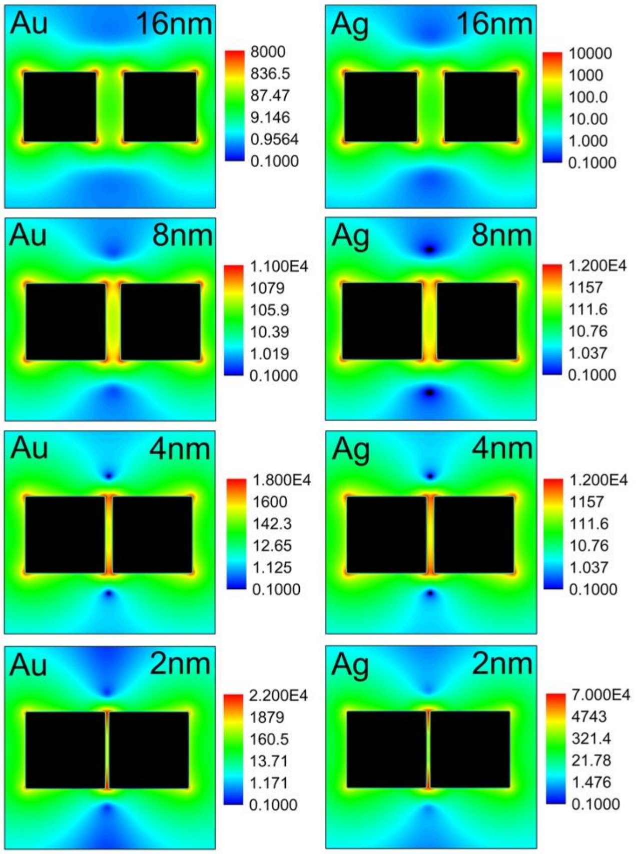

Figure 3.18. The plasmonic electromagnetic field distribution is calculated for the top slice of a Au-Au (Au) and Ag-Ag (Ag) 42 nm nanocube dimer at varying separation distances of the dimer (16, 8, 4, and 2 nm). The wavelength of excitation was chosen based on the peak maximum for peak 1 within each extinction spectrum and the light was polarized parallel to the inter-particle axis. There is a clear transition in the distribution of the enhanced electromagnetic field that occurs between the adjacent facets of the nanocube dimer that occurs between 6 and 4 nm. This transition is indicative of a break in the near-field coupling behavior that occurs at separation distance of roughly 4 nm.

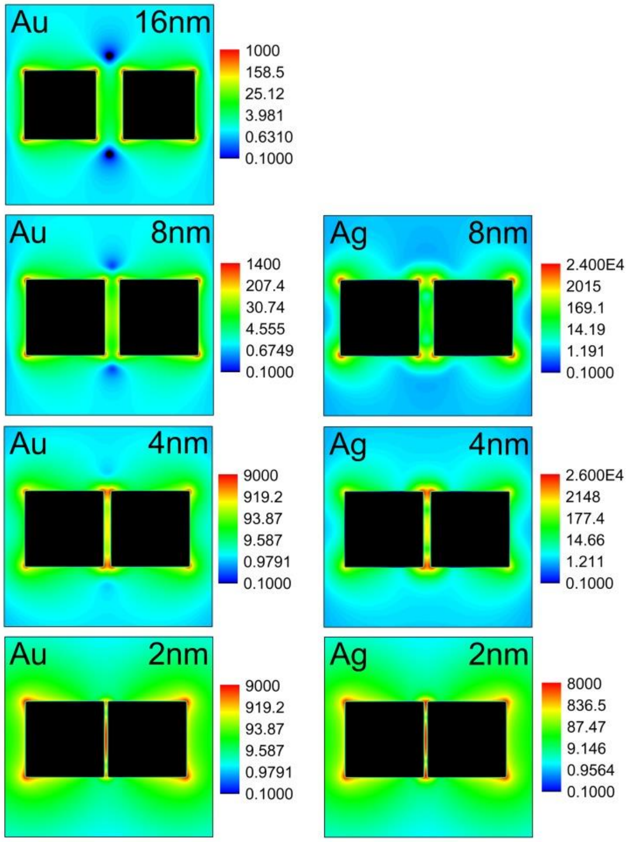

Figure 3.19. The plasmonic electromagnetic field distribution is calculated for the top slice of a Au-Au (Au) and Ag-Ag (Ag) 42 nm nanocube dimer at varying separation distances of the dimer (16, 8, 4, and 2 nm). The wavelength of excitation was chosen based on the peak maximum for peak 2 within each extinction spectrum and the light was polarized parallel to the inter-particle axis (peak 2 is not present in the extinction spectrum of the Ag-Ag dimer with a 16 nm separation distance). A clear development of the plasmonic electromagnetic field distribution between the facets of the adjacent monomers occurs between the separation distances of 6 and 4 nm. This transition results in a break of the expected exponential behavior of the near field coupling within the dimer.

This same delocalization of oscillating dipole density across the interfacial region of the adjacent nanocubes occurs in the Ag-Ag dimer. As seen in Figure 3.18 and Figure 3.19, the development of oscillating dipole density between the two adjacent faces of the Ag nanocubes becomes apparent at a separation distance of 4 nm. At a separation distance of 8 nm the plasmon field is again localized on the corners, and at a separation distance of 2 nm the plasmon field is almost entirely present along the adjacent faces of the nanocubes. This transition is further supported by the calculated polarization vector distribution for each peak at separation distances ranging from 16-2 nm (Figure 3.13 and 3.14). Here, we see that magnitude of polarization vectors found between the adjacent faces of the dimer increases drastically for both peaks when the separation distance is decreased below 6 nm. It is interesting to note here, that the observed break in the characteristic exponential behavior of the near field coupling between two nanocubes seen in Figure 3.18 and Figure 3.19 occurs at the same separation distance that induces a change in the oscillating dipole density distribution. We suggest that the break in exponential coupling behavior is due to a change in the distribution of the oscillating dipole density between the two faces of the adjacent nanobuces. Thus, the near-field coupling behavior between two nanocubes is defined by the distribution of the electromagnetic field and osciallating dipole density between the adjacent faces of two nanocubes.

3.4. Concluding Remarks

In summary, it is clear that there are two distinct regions of near-field coupling that result when two nanocubes are brought in close proximity to each other that is independent of the metal type. At large separation distances, the near-field coupling between the two nanocubes agrees well with previous reports of both Ag-Ag and Au-Au dimers. However, as the separation distance is decreased there is a clear emergence of a new region of near-field coupling. This region is marked by: a transition to a new major plasmonic mode within the extinction spectrum, a break from the expected exponential coupling behavior, and a delocalization of the oscillating dipole density across the interfacial region of the dimer. This can be explained by the sensitivity of the electromagnetic field distribution to the separation distance of the dimer. At a separation distance of 2nm, the electromagnetic field distribution is mostly present between the two facing facets. At 4nm separation, it was found that the field was strong between the facing facets as well as between the corners. At a separation distance of 6nm or greater, it was found that the density of oscillating dipoles was localized on the corners. As a result, the break in the near-field coupling behavior of a cubic dimer, 42 nm in size, at small separation distances is due to the unique distribution of oscillating dipole density that occurs at separation distances below 4-6 nm.

3.5. References

(1) J. A. Bordley, N. Hooshmand and M. A. El-Sayed: The Coupling between Gold or Silver Nanocubes in Their Homo-Dimers: A New Coupling Mechanism at Short Separation Distances. *Nano Lett.* **2015**, 15, 3391-3397.

(2) S. Link and M. A. El-Sayed: Spectral Properties and Relaxation Dynamics of Surface Plasmon Electronic Oscillations in Gold and Silver Nanodots and Nanorods. *J. Phys. Chem. B* **1999**, *103*, 8410-8426.

(3) K. L. Kelly, E. Coronado, L. L. Zhao and G. C. Schatz: The Optical Properties of Metal Nanoparticles: The Influence of Size, Shape, and Dielectric Environment. *J. Phys. Chem. B* **2002**, *107*, 668-677.

(4) P. K. Jain, K. S. Lee, I. H. El-Sayed and M. A. El-Sayed: Calculated Absorption and Scattering Properties of Gold Nanoparticles of Different Size, Shape, and Composition: Applications in Biological Imaging and Biomedicine. *J. Phys. Chem. B* **2006**, *110*, 7238-7248.

(5) E. Hao and G. C. Schatz: Electromagnetic Fields around Silver Nanoparticles and Dimers. *J. Chem. Phys.* **2004**, *120*, 357-366.

(6) N. J. Halas, S. Lal, W.-S. Chang, S. Link and P. Nordlander: Plasmons in Strongly Coupled Metallic Nanostructures. *Chem Rev.* **2011**, *111*, 3913-3961.

(7) D. Yelin, D. Oron, S. Thiberge, E. Moses and Y. Silberberg: Multiphoton Plasmon-Resonance Microscopy. *Opt. Express* **2003**, *11*, 1385-1391.

(8) N. J. Durr, T. Larson, D. K. Smith, B. A. Korgel, K. Sokolov and A. Ben-Yakar: Two-Photon Luminescence Imaging of Cancer Cells Using Molecularly Targeted Gold Nanorods. *Nano Lett.* **2007**, *7*, 941-945.

(9) Y. Wang, X. Xie, X. Wang, G. Ku, K. L. Gill, D. P. O'Neal, G. Stoica and L. V. Wang: Photoacoustic Tomography of a Nanoshell Contrast Agent in the in Vivo Rat Brain. *Nano Lett.* **2004**, *4*, 1689-1692.

(10) K. Sokolov, M. Follen, J. Aaron, I. Pavlova, A. Malpica, R. Lotan and R. Richards-Kortum: Real-Time Vital Optical Imaging of Precancer Using Anti-Epidermal Growth Factor Receptor Antibodies Conjugated to Gold Nanoparticles. *Cancer Res.* **2003**, *63*, 1999-2004.

(11) I. H. El Sayed, X. Huang and M. A. El-Sayed: Surface Plasmon Resonance Scattering and Absorption of Anti-Egfr Antibody Conjugated Gold Nanoparticles in Cancer Diagnostics: Applications in Oral Cancer. *Nano Lett.* **2005**, *5*, 829-834.

(12) A. M. Gobin, M. H. Lee, N. J. Halas, W. D. James, R. A. Drezek and J. L. West: Near-Infrared Resonant Nanoshells for Combined Optical Imaging and Photothermal Cancer Therapy. *Nano Lett.* **2007**, *7*, 1929-1934.

(13) X. Huang, X. Peng, Y. Wang, Y. Wang, D. M. Shin, M. A. El-Sayed and S. Nie: A Reexamination of Active and Passive Tumor Targeting by Using Rod-Shaped Gold Nanocrystals and Covalently Conjugated Peptide Ligands. *ACS Nano* **2010**, *4*, 5887 - 5896.

(14) P. V. Kamat: Meeting the Clean Energy Demand: Nanostructure Architectures for Solar Energy Conversion. *J. Phys. Chem. C* **2007**, *111*, 2834-2860.

(15) C. Sonnichsen, B. M. Reinhard, J. Liphardt and A. P. Alivisatos: A Molecular Ruler Based on Plasmon Coupling of Single Gold and Silver Nanoparticles. *Nat. Biotech.* **2005**, *23*, 741-745.

(16) R. Elghanian, J. J. Storhoff, R. C. Mucic, R. L. Letsinger and C. A. Mirkin: Selective Colorimetric Detection of Polynucleotides Based on the Distance-Dependent Optical Properties of Gold Nanoparticles. *Science* **1997**, *277*, 1078-1081.

(17) M. I. Shukoor, M. O. Altman, D. Han, A. T. Bayrac, I. Ocsoy, Z. Zhu and W. Tan: Aptamer-Nanoparticle Assembly for Logic-Based Detection. *ACS Appl. Mater. Interfaces* **2012**, *4*, 3007-3011.

(18) J. J. Storhoff, R. Elghanian, R. C. Mucic, C. A. Mirkin and R. L. Letsinger: One-Pot Colorimetric Differentiation of Polynucleotides with Single Base Imperfections Using Gold Nanoparticle Probes. *J. Am. Chem. Soc.* **1998**, *120*, 1959-1964.

(19) R. G. Freeman, K. C. Grabar, K. J. Allison, R. M. Bright, J. A. Davis, A. P. Guthrie, M. B. Hommer, M. A. Jackson, P. C. Smith, D. G. Walter and M. J. Natan: Self-Assembled Metal Colloid Monolayers: An Approach to Sers Substrates. *Science* **1995**, *267*, 1629-1632.

(20) Z. Q. Tian, B. Ren and D. Y. Wu: Surface-Enhanced Raman Scattering: From Noble to Transition Metals and from Rough Surfaces to Ordered Nanostructures. *J. Phys. Chem. B* **2002**, *106*, 9463-9483.

(21) M. Moskovits: Surface-Enhanced Raman Spectroscopy: A Brief Retrospective. *J. Ram. Spectrosc.* **2005**, *36*, 485-496.

(22) H. Xu, J. Aizpurua, M. Käll and P. Apell: Electromagnetic Contributions to Single-Molecule Sensitivity in Surface-Enhanced Raman Scattering. *Phys. Rev. E* **2000**, *62*, 4318-4324.

(23) K. L. Wustholz, A.-I. Henry, J. M. McMahon, R. G. Freeman, N. Valley, M. E. Piotti, M. J. Natan, G. C. Schatz and R. P. V. Duyne: Structure−Activity Relationships in

Gold Nanoparticle Dimers and Trimers for Surface-Enhanced Raman Spectroscopy. *J. Am. Chem. Soc.* **2010**, *132*, 10903-10910.

(24) T. Dadosh, J. Sperling, G. W. Bryant, R. Breslow, T. Shegai, M. Dyshel, G. Haran and I. Bar-Joseph: Plasmonic Control of the Shape of the Raman Spectrum of a Single Molecule in a Silver Nanoparticle Dimer. *ACS Nano* **2009**, *3*, 1988-1994.

(25) C. E. Talley, J. B. Jackson, C. Oubre, N. K. Grady, C. W. Hollars, S. M. Lane, T. R. Huser, P. Nordlander and N. J. Halas: Surface-Enhanced Raman Scattering from Individual Au Nanoparticles and Nanoparticle Dimer Substrates. *Nano Lett.* **2005**, *5*, 1569-1574.

(26) K. A. Willets and R. P. Van Duyne: Localized Surface Plasmon Resonance Spectroscopy and Sensing. *Annu. Rev. Phys. Chem.* **2007**, *58*, 267-297.

(27) G. Mie: Beiträge Zur Optik Trüber Medien, Speziell Kolloidaler Metallösungen. *Ann. Phys.* **1908**, *330*, 377-445.

(28) J. Aizpurua, P. Hanarp, D. S. Sutherland, M. Käll, G. W. Bryant and F. J. García de Abajo: Optical Properties of Gold Nanorings. *Phys. Rev. Lett.* **2003**, *90*, 057401.

(29) M. M. Miller and A. A. Lazarides: Sensitivity of Metal Nanoparticle Surface Plasmon Resonance to the Dielectric Environment. *J. Phys. Chem. B* **2005**, *109*, 21556-21565.

(30) P. K. Jain, S. Eustis and M. A. El-Sayed: Plasmon Coupling in Nanorod Assemblies: Optical Absorption, Discrete Dipole Approximation Simulation, and Exciton-Coupling Model. *J. Phys. Chem. B* **2006**, *110*, 18243-18253.

(31) S. Link, M. Mohamed and M. A. El-Sayed: Simulation of the Optical Absorption Spectra of Gold Nanorods as a Function of Their Aspect Ratio and the Effect of the Medium Dielectric Constant. *J. Phys. Chem. B* **1999**, *103*, 3073-3077.

(32) N. N. Nikolay, A. A. Petar and O. Minoru: Near-Field Properties of a Gold Nanoparticle Array on Different Substrates Excited by a Femtosecond Laser. *Nanotechnology* **2007**, *18*, 305703.

(33) L. Gunnarsson, T. Rindzevicius, J. Prikulis, B. Kasemo, M. Käll, S. Zou and G. C. Schatz: Confined Plasmons in Nanofabricated Single Silver Particle Pairs: Experimental Observations of Strong Interparticle Interactions. *J. Phys. Chem. B* **2004**, *109*, 1079-1087.

(34) O. L. Muskens, V. Giannini, J. A. Sánchez-Gil and J. Gómez Rivas: Optical Scattering Resonances of Single and Coupled Dimer Plasmonic Nanoantennas. *Opt. Express* **2007**, *15*, 17736-17746.

(35) A. M. Funston, C. Novo, T. J. Davis and P. Mulvaney: Plasmon Coupling of Gold Nanorods at Short Distances and in Different Geometries. *Nano Lett.* **2009**, *9*, 1651-1658.
(36) S. Dodson, M. Haggui, R. Bachelot, J. Plain, S. Li and Q. Xiong: Optimizing Electromagnetic Hotspots in Plasmonic Bowtie Nanoantennae. *J. Phys. Chem. Lett.* **2013**, *4*, 496-501.

(37) G. Raschke, S. Kowarik, T. Franzl, C. Sönnichsen, T. A. Klar, J. Feldmann, A. Nichtl and K. Kürzinger: Biomolecular Recognition Based on Single Gold Nanoparticle Light Scattering. *Nano Lett.* **2003**, *3*, 935-938.

(38) T. Endo, K. Kerman, N. Nagatani, Y. Takamura and E. Tamiya: Label-Free Detection of Peptide Nucleic Acid−DNA Hybridization Using Localized Surface Plasmon Resonance Based Optical Biosensor. *Anal. Chem.* **2005**, *77*, 6976-6984.

(39) A. Haes, D. Stuart, S. Nie and R. Van Duyne: Using Solution-Phase Nanoparticles, Surface-Confined Nanoparticle Arrays and Single Nanoparticles as Biological Sensing Platforms. *J. Fluoresc.* **2004**, *14*, 355-367.

(40) K. H. Su, Q. H. Wei, X. Zhang, J. J. Mock, D. R. Smith and S. Schultz: Interparticle Coupling Effects on Plasmon Resonances of Nanogold Particles. *Nano Lett.* **2003**, *3*, 1087-1090.

(41) P. K. Jain, W. Huang and M. A. El-Sayed: On the Universal Scaling Behavior of the Distance Decay of Plasmon Coupling in Metal Nanoparticle Pairs: A Plasmon Ruler Equation. *Nano Lett.* **2007**, *7*, 2080-2088.

(42) C. E. Tabor, R. Murali, M. A. Mahmoud and M. A. El-Sayed: On the Use of Plasmonic Nanoparticle Pairs as a Plasmon Ruler: The Dependence of the near-Field Dipole Plasmon Coupling on Nanoparticle Size and Shape. *J. Phys. Chem. A* **2009**, *113*, 1946-1953.

(43) P. K. Jain and M. A. El-Sayed: Plasmonic Coupling in Noble Metal Nanostructures. *Chem. Phys. Lett.* **2010**, *487*, 153-164.

(44) P. K. Jain, W. Huang and M. A. El-Sayed: On the Universal Scaling Behavior of the Distance Decay of Plasmon Coupling in Metal Nanoparticle Pairs: A Plasmon Ruler Equation. *Nano Lett.* **2007**, *7*, 2080-2088.

(45) P. K. Jain and M. A. El-Sayed: Surface Plasmon Coupling and Its Universal Size Scaling in Metal Nanostructures of Complex Geometry: Elongated Particle Pairs and Nanosphere Trimers. *J. Phys. Chem. C* **2008**, *112*, 4954-4960.

(46) T. V. Teperik, P. Nordlander, J. Aizpurua and A. G. Borisov: Robust Subnanometric Plasmon Ruler by Rescaling of the Nonlocal Optical Response. *Phys. Rev. Lett.* **2013**, *110*, 263901.

(47) T. V. Teperik, P. Nordlander, J. Aizpurua and A. G. Borisov: Quantum Effects and Nonlocality in Strongly Coupled Plasmonic Nanowire Dimers. *Opt. Express* **2013**, *21*, 27306-27325.

(48) A. Fernández-Domínguez, A. Wiener, F. García-Vidal, S. Maier and J. Pendry: Transformation-Optics Description of Nonlocal Effects in Plasmonic Nanostructures. *Phys. Rev. Lett.* **2012**, *108*, 106802.

(49) G. Toscano, S. Raza, A.-P. Jauho, N. A. Mortensen and M. Wubs: Modified Field Enhancement and Extinction by Plasmonic Nanowire Dimers Due to Nonlocal Response. *Opt. Express* **2012**, *20*, 4176-4188.

(50) C. Ciracì, R. Hill, J. Mock, Y. Urzhumov, A. Fernández-Domínguez, S. Maier, J. Pendry, A. Chilkoti and D. Smith: Probing the Ultimate Limits of Plasmonic Enhancement. *Science* **2012**, *337*, 1072-1074.

(51) N. A. Mortensen, S. Raza, M. Wubs, T. Søndergaard and S. I. Bozhevolnyi: A Generalized Non-Local Optical Response Theory for Plasmonic Nanostructures. *Nat. Commun.* **2014**, *5*.

(52) N. Hooshmand, J. A. Bordley and M. A. El-Sayed: Are Hot Spots between Two Plasmonic Nanocubes of Silver or Gold Formed between Adjacent Corners or Adjacent Facets? A Dda Examination. *J. Phys. Chem. Lett.* **2014**, *5*, 2229-2234.

(53) J. Zhao, A. O. Pinchuk, J. M. McMahon, S. Li, L. K. Ausman, A. L. Atkinson and G. C. Schatz: Methods for Describing the Electromagnetic Properties of Silver and Gold Nanoparticles. *Acc. Chem. Res.* **2008**, *41*, 1710-1720.

(54) B. T. Draine: The Discrete-Dipole Approximation and Its Application to Interstellar Graphite Grains. *Astrophys. J.* **1988**, *333*, 848-872.

(55) B. T. Draine and P. J. Flatau: Discrete-Dipole Approximation for Scattering Calculations. *J. Opt. Soc. Am. A* **1994**, *11*, 1491-1499.

(56) P. B. Johnson and R. W. Christy: Optical Constants of the Noble Metals. *Phys. Rev. B* **1972**, *6*, 4370-4379.

(57) L. A. Sweatlock, S. A. Maier, H. A. Atwater, J. J. Penninkhof and A. Polman: Highly Confined Electromagnetic Fields in Arrays of Strongly Coupled Ag Nanoparticles. *Phys. Rev. B* **2005**, *71*, 235408.

(58) W. Rechberger, A. Hohenau, A. Leitner, J. R. Krenn, B. Lamprecht and F. R. Aussenegg: Optical Properties of Two Interacting Gold Nanoparticles. *Opt. Commun.* **2003**, *220*, 137-141.

(59) S. Marhaba, G. Bachelier, C. Bonnet, M. Broyer, E. Cottancin, N. Grillet, J. Lermé, J.-L. Vialle and M. Pellarin: Surface Plasmon Resonance of Single Gold Nanodimers near the Conductive Contact Limit. *J. Phys. Chem. C* **2009**, *113*, 4349-4356.

(60) R. Esteban, G. Aguirregabiria, A. G. Borisov, Y. M. Wang, P. Nordlander, G. W. Bryant and J. Aizpurua: The Morphology of Narrow Gaps Modifies the Plasmonic Response. *ACS Photonics* **2015**, 2, 295-305.

(61) M. Gluodenis and C. A. Foss: The Effect of Mutual Orientation on the Spectra of Metal Nanoparticle Rod−Rod and Rod−Sphere Pairs. *J. Phys. Chem. B* **2002**, *106*, 9484-9489.

(62) S. A. Maier, M. L. Brongersma, P. G. Kik and H. A. Atwater: Observation of near-Field Coupling in Metal Nanoparticle Chains Using Far-Field Polarization Spectroscopy. *Phys. Rev. B* **2002**, *65*, 193408.

CHAPTER 4

PLASMONIC SPECTROSCOPY OF FACE-TO-FACE SILVER NANOCUBE DIMERS IN SOLUTION AND ON A SUBSTRATE[1]

4.1 Motivation

The plasmonic response of nanoparticles in close proximity to each other is strongly dependent on the size, the shape, the inter-particle separation, as well as the dielectric function of the surrounding medium or supporting material (substrate)[2-10]. The sensitivity of the optical and electromagnetic field properties to these external factors allows for nanoparticles to become useful for a variety of important applications which include imaging, near field scanning optical microscopy, optical energy transport, and chemical and biological sensing[11-14]. In most sensing applications, the sensitivity of the localized surface plasmon resonance (LSPR) to either the surrounding medium or the inter-particle separation is exploited for enhanced molecular detection. In order to predict the efficacy of a specific plasmonic nanoparticle system for sensing applications a specific figure of merit was developed, the sensitivity factor (SF)[15, 16]. As the refractive index of the surrounding medium increases there is a reduction in the repulsion between the in-phase oscillating dipoles of a given plasmonic band. This reduction decreases the energy of that oscillator, thus resulting in a red shift of its plasmonic band. As a result, the sensitivity of the plasmonic band, and the SF, is then related to the magnitude of the observed shift of the plasmonic band maximum per unit change of the refractive index of the surrounding medium[17].

The above sensitivity factor of a nanoparticle is strongly dependent on the plasmonic nanoparticle shape. Shapes having sharp corners have been shown to be most promising for nanoparticle sensing applications[18, 19]. Sharp corners facilitate the development of a high density of similarly oriented oscillating dipoles during their coherent resonant oscillation. This leads to: 1) high electromagnetic field and intra-oscillating dipole repulsions; and thus 2) large stabilization energies per unit change in the medium dielectric function, i.e., large values of sensitivity factors.

Along with the enhanced sensitivity, these shapes also exhibit drastically enhanced electromagnetic fields. Within the last five years studies of the optical properties of two coupled nanoparticles in close proximity to each other have led to a new development in the field of nanoparticle sensing[20-22]. As two nanoparticles are brought in close proximity to each other, a coupling between the resonant electronic oscillations of each nanoparticle results in a drastic increase in the electromagnetic field that is generated. This near field coupling behavior of a nanoparticle dimer was previously described by a near exponential decay behavior, commonly known as the plasmon ruler equation[23]. However, this dipolar coupling dependence fails at the short separations distances. The coupling behavior of a nanoparticle dimer at ~2-10 nanometer separations has been further explored and it has been found that the nonlocal optical properties of oscillating electrons, gap morphologies, and the distribution of the electromagnetic field that is generated for a specific plasmonic band influence the coupling behavior of a dimer. Furthermore, as the separation distance decreases even further (<1 nm), quantum effects begin to contribute to the observed optical properties of the dimer[24].

In the present work, a Ag nanocube dimer with a separation distance of 2 nm was studied in a variety of solutions and on top of a variety of substrates. While at this separation distance it is known that the quantum effects can be neglected[24], the nonlocal effects, gap morphology, and the electromagnetic field distribution are expected to generate strong and unique plasmonic properties. It is likely that both these properties and the magnitude of the electromagnetic field will determine the response of the dimer system to changes in the dielectric function of the surrounding medium. Herein the unique relationship between the magnitude of the electromagnetic field in a plasmonically coupled system of two silver nanocubes at a 2 nm separation and its corresponding sensitivity factors is explored. As well as the correlation between the maximum value of the electromagnetic field and the distribution of the electromagnetic field resulting from the induced oscillating dipoles is investigated.

This correlation is likely to determine the response of a plasmonic band to the changes in the dielectric function of the surrounding medium. Also, the dependence of the sensitivity factors and plasmonic band position on the dielectric constant of the substrate is observed and discussed. Previous reports have shown that substrates can have a negative effect on the plasmonic properties of nanoparticles and this has been alleviated by the use of a dielectric nanopillar[25]. Together with previous studies and our results herein, we believe that utilizing a substrate with a small refractive index will be the most convenient solution to creating a sensitive plasmonic sensor. Since most sensing applications involve aqueous solutions, one needs a substrate whose refractive index is lower than the refractive index of water (1.33), such as the silica nanorod-array films produced by Schubert and co-workers[26].

4.2. Theoretical Paramters

We aim to model the optical properties and interactions between two Ag nanocubes of edge length 42 nm and a separation distance of 2 nm on a substrate. It is well known that the discrete dipole approximation (DDA)[27] is one of the most powerful theoretical technique of modeling the optical properties of plasmonic nanoparticles (the extinction spectra as well as their absorption and scattering components) with various sizes and shapes. Also this method considers multipolar effects and finite size effects. Full details of this method have been described before[27] however, a brief description of the method is explained here.

For this calculation, we used the DDSCAT 6.1 code developed by Draine and Flatau[27]. The incident light is polarized along the inter-particle axis of the pair of Ag-Ag nanocubes. The nanocubes were illuminated from above and the exciting light is polarized parallel to the dimer axis. The dimer of silver nanocubes was represented as cubic array of several thousands of dipoles located on a cubic lattice. The point dipoles are excited by an external field and their response to the external field and their nearest oscillating dipole neighbors is solved self-consistently using Maxwell's equations. The size of the cube is defined by an equal volume of a sphere with an effective radius $r_{eff} = (3V/4\pi)^{1/3}$. Here the r_{eff} for that of the pair of the cube by itself is 32.82 nm and that of the dimer and substrate is 37 nm. Water, ethanol, carbon tetrachloride and toluene are used as the medium surrounding the dimer with a refractive index ranging from 1.33 for water to 1.495 for toluene. It was found that increasing the length, width or the thickness of the substrate did not alter the results[28]. The refractive index of silver cubes is assumed to be the same as that of the bulk metal and the refractive index of the glass and AlGaSb were

1.46 and 4.3 respectively. The plasmonic electromagnetic field intensity (in log scale of $|E|^2/|E_0|^2$) generated at various wavelengths of excitation was determine for the top surface of the dimer (unless otherwise noted).

4.3. Results and Discussion

4.3.1. Molecular and Plasmonic Spectroscopy

In molecular (one-electron excitation) spectroscopy, the extinction intensity of a spectral band resulting from a dipole allowed transition is proportional to the square of the size of the oscillating dipole moment resultant from the one-electron transition. In plasmonic spectroscopy, however, the extinction band intensity results from the excitation of a large number of coherently oscillating electrons (dipoles). Thus the intensity of the extinction spectrum of a dipolar plasmonic band is over one thousand times larger than the extinction of an allowed molecular absorption band.

For both molecular and plasmonic spectroscopy, the addition of dielectric medium tends to stabilize these resultant oscillating dipoles. This occurs as a result of the polarization stabilization of the dipoles generated in each system as well as minimizing the dipole-dipole repulsion between the in-phase dipoles of the plasmonic system. The latter effect compounded with the magnitude of electronic dipoles involved in a plasmonic transition results in a higher sensitivity of plasmonic spectroscopy to the surrounding dielectric medium compared to molecular spectroscopy. For plasmonic spectroscopy, the minimization of dipole-dipole repulsions by the surrounding dielectric induces a red shift of the plasmonic band that is much larger than the corresponding red shift of a molecular band. Particularly, Ag and Au nanoparticles of different shapes have been found to be highly sensitive exhibiting large red shifts when placed in environments with different dielectric constants.

For each plasmonic band within a given extinction spectrum, the large number of the oscillating dipoles within the plasmonic nanoparticle are distributed on the nanoparticle surface in different arrangements. Therefore, different plasmonic bands result in unique plasmonic field distributions which originate from the arrangement of the oscillating dipoles that can be used to characterize each specific band. This can be related to the way the linear polarization of a molecular absorption band characterizes the particular electronic distribution in an excited electronic state within the molecule. For plasmonic spectroscopy every plasmonic band now can be defined by the distribution of the oscillating dipole density on the surface of the nanoparticle(s). As you compare one plasmonic band to another the oscillating dipole density will vary in different locations of the nanoparticles resulting in the unique electromagnetic field distributions. Graphically, these electromagnetic field distributions can be represented by a contour plot where regions where the maximum electromagnetic field intensity can visually depict regions where the largest density (concentration) of oscillating dipoles occurs. Therefore, as the maximum value of the electromagnetic field increases for a given plasmonic system, the stabilization effect of the surrounding dielectric medium on the oscillating dipole distribution will also increase.

Since plasmonic spectroscopy is intimately related to both the extinction spectrum and the electromagnetic field intensity, herein we have investigated the relationship between the extinction intensity of a plasmonic band and the strength of the electromagnetic field. The optical properties of a 42 nm Ag nanocube dimer oriented face-to-face with a separation distance of 2 nm was calculated using DDA, and the corresponding extinction spectrum of this dimer can be seen in Figure 4.1A. Two dominant plasmonic bands are observed in the extinction spectrum of this dimer, a lower energy (608 nm) and higher energy (585 nm) band. For one electron spectroscopy the intensity of the extinction of a spectral band depends of the square of the oscillating transition dipole moment. In plasmonic spectroscopy, we assume the same relationship. The higher energy band is more intense than the lower energy band. As a result the transition dipole moment that is generated at this resonant wavelength, and resonant with the exciting light, is larger than the transition dipole moment that is generated at the lower energy LSPR. Contour plots of the electromagnetic field generated around the surface of the Ag dimer at each resonant wavelength were also calculated and can be seen in Figure 4.1B.

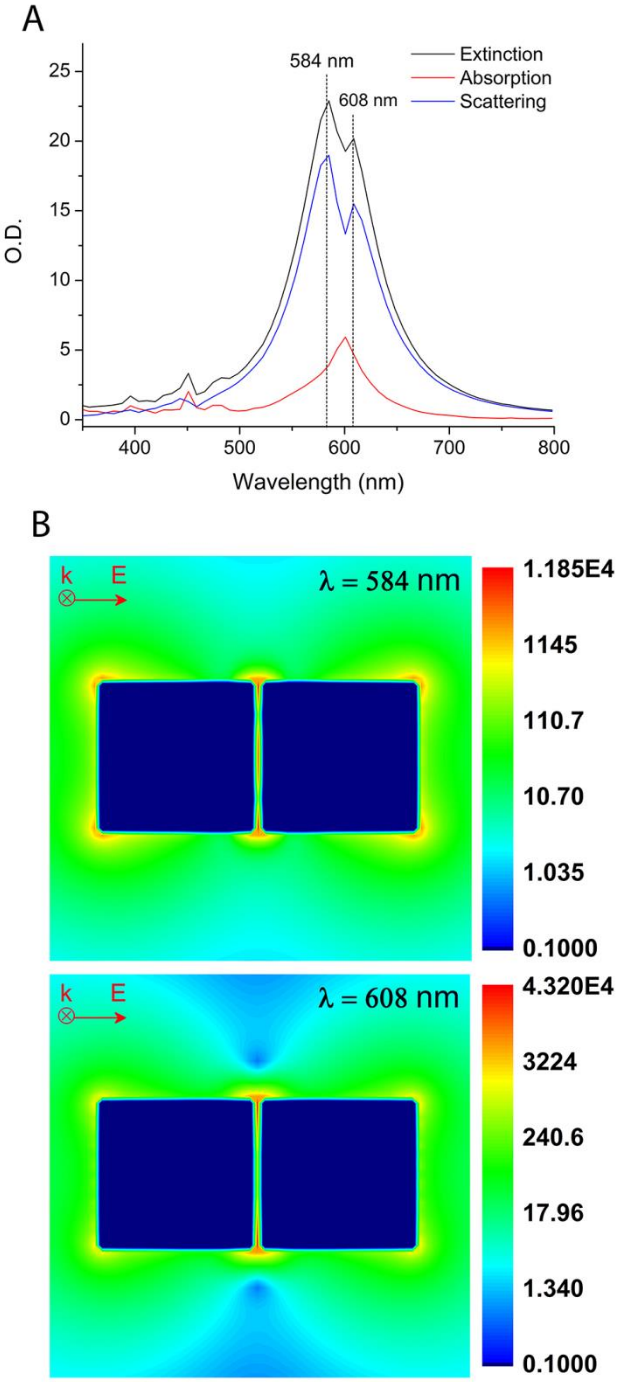

Figure 4.1. The extinction spectrum (extinction, absorption, and scattering) was calculated for a 42 nm Ag-Ag nanocube dimer with a separation distance of 2 nm in a surrounding medium of water (A). There are two prominent plasmonic bands present in the extinction spectrum which have differing extinction intensities. The corresponding electromagnetic field enhancement along the top xy plane of the dimer was calculated for both prominent plasmonic bands (B). The highest electromagnetic field enhancement was observed for the band having the weaker extinction intensity. Thus, the maximum value of the electromagnetic field intensity distribution appears to be dependent on the degree

of localization of the oscillating electronic dipoles whereas the extinction band intensity depends on the total number of oscillating dipoles involved in the resonant excitation.

When comparing the extinction intensity of each band to the intensity of the corresponding electromagnetic field that is generated, it is surprising to note that the band with the highest extinction intensity does not generate the highest electromagnetic field. As seen in Figure 1, the maximum value of the electromagnetic field that is generated by the higher energy band is 1.185×10^4. This is roughly one-fourth the maximum electromagnetic field intensity that is generated from the less intense lower energy plasmonic band. Thus, the plasmonic band with the highest extinction intensity does not always generate the strongest electromagnetic field.

When the shape of the electromagnetic field generated in each band is compared, it is evident that the degree of localization of electronic dipole density is greater for the lower energy plasmonic band. The shortest wavelength band displays an electromagnetic field distribution that is delocalized across the region between the adjacent facets of the dimer to a greater extent than the lower energy band. Consequently this results in a weaker electromagnetic field. Thus, the generation of a strong extinction band and a strong electromagnetic field do not always coincide. While the extinction intensity of a plasmonic oscillation can be related to the magnitude of electrons involved in the oscillation and the magnitude of the corresponding dipole moment that is generated, the electromagnetic field intensity is instead determined by the degree of localization of electronic dipole density.

4.3.2. The Sensitivity Factor and Corresponding Electromagnetic Field Distribution of Individual Plasmonic Bands

The sensitivity of the LSPR to the surrounding medium is a very important optical property of plasmonic nanoparticles that is used for many sensing applications[11-14]. In light of the unexpected relationship between the extinction intensity and the electromagnetic intensity of an individual plasmonic band, the sensitivity of each plasmonic band to the surrounding medium was investigated. This sensitivity is commonly known as the sensitivity factor (SF) of plasmonic nanoparticles and can be calculated from the magnitude of the shift in the LSPR of the nanoparticles per unit change of the refractive index of the surrounding medium. As the refractive index of the surrounding medium is increased, it is expected that the repulsion between the coherently oscillating dipoles is reduced and a corresponding red shift of the LSPR is observed. This provides a linear relationship from which the slope can be calculated to give the corresponding sensitivity factor.

Figure 4.2 shows the calculated extinction spectra for the Ag nanocube dimer in a solution of water, ethanol, carbon tetrachloride, and toluene. The LSPR peak position for both dominant bands in the extinction spectrum was plotted against the refractive index of the surrounding medium. As seen in Figure 4.2, the sensitivity factor for the higher energy and lower energy band was found to be 362.54 and 395.5 nm/RIU respectively.

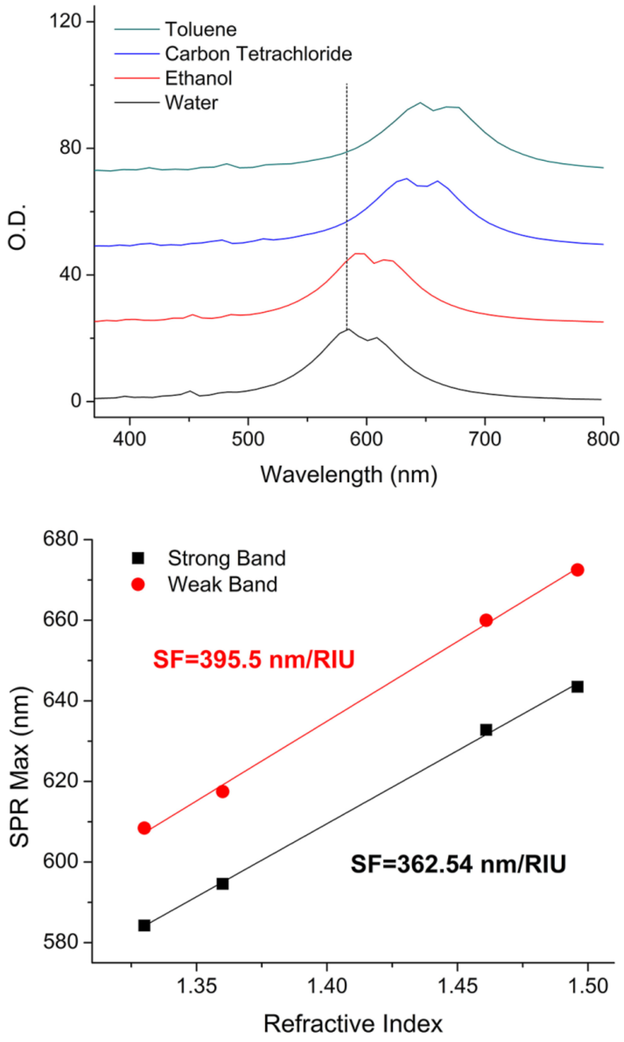

Figure 4.2. The extinction spectrum was calculated for a 42 nm Ag-Ag nanocube dimer with a separation distance of 2 nm in a surrounding medium of water, ethanol, carbon tetrachloride, and toluene (top). The surface plasmon resonance (SPR) maximum was determined as a function of the refractive index of the surrounding medium for both prominent plasmonic bands and the subsequent sensitivity factors were calculated. The band with the weaker extinction intensity was found to have a higher sensitivity factor (395.5) than the stronger band (362.54). It is apparent that the sensitivity of a plasmonic band is not solely dependent on the extinction intensity, but instead on the magnitude of oscillating electronic dipole density that occurs during the plasmonic excitation.

Here we see that the sensitivity of the strongest extinction band, the higher energy band, is actually lower than the sensitivity of the weaker extinction band (lower energy). It appears that the extinction intensity of each plasmonic band is not the only factor that determines its sensitivity. Looking at the electromagnetic field distribution of each plasmonic band (Figure 4.1) we see again that the lower energy band displays a higher degree of localization of electronic dipole density (giving rise to a higher maximum value of the electromagnetic field distribution shown on the bar on the far right of the electromagnetic field distribution in Figure 4.1). As mentioned previously, increasing the refractive index of the surrounding medium reduces the repulsions between oscillating dipoles. Thus, it appears that the plasmonic band with the highest degree of localization of its oscillating electronic dipole density will be most stabilized by a medium with a high refractive index. Therefore, its wavelength will be the most sensitive to the dielectric function of its environment.

4.3.3. The Effect of a Substrate

Now that we have determined that the sensitivity of a Ag nanocube dimer is a function the electromagnetic field distribution between the adjacent faces of the dimer, we must determine the effect of the refractive index of a substrate on the electromagnetic field distribution and the corresponding sensitivity of the dimer. It has been shown previously that when a single nanocube is placed on top of a substrate the coupling between the dipolar and quadrupolar bands is enhanced[25]. For this study, the nanocube dimer substrate system exhibits a C_{2V} symmetry whereas a nanocube dimer without a substrate has a higher symmetry of D_{4h} symmetry. This reduction in the symmetry of the system when the substrate is present is therefore expected to enhance the coupling between the dipolar and quadrupolar bands of the nanocube dimer.

To investigate the effect of both the reduction of symmetry induced by the substrate and the value of its refractive index, the extinction spectrum for a 42 nm Ag nanocube dimer with a separation distance of 2 nm was calculated for the dimer in water without a substrate, on top of a substrate with a low refractive index (glass, n = 1.46), a slightly larger refractive index (diamond, n = 2.4), and on top of a substrate with a high value of the refractive index (AlGaSb, n = 4.06). It is important to note here that when the nanocube dimer is placed on a substrate the reduction of symmetry is not as drastic as it is for a single nanocube. As a result, any changes in the extinction spectrum of the dimer can be attributed to the properties of the substrate.

As seen in Figure 4.3, it is interesting that there is little difference between the extinction spectrum of the Ag nanocube dimer without a substrate and the extinction spectrum of the dimer on top of a glass substrate. However, this is only true when the refractive index of the substrate is not different from that of the solution surrounding the other ten facets of the dimer. Thus when the refractive index of the substrate is similar to the refractive index of the surrounding medium the effect of the substrate on the extinction spectrum is minimal. When the substrate has a refractive index that is greater than the surrounding medium there is an evident shift in both the position and intensity of the plasmonic bands within the extinction spectrum.

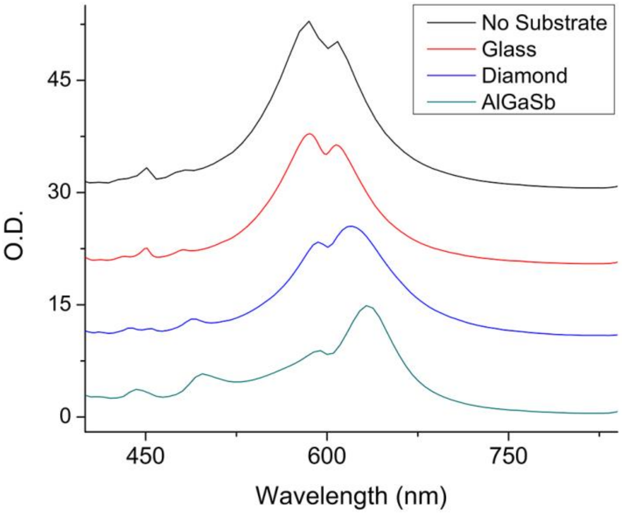

Figure 4.3. The extinction spectrum was calculated for a 42 nm Ag nanocube dimer with a separation distance of 2 nm in a surrounding medium of water without a substrate, on a glass substrate (n = 1.46), on a diamond substrate (n = 2.4), and on a substrate of AlGaSb (n = 4.06). There is little difference between the extinction spectrum when there is no substrate present and when the Ag-Ag dimer is placed on top of a glass substrate. This is due to a similarity between the refractive index of water (the surrounding medium) and the glass substrate. However, when the refractive index of the substrate is increased (diamond and AlGaSb), there is a drastic change in the resultant extinction spectrum with observed increase in the intensity of the long wavelength band relative to the short wavelength band.

Figure 4.3 shows that the relative peak intensity between the two prominent plasmonic modes (~586 nm and ~608 nm for glass) inverts as the refractive index of the substrate increases. It is clear that for a nanocube dimer on a glass substrate the higher energy band (586 nm) is more intense than the lower energy band (608 nm); however, when the substrate is AlGaSb the lower energy band (635 nm) is now roughly twice as intense as the higher energy band (591 nm). The question now arises, does the substrate only affect the intensity of each band as we have just suggested or is the relative intensity between both plasmonic modes roughly constant and the plasmonic bands energetically interchange as refractive index of the substrate is increased? If the second hypothesis is true, increasing the refractive index of the substrate results in a red shift of the higher energy and a blue shift in the lower energy band as the refractive index of the substrate is increased from glass to AlGaSb. In order to answer this question, first the identity of each band must be determined by its field distribution. Then we calculated the electromagnetic field distribution for each plasmonic band within the extinction spectrum for the Ag dimer on top of 3 different substrates.

It has been previously shown that the identity of a specific plasmonic mode can be correlated to the distribution of the electromagnetic field that is observed at its resonant wavelength[29]. Given that there are multiple overlapping plasmonic bands within the extinction spectrum, we have analyzed the electromagnetic field distribution at wavelengths near the maximum intensity for each band as well as at the tail of the band where band overlap is minimum (Figure 4.4).

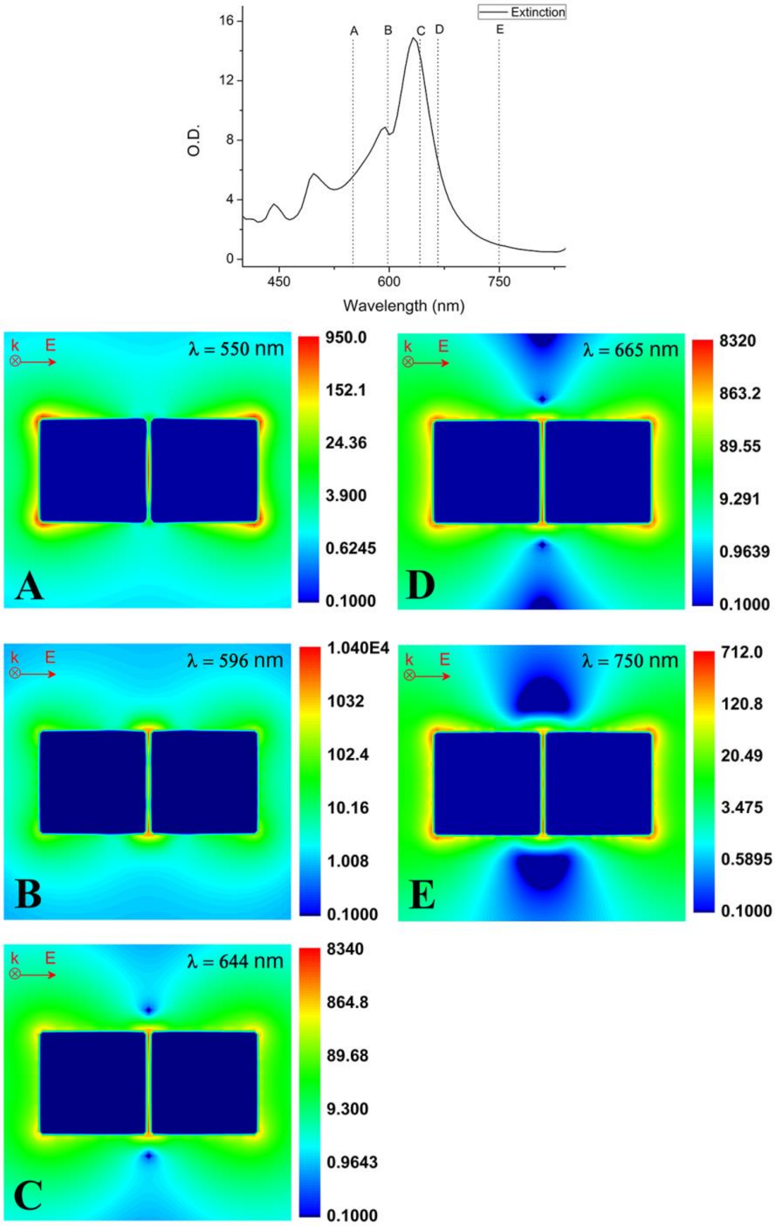

Figure 4.4. The extinction spectrum was calculated for a 42 nm Ag-Ag nanocube dimer with a separation distance of 2 nm on top of an AlGaSb substrate. The electromagnetic field distribution was calculated for various wavelengths corresponding to the two prominent plasmonic modes in the extinction spectrum. Wavelengths were chosen to be on resonance and off resonance in order to determine if wavelengths chosen to be off resonance (and away from the second prominent plasmonic band) increased the purity of the band. It is evident that as the wavelength of excitation is moved off resonance and away from the second prominent plasmonic band the distribution of each individual plasmonic band becomes more pronounced. Thus, to identify a given plasmonic band it is helpful to use wavelengths which are energetically separated from other plasmonic bands in order to increase the purity and clarity of the electromagnetic distribution.

As seen in Figure 4.4, the purity of an individual plasmonic band and its corresponding electromagnetic field distribution increases as one moves off resonance away from other major plasmonic bands. It is important to note here that while moving off resonance enhances the purity of the electromagnetic field distribution for a given band the overall intensity of the electromagnetic field is reduced. However, for the purpose of determining the identity of a plasmonic band, the intensity of the electromagnetic field is not as important as the distribution and localization of the oscillating electronic dipoles.

When the electromagnetic field distribution was calculated for the two prominent plasmonic bands within the corresponding extinction spectrum of the dimer without a substrate and on top of glass, diamond, and AlGaSb, it became apparent that the two strong plasmonic bands do not energetically interchange as the refractive index of the substrate increases. As seen in Figure 4.5A, the electromagnetic field distribution for the higher energy plasmonic band of the dimer without a substrate exhibits a high degree of localization of oscillating electronic dipoles at the exterior corners of the dimer and in the middle of the region in between the adjacent facets of the dimer. This is also true for the higher energy plasmonic band of the dimer on top of glass, diamond, and AlGaSb (Figure 4.5B-D). Therefore, this is in fact the same plasmonic band.

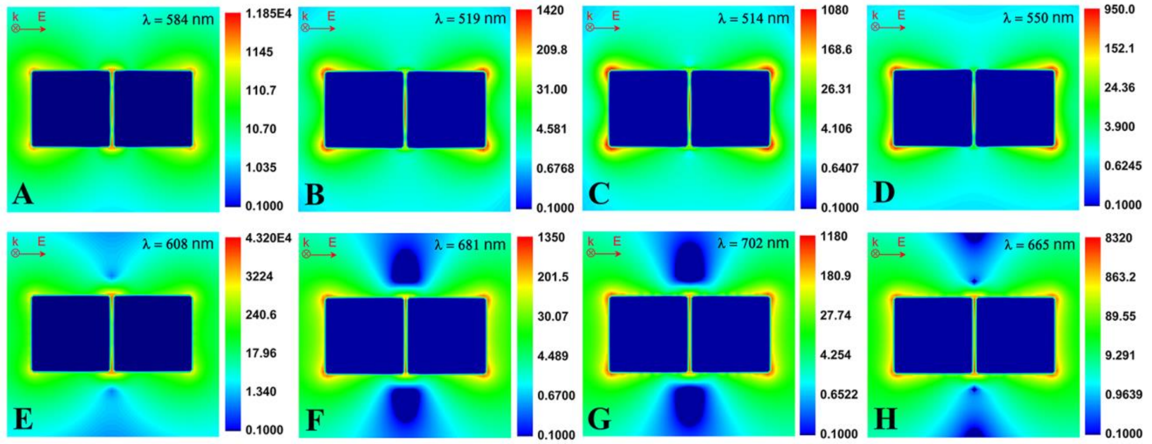

Figure 4.5. The electromagnetic field enhancement for the xy plane at the interface of a 42 nm Ag-Ag nanocube dimer and substrate was calculated for a dimer with a separation distance of 2 nm in a surrounding medium of water. The wavelength of excitation was chosen to be off resonance of the two prominent bands within the extinction spectrum of the Ag-Ag dimer without a substrate (A and E), on top of a glass substrate (B and F), on top of a diamond substrate (C and G), and on top of AlGaSb (D and H). The wavelength of excitation was chosen to be off resonance in order to enhance the purity of individual plasmonic bands. As the substrate is introduced into the system and its refractive index is increased, the electromagnetic field distribution for the higher and lower energy prominent plasmonic band is unchanged. Thus the substrate and its refractive index do not interchange the energetic position of the given plasmonic bands and only affects the observed extinction intensity.

The same is true for the lower energy plasmonic band. Without a substrate the electromagnetic field is localized along the exterior corners of the dimer as well as weakly throughout the entire region between the adjacent facets of the nanocubes (Figure 4.5E). As the refractive index of the substrate is increased, the distribution of the lower energy band does not change (Figure 4.5F-H). As a result, we can see that the plasmonic bands do not energetically interchange as the refractive index of the substrate is increased. Instead the refractive index of the substrate appears to affect the magnitude of oscillating electrons that are involved in a given plasmonic band. The ability for electrons to oscillate with a distribution described by the prominent band in the extinction spectrum (584 nm) of an isolated nanocube dimer is inhibited by the high refractive index of the substrate. Consequently the magnitude of the electronic dipole generated by that oscillation is reduced and the extinction intensity of that band is reduced. The opposite is true for the prominent lower energy band (609 nm) within the extinction spectrum of the isolated dimer. As the refractive index of the substrate is increased, it appears that that magnitude of electrons involved in this oscillation increases.

It is also interesting to note that there is an increase in intensity of the weak plasmonic band in the 475-500 nm region, likely a quadrupolar type band, as the refractive index of the substrate is increased (Figure 4.3). The electromagnetic field distribution of this weak mode was calculated (Figure 4.6) and there is an interesting comparison between the character of the electromagnetic field distribution of this smaller higher energy band (496 nm) and the prominent lower energy dipolar band at 632 nm. The distribution of the electromagnetic field is very similar, with a high intensity distributed along the exterior corners and throughout the entire region between adjacent faces of the dimer. The similarity in the electromagnetic field distribution between these two modes is also mimicked by a relative increase in the extinction intensity of these two bands as the refractive index of the substrate is increased. As mentioned earlier, the reduction of symmetry induced by the presence of the substrate enhances the coupling between the dipolar and quadrupolar modes. It is possible that due to the similarity in the character (electromagnetic field distribution) of these two plasmonic bands, the electrons involved in their resonant oscillations are intimately related and are similarly affected as the refractive index of the substrate is increased.

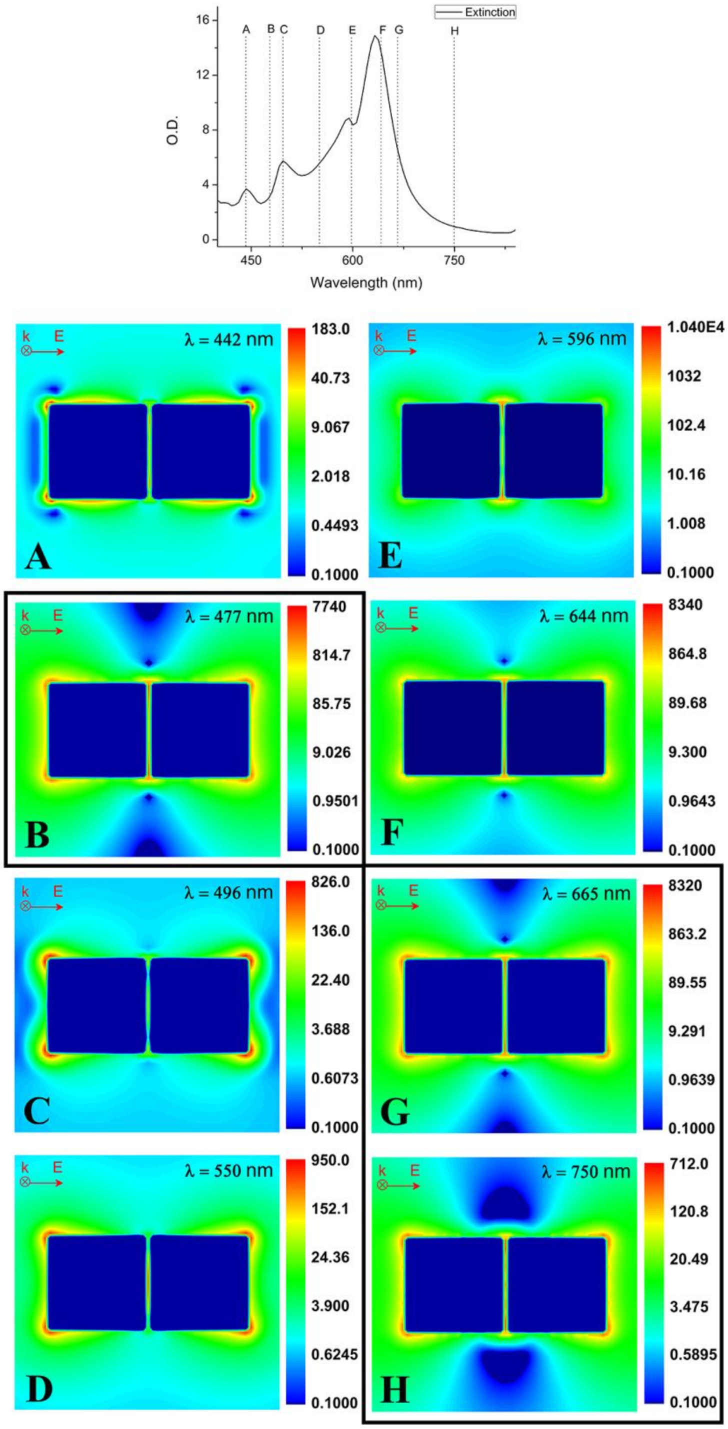

Figure 4.6. The extinction spectrum was calculated for a 42 nm Ag-Ag nanocube dimer with a separation distance of 2 nm on top of an AlGaSb substrate. The electromagnetic field distribution was calculated for four different plasmonic bands within the extinction spectrum. It is interesting to note the similarities in the electromagnetic field distribution of the higher energy plasmonic band (477 nm, likely quadrupolar) and the lower energy dipolar band (665, 750 nm). Both plasmonic bands exhibit an electromagnetic field that is

localized around the exterior corners and throughout the entire region between the adjacent facet of the dimer.

Along with understanding the spectroscopic effects introduced by a substrate with a high refractive index, it is important to investigate the effect of the substrate on the oscillating electrons along the height of the dimer. As seen in Figure 4.7, the electromagnetic field distribution for the top xy slice of the dimer (42 nm away from the dimer-substrate interface, Figure 4.7A and 4.7B) and the bottom xy slice of the dimer (at the dimer-substrate interface, Figure 4.7C and 4.7D) for a low refractive index substrate (glass, Figure 4.7A and 4.7C) and a high refractive index substrate (AlGaSb, Figure 4.7B and 4.7D) are shown. It is apparent that the substrate with a high refractive index effectively reduces the electromagnetic field intensity and redistributes the electromagnetic field associated with the observed plasmonic band. This redistribution results in an increased localization of the electronic dipoles near the interface of the dimer and the substrate by a factor of 2.5. It appears that the anisotropic introduction of a high refractive index material to the dimeric system induces an asymmetric electromagnetic field distribution along the height of the dimer. The oscillating electronic dipoles near the interface are localized to a greater extent, for the higher energy band, due to their proximity to the higher dielectric material. However, the introduction of the high refractive index substrate compared to a low refractive index substrate still results in an overall reduction in the electromagnetic field intensity as it is able to spread the oscillating dipoles over larger areas on the surface of the nanoparticle.

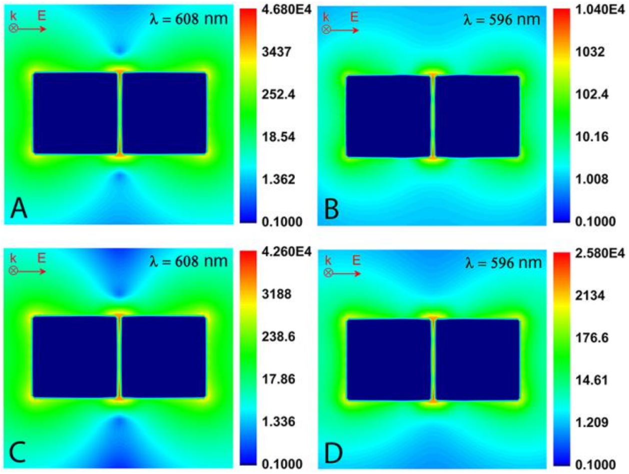

Figure 4.7. The electromagnetic field enhancement was calculated for the top (A and B) and bottom (C and D) xy plane of a 42 nm Ag-Ag nanocube dimer with a separation distance of 2 nm in a surrounding medium of water. The anisotropic effect of the substrate on the top and bottom of the nanocube dimer is only observed on a substrate of high dielectric constant. When the refractive index of the substrate was similar to that of the surrounding medium (glass, A and C), the magnitude of the electromagnetic field enhancement was found to be the same at the top surface of the dimer and at the bottom interface between the dimer and the substrate. However, when the refractive index of the substrate is much greater than the surrounding medium (AlGaSb, B and D) the electromagnetic field enhancement is much greater near the interface of the nanocube dimer and the substrate as the oscillating dipole density is higher due to the minimization of the dipole-dipole repulsion by the high dielectric constant of the substrate.

As noted previously, the degree of localization within the electromagnetic field distribution is associated with the sensitivity of the corresponding plasmonic band to the surrounding dielectric environment. Figure 4.8 shows the calculated sensitivity factor of the two dominant plasmonic bands within the corresponding extinction spectrum of the Ag dimer without a substrate, on a glass substrate, and on the AlGaSb substrate. It is evident that as the refractive index of the substrate decreases, the sensitivity factor of the lower energy band (Figure 4.8B) increases. This is not the case for the higher energy band (Figure 4.8A), where the sensitivity factor is statistically equivalent for all substrates that were analyzed.

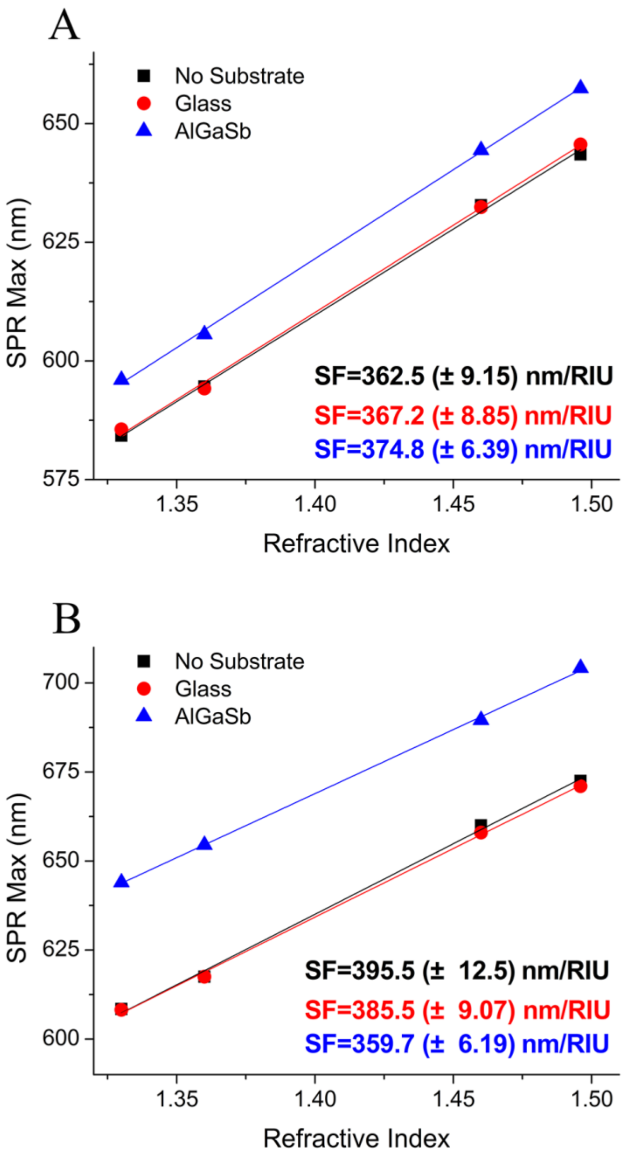

Figure 4.8. The dependence of the surface plasmon resonance peak position on the refractive index of the surrounding medium was determined for a 42 nm Ag nanocube dimer with a separation distance of 2 nm without a substrate, on a glass substrate, and on an AlGaSb substrate. The sensitivity factor was calculated for both the prominent higher energy band (A) and the lower energy band (B) in the corresponding extinction spectrum of each Ag dimer.

When this is compared to the electromagnetic field distributions that are shown in (Figure 4.9), the plasmonic bands with the highest sensitivity corresponds to plasmonic bands with highly localized electromagnetic fields (highest intensity). As a result, as the refractive index of the substrate decreases there is an increased localization of the electromagnetic field generated by the lower energy band which results in an increased sensitivity of the corresponding plasmonic band. It is clear that the localization of the electromagnetic field generated by the higher energy band is roughly the same on top of all substrates. Thus the sensitivity factors which were calculated for this band are equivalent.

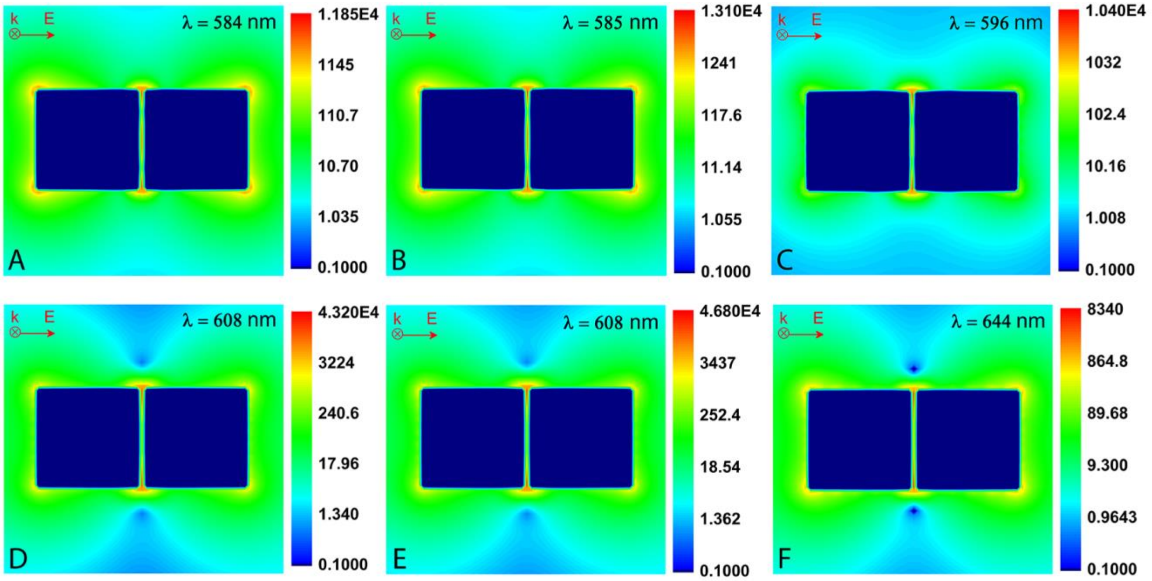

Figure 4.9. The electromagnetic field distribution was calculated at the peak maximum wavelength for the two prominent plasmonic bands in the extinction spectrum of a 42 nm Ag nanocube dimer with a separation distance of 2nm without a substrate (A and D), on top of a glass substrate (B and E), and on top of an AlGaSb substrate (C and F). It is clear that the electromagnetic field intensity is lowest for the dimer on top of a substrate with a high refractive index. This will likely have an effect on the sensitivity of the nanocube dimer to the surrounding medium when it is on top of a substrate with a high refractive index.

4.4 Concluding Remarks

Through our investigation of surface plasmon resonance spectroscopy (SPRS) it is evident that the relationship between the sensitivity of the plasmonic band and its extinction behavior is complex. It is known that as the refractive index of the surrounding medium increases, a decrease in the repulsion between the coherently oscillating electronic dipoles occurs resulting in a red shift of the plasmonic band. The degree by which the electronic dipole repulsions can be reduced thus defines the sensitivity of the surface plasmon resonance energy to the surrounding medium. Previous studies have found that the sensitivity of a nanocube dimer is much greater than that of a nanocube monomer[30]. Through SPRS, we further our understanding of the refractive index sensitivity of a given plasmonic system to more accurately be connected to the degree of electronic dipole density localization that occurs during a specific plasmonic resonance. Within a plasmonic system, the band which generates the highest localization of electronic dipole density will experience the greatest stabilization by increasing the refractive index of the surrounding medium; and thus, will be best to utilize for making sensors.

Using DDA a detailed examination of the optical and plasmonic properties of a face-to-face oriented Ag nanocube dimer with a 2 nm separation was carried out. From the results the following conclusions can be made:

(1) The intensity of a given plasmonic band is determined by the number and size of the excited oscillating electronic dipoles formed per unit of light intensity absorbed and not proportional to its maximum value of the electromagnetic field enhancement.

(2) The refractive index sensitivity of two plasmonic bands is dependent upon the relative values of their maximum electromagnetic field enhancement and thus their corresponding degree of localization of oscillating electronic dipoles and not

by the relative values of their extinction intensity. Increasing the refractive index of the surrounding medium helps to reduce the inter-dipole repulsion of the oscillating electronic dipoles. As a result, the plasmonic bands with the highest degree of electronic dipole density (and thus highest value of its electromagnetic distribution) can be stabilized most by a solvent with a different dielectric permittivity than the metal. Therefore, these bands shift most per unit change of dielectric constant and should have the highest value for their sensitivity factors.

(3) When a substrate with a high refractive index is used the relationship between the sensitivity of a plasmonic band and its corresponding electromagnetic field still holds. The substrate is found to redistribute the oscillating electronic dipoles along the height of the dimer. Consequently, the majority of the electronic dipole localization occurs at the interface of the dimer and the substrate. However, the overall maximum value of the electromagnetic field is reduced when a high refractive index substrate is introduced to the dimer system.

(4) The use of a high dielectric constant substrate changes the magnitude of electrons involved in a given type of plasmonic oscillation. Also, the number of the electrons and the corresponding extinction intensity of each plasmonic band can be either increased or decreased as the refractive index of the substrate is increased. As a result, the relative extinction intensity between two plasmonic bands can be inverted if the substrate interacts with each band differently. It was found that as the refractive index of the substrate increases, an increased coupling between quadrupolar and dipolar plasmonic bands occurred giving rise to similar electromagnetic field distribution and therefore similar field distributions.

(5) Due to the decrease in the electromagnetic field intensity and electronic dipole localization when a high refractive index substrate is used, the sensitivity of the dimer decreases.

Thus, when using a nanoparticle-substrate system to make a sensor, it is important to choose a substrate whose refractive index is much lower than the refractive index of the medium to be examined.

4.5. References

(1) N. Hooshmand, J. A. Bordley and M. A. El-Sayed: Plasmonic Spectroscopy: The Electromagnetic Field Strength and Its Distribution Determine the Sensitivity Factor of Face-to-Face Ag Nanocube Dimers in Solution and on a Substrate. *J. Phys. Chem. C* **2015**, *119*, 15579-15587.

(2) W. A. Murray, B. Auguié and W. L. Barnes: Sensitivity of Localized Surface Plasmon Resonances to Bulk and Local Changes in the Optical Environment. *J. Phys. Chem. B* **2009**, *113*, 5120-5125.

(3) C. L. Haynes and R. P. Van Duyne: Nanosphere Lithography: A Versatile Nanofabrication Tool for Studies of Size-Dependent Nanoparticle Optics. *J. Phys. Chem. B* **2001**, *105*, 5599-5611.

(4) T. R. Jensen, M. D. Malinsky, C. L. Haynes and R. P. Van Duyne: Nanosphere Lithography: Tunable Localized Surface Plasmon Resonance Spectra of Silver Nanoparticles. *J. Phys. Chem. B* **2000**, *104*, 10549-10556.

(5) S. Link, Z. L. Wang and M. A. El-Sayed: Alloy Formation of Gold−Silver Nanoparticles and the Dependence of the Plasmon Absorption on Their Composition. *J. Phys. Chem. B* **1999**, *103*, 3529-3533.

(6) L. J. Sherry, S.-H. Chang, G. C. Schatz, R. P. Van Duyne, B. J. Wiley and Y. Xia: Localized Surface Plasmon Resonance Spectroscopy of Single Silver Nanocubes. *Nano Lett.* **2005**, *5*, 2034-2038.

(7) L. M. Liz-Marzán: Tailoring Surface Plasmons through the Morphology and Assembly of Metal Nanoparticles. *Langmuir* **2005**, *22*, 32-41.

(8) K. L. Kelly, E. Coronado, L. L. Zhao and G. C. Schatz: The Optical Properties of Metal Nanoparticles: The Influence of Size, Shape, and Dielectric Environment. *J. Phys. Chem. B* **2002**, *107*, 668-677.

(9) K.-S. Lee and M. A. El-Sayed: Gold and Silver Nanoparticles in Sensing and Imaging: Sensitivity of Plasmon Response to Size, Shape, and Metal Composition. *J. Phys. Chem. B* **2006**, *110*, 19220-19225.

(10) N. Hooshmand, J. A. Bordley and M. A. El-Sayed: Are Hot Spots between Two Plasmonic Nanocubes of Silver or Gold Formed between Adjacent Corners or Adjacent Facets? A Dda Examination. *J. Phys. Chem. Lett.* **2014**, *5*, 2229-2234.

(11) B. M. Reinhard, M. Siu, H. Agarwal, A. P. Alivisatos and J. Liphardt: Calibration of Dynamic Molecular Rulers Based on Plasmon Coupling between Gold Nanoparticles. *Nano Lett.* **2005**, *5*, 2246-2252.

(12) J. Zhao, X. Zhang, C. R. Yonzon, A. J. Haes and R. P. Van Duyne: Localized Surface Plasmon Resonance Biosensors. *Nanomedicine* **2006**, *1*, 219-228.

(13) C. Xue, Z. Li and C. A. Mirkin: Large-Scale Assembly of Single-Crystal Silver Nanoprism Monolayers. *Small* **2005**, *1*, 513-516.

(14) A. J. Haes, L. Chang, W. L. Klein and R. P. Van Duyne: Detection of a Biomarker for Alzheimer's Disease from Synthetic and Clinical Samples Using a Nanoscale Optical Biosensor. *J. Am. Chem. Soc.* **2005**, *127*, 2264-2271.

(15) J. Becker, A. Trügler, A. Jakab, U. Hohenester and C. Sönnichsen: The Optimal Aspect Ratio of Gold Nanorods for Plasmonic Bio-Sensing. *Plasmonics* **2010**, *5*, 161-167.

(16) Otte, M.; Sepulveda, B.: Figures of Merit for Refractometric LSPR Biosensing. In *Nanoplasmonic Sensors*; Dmitriev, A., Ed.; Springer New York, 2012; pp 317-331.

(17) J. N. Anker, W. P. Hall, O. Lyandres, N. C. Shah, J. Zhao and R. P. Van Duyne: Biosensing with Plasmonic Nanosensors. *Nat. Mater.* **2008**, *7*, 442-453.

(18) E. Martinsson, M. A. Otte, M. M. Shahjamali, B. Sepulveda and D. Aili: Substrate Effect on the Refractive Index Sensitivity of Silver Nanoparticles. *J. Phys. Chem. C* **2014**, *118*, 24680-24687.

(19) C. E. Tabor, R. Murali, M. A. Mahmoud and M. A. El-Sayed: On the Use of Plasmonic Nanoparticle Pairs as a Plasmon Ruler: The Dependence of the near-Field Dipole Plasmon Coupling on Nanoparticle Size and Shape. *J. Phys. Chem. A* **2009**, *113*, 1946-1953.

(20) N. J. Halas, S. Lal, W.-S. Chang, S. Link and P. Nordlander: Plasmons in Strongly Coupled Metallic Nanostructures. *Chem. Rev.* **2011**, *111*, 3913-3961.

(21) O. Schubert, J. Becker, L. Carbone, Y. Khalavka, T. Provalska, I. Zins and C. Sönnichsen: Mapping the Polarization Pattern of Plasmon Modes Reveals Nanoparticle Symmetry. *Nano Lett.* **2008**, *8*, 2345-2350.

(22) J. I. Chen, Y. Chen and D. S. Ginger: Plasmonic Nanoparticle Dimers for Optical Sensing of DNA in Complex Media. *J. Am. Chem. Soc.* **2010**, *132*, 9600-9601.

(23) P. K. Jain, W. Huang and M. A. El-Sayed: On the Universal Scaling Behavior of the Distance Decay of Plasmon Coupling in Metal Nanoparticle Pairs: A Plasmon Ruler Equation. *Nano Lett.* **2007**, *7*, 2080-2088.

(24) N. A. Mortensen, S. Raza, M. Wubs, T. Søndergaard and S. I. Bozhevolnyi: A Generalized Non-Local Optical Response Theory for Plasmonic Nanostructures. *Nat. Commun.* **2014**, *5*.

(25) A. Dmitriev, C. Hägglund, S. Chen, H. Fredriksson, T. Pakizeh, M. Käll and D. S. Sutherland: Enhanced Nanoplasmonic Optical Sensors with Reduced Substrate Effect. *Nano Lett.* **2008**, *8*, 3893-3898.

(26) J. Q. Xi, J. K. Kim and E. F. Schubert: Silica Nanorod-Array Films with Very Low Refractive Indices. *Nano Lett.* **2005**, *5*, 1385-1387.

(27) B. T. Draine and P. J. Flatau: Discrete-Dipole Approximation for Scattering Calculations. *J. Opt. Soc. Am. A* **1994**, *11*, 1491-1499.

(28) E. Ringe, J. M. McMahon, K. Sohn, C. Cobley, Y. Xia, J. Huang, G. C. Schatz, L. D. Marks and R. P. Van Duyne: Unraveling the Effects of Size, Composition, and Substrate on the Localized Surface Plasmon Resonance Frequencies of Gold and Silver Nanocubes: A Systematic Single-Particle Approach. *J. Phys. Chem. C* **2010**, *114*, 12511-12516.

(29) J. A. Bordley, N. Hooshmand and M. A. El-Sayed: The Coupling between Gold or Silver Nanocubes in Their Homo-Dimers: A New Coupling Mechanism at Short Separation Distances. *Nano Lett.* **2015**.

(30) S. Dodson, M. Haggui, R. Bachelot, J. Plain, S. Li and Q. Xiong: Optimizing Electromagnetic Hotspots in Plasmonic Bowtie Nanoantennae. *J. Phys. Chem. Lett.* **2013**, *4*, 496-501.

CHAPTER 5

THE SENSITIVITY OF THE DISTANCE DEPENDENT PLASMONIC COUPLING BETWEEN TWO NANOCUBES TO THEIR ORIENTATION: EDGE-TO-EDGE VERSUS FACE-TO-FACE

5.1. Motivation

The strong electromagnetic field and the unique optical properties associated with two or more plasmonic nanoparticles in close proximity to each other[1-11] have proven to be useful for enhancing both the imaging[12-16] and chemical and biological sensing[17-21] capabilities of plasmonic systems. In 1908 the first solution for the scattering and absorption properties of a spherical nanoparticle was completed by Gustav Mie[22]. Since the initial development of Mie theory, it is now well known that the strong optical properties of plasmonic nanoparticles are resultant from an induced coherent oscillation of the free conduction band electrons within the plasmonic nanoparticle. This electronic response to an incident photon with the appropriate resonant wavelength is known as the localized surface plasmon resonance (LSPR). The confinement of this resonant oscillation to the physical structure of the nanoparticle results in both a strong electromagnetic field near the surface of the nanoparticle and a strong optical response (scattering and absorption). These properties have been shown to be dependent on a variety of factors including: the nanoparticle shape, its size, its composition, the dielectric of the surrounding medium, the presence of a substrate, and its proximity to another plasmonic material[23-30].

While all of these factors are important for designing an effective imaging or sensing plasmonic system, an intriguing dependence of the electromagnetic field and optical properties of a plasmonic nanoparticle on its proximity to a second plasmonic nanoparticle[31] has recently emerged as an increasingly important characteristic. Initially, a 2003 report[32] found that the LSPR peak position within the extinction spectrum of a gold elliptical disk dimer varied exponentially with the separation distance of the dimer. This dependence was further explored by El-Sayed and co-workers[8] where a universal relationship between the shift in the LSPR peak position and the separation distance of a gold (Au) nanodisk dimer, normalized to the size of the nanodisk, was developed and is now known as the plasmon ruler equation. Further experimental[33] and theoretical[34] studies have supported this relationship and suggested that the exponential behavior of a nanoparticle dimer is in fact independent of the shape, size, and composition of the plasmonic nanoparticle dimer. However, multiple recent reports have also suggested that the universal exponential behavior of the near-field coupling between two nanoparticles begins to breakdown when the separation distance of the dimer is much smaller than the size of the individual nanoparticle[35-40]. At these separation distances there is an unexpected enhancement in both the near-field coupling of the dimer and the sensitivity of the LSPR to the surrounding environment[41-42].

Along with the increased near-field coupling and sensitivity of the LSPR, there is an intense electromagnetic field that is generated between the two adjacent plasmonic nanoparticles with small separation distances[43]. It has been found that as the separation distance between two nanoparticles decreases the electromagnetic field generated between the adjacent nanoparticles increases[44-46]. Interestingly, as the separation distance of a nanocube dimer oriented face-to-face decreases beyond the threshold at which the dipole-dipole coupling behavior predicted by the plasmon ruler equation begins to breakdown, there is also a transition in the distribution of the electromagnetic field between the adjacent nanoparticles[41, 47]. This transition results in two different distinct plasmonic modes that are characterized by a unique electromagnetic field distribution between the adjacent faces of the dimer. These unique distributions were also denoted as the longitudinal antenna plasmon (LAP_1) and transverse cavity plasmon (TCP_2) modes for a pair of flat gap cylindrical antennas[48]. These results were intriguing due to the concomitant transition in the distribution of the electromagnetic field between the adjacent nanoparticles of the dimer and the unexpected break in the plasmon ruler equation. However, these studies have been limited to a flat or rounded gap separation between either two nanocubes or nanowires.

Due to the dependence of the magnitude of the electromagnetic field that is generated near the surface of an individual nanoparticle on its shape[49], it is important to also explore the dependence of the shape of the nanoparticle gap and subsequent orientation of the nanoparticles within a nanoparticle dimer on the electromagnetic field that is generated[50]. El-Sayed and co-workers have previously reported the electromagnetic field distribution and optical sensitivity of a single silver (Ag) nanocube as well as the electromagnetic field distribution, optical sensitivity, and near-field coupling of a 42 nm Ag-Ag nanocube dimer with a separation distance ranging from 2 nm to 200 nm[41-42, 47]. Herein this consideration is extended and focused specifically on the breakdown of the plasmon ruler equation, resultant electromagnetic field distribution and optical properties of a Ag-Ag nanocube dimer oriented edge-to-edge. Understanding the effects of the orientation of two nanocubes in close proximity will undoubtedly be useful for optimizing the future assembly of noble metal nanostructures in plasmonic devices utilized for imaging and sensing applications.

5.2. Theoretical Parameters

In order to model the optical properties and investigate the near-field coupling between a 42 nm Ag-Ag nanocube dimer in two different configurations, face-to-face and edge-to-edge, the discrete dipole approximation (DDA) was used. It is well known that the DDA is one of the most powerful theoretical techniques for modeling the optical properties of plasmonic nanoparticles (the absorption, scattering, and extinction) with various sizes and shapes. The advantage of this method is that it includes both multipolar and finite size effects. Using this method, the silver nanocube dimer was represented as a cubic array of several thousands of dipoles located on a cubic lattice (with volume $\mathbf{D}^3$). The point dipoles (18522 dipoles total, 1 dipole = 2nm resolution) are excited by an incident photon (external field) and the response of each dipole to both the external field and neighboring dipoles within the nanocube is solved self-consistently using Maxwell's equations. The extinction efficiency is considered by $Q_{ext} = C_{ext}/\pi r_{eff}^2$ where $r_{eff} =(3/4\pi)^{1/3}$ is the radius of a sphere with the same volume as the nanocube dimer utilized in this study. For our calculation the publicly offered DDSCAT 6.1 code developed by Draine and Faltau[51] was used and the refractive index of the silver nanocubes is assumed to be the same as that of the bulk metal[52]. The electromagnetic field distribution and polarization vector distribution were also calculated for the top surface of the Ag dimer in both orientations. The wavelength chosen for all electromagnetic field and polarization vector plots correspondes to the peak positon of the major dipolar plasmonic band within the extinction spectrum of a given dimer orientation and separation distance.

5.3. Results and Discussion

5.3.1. The Dependence of the Exponential Dipole-Dipole Coupling Behavior on Dimer Orientation

Herein the near-field coupling behavior of a 42 nm Ag-Ag nanocube dimer that is oriented in either an edge-to-edge or face-to-face configuration was compared. Even though the near-field coupling behavior between a face-to-face nanocube dimer has been previously calculated[47], the extinction spectra for both the face-to-face and edge-to-edge nanocube dimer were calculated again. It is clear that the results previously calculated agree well with the new results calculated for the face-to-face dimer (Figure 5.1).

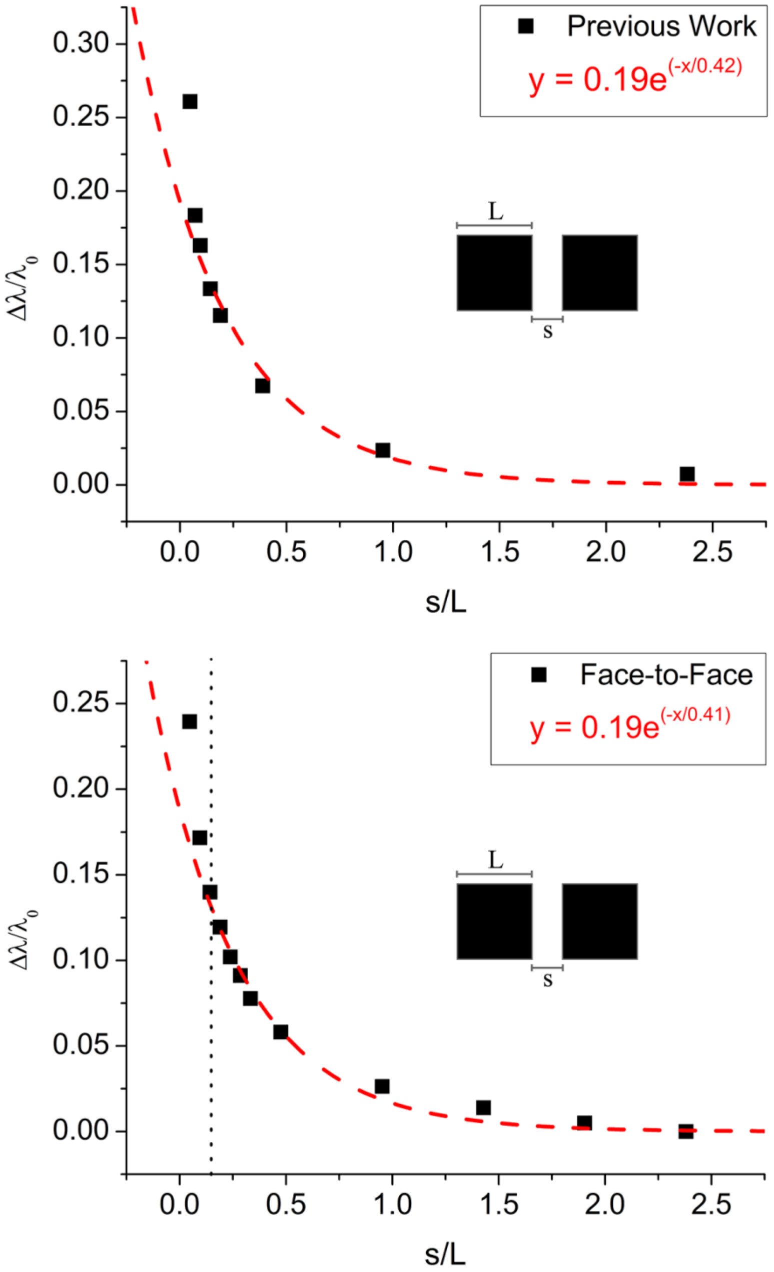

Figure 5.1. The fractional shift in the peak position of the major plasmonic band ($\Delta\lambda/\lambda_0$) in the extinction spectrum of a 42 nm Ag nanocube dimer oriented face-to-face is plotted as a function of the separation distance between the two nanocubes of the dimer normalized to the edge length of the individual nanocube (s/L). This calculation was previously conducted (top) with an increased total number of dipoles compared to the calculation conducted within this study (bottom). It is clear that there is no significant difference in the results of the two calculations.

The face-to-face dimer was recalculated here in order to ensure consistency between the calculated comparison of the face-to-face and edge-to-edge dimer due to differences in the theoretical parameters used in this study compared to the previously published work[47]. As seen in Figure 5.2, there is an expected red-shift in the extinction spectra of the nanocube dimers that is dependent on the separation distance of the dimer for both dimer orientations. The extinction spectra for separation distances ranging from 100-2 nm and 141-3 nm were analyzed for the face-to-face and edge-to-edge dimer respectively. However, several separation distances were omitted from Figure 5.2 for clarity. The separation distances chosen for the edge-to-edge and face-to-face dimer correspond to equivalent normalized separations (separation distance normalized to either the length of the diagonal or edge length on an individual nanocube for the edge-to-edge and face-to-face dimer respectively). Interestingly, as the separation between the two nanocubes decreases the extinction spectrum of the Ag-Ag dimer becomes increasingly dependent on the orientation of the dimer. For the edge-to-edge dimer there is an increased intensity for the higher energy bands within the extinction spectrum. This increase of higher energy bands is not mimicked in the extinction spectra of the face-to-face dimer. As a result, it appears that as the separation distance of the edge-to-edge dimer is decreased there is a unique enhancement of plasmonic bands with a higher energy.

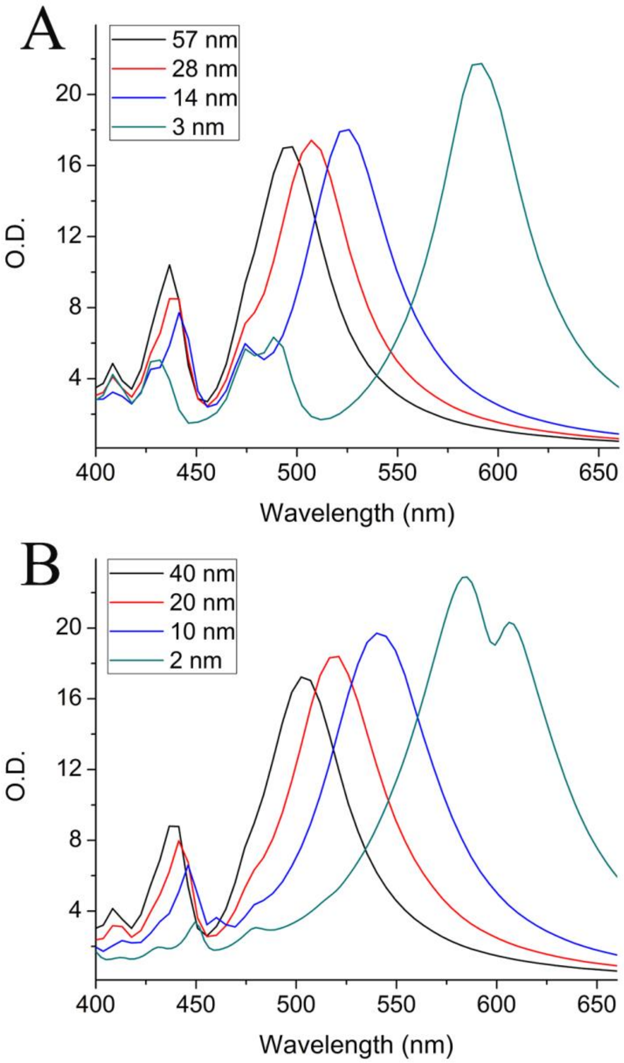

Figure 5.2. The extinction spectrum was calculated for a 42 nm Ag-Ag nanocube dimer oriented in a either an edge-to-edge (A) or face-to-face (B) configuration at varying separation distances. The separation distances chosen for each dimer orientation differed in absolute length, however, all four separation distances correspond to equivalent separation distances normalized to either the length of the diagonal (edge-to-edge) or the edge length (face-to-face) of an individual nanocube within the dimer. It is clear that there is an expected red shift in the plasmonic bands within the extinction spectra as the separation distance is decreased. Interestingly, there is an increased intensity of the higher energy bands within the extinction spectra of the edge-to-edge dimer (400-500 nm) that is not present in the face-to-face dimer. This likely corresponds to an increased higher order coupling within the edge-to-edge dimer.

For both the edge-to-edge and face-to-face nanocube dimer the shift in the peak position of the major plasmonic peak ($\Delta\lambda/\lambda_0$) within the extinction spectrum, previously described as peak 1[47], was monitored as a function of the separation distance of the dimer scaled to either the edge length (s/L) or the diagonal length (s/D) of an individual nanocube within the dimer. Even though the size of the nanocube is the same in both the face-to-face and edge-to-edge orientation, it is important to normalize the spectral data of each dimer to the length of the particle along the polarization direction of the incident electromagnetic field. If the data for the edge-to-edge dimer is normalized to the edge length of an individual nanocube (Figure 5.3), an exponential decay behavior with a pre-exponential factor and decay constant that does not agree well with previously observed studies for cubic based nanoparticle dimers[51] is produced.

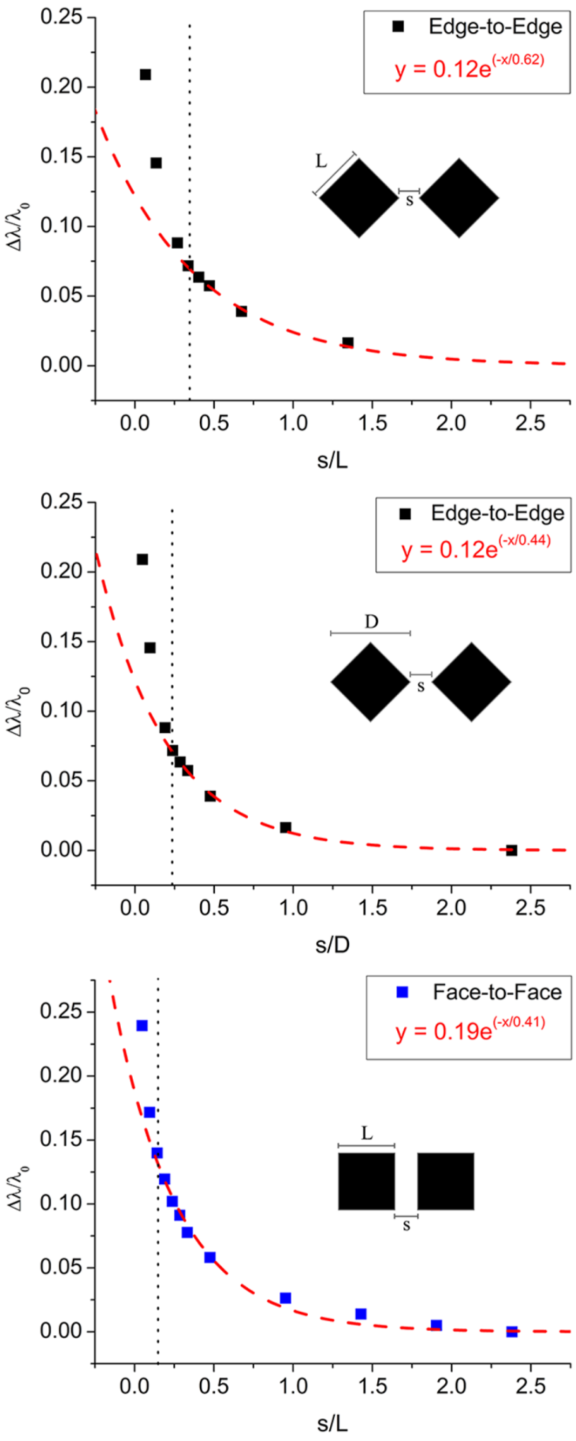

Figure 5.3. The fractional shift in the peak position of the major plasmonic band ($\Delta\lambda/\lambda_0$) in the extinction spectrum of a 42 nm Ag nanocube dimer oriented edge-to-edge (top, middle) and face-to-face (bottom) is plotted as a function of the separation distance between the two nanocubes of the dimer normalized to either the length of the diagonal of the individual nanocube (s/D, middle) or the edge length of the individual nanocube (s/L, top and bottom). The calculated data was fit to a first order exponential decay without any set parameters. It is clear that when the edge-to-edge orientation is

normalized to the edge length of an individual nanocube there is a drastic increase in the decay length of the exponential decay behavior (0.62). This behavior does not agree with previously reported values for cubic shaped nanoparticles as well as the decay length found for the face-to-face dimer. Since the decay length of near-field coupling behavior is dictated by the shape of the nanoparticle, normalizing the calculated data to the length of the diagonal of an individual nanoparticle is more appropriate. It is also important to note that the polarization of the incident electromagnetic field is along the diagonal of the edge-to-edge dimer, which provides further support for normalization of the separation distance to the length of the diagonal.

As shown in Figure 5.4, the exponential decay behavior predicted by the plasmon ruler equation (dotted red line) agrees well with the coupling behavior of both dimers until the separation distance decreases below roughly 17 nm. It is apparent here that at a separation distance of 14 nm (s/D~0.24) a deviation from the expected exponential coupling behavior begins for the nanocube dimer that is oriented edge-to-edge; while this deviation in the exponential behavior begins below a separation distance of only 6 nm (s/L~0.14) for the face-to-face dimer. It is important to note first that the near-field coupling behavior deviated from the expected dipole-dipole coupling behavior for both dimers and thus is independent of orientation. However, the distance at which the deviation occurs is strongly dependent on the orientation. In fact the deviation from expected near-field coupling behavior of the edge-to-edge dimer begins at a separation distance that is twice that of the face-to-face dimer. It appears that the orientation of the nanocube dimer drastically affects the separation distance at which the coupling behavior, predicted by the plasmon ruler equation, begins to breakdown.

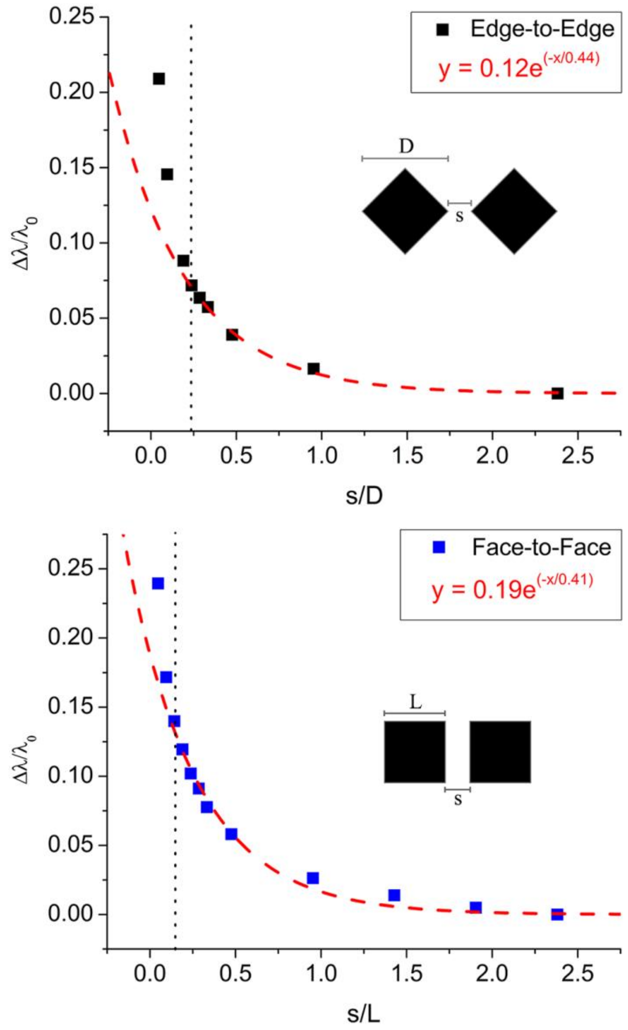

Figure 5.4. The fractional shift in the peak position of the major plasmonic band ($\Delta\lambda/\lambda_0$) in the extinction spectrum of a 42 nm Ag nanocube dimer oriented edge-to-edge (top) and face-to-face (bottom) is plotted as a function of the separation distance between the two nanocubes of the dimer normalized to either the length of the diagonal of the individual nanocube (s/D) or the edge length of the individual nanocube (s/L). It is clear that there is a break in the exponential dipole-dipole coupling behavior predicted by the plasmon ruler equation (dotted red line) for both the face-to-face and edge-to-edge nanocube dimer. However, it appears that the edge-to-edge orientation results in a break of the expected dipolar coupling behavior at a separation distance of roughly 14 nm which is twice as far as what is observed for the face-to-face nanocube dimer orientation (6 nm).

5.3.2. The Electromagnetic Field Distribution and Vectorial Dipole Polarization near the Failure of the Dipole-Dipole Coupling Behavior

In order to investigate the origin of the difference in the distance at which the expected coupling behavior begins to breakdown, the electromagnetic field enhancement and polarization vector distribution was calculated for both dimers. As seen in Figure 5.5, the electromagnetic field was calculated for separation distances that are slightly larger and smaller than the separation distance at which the expected dipole-dipole coupling behavior begins to deviate for both the edge-to-edge (17, 14, and 11 nm) and face-to-face (8, 6, and 4 nm) dimers. There is a clear difference in the maximum value of the electromagnetic field intensity for each orientation. The edge-to-edge dimer exhibits an electromagnetic field intensity (~7040) that is roughly 40% greater than the electromagnetic field generated by the face-to-face dimer (~5000).

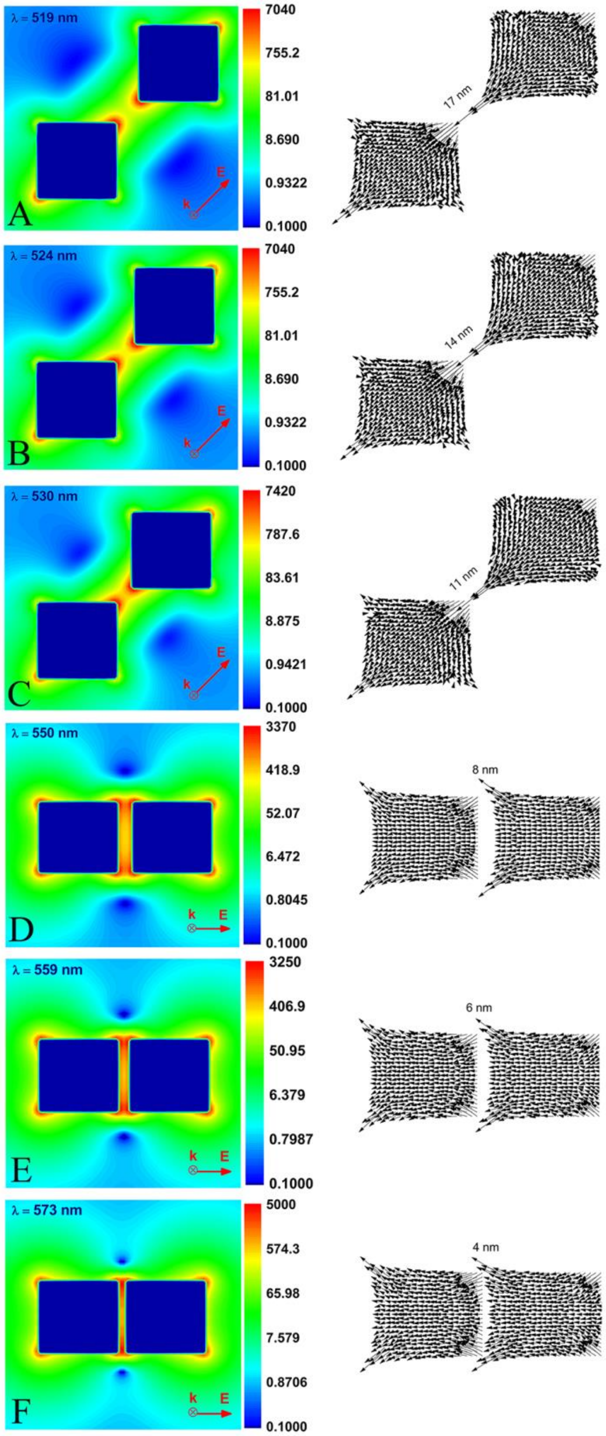

Figure 5.5. The calculated electromagnetic field distribution and polarization vector plots for the top surface of edge-to-edge (A-C) and face-to-face (D-F) 42 nm Ag nanocube dimers. The separation distances chosen for these calculations were centered around the distance where a break in the expected coupling behavior of the edge-to-edge (17, 14, 11 nm) and face-to-face (8, 6, 4 nm) begins. It is clear that there is an increased density of the oscillating dipoles at the adjacent vertices of the edge-to-edge dimer. As a result, an enhanced electromagnetic field of 7000 is observed for the edge-to-edge dimer which is

larger than the electromagnetic field generated by the face-to-face orientation (3000-5000). Thus, the edge-to-edge nanocube dimer exhibits a stronger near field coupling, which can be seen in both the increased electromagnetic field intensity and localization of polarization vector orientations near the adjoining vertices of the dimer, than the face-to-face configuration.

Along with varying electromagnetic field intensities, the orientation of the nanocube dimer results in different polarization vector distributions. As seen in Figure 5.5A-C, there is a strong localization of the polarization vector orientation towards the adjoining vertices of the edge-to-edge dimer. Even though the total number of dipoles on the surfaces of each dimer orientation is the same, it is clear that the polarization direction of the oscillating dipoles on the face-to-face dimer are both localized at the adjacent vertices of the dimer as well as spread over the large surface area present on the facing facets between the two nanocubes (Figure 5.5D-F). Compared to the edge-to-edge dimer the localization of oscillating dipole orientation in the interfacial region of the face-to-face dimer is diluted by the large surface area of the facing facets. For the edge-to-edge dimer, the orientation of the dipole polarization vectors is clearly confined to the small area between the facing vertices of the dimer. Thus, the summation of the polarization vector distribution for the edge-to-edge dimer will result in a high degree of localization towards the interacting vertices of the dimer.

Also, the calculated vector plots of the edge-to-edge dimer exhibit a large magnitude for the vectors present on the adjacent vertices of the dimer. At a separation distance of 17 nm the magnitude of the polarization vectors on the adjacent vertices of the dimer spans the entire inter-particle gap. As the separation distance decreases further, it is clear that the magnitude of the polarization vectors present on the vertices of the adjacent nanocubes continues to increase. Interestingly, the magnitude of the polarization vectors present on the face of one nanocube does not span across the inter-particle region to the second nanocube until the separation distance is decreased below 6 nm for the dimer that is oriented face-to-face[47]. This coincides well with the observed break in the dipolar coupling behavior for both dimer orientations seen in Figure 5.4. Clearly the orientation of the nanocube dimer affects the localization of the polarization vectors as well as the magnitude of polarization vectors present near the gap region of the dimer. As a result, one can infer that the increased magnitude of the oscillating dipoles generated by an incident electromagnetic field for the edge-to-edge orientation will produce an increased interaction between the adjacent nanocubes of the dimer at a longer separation distance than for the face-to-face dimer. Consequently it is likely that an increased localization could result in an increased magnitude of the resulting multipole moments relative to the dipole moment. This could ultimately lead to the observed failure of the dipolar coupling behavior for the edge-to-edge dimer at a longer separation distance than the face-to-face dimer.

5.3.3. Increased Mulitpole Moment Contribution Relative to the Dipole Moment for the Edge-to-Edge Dimer Orientation

A general relationship for the electrostatic interaction energy of two continuous charge distributions interacting across some distance R has been previously developed[52] and takes the general form

$$W = \Sigma_\alpha \int \rho_\alpha(R)\varphi(R)dR \qquad (1)$$

where W is the electrostatic interaction energy, $\rho_\alpha(R)$ is the individual or atomic charge densities, and $\varphi(R)$ is the electromagnetic field generated by the nearby charge distribution. There are two Taylor expansions which can be utilized to express this electrostatic interaction energy in terms of a multipole series. We have chosen to highlight the dipole-dipole, dipole-quadrupole, and quadrupole-quadrupole type interactions as they are most likely to contribute most to the coupling of this nanocube dimer system. As a result we can express the electrostatic energy as a sum of the electrostatic energy of each interaction type:

$$W = W_{DD} + W_{DQ} + W_{QQ} \tag{2}$$

where W_{DD}, W_{DQ}, and W_{QQ} are the dipole-dipole, dipole-quadrupole, and quadrupole-quadrupole electrostatic interaction energies between the two nanocubes of the dimer respectively. These different terms[52] are found to have the forms:

$$W_{DD} = (\mu \bullet \mu^{'})|R|^{-3} - 3(\mu \bullet \mathbf{R})(\mu^{'} \bullet \mathbf{R})|R|^{-5} \tag{3}$$

$$W_{DQ} = 2(\mu^{'} \bullet Q \bullet \mathbf{R})|R|^{-5} - 5(\mu^{'} \bullet \mathbf{R})(R \bullet Q \bullet \mathbf{R})|R|^{-7} \tag{4}$$

$$W_{QQ} = 0.11[Q:Q^{'}]|R|^{-5} - 6.67[\mathbf{R} \bullet Q^{'} \bullet Q \bullet \mathbf{R}]|R|^{-7} \tag{5}$$

In this system, μ and $\mu^{'}$ would be the resultant dipole moments generated from the vectorial sum of the oscillating dipoles in each respective nanocube. Q and $Q^{'}$ would be the quadrupole moments resulting from the vectorial sum of the oscillating quadrupoles in each respective nanocube. Again, R is the distance between the two interacting charge distributions (nanocubes) and **R** is the corresponding pointing vector. From the equations above, we see that the distance dependence of the quadrupolar contribution to the electrostatic interaction energy follow either a R^{-5} or R^{-7} dependence while the dipolar interaction exhibits a R^{-3} dependence. While the exact coupling mechanism between plasmonic nanoparticles may not be strictly quadrupole-dipole or quadrupole-quadrupole in character, it is likely that multipolar modes will begin to contribute at smaller separation distance.

In order for the multipolar interactions to compete at a longer separation distance the relative magnitude of the multipole moments for the edge-to-edge dimer must become increasingly large compared to the dipole moment. This can result from the higher density of the oscillating dipoles which is generated on the edge of each nanocube in the edge-to-edge dimer. As seen in Figure 5.4, there is clear evidence of this increased localization within the edge-to-edge dimer compared to the face-to-face orientation. A large maximum value of the electromagnetic field intensity of roughly 7000 is observed for the edge-to-edge dimer, whereas an electromagnetic field of only 3000-5000 is observed for the face-to-face orientation. Consequently, an intense electromagnetic field and high concentration of oscillating dipoles is expected to give rise to an increased contribution of the higher order multipoles relative to that of the dipole. We suggest this explains the observed deviation from the expected dipolar coupling behavior at a longer separation distance of 14 nm for the dimer with a higher oscillating dipole density (in the edge-to-edge orientation).

5.4. Concluding Remarks

In summary, the near-field coupling behavior of a 42 nm Ag-Ag nanocube dimer which is oriented in a face-to-face and an edge-to-edge configuration was investigated. The difference in the orientation of the nanocube dimer was found to affect:

(1) the separation distance at which the nanocube dimer begins to deviate from the expected dipolar coupling behavior,

(2) the localization of oscillating dipoles near the gap region of the dimer, and

(3) the contribution of the higher order multipoles to the electrostatic interaction energy of the dimer near the separation distance at which the dipolar coupling begins to fail.

The edge-to-edge nanocube dimer clearly begins to deviate from the expected dipolar coupling behavior at a separation distance that is twice as far as the face-to-face nanocube dimer. This early break in the dipolar coupling was found to coincide with an overlap of both the electromagnetic field and polarization vector distribution in the gap region between the nanocube dimer. Thus, the orientation of the dimer was found to increase the density of oscillating electrons near this region and facilitate an increased interaction at a farther distance.

This suggests that the higher oscillating dipole density present in the edge-to-edge orientation of the dimer facilitates an increased contribution of the higher order modes to the electrostatic energy of the interactions between the two adjacent nanocubes; which induces a break from the expected dipolar coupling of the edge-to-edge dimer at a separation distance of 14 nm. As a result, these fundamental discoveries regarding the dependence of the near-field coupling of a nanocube dimer on the orientation of the dimer have highlighted the importance of the morphology of the region between two coupled nanoparticles. One should not expect to have a single universal plasmonic ruler equation. The coupling behavior for any aggregated plasmonic nanoparticle system depends on the relative orientations of the plasmonic nanoparticles and the resultant gap morphologies which are produced. Thus, further research within the development of plasmonic nanoparticle based applications should not neglect the effect of orientation on the coupling between plasmonic nanoparticles in order to further enhance the optical properties of these devices.

5.5. References

(1) Hao, E.; Schatz, G. C. Electromagnetic Fields Around Silver Nanoparticles and Dimers. *J. Chem. Phys.* **2004,** *120*, 357-366.

(2) Nikolay, N. N.; Petar, A. A.; Minoru, O. Near-Field Properties of a Gold Nanoparticle Array on Different Substrates Excited by a Femtosecond Laser. *Nanotechnology* **2007,** *18*, 305703.

(3) Gunnarsson, L.; Rindzevicius, T.; Prikulis, J.; Kasemo, B.; Käll, M.; Zou, S.; Schatz, G. C. Confined Plasmons in Nanofabricated Single Silver Particle Pairs: Experimental Observations of Strong Interparticle Interactions. *J. Phys. Chem. B* **2004,** *109*, 1079-1087.

(4) Muskens, O. L.; Giannini, V.; Sánchez-Gil, J. A.; Gómez Rivas, J. Optical Scattering Resonances of Single and Coupled Dimer Plasmonic Nanoantennas. *Opt. Express* **2007,** *15*, 17736-17746.

(5) Funston, A. M.; Novo, C.; Davis, T. J.; Mulvaney, P. Plasmon Coupling of Gold Nanorods at Short Distances and in Different Geometries. *Nano Lett.* **2009,** *9*, 1651-1658.

(6) Prodan, E.; Radloff, C.; Halas, N. J.; Nordlander, P. A Hybridization Model for the Plasmon Response of Complex Nanostructures. *Science* **2003,** *302*, 419-422.

(7) Jain, P. K.; Eustis, S.; El-Sayed, M. A. Plasmon Coupling in Nanorod Assemblies: Optical Absorption, Discrete Dipole Approximation Simulation, and Exciton-Coupling Model. *J. Phys. Chem. B* **2006,** *110*, 18243-18253.

(8) Jain, P. K.; Huang, W.; El-Sayed, M. A. On the Universal Scaling Behavior of the Distance Decay of Plasmon Coupling in Metal Nanoparticle Pairs: A Plasmon Ruler Equation. *Nano Lett.* **2007,** *7*, 2080-2088.

(9) Olk, P.; Renger, J.; Wenzel, M. T.; Eng, L. M. Distance Dependent Spectral Tuning of Two Coupled Metal Nanoparticles. *Nano Lett.* **2008,** *8*, 1174-1178.

(10) Fan, J. A.; Wu, C.; Bao, K.; Bao, J.; Bardhan, R.; Halas, N. J.; Manoharan, V. N.; Nordlander, P.; Shvets, G.; Capasso, F. Self-Assembled Plasmonic Nanoparticle Clusters. *Science* **2010,** *328*, 1135-1138.

(11) Hentschel, M.; Saliba, M.; Vogelgesang, R.; Giessen, H.; Alivisatos, A. P.; Liu, N. Transition from Isolated to Collective Modes in Plasmonic Oligomers. *Nano Lett.* **2010,** *10*, 2721-2726.

(12) Yelin, D.; Oron, D.; Thiberge, S.; Moses, E.; Silberberg, Y. Multiphoton Plasmon-Resonance Microscopy. *Opt. Express* **2003,** *11*, 1385-1391.

(13) Durr, N. J.; Larson, T.; Smith, D. K.; Korgel, B. A.; Sokolov, K.; Ben-Yakar, A. Two-Photon Luminescence Imaging of Cancer Cells Using Molecularly Targeted Gold Nanorods. *Nano Lett.* **2007,** *7*, 941-945.

(14) Wang, Y.; Xie, X.; Wang, X.; Ku, G.; Gill, K. L.; O'Neal, D. P.; Stoica, G.; Wang, L. V. Photoacoustic Tomography of a Nanoshell Contrast Agent in the in Vivo Rat Brain. *Nano Lett.* **2004,** *4*, 1689-1692.

(15) Sokolov, K.; Follen, M.; Aaron, J.; Pavlova, I.; Malpica, A.; Lotan, R.; Richards-Kortum, R. Real-Time Vital Optical Imaging of Precancer Using Anti-Epidermal Growth Factor Receptor Antibodies Conjugated to Gold Nanoparticles. *Cancer Res.* **2003,** *63*, 1999-2004.

(16) El-Sayed, I. H.; Huang, X.; El-Sayed, M. A. Surface Plasmon Resonance Scattering and Absorption of anti-EGFR Antibody Conjugated Gold Nanoparticles in Cancer Diagnostics: Applications in Oral Cancer. *Nano Lett.* **2005,** *5*, 829-834.

(17) Dodson, S.; Haggui, M.; Bachelot, R.; Plain, J.; Li, S.; Xiong, Q. Optimizing Electromagnetic Hotspots in Plasmonic Bowtie Nanoantennae. *J. Phys. Chem. Lett.* **2013,** *4*, 496-501.

(18) Raschke, G.; Kowarik, S.; Franzl, T.; Sönnichsen, C.; Klar, T. A.; Feldmann, J.; Nichtl, A.; Kürzinger, K. Biomolecular Recognition Based on Single Gold Nanoparticle Light Scattering. *Nano Lett.* **2003,** *3*, 935-938.

(19) Endo, T.; Kerman, K.; Nagatani, N.; Takamura, Y.; Tamiya, E. Label-Free Detection of Peptide Nucleic Acid−DNA Hybridization Using Localized Surface Plasmon Resonance Based Optical Biosensor. *Anal. Chem.* **2005,** *77*, 6976-6984.

(20) Haes, A.; Stuart, D.; Nie, S.; Van Duyne, R. Using Solution-Phase Nanoparticles, Surface-Confined Nanoparticle Arrays and Single Nanoparticles as Biological Sensing Platforms. *J. Fluoresc.* **2004,** *14*, 355-367.

(21) Xu, H.; Aizpurua, J.; Käll, M.; Apell, P. Electromagnetic Contributions to Single-Molecule Sensitivity in Surface-Enhanced Raman Scattering. *Phys. Rev. E* **2000,** *62*, 4318-4324.

(22) G, M. Contributions to the Optics of Turbid Media, Especially Colloidal Metal Solutions. *Ann. Phys.* **1908,** *25*, 377.

(23) Kelly, K. L.; Coronado, E.; Zhao, L. L.; Schatz, G. C. The Optical Properties of Metal Nanoparticles: The Influence of Size, Shape, and Dielectric Environment. *J. Phys. Chem. B* **2002,** *107*, 668-677.

(24) Aizpurua, J.; Hanarp, P.; Sutherland, D. S.; Käll, M.; Bryant, G. W.; García de Abajo, F. J. Optical Properties of Gold Nanorings. *Phys. Rev. Lett.* **2003,** *90*, 057401.

(25) Miller, M. M.; Lazarides, A. A. Sensitivity of Metal Nanoparticle Surface Plasmon Resonance to the Dielectric Environment. *J. Phys. Chem. B* **2005,** *109*, 21556-21565.

(26) Jain, P. K.; Lee, K. S.; El-Sayed, I. H.; El-Sayed, M. A. Calculated Absorption and Scattering Properties of Gold Nanoparticles of Different Size, Shape, and Composition: Applications in Biological Imaging and Biomedicine. *J. Phys. Chem. B* **2006,** *110*, 7238-7248.

(27) Link, S.; El-Sayed, M. A. Spectral Properties and Relaxation Dynamics of Surface Plasmon Electronic Oscillations in Gold and Silver Nanodots and Nanorods. *J. Phys. Chem. B* **1999,** *103*, 8410-8426.

(28) El-Sayed, M. A. Some Interesting Properties of Metals Confined in Time and Nanometer Space of Different Shapes. *Acc. Chem. Res.* **2001,** *34*, 257-264.

(29) Sherry, L. J.; Chang, S.-H.; Schatz, G. C.; Van Duyne, R. P.; Wiley, B. J.; Xia, Y. Localized Surface Plasmon Resonance Spectroscopy of Single Silver Nanocubes. *Nano Lett.* **2005,** *5*, 2034-2038.

(30) Xu, G.; Chen, Y.; Tazawa, M.; Jin, P. Surface Plasmon Resonance of Silver Nanoparticles on Vanadium Dioxide. *J. Phys. Chem. B* **2006,** *110*, 2051-2056.

(31) Ghosh, S. K.; Pal, T. Interparticle Coupling Effect on the Surface Plasmon Resonance of Gold Nanoparticles: From Theory to Applications. *Chem. Rev.* **2007,** *107*, 4797-4862.

(32) Su, K. H.; Wei, Q. H.; Zhang, X.; Mock, J. J.; Smith, D. R.; Schultz, S. Interparticle Coupling Effects on Plasmon Resonances of Nanogold Particles. *Nano Lett.* **2003,** *3*, 1087-1090.

(33) Jain, P. K.; El-Sayed, M. A. Plasmonic Coupling in Noble Metal Nanostructures. *Chem. Phys. Lett.* **2010,** *487*, 153-164.

(34) Tabor, C.; Murali, R.; Mahmoud, M.; El-Sayed, M. A. On the Use of Plasmonic Nanoparticle Pairs As a Plasmon Ruler: The Dependence of the Near-Field Dipole Plasmon Coupling on Nanoparticle Size and Shape. *J. Phys. Chem. A* **2008,** *113*, 1946-1953.

(35) Teperik, T. V.; Nordlander, P.; Aizpurua, J.; Borisov, A. G. Robust Subnanometric Plasmon Ruler by Rescaling of the Nonlocal Optical Response. *Phys. Rev. Lett.* **2013,** *110*, 263901.

(36) Teperik, T. V.; Nordlander, P.; Aizpurua, J.; Borisov, A. G. Quantum Effects and Nonlocality in Strongly Coupled Plasmonic Nanowire Dimers. *Opt. Express* **2013,** *21*, 27306-27325.

(37) Fernández-Domínguez, A.; Wiener, A.; García-Vidal, F.; Maier, S.; Pendry, J. Transformation-Optics Description of Nonlocal Effects in Plasmonic Nanostructures. *Phys. Rev. Lett.* **2012,** *108*, 106802.

(38) Ciracì, C.; Hill, R.; Mock, J.; Urzhumov, Y.; Fernández-Domínguez, A.; Maier, S.; Pendry, J.; Chilkoti, A.; Smith, D. Probing the Ultimate Limits of Plasmonic Enhancement. *Science* **2012,** *337*, 1072-1074.

(39) Toscano, G.; Raza, S.; Jauho, A.-P.; Mortensen, N. A.; Wubs, M. Modified Field Enhancement and Extinction by Plasmonic Nanowire Dimers due to Nonlocal Response. *Opt. Express* **2012,** *20*, 4176-4188.

(40) Mortensen, N. A.; Raza, S.; Wubs, M.; Søndergaard, T.; Bozhevolnyi, S. I. A Generalized Non-Local Optical Response Theory for Plasmonic Nanostructures. *Nat. Commun.* **2014,** *5*.

(41) Hooshmand, N.; Bordley, J. A.; El-Sayed, M. A. Are Hot Spots between Two Plasmonic Nanocubes of Silver or Gold Formed between Adjacent Corners or Adjacent Facets? A DDA Examination. *J. Phys. Chem. Lett.* **2014,** *5*, 2229-2234.

(42) Hooshmand, N.; Bordley, J. A.; El-Sayed, M. A. Plasmonic Spectroscopy: The Electromagnetic Field Strength and its Distribution Determine the Sensitivity Factor of Face-to-Face Ag Nanocube Dimers in Solution and on a Substrate. *J. Phys. Chem. C* **2015,** *119*, 15579-15587.

(43) Willets, K. A.; Van Duyne, R. P. Localized Surface Plasmon Resonance Spectroscopy and Sensing. *Annu. Rev. Phys. Chem.* **2007,** *58*, 267-297.

(44) Jain, P. K.; El-Sayed, M. A. Surface Plasmon Coupling and its Universal Size Scaling in Metal Nanostructures of Complex Geometry: Elongated Particle Pairs and Nanosphere Trimers. *J. Phys. Chem. C* **2008,** *112*, 4954-4960.

(45) Davis, T. J.; Gomez, D. E.; Vernon, K. C. Simple Model for the Hybridization of Surface Plasmon Resonances in Metallic Nanoparticles. *Nano Lett.* **2010,** *10*, 2618-2625.

(46) Hentschel, M.; Dregely, D.; Vogelgesang, R.; Giessen, H.; Liu, N. Plasmonic Oligomers: The Role of Individual Particles in Collective Behavior. *ACS Nano* **2011,** *5*, 2042-2050.

(47) Bordley, J. A.; Hooshmand, N.; El-Sayed, M. A. The Coupling between Gold or Silver Nanocubes in their Homo-Dimers: A New Coupling Mechanism at Short Separation Distances. *Nano Lett.* **2015**, *15*, 3391-3397.

(48) Esteban, R.; Aguirregabiria, G.; Borisov, A. G.; Wang, Y. M.; Nordlander, P.; Bryant, G. W.; Aizpurua, J. The Morphology of Narrow Gaps Modifies the Plasmonic Response. *ACS Photonics*. **2015**, *2*, 295-305.

(49) Gersten, J. I. The Effect of Surface Roughness on Surface Enhanced Raman Scattering. *J. Chem. Phys.* **1980,** *72*, 5779-5780.

(50) Gao, B.; Arya, G.; Tao, A. R. Self-Orienting Nanocubes for the Assembly of Plasmonic Nanojunctions. *Nat. Nanotechnol.* **2012,** *7*, 433-437.

(51) Tabor, C. E.; Murali, R.; Mahmoud, M. A.; El-Sayed, M. A. On the Use of Plasmonic Nanoparticle Pairs As a Plasmon Ruler: The Dependence of the Near-Field Dipole Plasmon Coupling on Nanoparticle Size and Shape. *J. Phys. Chem. A* **2009,** *113*, 1946-1953.

(52) Rein, R. On Physical Properties and Interactions of Polyatomic Molecules with Application to Molecular Recognition in Biology. *Adv. Quantum Chem.* **1973,** *7*, 335-397.

CHAPTER 6

ENHANCED ELECTROCATALYTIC ACTIVITY TOWARDS THE OXYGEN REDUCTION REACTION THROUGH ALLOY FORMATION: PLATINUM-SILVER ALLOY NANOCAGES

6.1. Motivation

Platinum based materials are widely used catalysts. Their versatility within the chemical industry has been proven in a wide range of reactions including catalytic reforming[1, 2], oxidation[3, 4], and reduction[5, 6]. However, cost is a major hindrance to the utilization of platinum in new reactions and applications. One example of such applications is the commercialization of polymer electrolyte membrane fuel cells (PEMFCs)[7]. PEMFCs are an attractive alternative to current energy sources due to their high power density, minimal carbon footprint, and harmless byproduct (water). While platinum has already proven to be a catalyst material which is active towards the oxygen reduction reaction (ORR)[5], this expensive material is plagued by sluggish kinetics. As a result, high catalyst loadings are required to generate a sufficient power density.

In order to reduce the platinum loading currently required for this reaction, the activity of a platinum based catalyst can be improved. Previous reports of platinum based materials utilized as electrocatalysts have shown that there are two main components of platinum materials that drastically affect electrocatalytic activity: the physical and electronic structure of the catalyst[5, 8-12]. In 2004, El-Sayed and co-workers[13] demonstrated that the shape of platinum nanoparticles affected their catalytic activity towards the reduction of hexacyanoferrate. This study examined the activity of platinum spheres, cubes, and tetrahedra and found that there was a direct relationship between the percentage of available edge or corner sites and the catalyst activity. The under-coordination of these edge and corners sites was suggested to be advantageous for this reaction. Consequently, the tetrahedral catalysts (containing the most edge and corner sites) had the highest activity. These results suggested an important contribution from the physical structure of the catalyst surface to its activity

This consideration has been expanded to also include a dependence of a given reaction on the identity of the exposed lattice plane on the surface of a nanoparticle catalyst. Ross and co-workers[14] found that a platinum (100) surface exhibits the highest activity towards the oxygen reduction reaction (ORR) conducted in H_2SO_4. This is due to an increased anion adsorption on the (111) and (110) surface. Anion adsorption blocks active sites and reduces catalytic turnover.

Anion adsorption was also found to be dependent on the interatomic spacing between platinum sites on the catalyst surface. Introducing lattice strain to a nanoparticle is commonly accomplished through the formation of an alloy. When platinum is alloyed with a metal with a lattice constant that is different than platinum there will be a contraction or expansion of the lattice. The magnitude of the strain that is introduced is a function of the alloy composition and can therefore be tuned if the alloy composition can be controlled. In 2012 Manthiram and co-workers[15] also found this effect for a platinum skin on top of a PdCu alloy catalyst. These catalysts were found to exhibit an enhanced activity toward the ORR and thus a favorable interatomic distance for the adsorption of O_2[16, 17] and OH[18-20] species.

The activity of a platinum based catalyst has also been related to the d-band position of the platinum species present on the catalyst surface. Both DFT and experimental results suggest the incorporation of a second metal into the structure of platinum catalysts shifts the d-band center of platinum and alters the chemisorption properties of the catalyst surface. It has been found that for oxygen reduction reactions, this shifting d-band position affects the initial dissociative adsorption of molecular oxygen[21, 22] as well as the adsorption strength of oxygen containing intermediates[20, 23]. However, shifts that induce adsorption strengths that are either too large or too small will begin to limit the activity of the catalyst. The activity, in this regard, exhibits a volcano relationship with respect to the adsorption energy of these oxygen containing species[24].

In order to reduce the currently required platinum loading for the cathode of a PEMFC, the activity of a platinum based catalyst must be improved. With new developments in nanomaterial synthesis, platinum nanoparticles with well-defined shapes[25], sizes[26], and compositions[27] have become the predominant materials developed for new platinum cathodes. Methods of co-reduction[28] or sequential reduction of platinum on top of a particle template are effective; however, the galvanic replacement reaction[29] (GRR) offers a unique advantage to access platinum alloy nanostructures whose shape[30], size, and composition[31] can be precisely controlled without the need for post-synthetic modifications (annealing) or an applied potential.

In this account, the catalytic activity of 4 platinum-silver nanocage catalysts with varying platinum content towards the oxygen reduction reaction is explored. These catalysts are all cubic in structure and are mainly terminated by (100) lattice plane exposure. Due to the precise control over composition permitted by the GRR, the catalytic activity of a platinum-silver alloy (100) surface was investigated as a function of platinum content. The physical and electronic structure of all four catalysts were analyzed through transmission electron microscopy (TEM), X-ray Diffraction (XRD), and X-ray photoelectron spectroscopy (XPS). Cyclic voltammetry as well as rotating disk electrode measurements were conducted to determine the catalytic activity of all catalysts.

6.2. Experimental Methods

The GRR was used to synthesize five Pt-Ag alloy nanocages with varying platinum content. The shape of these particles was controlled both through the synthesis of the silver nanocube template and the galvanic replacement reaction itself. Once synthesized the particles were cleaned and analyzed by TEM, XRD and XPS.

6.2.1. Synthesis

6.2.1.1. Silver Nanocube

First, silver nanocubes of appropriate edge length were synthesized. A variation of the common polyol reduction synthesis[29] was used in order to both quickly and accurately prepare the silver nanocube templates. Trace amounts of Na_2S were used in order to catalyze the reduction of Ag ions present in solution[32] and begin the nucleation process. The increased rate of reduction of Ag ions, and, consequently, the rate of nucleation allows for the dominant formation of single crystal Ag seeds. The use of Na_2S and polyvinylpyrlidone as a capping agent facilitate the dominant formation of the desired cube shape[33].

In a 100ml round bottom flask, 20 ml of ethylene glycol (EG) was heated at 145℃ for 1 hour. After heating the EG for 1 hour, 5.00 ml of a 0.439 M polyvinylpyrrolidone (PVP 55k, molarity in terms of monomer) solution in EG was added and the temperature of the solution was allowed to increase to 154℃. At this temperature, 0.30 ml of a 3.48 mM Na_2S solution in EG was added to the reaction mixture and followed by 5.00 ml of a 141 mM $AgNO_3$ solution in EG. The solution was stirred briefly under constant heating until the solution turned an auburn color. A final silver nanocube template was achieved through careful monitoring of both the stirring and temperature until a turbid green solution was produced. The silver nanocubes were cleaned three times by centrifugation at 6000 rpm for 5 minutes and dispersed in a dilute solution of Nafion-117 prior to cyclic voltammetry and rotating disk electrode measurements. This was done to limit the effects of residual capping material on the surface of the catalyst.

6.2.1.2. Platinum-Silver Nanocage

The synthesized silver nanocubes were then diluted to five times the original volume with 18 MΩ deionized (DI) water. This solution was then spun at 6000 rpm for 5 minutes (Eppendorf centrifuge 5810R) and re-dispersed in DI water. A 5.08 mM solution of potassium tetrachloroplatinate (K_2PtCl_4) was then added to the new silver nanocube solution in 0.2 ml increments every five minutes under constant stirring. After 5, 9, 15, and 20 additions of potassium tetrachloroplatinate equivalent aliquots, the Pt-Ag nanocages were removed from the synthesis solution and immediately placed in a shaker at room temperature overnight. The Pt-Ag nanocage synthesis solutions were then centrifuged at 6000 rpm for 5 minutes (Eppendorf centrifuge 5810R) and re-dispersed in 18 MΩ DI water.

6.2.1.3. Silver/Silver Chloride Nanocube

Silver nanocubes with a silver chloride surface were synthesized through the addition of sodium chloride (NaCl) to a solution of cleaned silver nanocubes. Specifically, 87.1 μl of 10.5 μM NaCl was added to 285 μl of silver nanocubes cleaned three times by centrifugation. The solution was shaken for 5 minutes and allowed to sit for 1 hour. The synthesis was monitored with an Ocean Optics UV-Vis spectrometer equipped with a halogen/deuterium lamp. As seen in Figure 6.1, there is a decrease in the observed extinction of the Ag nanocubes upon addition of the NaCl salt. This dampening is attributed to the formation of AgCl on the surface of the nanocubes. Figure 6.1 also confirms the absence of any changes in shape or aggregation. These Ag/AgCl nanocubes were cleaned by centrifugation at 6000 rpm for 5 minutes and dispersed in a dilute solution of Nafion-117 prior to cyclic voltammetry and rotating disk electrode measurements.

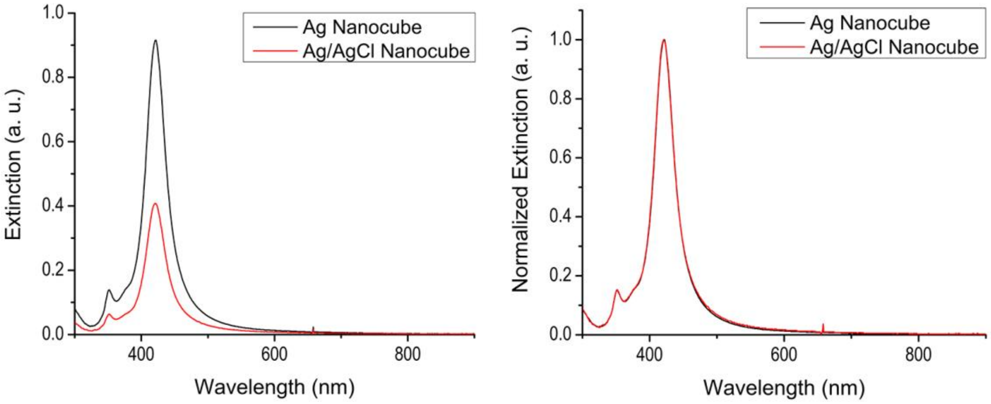

Figure 6.1. The UV-Vis spectra of Ag (black) and Ag/AgCl (red) nanocubes. Spectra were taken of equivalent volumes of particles (left) which indicate the formation of AgCl on the surface of the Ag nanocubes due to a decrease in the extinction intensity. A normalized spectrum of each particles supports a lack of aggregation and shape deformation upon addition of the NaCl salt.

6.2.2. Characterization

6.2.2.1. Transmission Electron Microscopy

An aqueous dispersion of particles was deposited on a formvar/carbon film covered grid and the shape and size distribution of the as synthesized nanocatalysts was determined by transmission electron microscopy (TEM). A JEOL 100CX TEM was utilized with an accelerating voltage of 100 kV. All images were analyzed with image processing software (Image J). At least 150 particles were used to find the average edge length of each type of particle. The distribution of sizes for each synthesized catalyst and a representative TEM image can be seen in Figure 6.2.

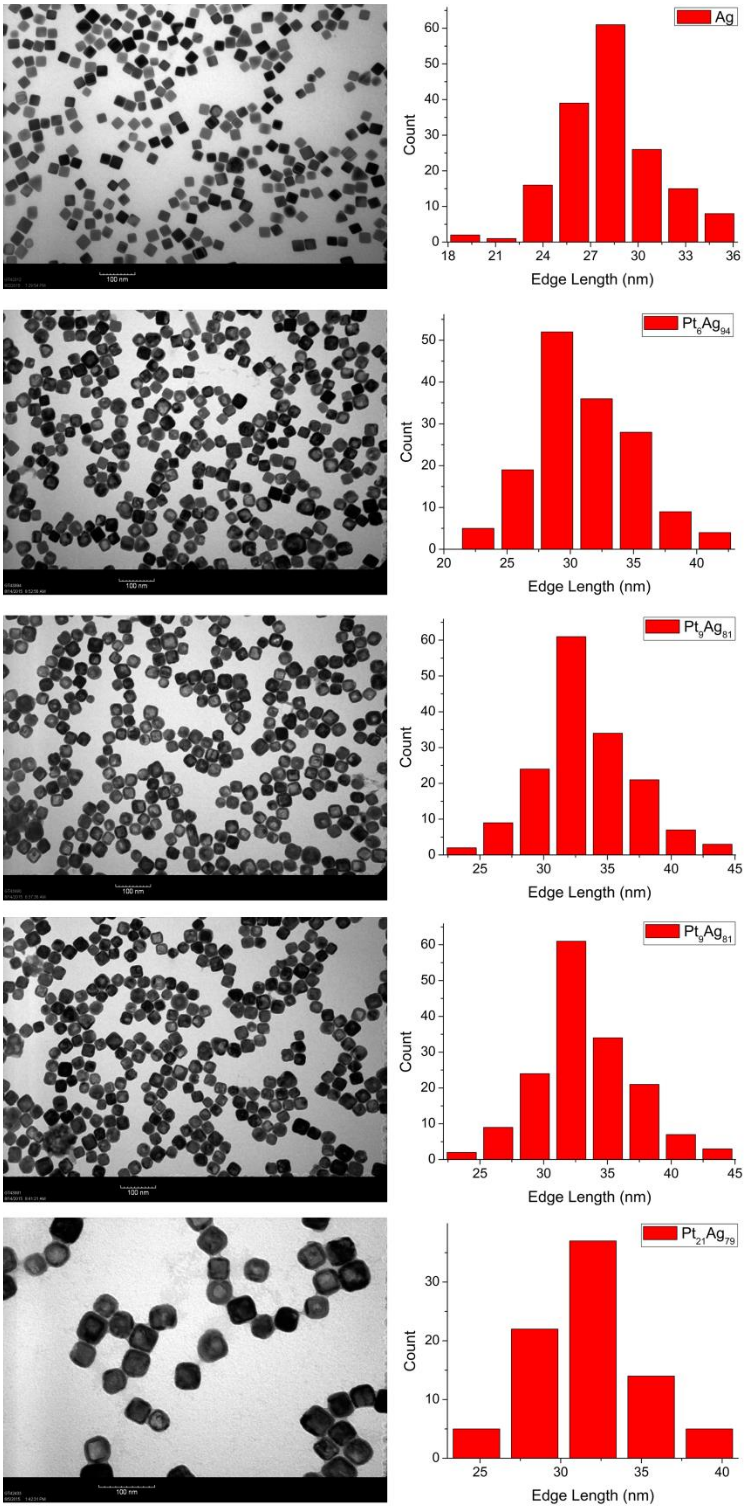

Figure 6.2. Transmission electron microcraphs of the Ag nanocube template and subsequent PtAg nanocages synthesized with varying platinum content (left). A histogram of the size distribution for each particle was analyzed from a sample size of atleast 150 particles (right). All scale bars represent 100 nm.

6.2.2.2. Platinum Content of Platinum-Silver Nanocages

The platinum and silver content for all synthesized Pt-Ag nanocages was determined through inductively coupled plasma emission spectroscopy (ICPES). A 0.5 ml sample of each Pt-Ag nanocage was digested in 10 ml of boiling concentrated nitric acid (~10ml). The solution was heated until the volume was reduced to 2 ml. In order to ensure a complete digestion a second aliquot of boiling nitric acid was added and the solution was again heated until a final volume of < 2 ml was reached. This solution was diluted to a final volume of 5.00 ml and then analyzed for both platinum and silver content. It is important to note that aqua regia is preferred for digestion, however, only nitric acid was utilized here in order to avoid the formation of $AgCl_{(s)}$.

6.2.2.3. X-ray Diffraction

All samples were deposited on a quartz slide prior to characterization by X-ray diffraction (XRD). First, the cleaned nanoparticle solutions were concentrated and transferred to an isopropanol solution. Then, 50 μl aliquots of the isopropanol/particle solution were deposited on a glass slide and spun at 1000 rpm for 60 seconds until a total volume of roughly 300 μl was reached. The physical structure of the catalysts was characterized by a PANAnaltical X'Pert Pro X-ray Diffractometer equipped with a CuKα source. A scan speed of 0.0005 ˚/s was implemented for an analysis range between 25 and 70^o.

6.2.2.4. X-ray Photoelectron Spectroscopy

The electronic state of the atoms present on the surface of each nanocage was characterized by a Kratos Axis Ultra X-ray photoelectron spectroscope (XPS). The same samples that were prepared for XRD were allowed to dry in a desiccator for two days prior to analysis by XPS. All four Pt-Ag nanocage samples were mounted and analyzed simultaneously in order to limit differential shifts in the measured XPS spectra due to surface charging. Both a survey scan and high resolution Pt 4f scan were conducted on all samples with a scan rate of 0.01 eV/s for the Pt 4f spectra. The Pt 4f spectra were obtained for binding energies ranging from 64 to 80 eV and all spectra were shift corrected using an averaged accepted C 1s binding energy of 286.46[34] eV (Figure 6.3).

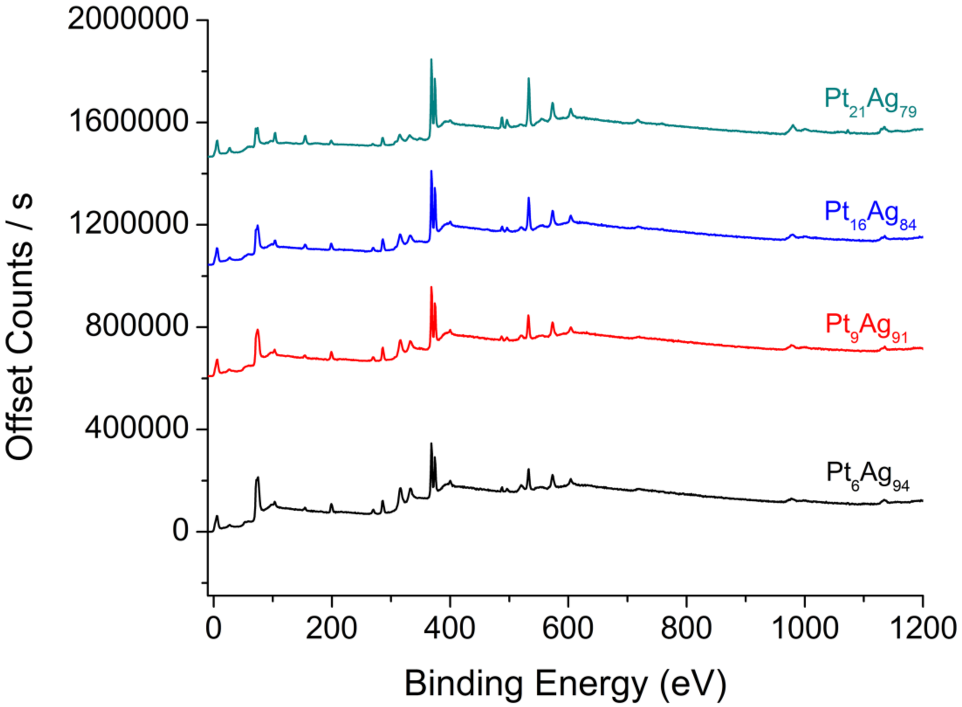

Figure 6.3. X-ray photoelectron survey spectra of all synthesized platinum-silver nanocage catalysts: Pt_6Ag_{94} (black), Pt_9Ag_{81} (red), $Pt_{16}Ag_{84}$ (blue), $Pt_{21}Ag_{79}$ (cyan). All survey spectra were shift correct to a C 1s binding energy of 286.46 eV.

6.2.2.5. Cyclic Voltammetry

The electrochemical activity of the Pt-Ag nanocages, Ag nanocubes, and Ag/AgCl nanocubes towards the oxygen reduction reaction was initially characterized through cyclic voltammetry in oxygen saturated 0.1M $HClO_4$ solution. Perchloric acid was utilized as the electrolyte for this reaction due to the minimal and unselective adsorption of the chlorate ion on the surface of all low index facets[14, 35]. All particles were dispersed on a polished glassy-carbon disk electrode (0.1963 cm^2 area) and mounted on an interchangeable RDE holder (Pine Instruments). A coiled platinum counter electrode and a single junction Ag/AgCl reference electrode (separated by an electrolyte bridge) were used. The measured potentials were converted to reversible hydrogen electrode scale given the measured pH of 1.0 for the 0.1 M $HClO_4$ electrolyte utilized in this study. Before deposition on the polished glassy carbon electrode, the Pt-Ag nanocage catalysts were dispersed in a dilute ionomer solution of Nafion-117. The optimized catalyst to ionomer ratio (g_{cat}/g_{ion}) was experimentally determined to be a ratio of at least 70:1 (Figure 6.4).

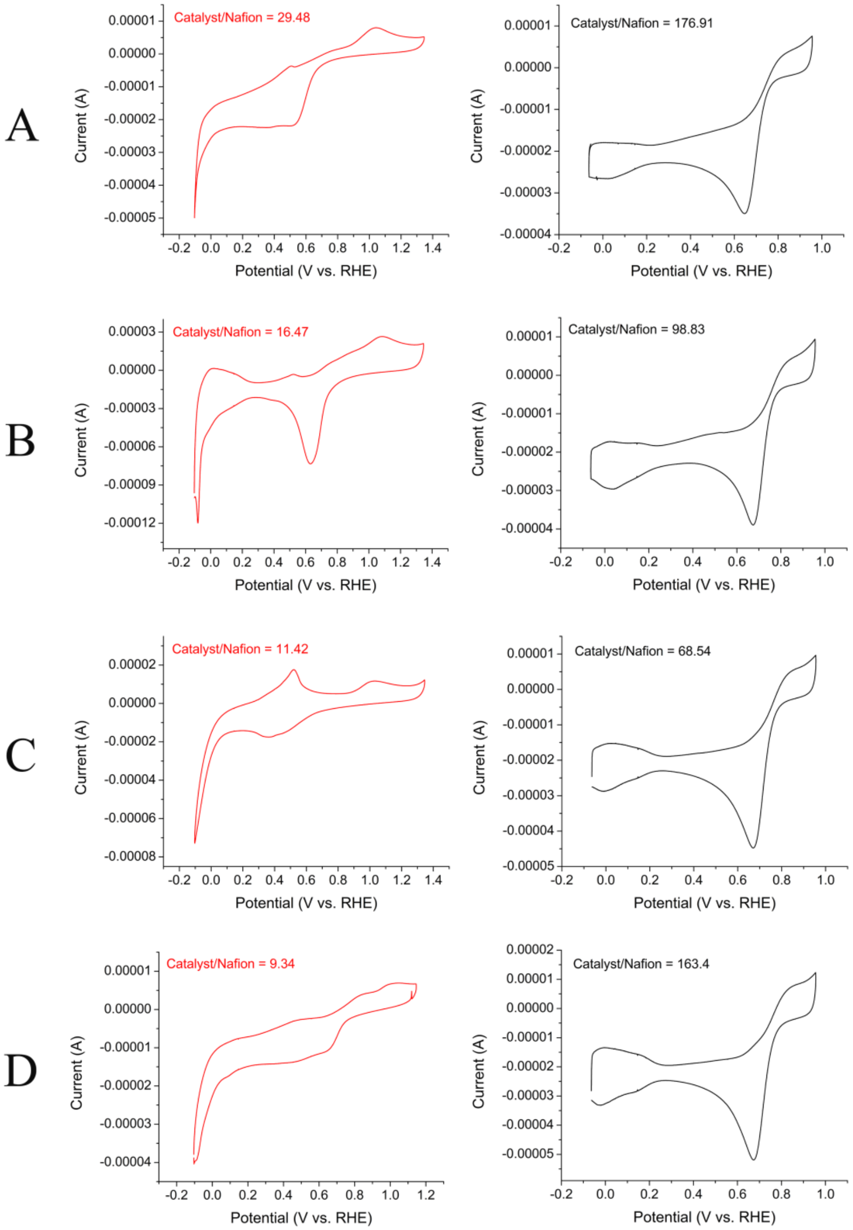

Figure 6.4. Cyclic voltammetry measurements conducted on PtAg nanocage catalysts with varying ratios of catalysts to Nafion (g_{cat}/g_{Nafion}). Low ratios (red) prevented the observation of hydrogen adsorption/desorption (0-0.2 V) as well as oxygen adsorption (~0.7 V). Ratios above 70 facilitated reactant diffusion to the catalyst surface.

A 20 μl aliquot of the catalyst/ionomer mixture was then deposited on the polished glassy carbon electrode and allowed to dry at room temperature. The catalyst loadings ranged from 7-27$\mu g_{Pt}/cm^2_{electrode}$ which corresponds to a total catalyst loading ranging from 23-81$\mu g_{cat}/cm^2_{electrode}$. These low catalyst loadings were implemented in order to minimize mass transport losses incurred by poor O_2 transport through the diffusion medium and electrode layer[5]. Figure 6.5 shows the observed cyclic voltammetry measurements of all catalyst particles. The potential was scanned from roughly 0-1.0 V (vs RHE) at a scan rate of 20 mV/s until a stable signal was achieved. The observed oxidation and reduction couple centered near 0.45 V of the Ag and Ag/AgCl nanocubes suggested the surfaces of both particles are in fact exposed. However, both the Ag and Ag/AgCl nanocubes lack hydrogen adsorption/desorption (0-0.2 V) as well as oxygen adsorption (~0.7 V). As a result, the hydrogen adsorption/desorption regions exhibited by PtAg nanocages is attributed solely to the presence of available platinum sites on the surface of these catalysts.

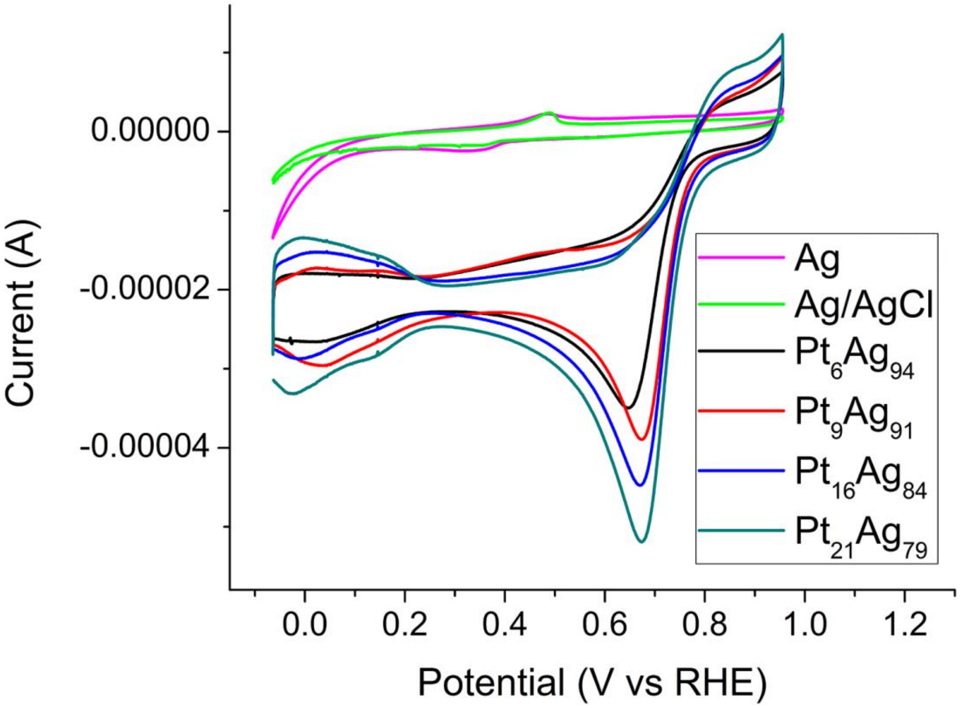

Figure 6.5. Cyclic voltammetry measurements of Ag nanocubes (pink), Ag/AgCl nanocubes, and PtAg nanocages with increasing platinum content (black, red, blue, cyan). There is a lack of hydrogen adsorption/desorption and oxygen adsorption on the surface of the Ag and Ag/AgCl nanocubes. As a result, the hydrogen adsorption/desorption and oxygen adsorption observed for all PtAg nanocages is attributed to the Pt sites present on the surface of these catalysts.

6.2.2.6. Platinum Specific Surface Area

The platinum specific surface area was determined by cyclic voltammetry in 0.1M $HClO_4$ at room temperature and a scan rate of 20 mV/s. The hydrogen/desorption areas of the cyclic voltammogram (Figure 6.6) were integrated and converted to platinum surface areas assuming 210 $\mu C/cm^2_{Pt}$ after a double layer correction[36, 37]. Again, negligible hydrogen adsorption/desorption was observed on both the Ag and Ag/AgCl particles and therefore it was assumed that all hydrogen adsorption/desorption measured for the Pt-Ag alloys is due solely to the platinum sites present on the surface. Also, care was taken to limit the potential to below 1.0 V in order to prevent capacitive charging. The hydrogen adsorption region of platinum based catalysts has previously been shown to exhibit distinct regions of hydrogen adsorption/desorption on different lattice planes exposed by the catalyst[38]. However, all platinum-silver nanocage catalysts herein exhibit a fairly monotone and indiscriminant hydrogen adsorption/desorption. This is likely due to the dominant exposure of only the (100) lattice plane on these platinum based catalysts.

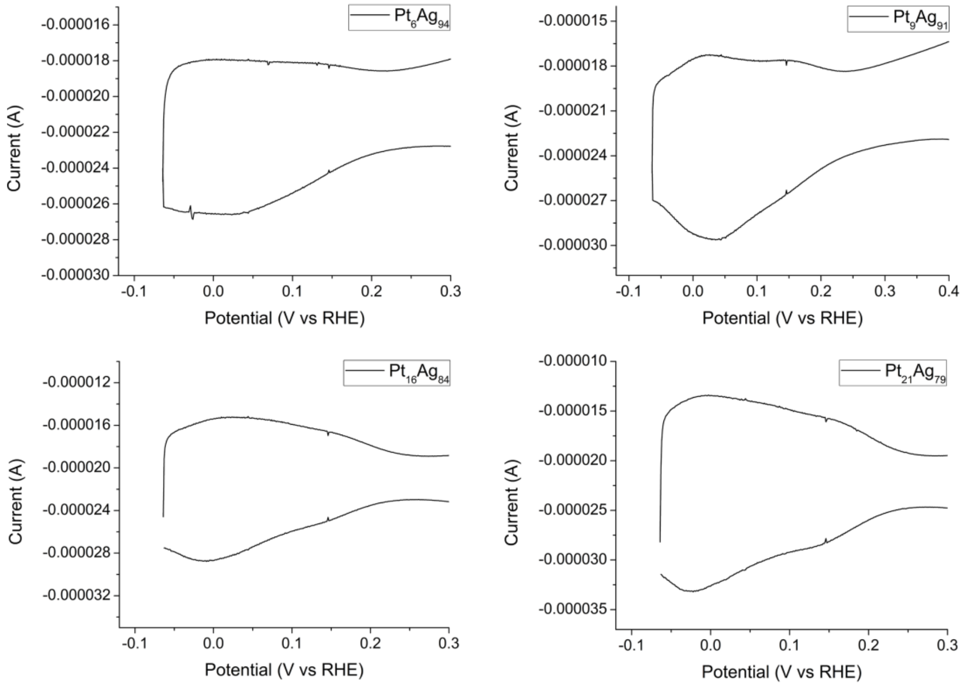

Figure 6.6. The hydrogen adsorption/desorption region of the cyclic voltammetry measurement for all PtAg nanocage catalysts. This signal was utilized to quantify the platinum specific area of these PtAg catalysts.

6.2.2.7. Rotating Disk Electrode Measurements

The specific current density was measured in an oxygen saturated solution of 0.1M $HClO_4$ with a rotation rate of 1600 rpm. All reported values for the specific current density were mass transport corrected and normalized to the measured platinum specific current density. Oxygen reduction activities were recorded at 1600 rpm in oxygen saturated 0.1M$HClO_4$ at room temperature and 20 mV/s. Care was again taken to limit the positive going potential to <1.0 V and utilize a low sweep rate in order to minimize interference from capacitive currents. The current density of each catalyst was normalized to the electrochemically determined surface area of each catalyst. The specific catalytic activity is frequently reported as the fundamental intrinsic kinetic parameter, the exchange current density. However, these values are obtained through extrapolation of the experimentally measured currents over four orders of magnitude and thus introduce significant error[5]. In order to minimize this error all specific activities will be evaluated at 0.9V vs RHE. This voltage has previously been utilized and will be useful to compare catalytic activity to previously reported values[5]. As seen in Figure 6.7, there is negligible current density for both the Ag nanocube and Ag/AgCl nanocube catalysts.

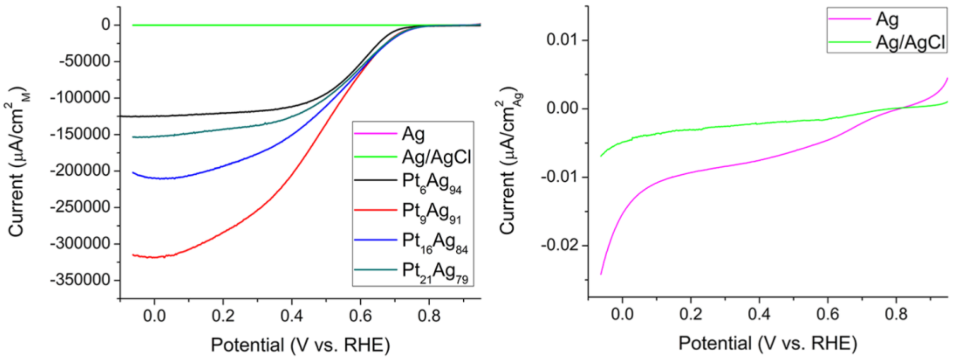

Figure 6.7. Oxygen reduction specific current densities of Ag nanocube, Ag/AgCl nanocube, and all PtAg alloy nanocage catalysts (left). Zoomed in portion of Ag nanocube and Ag/AgCl nanocube catalysts, which exhibit negligible current density at all potentials which were analyzed.

6.3. Results and Discussion

Platinum-silver nanocage catalysts with a precisely defined shape and composition were synthesized using the galvanic replacement reaction and utilized as catalysts for the oxygen reduction reaction. A silver nanoparticle template was chosen due to both the synthetic control over the shape and size currently available for silver nanoparticles as well as the advantageous reduction potential of silver which permits the utilization of the galvanic replacement reaction to form a platinum alloy. The cubic shape was exploited for its exclusive exposure of (100) surface morphology. To ensure consistency between samples, all platinum-silver nanocage catalysts were synthesized from the same silver nanocube template (Figure 6.8A-E).

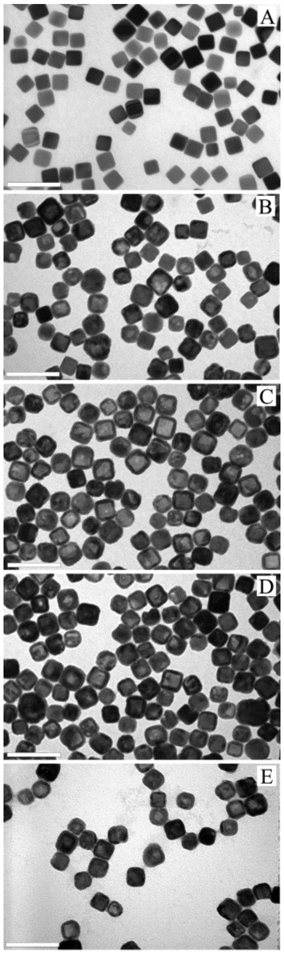

Figure 6.8. Transmission electron microscopy (TEM) images of the as synthesized Ag nanocube template (A) and the subsequent Pt-Ag nanocages with increasing platinum content (B), (C), (D), (E). The cubic shape is preserved for all Pt-Ag nanocages regardless of platinum content. However, there is a slight increase in the average size of

the Pt-Ag nanocages (32.8 nm ± 4.0 nm) after the initial incorporation of platinum into the Ag nanocube template (29.4 nm ± 3.0 nm). Scale bar: 100 nm for all images.

This reaction is a convenient and easy synthetic approach towards platinum based nanocatalyst due to both a facile control of the shape and size of the resulting platinum catalyst[30] as well as extremely mild synthetic conditions. It has been previously suggested that the process of galvanic replacement is initiated by the formation of pits in the walls of the template particle through which interior atoms can be selectively lost. As the reaction proceeds, a cavity within the interior of the structure develops which is followed by the pits within the walls of the structure progressively become visually distinct pores[39]. The formation of pores is especially prevalent in Au-Ag nanocages synthesized with a gold salt with a high oxidation state[40, 41]. However, for platinum based particles synthesized using GRR significant formation of porosity is not observed likely due to a lack of electrochemical driving force as the reaction continues[42]. As seen in Figure 6.8, the development of an interior cavity, retention of both the shape and size of the template structure, and a lack of porosity was observed for all platinum-silver nanocages.

As seen in Table 6.1, there is a slight increase in the average size of each catalyst compared to the silver nanocube template; however, this difference is not statistically significant. The composition of each platinum-silver alloy catalyst was determined by ICPES and can also be seen in Table 6.1. The composition of the four platinum-silver alloy catalysts range from 6-21% platinum. It is important to note that structural differences between pure platinum and silver preclude platinum-silver alloys with compositions much greater than 21% when synthesized using the galvanic replacement reaction. However, the effects of alloy formation on the electronic structure of the platinum species present on the surface of these catalysts will be strongest at low platinum contents and thus low platinum contents are desirable.

Table 6.1. Summary of the physical characterization of all synthesized catalysts. The sizes reported are the mean ± SD (n=150) and the composition of the Pt-Ag nanocages were determined through ICP-AES. All lattice parameter, lattice expansion, and interatomic spacing was calculated as an average value from all low index facets within each corresponding XRD pattern.

Particle	Size (nm)	Composition (% Pt)	Lattice Parameter (a)	Lattice Expansion (%)	Interatomic Spacing (Å)
Ag Nanocube	29.39 (± 3.02)	---	---	---	---
Pt_6Ag_{94}	32.77 (± 4.00)	6.00	4.07	3.74	2.88
Pt_9Ag_{91}	34.73 (± 3.52)	9.07	4.04	2.91	2.86
$Pt_{16}Ag_{84}$	33.69 (± 3.93)	16.0	4.03	2.75	2.85
$Pt_{21}Ag_{79}$	33.36 (± 3.15)	21.1	4.02	2.49	2.84

6.3.1. Electrochemical Measurements

As seen in Figure 6.9, the resulting cyclic voltammograms exhibit a prominent oxygen adsorption region between 0.646-0.674 V (vs. RHE) as well as a characteristic hydrogen adsorption/desorption region at $E < 0.3$ V. While an oxygen adsorption peak potential of roughly 0.7-0.8 V is commonly reported[5] for solid platinum catalysts the potential seen in Figure 6.9 is slightly shifted to more negative potentials (-50 mV). This negative shift has been previously attributed to an increased presence of site blocking OH_{ads} species on the surface of the catalyst[5]. A previous investigation of the low index facets of PtNi catalysts suggested an increased surface coverage by OH_{ads} on the (100) surface compared to both the (111) and (110) lattice planes[11]. Due to the cubic structure of these catalysts it is likely that this negative potential shift is in fact due to an increased surface coverage of OH_{ads}. It is important to note that there is a slight positive shift in the adsorption/desorption region of oxygen in the cyclic voltammogram as the platinum content of the Pt-Ag nanocage is increased (~30 mV). There appears to be a possible decrease in the OH_{ads} surface coverage that is dependent on the platinum content of these platinum-silver alloy nanocage catalysts.

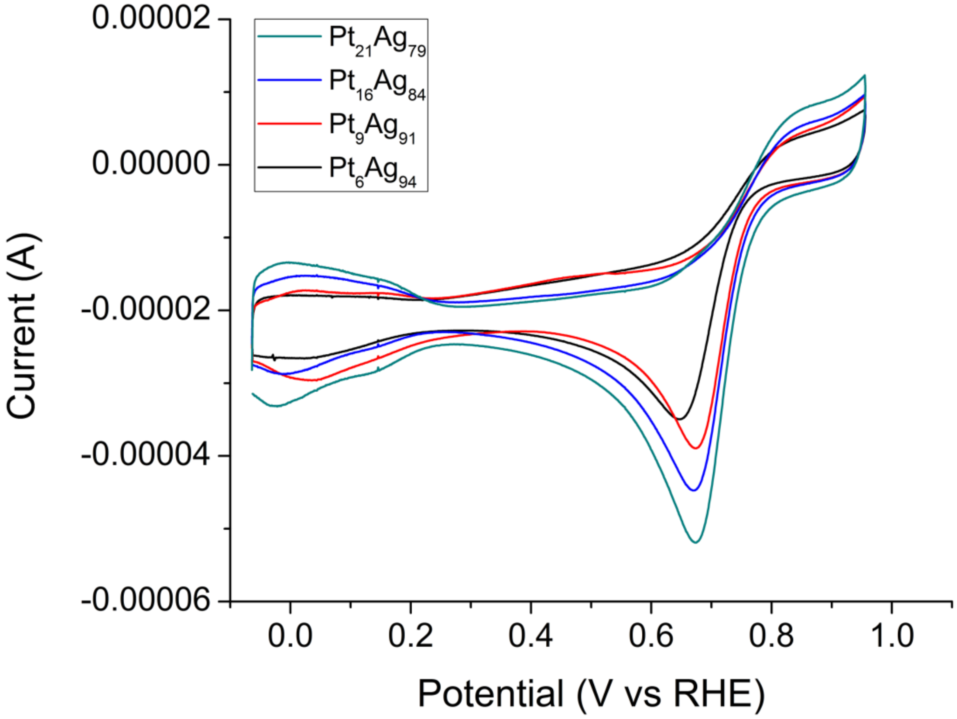

Figure 6.9. Cyclic voltammograms of catalyst-Nafion 117 mixtures of Pt-Ag nanocages with platinum contents ranging from 21% (Green), 16% (Blue), 9% (Red), and 6% (Black). Data was recorded with a scan rate of 20 mV/s in a solution of oxygen saturated 0.1 M $HClO_4$ at 20˚C. There is a progressive shift in the oxygen reduction peak potential to higher voltages as the platinum content of the Pt-Ag nanocages increases.

As seen in Figure 6.10, the specific activities of the platinum-silver alloy nanocage catalysts exhibit an interesting activity that is dependent on the platinum content of the catalyst. The platinum-silver nanocage catalyst with the lowest platinum content exhibits a maximum specific activity of $660 \mu A/cm^2_{Pt}$. This is a 3 fold enhancement previously reported activities for high surface area solid platinum catalysts which were analyzed at an elevated temperature (60 °C)[5]. Other than a lower temperature, these platinum-silver nanocages were analyzed under identical conditions (the same electrolyte, ionomer, catalyst loading, and sweep rate). Here the formation of a platinum-silver alloy on a cubic structure has led to a platinum based catalyst with an enhanced activity.

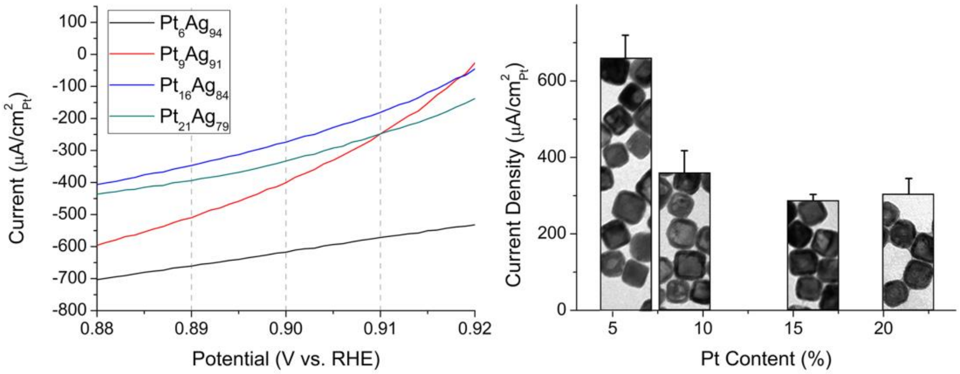

Figure 6.10. Oxygen reduction reaction (ORR) activities of Pt-Ag nanocages with varying platinum content at 0.9V (vs. RHE) and 20˚C determined through rotating disk electrode (RDE) measurements in oxygen saturated 0.1M $HClO_4$ with a rotation rate of 1600 rpm. Specific activities were obtained for scans from 0–1.0V at a scan rate of 20mV/s and are listed as the mass transport corrected current densities normalized to the available platinum surface area of each catalyst. A zoomed in portion of the polarization curve (0.88-0.92V) for all catalysts (left) and the corresponding specific current density as a function of platinum content (right) are shown. There is an apparent increase in the specific activity of these Pt-Ag nanocages as the platinum content of the nanocage decreases.

6.3.2. Oxygen Reduction Reaction Kinetic Parameters

A kinetic analysis of the ORR over the Pt-Ag alloy catalysts is presented in the form of a Tafel plots and Koutecky-Levich plots (Figure 6.11). The mass-transport free kinetic current was determined using the well know mass-transport correction for rotating disk electrodes[5]:

$$i_k = \frac{i_d * i}{i_d - i} \qquad 1$$

where i is the experimentally measured current and i_d is the measured diffusion-limited current. Two regions described by different Tafel slopes can be identified for all catalysts investigated (Table 6.2). The high current density (hcd), $i_k > 0.1$ mA/cm$^2_{Pt}$, and low current density (lcd), $i_k < 0.1$ mA/cm$^2_{Pt}$, regions are described by Tafel slopes of roughly 120 mV/decade and 54 mV/decade for both Pt_6Ag_{94} and Pt_9Ag_{91} catalysts. These values agree well with the ideal temperature dependent Tafel slopes (proportional to 2.3(RT/F)). Notably, there is a decrease in the observed Tafel slope of both the lcd and hcd regions as the platinum content of the alloy catalysts increases. The observed Tafel slopes of $Pt_{21}Ag_{79}$ reach a minimum of 91 and 42 for the hcd and lcd regions respectively. This decrease has been previously attributed to a decreased blockage of active sites by oxygen species[38, 43], which agrees well with the previously observed shift in the oxygen adsorption peak of the cyclic voltammogram of $Pt_{21}Ag_{79}$.

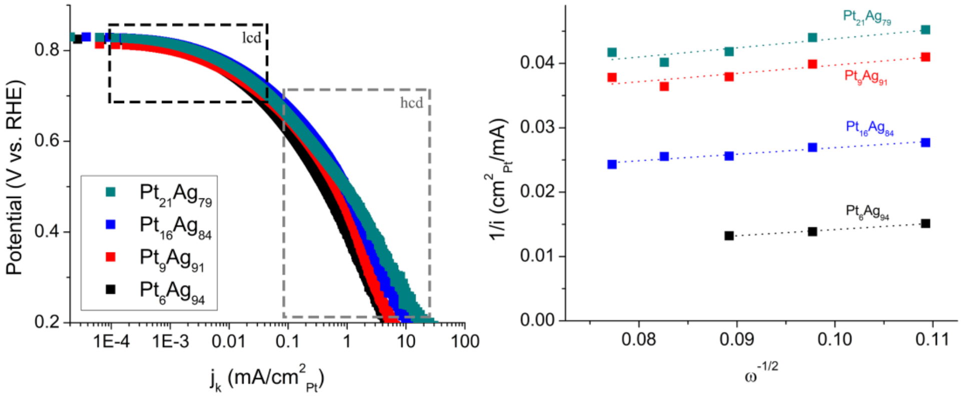

Figure 6.11. Tafel plot for all for PtAg alloy catalysts with designated low current density (lcd) and high current density (hcd) regions (left). The Tafel slope of both the lcd

and hcd region agree well with previously reported values. A slight decrease in the lcd/hcd Tafel slope of the $Pt_{21}Ag_{79}$ compared to all other catalysts is indicative of a decrease in the blockage of active sites on the surface of this catalyst. Koutecky-Levich plot of all four PtAg alloy catalysts at a voltage of 0.6V (right). The slope obtained for all catalysts agrees well with the accepted 4 electron transfer reaction mechanism previously described for the ORR.

As seen in Figure 6.11, the Koutecky-Levich plots express a similar slope for all Pt-Ag alloy catalysts analyzed. Based on the Levich equation, the slope of these plots can be related to the number of electrons transferred in the ORR:

$$\frac{1}{j} = \frac{1}{j_k} + \frac{1}{j_d} = \frac{1}{j_k} + \frac{1}{0.2nF{D_0}^{2/3}\omega^{1/2}v^{-1/6}C_0} = \frac{1}{j_k} + \frac{1}{B\omega^{1/2}} \qquad 2$$

where j is the measured current density, j_k is the kinetic current density, j_d is the diffusion limited current density, F is Faradays constant, D_0 is the diffusion coefficient of O_2, ω is the electrode rotation rate, υ is the kinematic viscosity of perchloric acid, and C_0 is the concentration of O_2 in dilute perchloric acid. Published values for D_0 (1.67×10^{-5} cm^2/s)[44], υ (9.99×10^{-3} cm^2/s)[45], and C_0 (1.38×10^{-6} mol/cm^3)[44] were used. From the B values obtained from the slopes in Figure 6.10, the estimated number of electrons transferred during the reaction could be calculated (Table 6.2). Slight variations in the number of electrons transferred were observed, however, the data is statistically consistent with the 4 electron oxygen reduction mechanism.

Table 6.2. Kinetic Parameters for the ORR on PtAg alloy catalysts in 0.1M $HClO_4$ as a function of platinum content.

Particle	**Tafel Slope (mV/dec)**		**n**
	lcd	**hcd**	
Pt_6Ag_{94}	53	119	4.6 (± 0.5)
Pt_9Ag_{91}	55	128	3.4 (± 1.0)
$Pt_{16}Ag_{84}$	54	108	4.3 (± 0.6)
$Pt_{21}Ag_{79}$	42	91	3.1 (± 1.0)

6.3.3. Influence of Interatomic Spacing

All Pt-Ag alloy catalysts were further analyzed by X-ray diffraction (XRD). The diffraction patterns of each catalyst can be seen in Figure 6.12. The low index facets (111), (200), and (220) are identified within the XRD pattern. The positions for the low index facets of pure Ag and Pt are denoted as vertical dashed and dotted lines respectively. All other peaks within each pattern are consistent with the low index facets of AgCl. The formation of AgCl is an expected byproduct of the galvanic replacement reaction between silver nanocubes and a $PtCl_4^{2-}$ salt. The alloy catalysts primarily exhibit strong diffraction from the (111) and (200) lattice planes. At low platinum contents there is an uncharacteristic (200) peak intensity compared to a bulk platinum XRD pattern[46]. This is indicative of the cubic shape of the catalysts; however, upon increasing the platinum content within the alloy there is a transition to an increased exposure of the (111) lattice plane. Due to the weak electrolyte adsorption characteristics of perchloric acid it is likely that this transition will have a minimal effect on the catalytic properties of these materials[14].

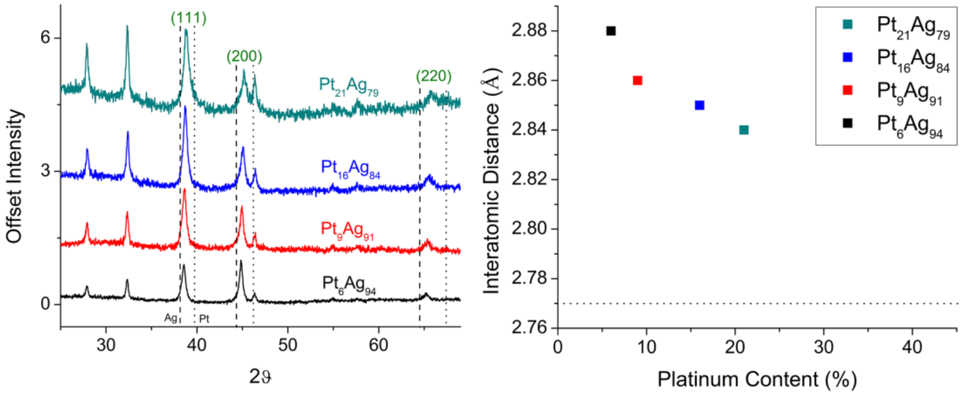

Figure 6.12. X-ray diffraction patterns for Pt-Ag nanocages with varying Pt content: 6% (black), 9% (red), 16% (blue), 21% (green). Peaks identified in green ((111), (200), and (220)) correspond to the crystal lattice of the Pt-Ag nanocage (left). Unidentified peaks result from the crystal lattice of AgCl contaminants. There is an absence of diffraction peaks corresponding to either purely Ag (dashed) or purely Pt (dotted), thus supporting the classification of this material as an alloy. The corresponding interatomic distances for each catalyst were determined as a function of platinum content.

The diffraction from all of the low index facets is shifted to lower 2Θ angles and is indicative of a lattice expansion compared to pure platinum for all platinum-silver alloy catalysts. Upon incorporation of platinum into the lattice of a pure silver nanocube the lattice parameter of the Pt-Ag alloy ranges from 4.071-4.022 Å. This corresponds to an expansion of a pure platinum lattice by 2.5-3.7% and a Pt-Pt interatomic distance ranging from 2.84-2.88 Å (Table 6.1). The calculation for the lattice expansion, a_{exp}, was adapted from a previous description of the lattice strain present within a dealloyed core-shell PtCu catalyst developed by Nilsson and co-workers[20]. Herein, the lattice expansion was calculated as a function of a reference lattice parameter for pure platinum, a_{Pt}, and the average lattice parameter, $a_{Pt\text{-}Ag}$, calculated from all low index facets found within the XRD pattern for each Pt-Ag alloy catalyst (equation 1).

$$a_{exp} = \frac{a_{Pt-Ag} - a_{Pt}}{a_{Pt}} \times 100 \qquad 3$$

The dissociative adsorption of molecular oxygen has been previously shown to be dependent on the interatomic spacing of platinum atoms on the surface of a catalyst. Larger than optimum interatomic spacing would inhibit the formation of intermediate adsorbed molecular oxygen species upon adsorption[16]. As a result, dissociation would occur prior to adsorption. Smaller than optimum separations would introduce repulsive forces which would retard duel site adsorption and inhibit oxygen reduction[16]. The observed lattice parameters herein correspond to interatomic Pt-Pt spacings that are larger than both pure platinum and other active platinum alloys utilized for this reaction[15, 16, 20, 21]. This would suggest a large barrier toward molecular adsorption on the surface of these catalysts. It is possible that this could contribute to the high surface coverage of OH_{ads} species indicated by Figure 6.8. As mentioned previously, when the platinum content of the alloy is increased to 9 % there is a positive shift in the oxide adsorption. This is indicative of a weakening oxygen adsorption which has also been found to be consistent with a decreasing interatomic spacing. It appears however, that this oxygen adsorption is not further affected upon decreasing the interatomic spacing from 2.86 to 2.84 Å.

6.3.4. Influence of Platinum Binding Energy

The core-level Pt 4f X-ray photoelectron spectroscopy (XPS) spectra of all Pt-Ag alloy catalysts are shown in Figure 6.13. There is a characteristic doublet representative of the two possible spin orbit coupling states, Pt $4f_{7/2}$ and $4f_{5/2}$, for all catalysts. The dotted lines denote an averaged binding energy for Pt $4f_{7/2}$ (71.08 eV) and $4f_{5/2}$ (74.38 eV) peaks corresponding to pure platinum[34]. As the platinum content decreases there is also the development of a strong second doublet at slightly higher binding energies. This is likely due to an increased presence of Pt-O (Pt^{II}) compared to Pt^0 sites as the platinum content of the catalyst is decreased.

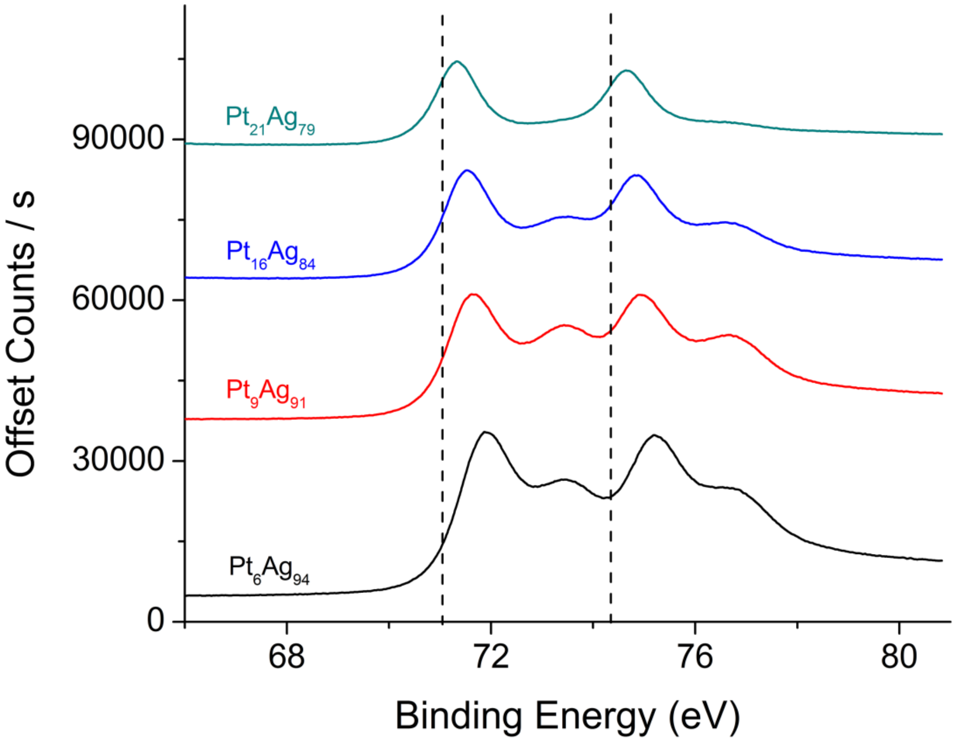

Figure 6.13. X-ray photoelectron spectroscopy data for Pt-Ag nanocages with a platinum content of 6% (black), 9% (red), 16% (blue), 21% (green). All catalyst exhibit a higher binding energy than pure platinum (dashed lines). There is a consistent increase in the binding energy of the platinum species present within the Pt-Ag nanocages as the platinum content decreases. Along with a shift to higher binding energies there is a progressive increase in the presence of Pt^{II} species as the platinum content of the Pt-Ag nanocages decreases. A positive shift in the Pt 4f binding energies suggests a down-shifted d-band position for the Pt-Ag alloys.

There is a positive shift in the binding energy of all Pt-Ag catalysts that reaches a maximum, with respect to pure platinum, of +0.85 eV at a platinum content of 6%. Previous reports have attributed a positive shifting binding energy to a downshifted d-band position. Norskov and co-workers[22] have developed a model to relate the adsorption properties of oxygen species on the surface of various metal materials to the d-band position of the metal. It has proven to be useful for describing the activity of many platinum based alloys towards the oxygen reduction reaction. For simple oxygen containing adsorbates, the adsorption process can be described as an electron-interaction between the adsorbate 2p and metal d states. This interaction forms a bonding and anti-bonding states whose population is largely dependent on the d-band position of the metal. For pure platinum, the d-band position is such that the antibonding interaction between atomic O and Pt is above the Fermi level. The antibonding state is unfilled and chemisorption is strong. However, upon decreasing the d-band position of the metal the antibonding interaction begins to drop below the Fermi level of the metal and is subsequently filled. As the antibonding interaction becomes occupied weaker adsorbate bonding ensues.

With respect to the synthesized Pt-Ag alloy catalysts there is an increase in the observed binding energy of the platinum with respect to pure platinum and thus a weakened adsorbate bonding for simple oxygen containing intermediates. Interestingly, the specific activity of the Pt-Ag alloy catalysts increase as the platinum content decreases. Assuming Norskov’s model, the data suggests that the observed maximum specific activity for the Pt-Ag alloy catalyst with the lowest platinum content is due to a downshifted d-band position and weakened adsorbate bonding. Despite the proposed high OH_{ads} surface coverage, the d-band position of the Pt_6Ag_{94} resulted in a platinum based catalyst with a high specific current density. As the platinum content of these catalysts increases the Pt 4f binding energies shift to lower values and loose the advantageous effects of a lowered d-band position.

6.4. Concluding Remarks

The galvanic replacement reaction is a useful and efficient method for the development of platinum alloy catalysts. Herein, the specific activity of four platinum-silver alloy nanocage catalysts was determined as a function of platinum content. It was found that for all platinum-silver nanocage catalysts analyzed, incorporation of platinum into the structure of a silver nanocube enhances the specific current density over pure platinum by at least a factor of 1.5. The platinum-silver nanocage catalysts with the highest activity were found to be the nanocages with the lowest platinum content. This catalyst exhibited a negatively shifted oxygen adsorption and thus a possible high surface coverage of OH_{ads}. Both the large interatomic spacing and (100) lattice plane exposure are likely to contribute to this increased surface coverage; however, this Pt_6Ag_{94} exhibits a large positive shift in the binding energy of the Pt 4f electrons on its surface. This positive shift correlates to a downshifted d-band position and subsequent weakened metal adsorbate interaction. It is this weakened interaction that results in a platinum based catalyst that exhibits a 3 fold enhancement in the specific current density of pure platinum catalysts. In conclusion, the formation of a platinum-silver alloy with minimal platinum content produces a catalyst with a d-band position that is highly desirable for the oxygen reduction reaction.

6.5. References

(1) I. Moiseev: Catalysis: 2000 Ad1. *Kinet. Catal.* **2001**, *42*, 1-22.

(2) R. Cortright, R. Davda and J. A. Dumesic: Hydrogen from Catalytic Reforming of Biomass-Derived Hydrocarbons in Liquid Water. *Nature* **2002**, *418*, 964-967.

(3) J. Zheng, D. A. Cullen, R. V. Forest, J. A. Wittkopf, Z. Zhuang, W. Sheng, J. G. Chen and Y. Yan: Platinum–Ruthenium Nanotubes and Platinum–Ruthenium Coated Copper Nanowires as Efficient Catalysts for Electro-Oxidation of Methanol. *ACS Catal.* **2015**, *5*, 1468-1474.

(4) S. E. Voltz, C. R. Morgan, D. Liederman and S. M. Jacob: Kinetic Study of Carbon Monoxide and Propylene Oxidation on Platinum Catalysts. *Ind. Eng. Chem. Prod. Res. Dev.* **1973**, *12*, 294-301.

(5) H. A. Gasteiger, S. S. Kocha, B. Sompalli and F. T. Wagner: Activity Benchmarks and Requirements for Pt, Pt-Alloy, and Non-Pt Oxygen Reduction Catalysts for Pemfcs. *Appl. Catal., B* **2005**, *56*, 9-35.

(6) R. Burch, J. Breen and F. Meunier: A Review of the Selective Reduction of No X with Hydrocarbons under Lean-Burn Conditions with Non-Zeolitic Oxide and Platinum Group Metal Catalysts. *Appl. Catal., B* **2002**, *39*, 283-303.

(7) Goswami, D. Y.; Kreith, F.: *Handbook of energy efficiency and renewable energy*; Crc Press, 2007.

(8) C. Wang, H. Daimon and S. Sun: Dumbbell-Like Pt− Fe3o4 Nanoparticles and Their Enhanced Catalysis for Oxygen Reduction Reaction. *Nano Lett.* **2009**, *9*, 1493-1496.

(9) C. Wang, M. Chi, D. Li, D. Strmcnik, D. Van der Vliet, G. Wang, V. Komanicky, K.-C. Chang, A. P. Paulikas and D. Tripkovic: Design and Synthesis of Bimetallic Electrocatalyst with Multilayered Pt-Skin Surfaces. *J. Am. Chem. Soc.* **2011**, *133*, 14396-14403.

(10) C. Wang, D. Van der Vliet, K. L. More, N. J. Zaluzec, S. Peng, S. Sun, H. Daimon, G. Wang, J. Greeley and J. Pearson: Multimetallic Au/Fept3 Nanoparticles as Highly Durable Electrocatalyst. *Nano Lett.* **2010**, *11*, 919-926.

(11) V. R. Stamenkovic, B. Fowler, B. S. Mun, G. Wang, P. N. Ross, C. A. Lucas and N. M. Marković: Improved Oxygen Reduction Activity on Pt3ni (111) Via Increased Surface Site Availability. *Science* **2007**, *315*, 493-497.

(12) B. Lim, M. Jiang, P. H. Camargo, E. C. Cho, J. Tao, X. Lu, Y. Zhu and Y. Xia: Pd-Pt Bimetallic Nanodendrites with High Activity for Oxygen Reduction. *Science* **2009**, *324*, 1302-1305.

(13) R. Narayanan and M. A. El-Sayed: Shape-Dependent Catalytic Activity of Platinum Nanoparticles in Colloidal Solution. *Nano Lett.* **2004**, *4*, 1343-1348.

(14) N. Markovic, H. Gasteiger and P. N. Ross: Kinetics of Oxygen Reduction on Pt (Hkl) Electrodes: Implications for the Crystallite Size Effect with Supported Pt Electrocatalysts. *J. Electrochem. Soc.* **1997**, *144*, 1591-1597.

(15) T. Cochell and A. Manthiram: Pt@ Pd X Cu Y/C Core–Shell Electrocatalysts for Oxygen Reduction Reaction in Fuel Cells. *Langmuir* **2012**, *28*, 1579-1587.

(16) V. Jalan and E. Taylor: Importance of Interatomic Spacing in Catalytic Reduction of Oxygen in Phosphoric Acid. *J. Electrochem. Soc.* **1983**, *130*, 2299-2302.

(17) A. Stassi, C. D'urso, V. Baglio, A. Di Blasi, V. Antonucci, A. Arico, A. C. Luna, A. Bonesi and W. Triaca: Electrocatalytic Behaviour for Oxygen Reduction Reaction of Small Nanostructured Crystalline Bimetallic Pt–M Supported Catalysts. *J. Appl. Electrochem.* **2006**, *36*, 1143-1149.

(18) J. R. Kitchin, J. K. Nørskov, M. A. Barteau and J. Chen: Role of Strain and Ligand Effects in the Modification of the Electronic and Chemical Properties of Bimetallic Surfaces. *Phys. Rev. Lett.* **2004**, *93*, 156801.

(19) M. Shao, P. Liu, J. Zhang and R. Adzic: Origin of Enhanced Activity in Palladium Alloy Electrocatalysts for Oxygen Reduction Reaction. *J. Phys. Chem. B* **2007**, *111*, 6772-6775.

(20) P. Strasser, S. Koh, T. Anniyev, J. Greeley, K. More, C. Yu, Z. Liu, S. Kaya, D. Nordlund and H. Ogasawara: Lattice-Strain Control of the Activity in Dealloyed Core–Shell Fuel Cell Catalysts. *Nat. Chem.* **2010**, *2*, 454-460.

(21) T. Toda, H. Igarashi, H. Uchida and M. Watanabe: Enhancement of the Electroreduction of Oxygen on Pt Alloys with Fe, Ni, and Co. *J. Electrochem. Soc.* **1999**, *146*, 3750-3756.

(22) B. Hammer and J. K. Nørskov: Theoretical Surface Science and Catalysis—Calculations and Concepts. *Adv. Catal.* **2000**, *45*, 71-129.

(23) S.-I. Choi, S. Xie, M. Shao, J. H. Odell, N. Lu, H.-C. Peng, L. Protsailo, S. Guerrero, J. Park and X. Xia: Synthesis and Characterization of 9 Nm Pt–Ni Octahedra with a Record High Activity of 3.3 a/Mgpt for the Oxygen Reduction Reaction. *Nano Lett.* **2013**, *13*, 3420-3425.

(24) J. K. Nørskov, J. Rossmeisl, A. Logadottir, L. Lindqvist, J. R. Kitchin, T. Bligaard and H. Jonsson: Origin of the Overpotential for Oxygen Reduction at a Fuel-Cell Cathode. *J. Phys. Chem. B* **2004**, *108*, 17886-17892.

(25) L. Ma, C. Wang, B. Y. Xia, K. Mao, J. He, X. Wu, Y. Xiong and X. W. D. Lou: Platinum Multicubes Prepared by Ni2+-Mediated Shape Evolution Exhibit High Electrocatalytic Activity for Oxygen Reduction. *Angew. Chem.* **2015**, *127*, 5758-5763.

(26) A. Von Weber, E. T. Baxter, H. S. White and S. L. Anderson: Cluster Size Controls Branching between Water and Hydrogen Peroxide Production in Electrochemical Oxygen Reduction at Pt N/Ito. *J. Phys. Chem. C* **2015**, 119, 11160-11170.

(27) J. Park, L. Zhang, S.-I. Choi, L. T. Roling, N. Lu, J. A. Herron, S. Xie, J. Wang, M. J. Kim and M. Mavrikakis: Atomic Layer-by-Layer Deposition of Platinum on Palladium Octahedra for Enhanced Catalysts toward the Oxygen Reduction Reaction. *ACS Nano* **2015**, *9*, 2635-2647.

(28) C. Zhu, S. Guo and S. Dong: Pdm (M= Pt, Au) Bimetallic Alloy Nanowires with Enhanced Electrocatalytic Activity for Electro-Oxidation of Small Molecules. *Adv. Mater.* **2012**, *24*, 2326-2331.

(29) Y. Sun and Y. Xia: Shape-Controlled Synthesis of Gold and Silver Nanoparticles. *Science* **2002**, *298*, 2176-2179.

(30) B. Wiley, Y. Sun, J. Chen, H. Cang, Z.-Y. Li, X. Li and Y. Xia: Shape-Controlled Synthesis of Silver and Gold Nanostructures. *MRS Bull.* **2005**, *30*, 356-361.

(31) V. Bansal, A. P. O'Mullane and S. K. Bhargava: Galvanic Replacement Mediated Synthesis of Hollow Pt Nanocatalysts: Significance of Residual Ag for the H 2 Evolution Reaction. *Electrochem. Commun.* **2009**, *11*, 1639-1642.

(32) A. I. Kryukov, A. L. Stroyuk, N. N. Zin'chuk, A. V. Korzhak and S. Y. Kuchmii: Optical and Catalytic Properties of Ag2s Nanoparticles. *J. Mol. Catal. A: Chem.* **2004**, *221*, 209-221.

(33) C. M. Cobley, S. E. Skrabalak, D. J. Campbell and Y. Xia: Shape-Controlled Synthesis of Silver Nanoparticles for Plasmonic and Sensing Applications. *Plasmonics* **2009**, *4*, 171-179.

(34) National Institute of Standards and Technology: *NIST X-ray Photoelectron Spectroscopy Database*, version 4.1 [online] **2012** http://srdata.nist.gove/xps/ (accessed March 10, 2016).

(35) M. Nesselberger, S. Ashton, J. C. Meier, I. Katsounaros, K. J. Mayrhofer and M. Arenz: The Particle Size Effect on the Oxygen Reduction Reaction Activity of Pt

Catalysts: Influence of Electrolyte and Relation to Single Crystal Models. *J. Am. Chem. Soc.* **2011**, *133*, 17428-17433.

(36) T. Ralph, G. Hards, J. Keating, S. Campbell, D. Wilkinson, M. Davis, J. St-Pierre and M. Johnson: Low Cost Electrodes for Proton Exchange Membrane Fuel Cells Performance in Single Cells and Ballard Stacks. *J. Electrochem. Soc.* **1997**, *144*, 3845-3857.

(37) T. Schmidt, H. Gasteiger, G. Stäb, P. Urban, D. Kolb and R. Behm: Characterization of High-Surface-Area Electrocatalysts Using a Rotating Disk Electrode Configuration. *J. Electrochem. Soc.* **1998**, *145*, 2354-2358.

(38) C. Zinola, A. C. Luna, W. Triaca and A. Arvia: Electroreduction of Molecular Oxygen on Preferentially Oriented Platinum Electrodes in Acid Solution. *J. Appl. Electrochem.* **1994**, *24*, 119-125.

(39) Y. Sun and Y. Xia: Alloying and Dealloying Processes Involved in the Preparation of Metal Nanoshells through a Galvanic Replacement Reaction. *Nano Lett.* **2003**, *3*, 1569-1572.

(40) L. Au, X. Lu and Y. Xia: A Comparative Study of Galvanic Replacement Reactions Involving Ag Nanocubes and Aucl2− or Aucl4−. *Adv. Mater. (Deerfield Beach, Fla.)* **2008**, *20*, 2517.

(41) M. H. Kim, X. Lu, B. Wiley, E. P. Lee and Y. Xia: Morphological Evolution of Single-Crystal Ag Nanospheres During the Galvanic Replacement Reaction with Haucl4†. *J. Phys. Chem. C* **2008**, *112*, 7872-7876.

(42) S. E. Skrabalak, J. Chen, Y. Sun, X. Lu, L. Au, C. M. Cobley and Y. Xia: Gold Nanocages: Synthesis, Properties, and Applications. *Acc. Chem. Res.* **2008**, *41*, 1587-1595.

(43) V. Stamenkovic, T. Schmidt, P. Ross and N. Markovic: Surface Composition Effects in Electrocatalysis: Kinetics of Oxygen Reduction on Well-Defined Pt3ni and Pt3co Alloy Surfaces. *J. Phys. Chem. C* **2002**, *106*, 11970-11979.

(44) N. Wakabayashi, M. Takeichi, M. Itagaki, H. Uchida and M. Watanabe: Temperature-Dependence of Oxygen Reduction Activity at a Platinum Electrode in an Acidic Electrolyte Solution Investigated with a Channel Flow Double Electrode. *J. Electroanal. Chem.* **2005**, *574*, 339-346.

(45) L. H. Brickwedde: Properties of Aqueous Solutions of Perchloric Acid. *Natl. Bur. Stand.* **1949**, *42*, 309.

(46) Downs, R.T. and Hall-Wallace, M. The American Mineralogist Crystal Structure Database. American Mineralogist **2003**, 88, 247-250.

APPENDIX A

COLLABORATOR CONTRIBUTIONS

All of the theoretical work presented in this thesis was the result of collaborative efforts. This appendix gives credit to all collaborators for their respective contributions.

A.1. The Formation of Hot Spots Between Cubic Dimers

Dr. Nasrin Hooshmand executed the initial calculations for both the Au-Au and Ag-Ag dimers at all separation distances, polarization directions, and wavelengths presented in chapter 2. I was responsible for aiding in modifing the publicly offered DDSCAT 6.1 code before execution and also analyzing all raw data. I was also responsible for the final preparation of all content found within the submitted manuscript.

A.2. The Development of New Plasmonic Modes at Short Separation Distances

Dr. Nasrin Hooshmand aided in executing supplemental calculations for the Ag-Ag 2 nm dimer; however, I completed all calculations and analyzed all raw data presented within chapter 3. I was also responsible for the final preparation of all content found within the submitted manuscript.

A.3. Plasmonic Spectroscopy of Face-to-Face Silver Nanocube Dimers in Solution and on a Substrate

Dr. Nasrin Hooshmand executed all calcualtions of the face-to-face Ag-Ag dimer on various substrates and in various surrounding media. Both Dr. Nasrin and myself analyzed all of the data presented within chapter 4. I was also responsible for the final preparation of all content found within the submitted manuscript.

A.4. The Sensitivity of the Distance Dependent Plasmonic Coupling Between Two Nanocubes to their Orientation: Edge-to-Edge vs Face-to-Face

Dr. Nasrin Hooshmand executed all of the calculations pertaining to Ag-Ag nanocube dimers oriented in either a face-to-face or edge-to-edge manor. I aided in developing the input files for the two different dimer orientations as well as analyzed all of the raw data. I was also responsible for the final preparation of all content found within the submitted manuscript.

APPENDIX B

THEORETICAL INVESTIGATIONS

B.1. Mie Theory

When the dimensions of a spherical particle are reduced below 100 nm, it can be assumed that the size of the particle is in fact much smaller than the various wavelengths of light that are found with the Ultra-Violet (UV) and visible light portion of the electromagnetic spectrum ($2r \ll \lambda$, where r is the radius of the particle). Under this assumption the phase of the electric field component of the incident electromagnetic field interacting with the particle can be considered to be constant. This is considered the quasistatic approximation (Figure B.1)[1].

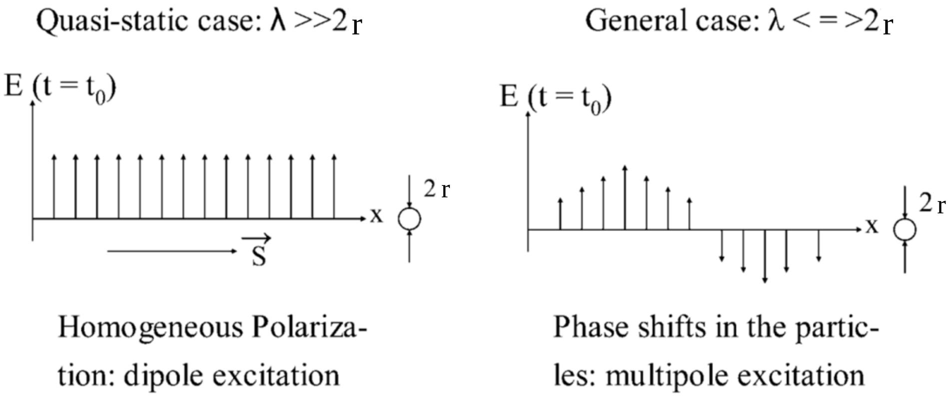

Figure B.1. A schematic describing conditions which satisify the quasistatic approximation (left) and those which this approximation no longer holds (right). Without a uniform polarization of the incident electric field, the optical response of a metal nanoparticle becomes increasingly complicated.

If the polarizability of the material is appropriate, then this uniform electric field subsequently induces a uniform polarization of the free conduction band electrons within the particle. The resultant polarization of the particle generates an electronic dipole moment, μ, which can be described as $\mu = \varepsilon_m \alpha \mathbf{E}_0$[1]; where ε_m is the dielectric permittivity of the surrounding medium, α is the dipole polarizability of the sphere, and $\mathbf{E}_0$ is the electric field vector of the incident electromagnetic field. The dipole polarizability of a sphere can be mathematically determined through the solution of the Laplace's equation and takes the form[1]:

$$\alpha = (3\varepsilon_0 V)\frac{\varepsilon-\varepsilon_m}{\varepsilon+2\varepsilon_m} \qquad 1$$

where V is the volume of the individual particle, ε_0 is the vacuum permittivity, ε is the wavelength dependent dielectric permittivity of the metal. It is important to note that a LSPR is not supported by all materials, however, both gold and silver are two materials which exhibit strong plasmonic properties[2, 3]. The dielectric permittivity of silver and gold is both complex with both a real and imaginary component ($\varepsilon = \varepsilon_R + i\varepsilon_I$). Furthermore, it is assumed that the dielectric permittivity of the surrounding medium is only real constant without a complex component or wavelength dependence within this region[1].

Under these conditions it is clear from equation 1 that the maximum polarizability of a sphere, and the generation of a LSPR, will occur when the denominator, $\varepsilon + 2\varepsilon_m$, approaches 0. Here the imaginary component of the dielectric permittivity is considered to be small for the UV, visible, and near-IR region of the electromagnetic spectrum for both silver and gold. Therefore, the position of a LSPR will be determined by the wavelength of the incident electromagnetic field which satisfies the condition:

$$\varepsilon = -2\varepsilon_m \qquad 2$$

Luckily for both silver and gold the dielectric permittivity of most common solvents is greater than zero and the dielectric permittivity of both metals is negative in most regions of the electromagnetic spectrum. As a result, the generation of a strong LSPR is possible for these materials and can occur throughout the UV, visible, and near-IR region of the electromagnetic spectrum.

B.2. The Plasmon Ruler Equation

Under the quasistatic approximation the polarization of the electrons within a plasmonic nanoparticle is assumed to be uniform. Subsequently, for a system containing two particles a uniform dipole would be formed by each nanoparticle. As a result, the coupling between two nanoparticles in close proximity to each other is treated as the interaction of two individual dipoles across a set separation distance. The electric dipole moment, μ, produced for an individual nanoparticle can be expressed as a function of the incident electric field, E_0, and takes the form[4]:

$$\mu = \alpha\varepsilon_m E_0 \qquad 3$$

When a second electric dipole/nanoparticle is in close proximity to the first, the electric field felt by the first nanoparticle will now become a function of the incident electric field as well as the near-field from the electric dipole of the neighboring nanoparticle. This composite electric field, $E^{'}$, can be expressed in terms of the uniform incident electric field and the distance dependent electric field of the second nanoparticle[4]:

$$E' = E + \frac{\kappa\mu'}{4\pi\varepsilon_m\varepsilon_0 d^3} \qquad 4$$

where κ is an orientation factor that is dependent on the alignment of the dipoles (commonly either parallel or perpendicular) and d is the distance between the two dipoles (taken as the distance between the center of each particle). From equation 3 and 4, the net polarizability of the two-particle system can be given as:

$$\alpha' = \frac{\alpha}{1-\left(\frac{\kappa\alpha}{4\pi\varepsilon_0 d^3}\right)} \qquad 5$$

Substituting the polarizability of an individual spherical nanoparticle ($V = \pi D^3/6$) into the polarizability of the two particle system takes the form:

$$\alpha' = \frac{4\pi\varepsilon_0 D^3(\varepsilon-\varepsilon_m)}{\varepsilon\left(8-\left(\frac{\kappa D^3}{d^3}\right)\right)+\varepsilon_m\left(16+\left(\frac{\kappa D^3}{d^3}\right)\right)} \qquad 6$$

As previously developed for an individual nanoparticle in Mie theory, the condition which generates the maximum polarizability of this two particle system can be determined. Again, the polarizability of the system reaches a maximum as the denominator approaches 0:

$$\varepsilon = -\varepsilon_m\left(\frac{2\left(\frac{d}{D}\right)^3+\frac{\kappa}{8}}{\left(\frac{d}{D}\right)^3-\frac{\kappa}{8}}\right) \qquad 7$$

Since the dielectric permittivity of both silver and gold is wavelength dependent the energy at which the dielectric permittivity of the metal approaches equation 7 will generate a LSPR. For gold specifically, this would take the form[4]:

$$\lambda = 464.6 + 14.3\varepsilon_m\left(\frac{2\left(\frac{d}{D}\right)^3+\frac{\kappa}{8}}{\left(\frac{d}{D}\right)^3-\frac{\kappa}{8}}\right) \qquad 8$$

Here it can be seen that the conditions for resonant excitation of the LSPR are clearly dependent on the distance between the two nanoparticles normalized to the size of the individual nanoparticle. As a result, the magnitude of the shift in the LSPR energy, with respect to an isolated nanoparticle, can be treated as a measure of the interaction between the two plasmonic nanoaprticles and thus the coupling behavior. If the distance between the surfaces of the two interacting nanoparticles, s, is defined as s = d – D then the wavelength of the LSPR for a gold sphere can be written in terms of the normalized separation distance (s/D) between two nanoparticles:

$$\lambda = 464.6 + 14.3\varepsilon_m \left(\frac{2\left(\frac{s}{D}+1\right)^3 + \frac{\kappa}{8}}{\left(\frac{s}{D}+1\right)^3 - \frac{\kappa}{8}} \right) \qquad 9$$

Assuming an infinite separation, (s/D → ∞), for an isolated nanoparticle the fractional shift in the SPR position with respect to an individual nanoparticle ($\Delta\lambda/\lambda_0$) in terms of the normalized separation distance of two nanoparticles can be expressed as:

$$\frac{\Delta\lambda}{\lambda_0} = \frac{42.9\varepsilon_m}{\left(4\left(\frac{s}{D}+1\right)^3 - 1\right)(464.6 + 28.6\varepsilon_m)} \qquad 10$$

This relationship has been shown to be very nearly approximated by a first order exponential decay behavior, $y = Ae^{-(x/\tau)}$. Consequently, the near-field coupling behavior of plasmonic nanoparticle ($\Delta\lambda/\lambda_0$) is expected to follow an exponential decay dependence on the normalized separation distance known as the plasmon ruler equation[4]:

$$\frac{\Delta\lambda}{\lambda_0} = Ae^{\left(\frac{-\frac{s}{D}}{\tau}\right)} \qquad 11$$

where the pre-exponential factor, A, and decay constant, τ, can be used to qualitatively characterize both the near field coupling strength and decay length of a two particle system respectively.

B.3. References

(1) S. K. Ghosh and T. Pal: Interparticle Coupling Effect on the Surface Plasmon Resonance of Gold Nanoparticles: From Theory to Applications. *Chem. Rev.* **2007**, *107*, 4797-4862.

(2) E. Hao and G. C. Schatz: Electromagnetic Fields around Silver Nanoparticles and Dimers. *J. Chem. Phys.* **2004**, *120*, 357-366.

(3) S. Link and M. A. El-Sayed: Spectral Properties and Relaxation Dynamics of Surface Plasmon Electronic Oscillations in Gold and Silver Nanodots and Nanorods. *J. Phys. Chem. B* **1999**, *103*, 8410-8426.

(4) P. K. Jain, W. Huang and M. A. El-Sayed: On the Universal Scaling Behavior of the Distance Decay of Plasmon Coupling in Metal Nanoparticle Pairs: A Plasmon Ruler Equation. *Nano Lett.* **2007**, *7*, 2080-2088.

APPENDIX C

PLATINUM-SILVER ALLOY NANOCAGE CATALYSTS TOWARDS THE REDUCTION OF HEXACYANOFERRATE

C.1. Motivation

Platinum based materials are highly utilized catalysts. These materials are versatile catalysts which can catalyze a wide range of reactions including catalytic reforming[1-2], oxidation[3-4], and reduction[5-6]. However, according to the most recent mineral commodity summary platinum is still the most expensive platinum-group metal[7]. As a result, the implementation of platinum based catalytic materials in any new industrial applications has been limited by the resultant cost of such devices[5]. This increasing financial burden has driven recent research efforts towards two major aims: increasing the specific activity of platinum towards a given reaction and reducing the effective platinum loading within the material.

A promising new approach towards addressing these two aims has been the development of platinum based nanomaterials. Firstly, reducing the size of the platinum catalyst will result in an increased surface area to volume ratio which will inherently reduce the platinum loading for these catalysts and thus reduce cost. However, simply reducing the size of the material is not the only way to reduce the cost of these materials. Within the last fifteen years, the synthetic advancements of platinum nanoparticles and their alloys have led to a wide variety of bi-metallic[8-11] and tri-metallic[12-14] catalysts with interesting shapes[15-19] and surface structures. Along with the synthetic development of new platinum based nanomaterials an increased understanding of the intimate relationship between either the shape or composition of the nanocatalyst and its catalytic activity has evolved[20-26]. From this we now see that the d-band position of the catalyst material, and thus the adsorption and desorption energetics of the reacting material on the surface of the catalyst is a vital component of the catalytic activity of these materials.

The d-band position and adsorption characteristics of a platinum nanomaterial have recently been shown to be effected by both the identity of the exposed lattice planes of the material and the formation of a platinum alloy. In 2004 initial reports from El-Sayed and coworkers[27] indicated a correlation between the shape of solid platinum nanocatalysts and the catalytic activity of these particles towards the reduction of ferricyanide. It was found that the catalytic activity of the catalyst was correlated to a percentage of surface atoms present which occupied unsaturated edge/corner positions. This relationship was further explored theoretically by Lu and Meng[28] who found that the activation energy for electron transfer reactions on top of platinum nanomaterials is directly related to the identity of the exposed lattice planes. Many recent studies have been conducted on the catalytic activity of platinum based nanomaterials towards the oxygen reduction reaction. Again it was suggested that the identity of the exposed lattice planes of the catalyst material directly affect oxygen adsorption and thus catalytic activity[29-32].

These recent studies have not only focused on the exposed lattice planes of the nanocatalys, but have also investigated the effect of alloy formation on catalytic activity[9,33-34]. Theoretical investigations of the core level binding energy of the platinum within Pt-Ru and Pt-Co alloys and the corresponding adsorption energies of CO on the surface of these alloys was conducted by Watanabe and co-workers[35]. In 2006 it was found that a reduction in the work function of the Pt alloy compared to pure Pt resulted in a subsequent downshift in the d-band position of the alloy. This downshift in the d-band position led to a higher binding energy for the core level Pt 4f electrons and a reduction in the adsorption energy of CO on the surface of the alloy. Similarly a reduction in the adsorption energy of oxygen species has also been attributed to the formation of a platinum alloy. This reduction has been shown to result in an increase in the catalytic activity of platinum alloy catalysts towards the oxygen reduction reaction[5]. Due to this apparent correlation between the catalytic activity of a catalyst and its shape and composition, the need for a versatile synthetic approach with precise control over these two characteristics is vital.

Herein we have utilized the galvanic replacement reaction[36] (GRR) to synthesize a set of platinum-silver alloy nanocage catalysts that exhibit a high degree of control over both their shape and composition. Previous reports which have utilized methods of either co-reduction[37-38] or sequential reduction[39-40] have shown to be very useful in the development of new platinum based catalysts with a variety of different alloy compositions. However, many of these new catalysts exhibit poor shape definition and utilize high calcination temperatures to induce metal-metal diffusion[12] and alloy formation within the nanomaterial. Conversely the GRR is a highly desirable option due to the extremely mild synthetic conditions and the high degree of control over both the shape and composition of the resultant catalyst.

C.2. Experimental Methods

The platinum-silver nanocages were synthesized using the galvanic replacement reaction[46]. First, silver nanocubes of appropriate edge length were synthesized and used as nanocage templates. A variation of the common polyol reduction synthesis[47] was used in order to both quickly and accurately prepare the silver nanocube templates. Once the Ag nanocubes were synthesized they were diluted to five times the original volume and cleaned by centrifugation. Then, a solution of potassium tetrachloroplatinate was slowly added to the cleaned Ag nanocube solution and the platinum content was varied by the total volume of potassium salt which was added.

The solid platinum nanoparticles were synthesized by the polyol reduction of both potassium tetrachhloroplatinate (K_2PtCl_4) and chloroplatinic acid (H_2PtCl_6) using ethylene glycol as the reducing agent. After synthesis and subsequent cleaning, all nanoparticles were structurally characterized by TEM. The platinum-silver nanocages were characterized further by STEM-EDX mapping and XRD. All experimental activation energy data was conducted with an Ocean Optics UV-Vis spectrometer equipped with a halogen/deuterium lamp and a temperature/stir controlled sample holder. The rate constant for each platinum-silver nanocage catalyst was determined at 20, 30, and 40˚C and the subsequent activation energy was calculated.

C.2.1. Synthesis

Pt nanocages were synthesized using the galvanic replacement reaction. First, silver nanocubes of appropriate edge length were synthesized and used as templates. A variation of the common polyol reduction synthesis was used in order to both quickly and accurately prepare the silver nanocube templates. Trace amounts of Na_2S were used in order to catalyze the reduction of Ag ions present in solution and begin the nucleation process. The increased rate of reduction of Ag ions, and, consequently, the rate of nucleation allows for the dominant formation of single crystal Ag seeds. Along with the use of the correct capping agent, the quick nucleation facilitates the dominant formation of the desired cubic shape.

C.2.1.1. Silver Nancube Template

In a 100ml round bottom flask, 20 ml of ethylene glycol (EG) was heated at 145℃ for 1 hour. After heating the EG for 1 hour, 5.00 ml of a 0.439 M polyvinylpyrrolidone (PVP 55k, molarity in terms of monomer) solution in EG was added and the temperature of the solution was allowed to increase to 154℃. At this temperature, 0.30 ml of a 3.48 mM Na_2S solution in EG was added to the reaction mixture and followed by 5.00 ml of a 141 mM $AgNO_3$ solution in EG. The solution was stirred briefly until the solution turned an auburn color, at which point the single crystal silver seeds are produced. Growth of these particles into nanocubes was achieved through careful monitoring of both the stirring and solution temperature until a turbid green solution was produced.

C.2.1.2. Platinum-Silver Nanocage

In order to synthesize the Pt nanocages, the galvanic replacement method was used. First, the silver nanocubes were diluted to five times the original volume with 18 MΩ deionized (DI) water. The particles were then cleaned by centrifugation at 4050rpm for 10 minutes and re-dispersed in DI water. A 5.08 mM solution of potassium tetrachloroplatinate (K_2PtCl_4) was then added to the silver nanocube solution in 0.2ml increments every five minutes under constant stirring. The platinum content of the platinum-silver nanocages was controlled by varying the total volume of platinum salt that was added to the template particle solution. Aliquots of the platinum-silver nanocage synthesis solution were removed once the desired volume of platinum salt was added.

Each aliquot was placed in a shaker at room temperature overnight and subsequently cleaned by centrifugation at 4050 rpm for 10 minutes and re-dispersed in DI water.

C.2.1.3. Solid Platinum Nanoparticle

Solid platinum nanoparticles were synthesized by the polyol reduction of both potassium tetrachhloroplatinate (K_2PtCl_4) and chloroplatinic acid (H_2PtCl_6) using ethylene glycol as the reducing agent. In a 50 ml round bottom flask 30 ml of EG was heated at 148 ℃. After the EG was heated for roughly 25 minutes, 1.0 g of polyvinylpyrolidone (PVP, 55k) was added and allowed to fully dissolve. When the solution of EG had been heating for 30 minutes, 1 ml of a 0.010 M $AgNO_3$ solution was added and allowed to stir. A yellow color ensued thus indicating the formation of silver seed particles. The stir speed was increased and a 0.012 M K_2PtCl_4 solution was added dropwise until the color of the solution became black. The temperature was then raised to 180℃ and 5 ml of a 0.120 M H_2PtCl_6 solution was added dropwise (roughly 0.4 ml/min). The resulting solution was left to stir for 10 minutes and then allowed to cool. Cleaning of the Pt particles was done through first diluting the Pt solution to 3 times its original volume with an acetone:water mixture (acetone:water ratio dependent on the size of the particle) and centrifuged at 13,000 rpm for 15 minutes.

C.2.2. Characterization

C.2.2.1. Transmission Electron Microscopy

An aqueous dispersion of particles was deposited on a formvar/carbon film covered grid and the shape and size distribution of the as synthesized nanocatalysts was determined by transmission electron microscopy (TEM). A JEOL 100CX TEM was used with an accelerating voltage of 100 kV and all images were analyzed with image J software.

C.2.2.2. X-ray Energy Dispersive Spectroscopy

The surface composition of all platinum-silver nanocages was analyzed by STEM-EDX. A Tecnai F30 high resolution TEM equipped with both an S/TEM mode and EDX detector was used to obtain all EDX images in this study. An aqueous dispersion of particles was deposited on a formvar/carbon film covered grid and dried prior to analysis. A minimum of 50 particles were analyzed to determine the average platinum content of all platinum-silver nanocages. In order to obtain the EDX map of each platinum-silver nanocage, a single nanocage particle whose composition was representative of the average platinum content of the sample was analyzed. The pixel resolution utilized for each images was roughly 1 nm per pixel.

C.4.2.3. X-ray Diffraction

The physical structure of the catalysts was also characterized by a PANAnaltical X'Pert Pro X-ray Diffractometer. All samples were cleaned and transferred into an isopropanol solution. Then a small volume of the cleaned particle solution was deposited on a glass substrate using a Chemat Technology KW4A spin coater prior to XRD analysis. A maximum of three aliquots were deposited on the glass substrate for each sample in order to limit stacking of particles on each substrate. A scan speed of 0.0005 °/s was used for all samples.

C.2.2.4. Activation Energy

All experimental activation energy data was conducted with an Ocean Optics UV-Vis spectrometer equipped with a halogen/deuterium lamp and a temperature/stir controlled sample holder. The rate constant for each platinum-silver nanocage catalyst was determined at 20, 30, and 40˚C and the subsequent activation energy was calculated. For each trial roughly 10 µl of each catalyst was added to 1 ml of a 0.1M $NaBH_4$ in 0.1M NaOH solution. This solution was allowed to mix under constant stirring at 200 rpm and equilibrate at either 20, 30, or 40˚C. Then 10 µl of a 0.01M hexacyanoferrate solution was added to the alkaline catalyst/BH_4^- solution. A decrease in the extinction peak of hexacyanoferrate was monitored as a function of time. Due to the 100:1 mol ratio of borohydride to hexacyanoferrate pseudo-first order kinetics were assumed during the analysis of all data. A sample set of kinetic data shown in Figure C. supports this pseudo-first order assumption. At least three values for the rate constant were determined for every temperature and the average value is reported herein.

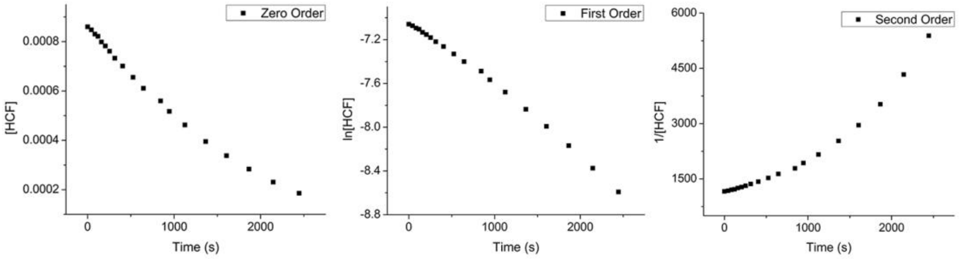

Figure C.1. Raw kinetic data of the reduction of hexacyanoferrate (HCF) plotted as either a zero order (left), first order (middle), second order (right) reaction.

C.3. Results and Discussion

C.3.1 Synthesis

In light of recent studies highlighting the activity dependence of platinum alloy catalysts on the lattice plane that is exposed to the reacting material, we have utilized a nanocube template in order to investigate the catalytic activity of a set of platinum-silver alloys with vary platinum content but consistent (100) lattice plane exposure. A silver nanocube template was synthesized using a modified polyol reduction in the presence of polyvinylpyrrolidone (Figure C.2A). The resulting nanocube was 44.8 nm (± 4.9 nm) and was then utilized as the template for three platinum-silver nanocages with varying platinum content (Figure C.2B-D). Here it is clear to see the advantage of using the galvanic replacement reaction (GRR) due to the precise control of the shape of the silver nanocube template and the retention of this original shape for all platinum-silver nanocages.

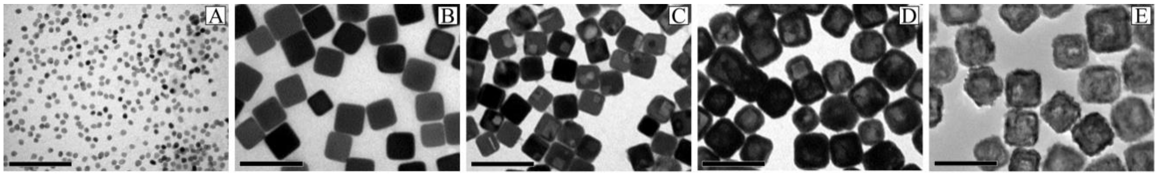

Figure C.2. Transmission Electron Microscopy images of solid platinum nanoparticles (A), solid silver nanocubes (B), and the subsequent platinum-silver alloy nanocages Pt_6Ag_{94} (C), $Pt_{17}Ag_{83}$ (D), $Pt_{37}Ag_{63}$ (E). There is a slight loss of edge definition which occurs as the platinum content increases, however, the cubic shape of the silver template is clearly retained in all of the synthesized platinum-silver nanocages. All black scale bars represent 100 nm.

It is apparent that upon further incorporation of platinum into the structure of silver nanocubes there is a progressive removal of silver from the interior of the structure and a slight loss of edge definition of the cubic shape. However, the development of porosity within the nanocage structure, which is expected with a gold-silver nanocage, was not observed[41]. This porosity could be induced through post-synthetic etching of the residual silver within the structure[42-43], however this was not employed in order to preserve the dominant (100) lattice plane exposure of the cubic shape. The platinum content for all synthesized platinum-silver nanocages was determined by energy dispersive x-ray (EDX) analysis and the three different platinum-silver nanocages were found to have platinum contents ranging from 6% to 37% platinum (Table C.1).

Table C.1. Platinum Content of Synthesized Platinum-Silver Nanocages

Catalyst	**% Pt**
Pt_6Ag_{94} Nanocage	5.6 (± 2.2)
$Pt_{17}Ag_{83}$ Nanocage	17.4 (± 7.9)
$Pt_{37}Ag_{63}$ Nanocage	37.0 (±6.6)

The surface composition of each catalyst was also investigated using EDX mapping. The spatial distribution of platinum and silver for a single particle within each batch can be seen in Figure 2. The spatial distribution of platinum atoms present on the surface of the platinum-silver nanocage can be seen in red for Pt_6Ag_{94} (Figure C.3I), $Pt_{17}Ag_{83}$ (Figure C.3II), and $Pt_{37}Ag_{63}$ (Figure C.3III). For the Pt_6Ag_{94} nanocage, the EDX image suggests a relatively homogeneous dispersion of platinum on the particle. This suggests a spatially indiscriminant reduction of platinum on the surface of the silver template structure during the GRR, which facilitates a high utilization of the platinum on the exterior surface of the Pt_6Ag_{94} nanocage. As a result, implementation of the GRR for the synthesis of low platinum content alloys increases the percentage of platinum atoms on the surface of the particle which can consequently be available for catalysis. Upon further incorporation of platinum into the particle, it is evident from the EDX image for the silver content of each particle (blue) that the interior of the particle is slowly emptied. The composite image of each platinum-silver nanocage further suggests that as the platinum content increases the incorporation of platinum into the interior of the nanocage wall also increases resulting in a thickened platinum-silver alloy layer. This in turn could result in the incorporation of platinum atoms which will not be available for catalysis due to a lack of exposure to reacting material.

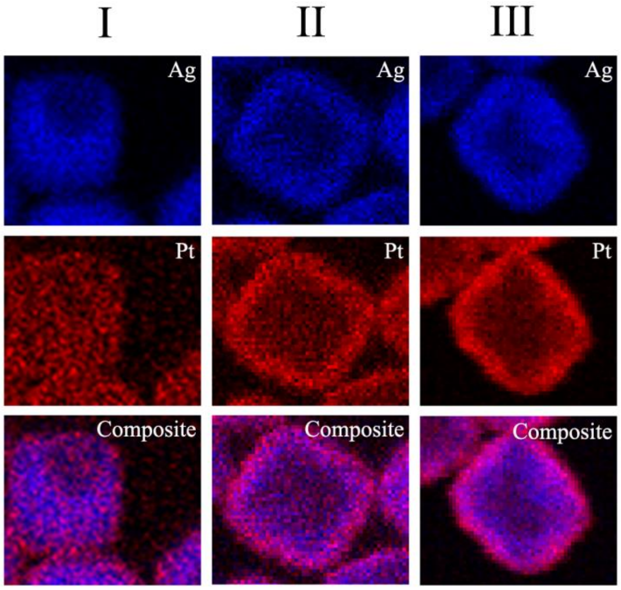

Figure C.3. Individual EDX images of the silver (blue) and platinum (red) content within Pt_6Ag_{94} (I), $Pt_{17}Ag_{83}$ (II), and $Pt_{37}Ag_{63}$ (III) nanocages. Both the silver and platinum content were combined to give a composite spatial distribution of the silver and platinum atoms present on the surface of each particle. There is an apparent spatial indiscrimination of platinum reduction on the surface of the silver nanocube template for the Pt_6Ag_{94} nanocage. This causes a high percentage of platinum atoms incorporated into the nanocage structure to be available on the surface for catalysis.

C.3.2. Lattice Plane Exposure

As mentioned previously, the incorporation of platinum into an alloy has led to increased catalytic activity for various reactions. It is important here to determine if the solid state structure of these platinum silver nanocages is consistent with a platinum-silver alloy or if a platinum skin is in fact formed on top of the silver nanocube template. In order to investigate the platinum-silver alloy formation x-ray diffraction was utilized.

Figure 3A shows that the XRD spectrum of the silver nanocube template is dominated by a single diffraction peak which corresponds to the (200) lattice plane. As expected from the TEM images of the platinum-silver nanocages, the XRD pattern corresponding to the Pt_6Ag_{94}, $Pt_{17}Ag_{83}$, and $Pt_{37}Ag_{63}$ also exhibit one major diffraction peak, which corresponds to the (200) lattice plane. There is a progressive shift in the position of the (200) diffraction peak to high angles as the platinum content within the nanocage increases, (Figure C.4B). This is an indication of the continued formation of a platinum-silver alloy surface. Along with a shift in the peak position of the (200) diffraction peak, there is a progressive broadening of the (200) peak itself. This has been previously shown to indicate an increased lattice strain within solid state structure of the particles and is expected for the formation of an alloy between silver and platinum due to the difference in lattice constants of the pure metals. Lastly, it is important to note that the exclusive (200) lattice plane termination that is observed for the silver nanocube template is retained for all platinum-silver alloy nanocages that were synthesized. This is important due to the differences in catalytic activity that can arise from the different lattice planes of a material.

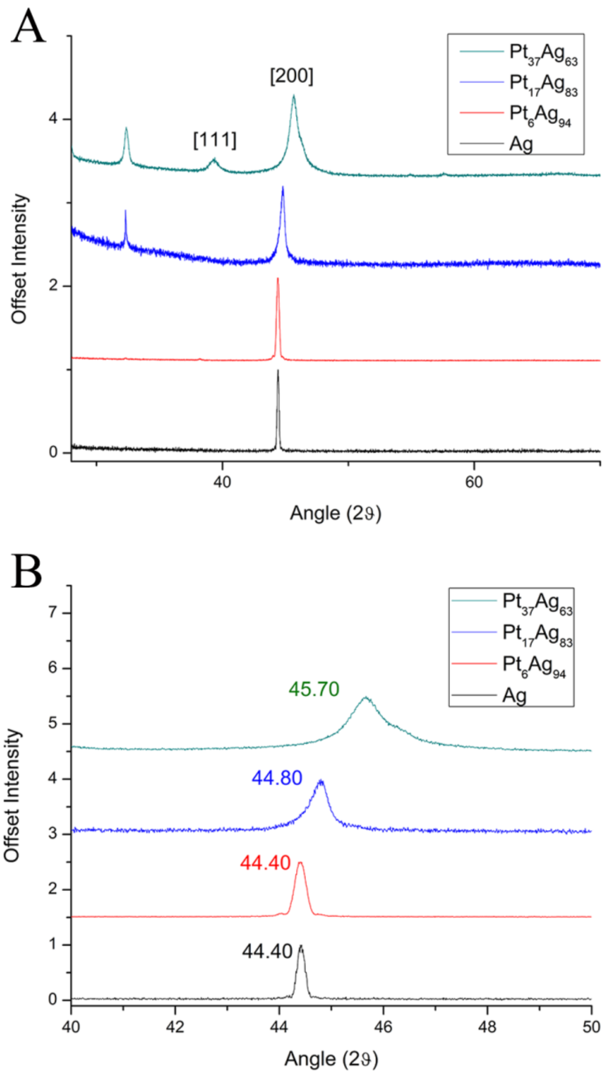

Figure C.4. (A) The XRD pattern for a silver nanocube (black), Pt_6Ag_{94} (red), $Pt_{17}Ag_{83}$ (blue), and $Pt_{37}Ag_{63}$ (green). (B) A zoomed in portion of the XRD pattern highlighting the gradual shift and broadening of the (200) diffraction peak. This shift is indicative of the formation of a platinum-silver alloy and the progressive broadening of the diffraction peak is indicative of the expected lattice strain that is induced by the mismatch between the lattice constants of the two metals.

C.3.3. Reduction of Hexacyanoferrate

The catalytic activity of Pt_6Ag_{94}, $Pt_{17}Ag_{83}$, and $Pt_{37}Ag_{63}$ was investigated by determining the activation energy of each catalyst towards the reduction of ferricyanide in the presence of alkaline sodium borohydride. This reaction has been previously used as an indication of the catalytic activity of platinum nanocatalysts[44]. The disappearance of a characteristic absorbance peak for ferricyanide was monitored over time with an Ocean Optics UV-Vis spectrometer equipped with a halogen/deuterium lamp and a temperature/stir controlled sample holder. Reaction conditions were set to assume first-order kinetics with respect to ferricyanide and the corresponding activation energy was determined for the reduction of ferricyanide in the presence of solid silver, solid platinum, and three platinum-silver alloy nanocage catalysts. Previous reports of the catalytic activity of platinum-silver, palladium-silver, and mixed platinum-palladium nanocages have observed a substantial difference in the frequency factors attributed to each catalyst[45]; however, here we do not see a statistically significant variation in the frequency factor calculated for each catalyst (Figure C.5).

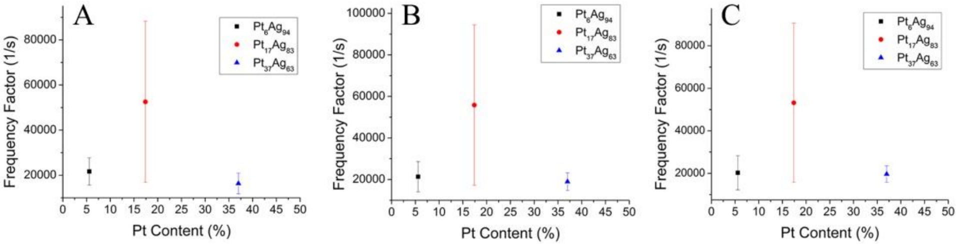

Figure C.5. The frequency factor was determined from the experimental kinetic data for each catalyst at 20 °C (A), 30 °C (B), and 40 °C (C). The frequency factor is not affected by the platinum content of the catalyst.

As seen in Figure C.6, it is evident that solid platinum nanoparticles exhibit a lower activation energy than solid silver nanocubes displaying activation energies of 21.1 KJ/mol and 49.1 KJ/mol respectively. Furthermore, the activation energy of the reduction of ferricyanide when platinum-silver nanocage catalysts are present is lower than solid platinum nanoparticles by a factor of 2 and solid silver nanoparticles by a factor of 4.5.

As stated previously the formation of a platinum alloy has been shown to affect the d-band position and subsequent adsorption of reacting material on the surface of the alloy. Due to the difference in work functions of both pure silver and platinum, it is expected that the platinum-silver alloy nanocage will exhibit a lower work function than pure platinum and thus a downshifted d-band position whose exact position would be dependent on alloy composition. It is also important to consider the predominant (200) lattice plane exposure which is present for all platinum-silver nanocage catalyst which were analyzed. The consistent (200) exposure for these platinum-silver nanocages suggests that the effect of the lattice plane on the adsorption/desorption of reacting material on the surface of the catalysts will also be consistent for all synthesized platinum-silver nanocages.

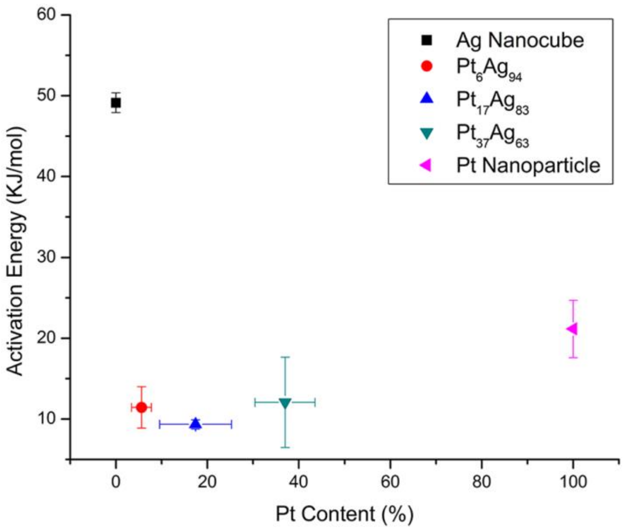

Figure C.6. The activation energy of the reduction of ferricyanide in the presence of silver nanocubes (black), Pt_6Ag_{94} alloy nanocage (red), $Pt_{17}Ag_{83}$ alloy nanocage (blue), $Pt_{37}Ag_{63}$ alloy nanocage (green), and solid platinum nanoparticles (pink). There is a marked decrease in the activation energy of this reaction when the platinum-silver alloy catalysts are present. It is likely that the formation of a platinum-silver alloy and the exposure of the (200) lattice plane are responsible for this increased activity.

While it is difficult to differentiate between these two factors, both factors can be attributed to the observed low activation energy for the platinum-silver nanocage catalysts. However, it is important to note that all platinum-silver nanocages exhibit statistically equivalent activation energies towards this reaction regardless of platinum content. As a result, it is apparent that the maximum reduction in the activation energy of this reaction can be achieved at a very low platinum content. Thus it is possible that increasing the platinum content within these alloys neither favorably nor unfavorably affects the d-band position of the alloy and the resultant adsorption/desorption of reacting material on the surface of the catalyst. For an expensive catalyst material like platinum, this is a very promising result.

When this result is compared to the EDX map of Pt_6Ag_{94} (Figure C.3I), the GRR provides a low platinum content alloy nanocatalyst with both a high utilization of platinum atoms on the exterior surface of the catalyst and an equivalent activity to catalysts with higher platinum contents. As a result, we can see that the GRR is a synthetic route which produces a highly cost effective platinum based catalytic material. Additionally, this synthetic route is not limited to this reaction alone. Due to the high degree of control of the shape of silver nanoparticles, the synthesis of nonporous platinum alloys through the GRR can be applied to a wide range of catalyst shapes and thus be tailored to a wide range of catalytic reactions.

C.4. Concluding Remarks

In this study we have shown the GRR to be a viable synthetic route for the formation of new platinum based alloy catalysts with both an increased catalytic activity and reduced platinum loading. The GRR is a versatile synthetic approach that provides precise control over the shape and composition of the resultant catalyst. Both the shape and the identity of the dominant exposed lattice planes of the template nanoparticle can be preserved throughout the progression of the GRR. Due to recent developments regarding the correlation between favorable adsorption/desorption of reacting species and the lattice plane that is exposed to the surrounding solution, the degree of control over the synthesis of platinum based catalysts the GRR offers will be vital to the development of new platinum based catalysts whose activity can be tailored to any given reaction. Herein we see that a maximum reduction in the activation energy for the reduction of ferricyanide can be achieved for a platinum-silver alloy nanocage catalyst with only 6% platinum content. This platinum-sivler nanocage exhibits a high degree of platinum utilization at the surface of the catalyst. Finally, it is important to note that all kinetic data collected in this study was not normalized to mass or surface area. As a result, conclusions regarding the activity of these materials towards this reaction cannot be drawn. Even so, the GRR is highly versatile synthetic method which can be applied to any shape, size or composition and will be very useful for the development of new low cost and potentially highly active platinum based catalysts.

C.5. References

(1) Moiseev, I. Catalysis: 2000 AD1. Kinet. Catal. **2001**, 42, 1-22.

(2) Cortright, R.; Davda, R.; Dumesic, J. A. Hydrogen from Catalytic Reforming of Biomass-Derived Hydrocarbons in Liquid Water. Nature **2002**, 418, 964-967.

(3) Zheng, J.; Cullen, D. A.; Forest, R. V.; Wittkopf, J. A.; Zhuang, Z.; Sheng, W.; Chen, J. G.; Yan, Y. Platinum–Ruthenium Nanotubes and Platinum–Ruthenium Coated Copper Nanowires as Efficient Catalysts for Electro-Oxidation of Methanol. ACS Catal. **2015**, 5, 1468-1474.

(4) Voltz, S. E.; Morgan, C. R.; Liederman, D.; Jacob, S. M. Kinetic Study of Carbon Monoxide and Propylene Oxidation on Platinum Catalysts. Ind. Eng. Chem. Prod. Res. Dev. **1973**, 12, 294-301.

(5) Gasteiger, H. A.; Kocha, S. S.; Sompalli, B.; Wagner, F. T. Activity Benchmarks and Requirements for Pt, Pt-Alloy, and Non-Pt Oxygen Reduction Catalysts for PEMFCs. Appl. Catal., B **2005**, 56, 9-35.

(6) Burch, R.; Breen, J.; Meunier, F. A Review of the Selective Reduction of NOx With Hydrocarbons Under Lean-Burn Conditions with Non-Zeolitic Oxide and Platinum Group Metal Catalysts. Appl. Catal., B **2002**, 39, 283-303.

(7) Survey, U. S. G. Mineral Commodity Summaries 2015: U.S. Geological Survey. Interior, U. S. D. o. t., Ed. **2015**; pp 1-196.

(8) Luo, J.; Maye, M. M.; Petkov, V.; Kariuki, N. N.; Wang, L.; Njoki, P.; Mott, D.; Lin, Y.; Zhong, C.-J. Phase Properties of Carbon-Supported Gold-Platinum Nanoparticles with Different Bimetallic Compositions. Chem. Mater. **2005**, 17, 3086-3091.

(9) Chen, Y.; Liang, Z.; Yang, F.; Liu, Y.; Chen, S. Ni–Pt Core–Shell Nanoparticles as Oxygen Reduction Electrocatalysts: Effect of Pt Shell Coverage. J. Phys. Chem. C **2011**, 115, 24073-24079.

(10) Alia, S. M.; Jensen, K. O.; Pivovar, B. S.; Yan, Y. Platinum-Coated Palladium Nanotubes as Oxygen Reduction Reaction Electrocatalysts. ACS Catal. **2012**, 2, 858-863.

(11) Carpenter, M. K.; Moylan, T. E.; Kukreja, R. S.; Atwan, M. H.; Tessema, M. M. Solvothermal Synthesis of Platinum Alloy Nanoparticles for Oxygen Reduction Electrocatalysis. J. Am. Chem. Soc. **2012**, 134, 8535-8542.

(12) Zhang, J.; Lima, F.; Shao, M.; Sasaki, K.; Wang, J.; Hanson, J.; Adzic, R. Platinum Monolayer on Nonnoble Metal-Noble Metal Core-Shell Nanoparticle Electrocatalysts for O2 Reduction. J. Phys. Chem. B **2005**, 109, 22701-22704.

(13) Cochell, T.; Manthiram, A. Pt@PdxCuy/C Core–Shell Electrocatalysts for Oxygen Reduction Reaction in Fuel Cells. Langmuir **2012**, 28, 1579-1587.

(14) Mani, P.; Srivastava, R.; Strasser, P. Dealloyed Binary PtM 3 (M= Cu, Co, Ni) and Ternary PtNi3 M (M= Cu, Co, Fe, Cr) Electrocatalysts for the Oxygen Reduction Reaction: Performance in Polymer Electrolyte Membrane Fuel Cells. J. Power Sources **2011**, 196, 666-673.

(15) Wang, Y.-J.; Zhao, N.; Fang, B.; Li, H.; Bi, X. T.; Wang, H. Carbon-Supported Pt-Based Alloy Electrocatalysts for the Oxygen Reduction Reaction in Polymer Electrolyte Membrane Fuel Cells: Particle Size, Shape, and Composition Manipulation and Their Impact to Activity. Chem. Rev. **2015**, 115, 3433-3467.

(16) Dhavale, V. M.; Kurungot, S. Cu–Pt Nanocage with 3-D Electrocatalytic Surface as an Efficient Oxygen Reduction Electrocatalyst for a Primary Zn–Air Battery. ACS Catal. **2015**, 5, 1445-1452.

(17) Zhao, X.; Chen, S.; Fang, Z.; Ding, J.; Sang, W.; Wang, Y.; Zhao, J.; Peng, Z.; Zeng, J. Octahedral Pd@ Pt1. 8Ni Core–Shell Nanocrystals with Ultrathin PtNi Alloy Shells as Active Catalysts for Oxygen Reduction Reaction. J. Am. Chem. Soc. **2015**, 137, 2804-2807.

(18) Yu, T.; Kim, D. Y.; Zhang, H.; Xia, Y. Platinum Concave Nanocubes with High-Index Facets and their Enhanced Activity for Oxygen Reduction Reaction. Angew. Chem. Int. Ed. **2011**, 50, 2773-2777.

(19) Wang, C.; Daimon, H.; Sun, S. Dumbbell-Like Pt−Fe3O4 Nanoparticles and their Enhanced Catalysis for Oxygen Reduction Reaction. Nano Lett. **2009**, 9, 1493-1496.

(20) Rabis, A.; Rodriguez, P.; Schmidt, T. J. Electrocatalysis for Polymer Electrolyte Fuel Cells: Recent Achievements and Future Challenges. ACS Catal. **2012**, 2, 864-890.

(21) Watanabe, M.; Tryk, D. A.; Wakisaka, M.; Yano, H.; Uchida, H. Overview of Recent Developments in Oxygen Reduction Electrocatalysis. Electrochim. Acta **2012**, 84, 187-201.

(22) Wanjala, B. N.; Fang, B.; Loukrakpam, R.; Chen, Y.; Engelhard, M.; Luo, J.; Yin, J.; Yang, L.; Shan, S.; Zhong, C.-J. Role of Metal Coordination Structures in Enhancement of Electrocatalytic Activity of Ternary Nanoalloys for Oxygen Reduction Reaction. ACS Catal. **2012**, 2, 795-806.

(23) Nesselberger, M.; Ashton, S.; Meier, J. C.; Katsounaros, I.; Mayrhofer, K. J.; Arenz, M. The Particle Size Effect on the Oxygen Reduction Reaction Activity of Pt Catalysts: Influence of Electrolyte and Relation to Single Crystal Models. J. Am. Chem. Soc. **2011**, 133, 17428-17433.

(24) Manbeck, K. A.; Musselwhite, N. E.; Carl, L. M.; Kauffman, C. A.; Lyons, O. D.; Navin, J. K.; Marsh, A. L. Factors Affecting Activity and Selectivity During Cyclohexanone Hydrogenation with Colloidal Platinum Nanocatalysts. Appl. Catal., A **2010**, 384, 58-64.

(25) Narayanan, R.; El-Sayed, M. A. Some Aspects of Colloidal Nanoparticle Stability, Catalytic Activity, and Recycling Potential. Top. Catal. **2008**, 47, 15-21.

(26) Cuenya, B. R. Synthesis and Catalytic Properties of Metal Nanoparticles: Size, Shape, Support, Composition, and Oxidation State Effects. Thin Solid Films **2010**, 518, 3127-3150.

(27) Narayanan, R.; El-Sayed, M. A. Shape-Dependent Catalytic Activity of Platinum Nanoparticles in Colloidal Solution. Nano Lett. **2004**, 4, 1343-1348.

(28) Lu, H. M.; Meng, X. K. Theoretical Model to Calculate Catalytic Activation Energies of Platinum Nanoparticles of Different Sizes and Shapes. J. Phys. Chem. C **2010**, 114, 1534-1538.

(29) Viswanathan, V.; Hansen, H. A.; Rossmeisl, J.; Nørskov, J. K. Universality in Oxygen Reduction Electrocatalysis on Metal Surfaces. ACS Catal. **2012**, 2, 1654-1660.

(30) Rana, M.; Chhetri, M.; Loukya, B.; Patil, P. K.; Datta, R.; Gautam, U. K. High-Yield Synthesis of Sub-10 nm Pt Nanotetrahedra with Bare⟨111⟩ Facets for Efficient Electrocatalytic Applications. ACS Appl. Mater. Interfaces **2015**, 7, 4998-5005.

(31) Pinto, L. M.; Maia, G. Oxygen Adsorption on PdPt/Au (111)–DFT Calculations. J. Phys. Chem. C **2015**, 119, 8213-8216.

(32) Stamenkovic, V. R.; Fowler, B.; Mun, B. S.; Wang, G.; Ross, P. N.; Lucas, C. A.; Marković, N. M. Improved Oxygen Reduction Activity on Pt3Ni (111) via Increased Surface Site Availability. Science **2007**, 315, 493-497.

(33) Cui, C.; Gan, L.; Li, H.-H.; Yu, S.-H.; Heggen, M.; Strasser, P. Octahedral PtNi Nanoparticle Catalysts: Exceptional Oxygen Reduction Activity by Tuning the Alloy Particle Surface Composition. Nano Lett. **2012**, 12, 5885-5889.

(34) Oezaslan, M.; Hasché, F.; Strasser, P. PtCu3, PtCu and Pt3Cu Alloy Nanoparticle Electrocatalysts for Oxygen Reduction Reaction in Alkaline and Acidic Media. J. Electrochem. Soc. **2012**, 159, B444-B454.

(35) Wakisaka, M.; Mitsui, S.; Hirose, Y.; Kawashima, K.; Uchida, H.; Watanabe, M. Electronic Structures of Pt-Co and Pt-Ru Alloys for CO-Tolerant Anode Catalysts in Polymer Electrolyte Fuel Cells Studied by EC-XPS. J. Phys. Chem. B **2006**, 110, 23489-23496.

(36) Sun, Y.; Mayers, B. T.; Xia, Y. Template-Engaged Replacement Reaction: A One-Step Approach to the Large-Scale Synthesis of Metal Nanostructures with Sollow Interiors. Nano Lett. **2002**, 2, 481-485.

(37) Lu, P.; Teranishi, T.; Asakura, K.; Miyake, M.; Toshima, N. Polymer-Protected Ni/Pd Bimetallic Nano-Clusters: Preparation, Characterization and Catalysis for Hydrogenation of Nitrobenzene. J. Phys. Chem. B **1999**, 103, 9673-9682.

(38) Toshima, N.; Yonezawa, T. Bimetallic Nanoparticles—Novel Materials for Chemical and Physical Applications. New J. Chem. **1998**, 22, 1179-1201.

(39) Wang, Y.; Toshima, N. Preparation of Pd-Pt Bimetallic Colloids with Controllable Core/Shell Structures. J. Phys. Chem. B **1997**, 101, 5301-5306.

(40) Ferrer, D.; Torres-Castro, A.; Gao, X.; Sepulveda-Guzman, S.; Ortiz-Mendez, U.; Jose-Yacaman, M. Three-Layer Core/Shell Structure in Au-Pd Bimetallic Nanoparticles. Nano Lett. **2007**, 7, 1701-1705.

(41) Sun, Y.; Xia, Y. Alloying and Dealloying Processes Involved in the Preparation of Metal Nanoshells through a Galvanic Replacement Reaction. Nano Lett. **2003**, 3, 1569-1572.

(42) Lu, X.; Au, L.; McLellan, J.; Li, Z.-Y.; Marquez, M.; Xia, Y. Fabrication of Cubic Nanocages and Nanoframes by Dealloying Au/Ag Alloy Nanoboxes with an Aqueous Etchant Based on Fe (NO3) 3 or NH4OH. Nano Lett. **2007**, 7, 1764-1769.

(43) Wu, H.; Wang, P.; He, H.; Jin, Y. Controlled Synthesis of Porous Ag/Au Bimetallic Hollow Nanoshells with Tunable Plasmonic and Catalytic Properties. Nano Res. **2012**, 5, 135-144.

(44) Mahmoud, M. A.; El-Sayed, M. A. Reaction of Platinum Nanocatalyst with the Ferricyanide Reactant to Produce Prussian Blue Analogue Complexes. J. Phys. Chem. C **2007**, 111, 17180 - 17183.

(45) Mahmoud, M. A.; Saira, F.; El-Sayed, M. A. Experimental Evidence For The Nanocage Effect In Catalysis With Hollow Nanoparticles. Nano Lett. **2010**, 10, 3764-3769.

(46) Mahmoud, M. A.; Saira, F.; El-Sayed, M. A. Experimental Evidence For The Nanocage Effect In Catalysis With Hollow Nanoparticles. Nano Lett. **2010**, 10, 3764-3769.

(47) Sun, Y.; Xia, Y. Shape-Controlled Synthesis of Gold and Silver Nanoparticles. Science **2002**, 298, 2176-2179.